IPP-Report

Ralph Dux

Impurity Transport in Tokamak Plasmas

Impurity Transport in Tokamak Plasmas

Ralph Dux

Max-Planck-Institut für Plasmaphysik

D–85748 Garching b. München

Assoziation EURATOM–IPP

June 2004

Contents

1. Introduction
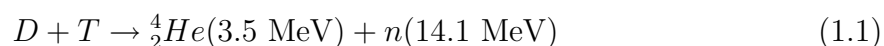
1.1   Fusion and Magnetic Confinement

The research of *controlled nuclear fusion* aims at the production of energy from the fusion of the two hydrogen isotopes deuterium and tritium. The cross section for the reaction

$$D + T \rightarrow {}_{2}^{4}He(3.5 \text{ MeV}) + n(14.1 \text{ MeV}) \tag{1.1}$$

reaches a maximum value of $\sigma_{DT,max} = 4.9 \times 10^{-28} \text{m}^2$ at a collision energy of 64 keV in the centre-of-mass frame. The fusion cross section is small against the relevant cross sections for Coulomb collisions between D^+ and T^+, and D^+ or T^+ with electrons. Thus, only a very small fraction of accelerated D^+ ions would cause a fusion reaction, when injected into a tritium rich target, because energy loss to the cold electrons has a factor of $> 10^7$ higher cross section than the fusion reaction. A net energy production can only be achieved when confining a sufficiently hot DT-plasma with almost equal temperatures of ions and electrons, such that the unavoidable Coulomb collisions do not lead to a loss of mean kinetic energy of the two fuel ions D^+ and T^+.

In a thermal plasma, the number of reactions per volume is given by the product of the densities of the reaction partners and the reaction parameter $\langle \sigma v \rangle$. Here, v is the relative velocity of the colliding particles and $\langle \rangle$ denotes an average over the Maxwellian velocity distribution. The reaction parameter $\langle \sigma_{DT} v \rangle$ of the DT-reaction and a few other fusion reactions is shown in Fig.1.1. The DT-reaction has the highest values with a broad maximum for ion temperatures T_i between 20 keV and 100 keV. Below T_i=10 keV, there is a steep decrease of $\langle \sigma_{DT} v \rangle$ and the envisaged fusion plasma needs to have a temperature above 10 keV.

Two schemes for the plasma confinement are subject to present day research. In the *inertial confinement* scheme, a DT-pellet with a diameter of $\approx$1 mm is compressed by about a factor of 1000 and heated up very rapidly to $T \approx$10 keV with a high power energy source (laser or heavy ion beams). Even at this temperature, inertia is sufficient to confine the plasma for a time duration of $\approx$1 ns, during which a considerable fraction of the DT-mixture fuses in a controlled explosion. The *magnetic confinement* scheme, which will be discussed below in more detail, uses a steady state plasma, which is confined
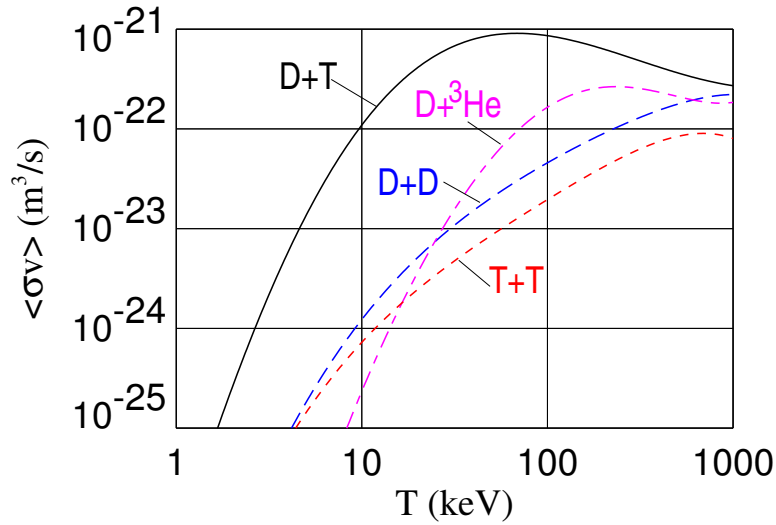
Figure 1.1:   *Reaction parameter $\langle \sigma v \rangle$ of some fusion reactions in a thermal plasma of temperature T.*

by magnetic fields. Net energy production in both schemes is only possible, if most of the energy needed for the heating of the plasma is drawn from the fusion reaction itself, i.e. from the $3.5\,\mathrm{MeV}$ α-particles, which are 'stopped' in the plasma by Coulomb collisions (α-*heating*).

The magnetic fields, which confine the plasma, have a toroidal topology. With this geometry, it is possible to avoid 'end losses', which arise due to the very high transport coefficients in hot plasmas in the direction of the magnetic field. The Lorentz force guides the charged particles along the magentic field. Due to the toroidal field line bending and the inhomogenity of the magnetic field, which has increasing field strength towards the axis of the torus, there is an extra drift velocity with opposite sign for ions and electrons in the direction of the torus axis (curvature- and ∇B-drift). For a purely toroidal magnetic field with $\vec{B} = \vec{B}_t$, these drifts lead to a charge seperation and the build up of an electric field along the torus axis causing a loss of the plasma due to $\vec{E} \times \vec{B}$-drifts on a ms time scale. This problem can be solved by an additional poloidal field $\vec{B}_p$, which produces a helical field line geometry. A magnetic field line winds around the centre of the plasma and spans a toroidal surface, which is called a *magnetic surfaces*. The particles, which follow the magnetic field lines are guided around the plasma centre and the vertical drift velocity moves the particle away and towards the field line depending on the particle position above or below the mid plane of the torus. Thus, the particle orbits have only a minor displacement from the magnetic field lines as discussed in section 3.1.

The poloidal magnetic field is either produced by external coils, as in the *stellarator* or by a toroidal plasma current, as in the *tokamak*. The tokamak approach yields a field line geometry, which is symmetric with respect to the torus axis and we restrict the following discussion to axi-symmetric solutions, i.e the tokamak case. Magnetic surfaces
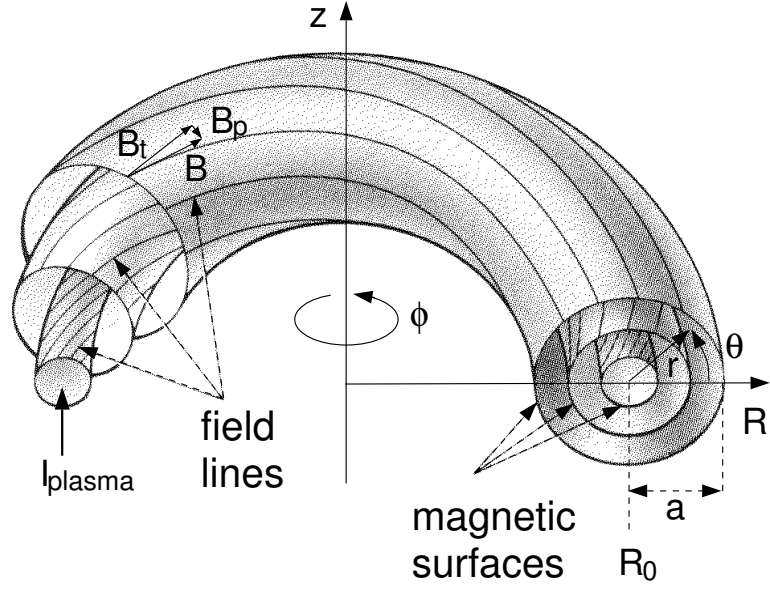
Figure 1.2:   *Geometry of magnetic field lines on the nested magnetic surfaces in a tokamak.*

in the tokamak are shown in Fig.1.2. The helicity of the magnetic field on a magnetic surface is described by the 'safety factor' q. q gives the number of toroidal turns, which the field line has to complete for 1 poloidal turn around the toroidal surface.

In the tokamak, the poloidal field is produced by a toroidal plasma current I_p. I_p is induced by a transformer, where the primary winding is fomed by a central solenoid and the plasma is the secondary winding. Due to the high electrical conductivity of hot plasmas, induced loop voltages of a few V are sufficient to drive plasma currents of several MA. The poloidal field at the plasma edge is of the order of 0.1 T and the toroidal field has a few T. The combination of toroidal field and plasma current is typically chosen such, that the safety factor at the plasma edge is in the range $q_{edge} \approx$ 3-5.

In equilibrium, the forces due to the radial gradient of the plasma pressure ∇p are counteracted by $\vec{j} \times \vec{B}$ forces.

$$\nabla p = \vec{j} \times \vec{B} \tag{1.2}$$

Thus, $\vec{j}$ and $\vec{B}$ are perpendicular to the pressure gradient: $\vec{j} \cdot \nabla p = \vec{B} \cdot \nabla p = 0$. The pressure is constant on the magnetic surfaces and the electric currents flow in the magnetic surface. The magnetic flux and the total current through any poloidally or toroidally closed line on the magnetic surface is constant and the poloidal or toroidal magnetic flux is commonly used to label the *flux surfaces*. For a fusion reactor, the central plasma pressure, which has to be stabilised by the $\vec{j} \times \vec{B}$ forces, is $\approx 1\,\text{MPa}$.

The shape and position of the magnetic surfaces is controlled by additional external toroidal coils. Toroidal magnetic surfaces can only be produced in a certain inner volume of the tokamak and the magnetic *separatrix* separates the *confined* inner region from the
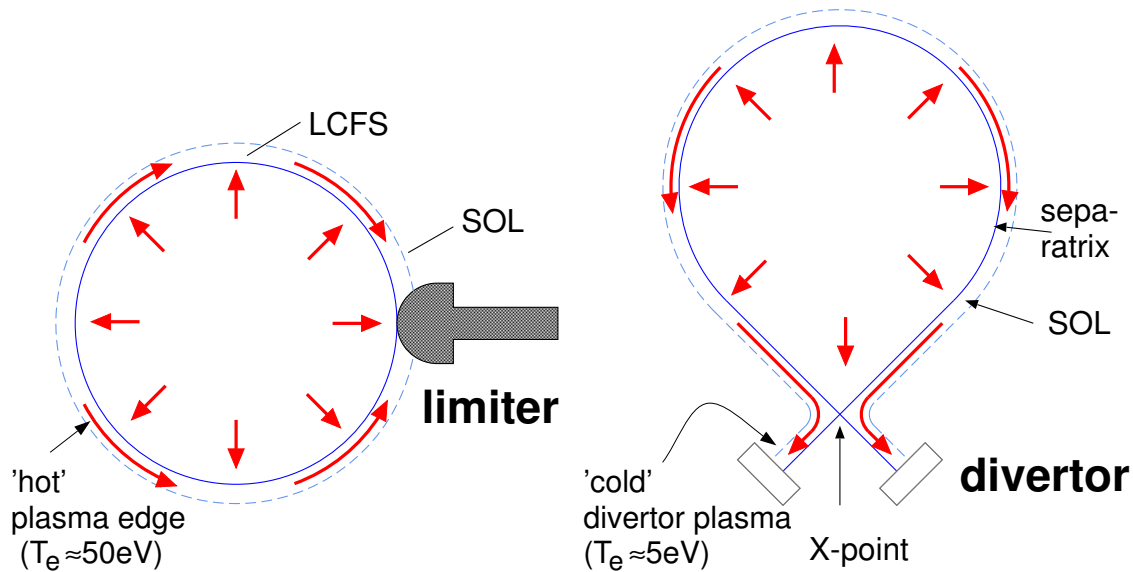
Figure 1.3: *Poloidal cross section of a tokamak with limiter and divertor configuration.*

outer region where the field lines close outside of the plasma vessel. The *last closed flux surface* (LCFS) is either given by the magnetic separatrix as in the *divertor* configuration or by a part of the plasma wall, which limits the confined plasma inside the magnetic separatrix, as in the *limiter* configuration. The two configurations are illustrated in Fig.1.3. The plasma region outside the LCFS is termed the *scrape off layer* (SOL) and loosely called the region of 'open' field lines, i.e. field lines which intersect with some part of the vessel wall. The separatrix in the depicted divertor configuration has the shape of an X in the lower part and the poloidal field is zero at this so called *X-point*. In the divertor configuration, the plasma wall interaction mainly takes place in a specially designed part of the plasma vessel, which is somewhat removed from the confined plasma and is termed the *divertor*. Here, it is possible to achieve a reduction of the plasma temperatures compared to the temperature at the LCFS which is advantageous with respect to the release of wall materials into the plasma (see section 1.3). Present day designs of a fusion reactor are based on the divertor concept.

The ideal fusion plasma just consists of electrons, deuterium and tritium ions. All other ions, which contribute to the pressure, that has to be balanced, are considered as impurities. For a given achievable plasma pressure, impurity ions cause a dilution of the DT mixture and reduce the α-heating, which is necessary for a positive energy balance. Furthermore, plasma radiation increases with the introduction of impurities (line and continuum radiation) and the increased energy loss of the optically thin plasma makes the sustainment of the high plasma temperatures more difficult. Helium from the DT reaction is of course unavoidable. Other impurities originate from the plasma facing wall components, which are eroded due to the bombardment with energetic plasma ions. Several materials are investigated as candidates for different plasma facing components

including low-Z elements beryllium and carbon up to the high-Z element tungsten. Many aspects of these materials, like thermal heat conduction, mechanical, chemical, electrical properties, and erosion yields come into play and have to be judged against the behaviour of these elements in the plasma. The present design for the next step device ITER is based on a mixture of low-Z and high-Z materials, while in a steady state power producing device, the erosion rate and the degradation of material properties due to neutron damage seems to be far to high for a low-Z plasma facing material. Furthermore, the injection of the noble gases neon and argon is considered to achieve low plasma temperatures in front of the plasma facing wall components. In the next section, upper limits for the allowed impurity concentrations in the central part of the confined plasma are evaluated.

1.2 Burn Condition and Confinement Times

The term *burning* or *ignited* plasma describes the situation, where the confined plasma burns the fuel nuclei D and T to He without any external heating sources. In the concept of magnetic confinement, this is a steady-state situation, where all energy losses of the plasma are balanced by the α-heating.

$$P_\alpha = P_{Loss} = P_{trans} + P_{rad} \tag{1.3}$$

The energy losses are separated into heat transport losses P_{trans} due to conduction and convection and radiation losses P_{rad}. In the following, we will investigate the power balance without considering profile effects and the power densities shall represent some mean values over the plasma volume. Furthermore, we assume equal temperatures of all ions and electrons.

The plasma shall consist of the four ion species deuterium, tritium, helium and another not yet specified impurity. The fuel densities shall have the optimum 50/50 mixture, i.e. $n_D = n_T$, and the total DT-ion density is $n_D + n_T = n_i$. The impurity concentrations are denoted by $f_{He} = n_{He}/n_e$ and $f_I = n_I/n_e$. At the considered temperatures, He is doubly ionised and the other impurity has an average charge $\langle Z \rangle = \sum_Z Z n_{I,Z}/n_I$, where the fractional abundances of the impurity charge states $f_{I,Z} = n_{I,Z}/n_I$ shall be in corona ionisation equilibrium. The impurity concentrations determine the dilution of the fuel ions and we find from quasi-neutrality the fraction of fuel ions.

$$f_i = \frac{n_i}{n_e} = 1 - 2f_{He} - \langle Z \rangle f_I \tag{1.4}$$

The total particle density can also be expressed with the electron density and the impurity concentrations.

$$\frac{n_{tot}}{n_e} = 1 + f_i + f_{He} + f_I = 2 - f_{He} - (\langle Z \rangle - 1)f_I = f_{tot} \tag{1.5}$$
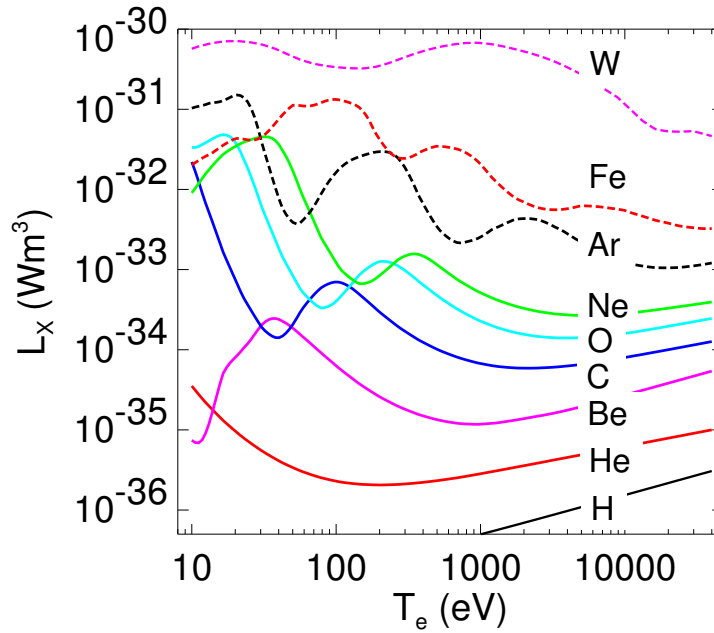
Figure 1.4:   *Radiative power parameter for some elements in the range from H to W.*

The α-particles, which are produced with energy E_α=3.52 MeV in the DT-fusion reaction, shall be perfectly confined during the slowing down to thermal energies. They are lost as thermal particles and transfer their whole initial energy E_α to the plasma. Thus, the α-heating power density is.

$$P_\alpha = n_D n_T \langle \sigma_{DT} v \rangle E_\alpha = \frac{1}{4} f_i^2 n_e^2 \langle \sigma_{DT} v \rangle E_\alpha \tag{1.6}$$

The fusion reaction rate $\langle \sigma_{DT} v \rangle$ is the average over a Maxwellian energy distribution being only a function of the ion temperature. It can be evaluated from the formulas given in Ref.[1, 2] and is displayed in Fig.1.1.

The power density due to radiative losses from line radiation (bound-bound transitions) and continuum radiation (free-bound and free-free transitions) can be expressed with the radiative power parameter $L_X(T)$ for the element X at temperature T, which adds the contributions from all charge states assuming corona ionisation equilibrium.

$$P_{rad} = n_e^2 L_{rad}(T) = n_e^2 (f_i L_H + f_{He} L_{He} + f_I L_I) \tag{1.7}$$

For the fully ionised light elements, L_X is dominated by the bremsstrahlung contribution being proportional to Z^2 and line radiation becomes important for heavy elements. The relevant atomic data are taken from the ADAS atomic data base [3] and for tungsten from the ADPACK data base [4, 5]. The radiative power parameter for a number of elements is shown in Fig.1.4.

The loss power density due to heat conduction and convection shall be described by the

empirical energy confinement time τ_E.

$$P_{trans} = \frac{W}{\tau_E} = \frac{3n_{tot}k_BT}{2\tau_E} = \frac{3f_{tot}n_ek_BT}{2\tau_E} \tag{1.8}$$

We replace each term in Eq.(1.3) by the according expressions of Eq.(1.6), (1.7) and (1.8).

$$n_e\tau_E = \frac{\frac{3}{2}f_{tot}k_BT}{\frac{1}{4}\langle\sigma_{DT}v\rangle f_i^2 E_\alpha - L_{rad}(T)} \tag{1.9}$$

The power balance defines the parameter $n_e\tau_E$ as a function of the temperature and the impurity concentrations f_{He} and f_I. However, the He density is not a free parameter being proportional to the fusion reactions per volume. By introducing a global particle confinement time τ_α^* for the α-particles, the particle balance reads.

$$\frac{1}{4}f_i^2 n_e^2\langle\sigma_{DT}v\rangle = \frac{n_{HE}}{\tau_\alpha^*} = \frac{n_e f_{He}}{\rho\tau_E} \tag{1.10}$$

We use the term global particle confinement time to denote the fact, that the decay time of He from the system is not only a function of the transport parameters of the confined plasma, i.e. diffusion coefficient and drift velocity, but depends strongly on the He recycling at the plasma walls and the pumping efficiency. Only some fraction of the He particles, which are lost from the confined plasma, arrive in the pumping duct, while the rest recycles as neutral helium from the plasma walls and can again enter the confined plasma. Thus, τ_α^* will be significantly larger than τ_E and the factor is denoted with ρ: $\tau_\alpha^*=\rho\tau_E$.

Equations (1.9) and (1.10) allow the calculation of $n_e\tau_E$ and f_{HE} as a function of T, ρ and f_I. In Fig.1.5, we show some solutions assuming carbon and tungsten as additional impurity. The upper figures depict the so called *triple product* or *fusion product* $n_eT\tau_E$, which has to be achieved in a steady state burning plasma and the lower figures give the according He concentrations. The black line is the idealised burn condition for $\rho = 0$ and f_I=0, i.e. no fuel dilution and radiation due to impurities and infinitely fast removal of He. The minimum is found at $T = 14\,\text{keV}$ with $n_eT\tau_E$=3×10²¹ keVm⁻³s. For finite ρ, the ignition lines are closed. For each possible temperature, there is a solution with low triple product and low f_{He} and a branch with high $n_eT\tau_E$ and high f_{He}. The blue line is calculated for $\rho = 5$ and f_I=0, where the minimum fusion product has an increased value of $n_eT\tau_E$=3.8×10²¹ keVm⁻³s at $T = 13\,\text{keV}$ with a He concentration of f_{HE}=6%. Finally, C and W are added each with two different concentrations. For both impurities, the lower concentration was chosen such, that it leads to a further increase of the minimum fusion product by 20%. The value of the respective concentration is $f_{C,20\%}$=1% for C and for W, it is only $f_{W,20\%}$=0.0045% due to the strongly increased radiative power L_W of the high-Z element. The next line of each impurity shows the behaviour for a concentration, which is a factor of 4 above the 20%-value. We note,
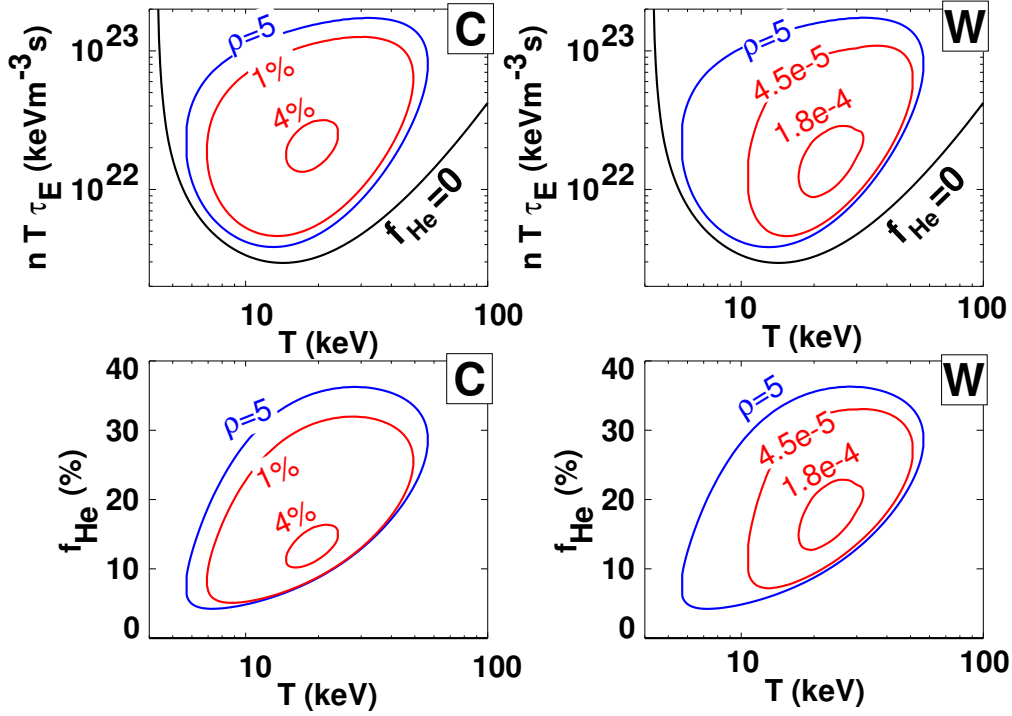
Figure 1.5:   *Fusion product $n_e T \tau_E$ and helium concentration f_{He} for a burning DT-plasma: Black lines are for zero helium concentration $f_{He}=0$, blue lines for global helium confinement time $\tau_\alpha^* = 5\tau_E$ and red lines for $\tau_\alpha^* = 5\tau_E$ and additional carbon(tungsten) impurity on the left(right) side.*

how quickly the operating window vanishes. Above a certain impurity concentration, the power balance can not be fulfilled.

For a global helium confinement time $\tau_\alpha^* = 5\tau_E$, the impurity concentration $f_{I,20\%}$ was calculated for the impurity elements Be, C, O, Ne, Ar, Fe, Kr, Xe, and W, i.e. the concentration which increases the minimum fusion product for $f_I=0$ by 20% to a value of $n_e T \tau_E = 4.6 \times 10^{21}$ keVm^{-3}s. In Fig.1.6, the 20%-concentrations are plotted as diamonds versus the nuclear charge of the added impurity demonstrating the fact that the maximum allowed impurity fraction strongly decreases with the nuclear charge of the element. The upper x-axis gives the temperatures of the respective minima, which are close to the 13 keV value at $f_I=0$. The detrimental effect of the different elements depends again on the impurity charge. The light, fully ionised elements mainly decrease the heating power by diluting the fuel ions, while the heavy elements mainly cause an increased radiation loss of the plasma. ΔP_{rad} and ΔP_α shall be the difference of radiated power and α-heating power with respect to the case with zero impurity concentration $f_I = 0$ and the parameter $\Delta P_{rad}/\Delta P_\alpha$ quantifies the main effect of the different impurities. For Be, radiation is negligible with $\Delta P_{rad}/\Delta P_\alpha$ below 0.1, while for Fe and the heavier elements, the increased radiation is about a factor of 10 above the α-heating power reduction.

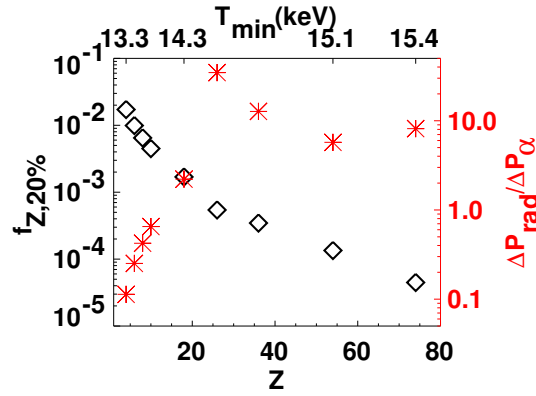Figure 1.6:   *Impurity concentrations(diamonds), which lead to a 20% increase of the minimum fusion product with respect to $f_I=0$ at a given global helium confinement time $\tau_\alpha^* = 5\tau_E$. The parameter $\Delta P_{rad}/\Delta P_\alpha$ (red stars) allows a comparison of the different detrimental effects of the impurity on the α-power and the radiative loss power.*

We conclude, that the requirements for plasma purity in the fusion reactor are very high. When considering the presence of more than one impurity from the plasma wall, the maximum allowed concentrations for the single impurity, which are approximately the values given in Fig.1.6, have to be reduced even further to guarantee enough operational space. More detailed investigations [6, 7, 8], which account for profile effects, need to specify the transport parameters for heat and particle transport, as well as the heating profile due to the slowing down of the MeV α-particles or the eventual loss of the α-particles before thermalization [9, 10].

1.3   Relevance of Impurity Transport

We found in the previous section, that it is essential to have low impurity concentrations in the plasma to fulfil the condition of a steady burning fusion plasma. These concentration limits apply only to the hot central part of the confined plasma. Here, where D and T predominantly fuse, dilution matters and only radiation losses in the centre shortcut the transport of energy from centre to edge. In equilibrium, central impurity densities increase with the the rate of impurity production. Furthermore, they depend on the location of the impurity sources, and the impurity transport perpendicular and parallel to the magnetic field lines.

We begin with a few remarks about the impurity sources. The helium production rate is defined by the rate of fusion reactions and has a fixed value, when a certain fusion power shall be achieved. For the impurities, which are eroded from the plasma facing components, the production rate strongly depends on the choice of the material. First of all, the heat conductivity of the material has to be high enough to enable operation
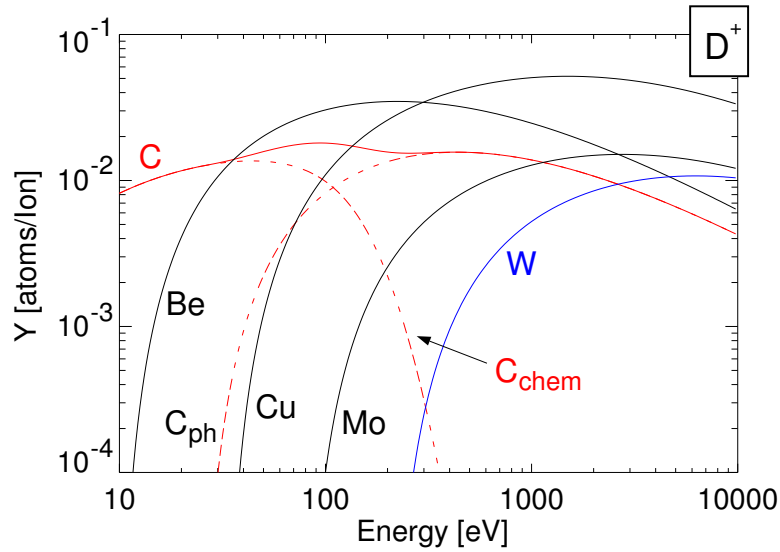
Figure 1.7:   *Erosion yields for various target materials as a function of the projectile energy for incident deuterium ions under normal incidence.*

at surface temperatures, which are well below the melting or sublimation temperature for a given steady state power load from the plasma. Besides this condition, two erosion mechanisms need to be distinguished: the *physical sputtering*, which is due to elastic energy transfer from the incident particles onto the target atoms, and *chemical erosion*, where the incident particles form volatile molecules with the target atoms. Physical sputtering takes place, when the energy transfered onto surface atoms is above the surface binding energy E_s, which happens only, when the kinetic energy of the incident particle is above a certain threshold value E_{th}. The energy transfer between the projectile with mass m_p and the target atoms with mass m_t depends on the mass ratio, where the maximum transferable energy fraction in a single collision is $\gamma = 4m_t m_p/(m_t + m_p)^2$. Thus, the ratio E_{th}/E_s becomes large for small values of γ [11, 12], while E_s of different materials considered for plasma facing components do not vary that strongly. A few examples for the physical sputtering yield Y_{phys} by deuterium projectiles under normal incidence are shown in Fig.1.7. The surface binding energies of Be, C, and W are 3.4 eV, 7.4 eV and 8.7 eV, while the respective sputtering thresholds are 10 eV , 27 eV, and 209 eV [13]. For carbon, chemical reactions with hydrogen dominate the carbon erosion at ion energies below 100 eV as is shown in Fig.1.7. The hydrocarbon formation is a complex multi-step process depending on particle energy, particle flux density, surface temperature and material properties [14]. The formation of oxides is of less importance due to the small oxygen concentrations, which are below 1% in present day devices.

The energy spectrum of the incident particles has contributions from different loss mechanisms, and the particle load varies significantly between different locations. The main contribution in the divertor is the parallel ion flow along the magnetic field lines, while

in the main chamber fast ions from the neutral beam injection or the ion cyclotron heating and fast hydrogenic neutrals, which are formed in charge exchange processes, come into play. The parallel losses are strongest at the separatrix and show a steep decay with the distance to the separatrix due to the large anisotropy of the transport coefficients being much smaller perpendicular to the magnetic field direction. For equal temperatures of ions and electrons, the mean ion energy on the target is approximately $\langle E \rangle \approx 2k_B T + 3Zk_B T$, where the second term proportional to the ion charge Z is due to the acceleration in the sheath potential. This term is especially important for the physical sputtering of high-Z materials, where a low fraction of higher charged impurity ions leads to a substantial increase of Y_{phys} due to the increased energy of the projectile, and since impurity ions also have a reduced threshold energy due to the higher mass.

Besides fusion produced helium and impurities from the plasma facing components, injection of noble gases is foreseen in a fusion reactor in order to increase the radiation losses in the edge region of the plasma. According to the radiative power parameters depicted in Fig.1.4, the radiated power per impurity density is considerably higher in the low temperature edge region at 10-1000 eV compared to the hot core at a few 10 keV. This dependence is used by the concept of a *radiative mantle* [15, 5, 16, 17], where a well controlled amount of added impurities shall help to spread the power load over larger areas and to reduce the temperature in front of the plasma facing components, while central radiation losses are still kept low. It is thus a measure to reduce the strong localised power deposition and erosion close to the separatrix.

The acceptable erosion rates are determined by the required life time of the plasma facing components as well as by the low limits for the allowed central impurity concentrations, which are very low for the high-Z elements and in the percent range for beryllium and carbon. Here, impurity transport between the wall components and the plasma centre is the key element, which has to be considered. The radial impurity flows can either be driven by the radial impurity gradients being caused by diffusion, but may also have a convective component, which is inwardly or outwardly directed independent of the impurity gradient. For purely diffusive transport, the radial flows will reduce the driving gradient. For the case of the fusion produced helium, there is a central source of helium ions, which maintains the radial gradient to the outside, and in equilibrium, diffusion leads to a steady outwardly directed net flow of helium. The total radial helium flux is of course just equal to the production rate and the diffusion coefficient decides, whether a large or low radial helium gradient is needed to maintain that radial flow. For the other impurities as well as for the recycling helium, the source location is at the very edge of the plasma, and inside the source region, the radial impurity gradient will become zero in equilibrium for purely diffusive transport independent of the diffusion coefficient. In this case, radial and parallel transport in the edge, and the impurity source distribution in the edge play the dominant role. For edge produced impurities, also the

role of the convective flows are very important, since they can provoke strong radial impurity gradients for cases, where the directed convective component is the dominant flow contribution. The contribution of the convective flows depends on the impurity charge and on the type of plasma transport mechanism.

Thus, the radial transport requirements for helium and the other impurities are somewhat different. The fusion produced helium has to be removed from the central plasma at a similar pace as the energy is transported towards the edge, while for the other impurities the edge transport and the influence of convective flows are very important. Transport investigations have to be performed for the whole range of elements from He up to W. Since the construction of large fusion plasma experiments is expensive and time consuming, it is not possible to test many elements as plasma wall components on a large scale. It is therefore not of mere academic interest to understand the transport behaviour of the different elements in terms of the underlying physical mechanisms. This knowledge is rather needed to predict impurity transport in next step fusion devices, and will influence the material choice or indicate advantageous plasma operation scenarios with low central impurity concentrations.

2. The Radial Impurity Transport Equation

For the description of impurity fluxes perpendicular to the magnetic surfaces, the common ansatz uses a sum of a diffusive and a convective flux density. With this ansatz the continuity equation can be transformed into a radial transport equation, which allows to calculate the temporal evolution of the radial impurity profiles in terms of the diffusion coefficient and the drift velocity for given boundary conditions. The characteristics of the general solution and specific cases with simple analytical solutions will illustrate the main influences of the transport coefficients on characteristic time scales and the equilibrium density profiles for a constant influx of neutral impurities.

For the analysis of spectroscopic measurements, it is necessary to know the radial location and the fractional abundance of each ion stage and the system of the coupled transport equations for all ion stages of the impurity has to be solved. In these equations, neighbouring ion stages couple through ionisation and recombination and solutions can only be obtained by numerical methods. The preferred algorithm will be given and applied to calculate the change of ion stage abundances from the corona ionisation equilibrium.

Radial impurity transport is caused by various physical phenomena. The mechanisms, which might be treated with the above ansatz are turbulence due to micro-instabilities and Coulomb collisions, while macroscopic instabilities might have larger radial scale lengths than the density gradient lengths. The different contributions to the collisional transport coefficients can be calculated in most circumstances, while there is still very little knowledge of turbulent impurity transport.

2.1   Flux Surface Averaged Transport

The law of particle conservation for the particle density $n_{I,Z}$ of impurity I in ion stage Z may be written as:

$$\frac{\partial n_{I,Z}}{\partial t} = -\nabla \vec{\Gamma}_{I,Z} + Q_{I,Z} \tag{2.1}$$

where $\vec{\Gamma}_{I,Z}$ is the flux density of the impurity and $Q_{I,Z}$ represents the sources and sinks due to ionisation, recombination and charge exchange. The source and sink term connects neighbouring charge states. With an ansatz for the density dependence of the transported
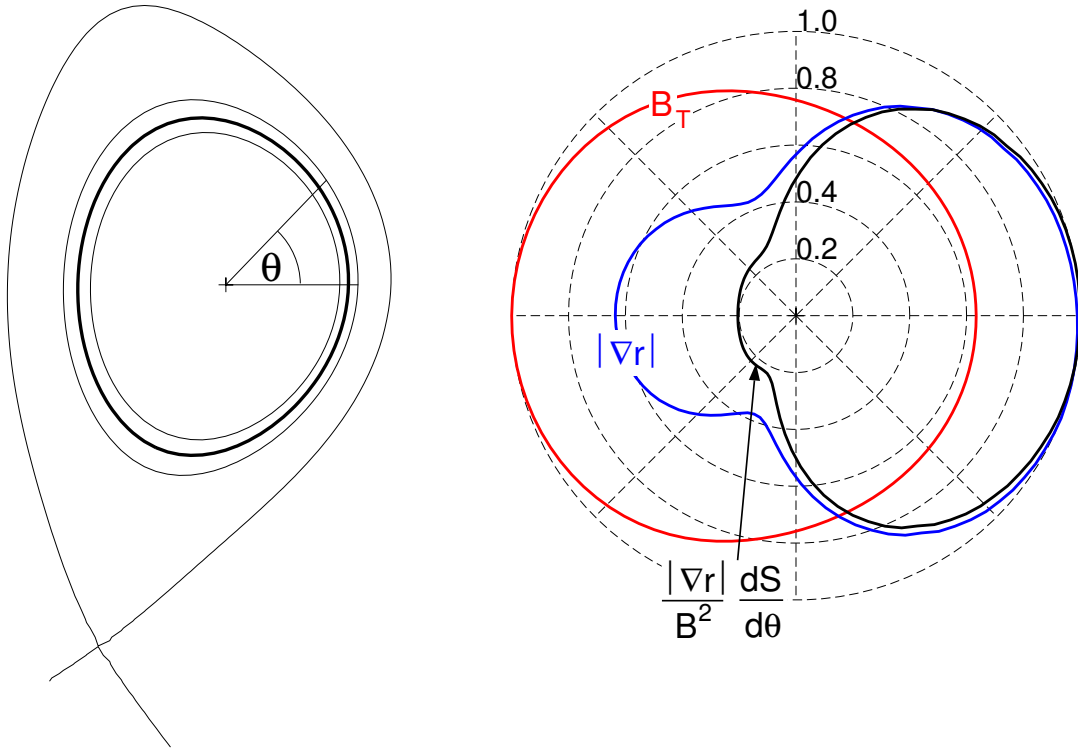
Figure 2.1:   *For the magnetic flux surface, whose poloidal projection is drawn on the left with a thick line, the poloidal variation of the toroidal magnetic field(red), the gradient(blue), and the contributions to the classical part of the collisional radial impurity fluxes(black) are shown in the polar plot on the right. All values are normalized to their maximum value.*

flux density $\vec{\Gamma}_{I,Z}$, the particle conservation equation shall be transformed into an impurity transport equation. Here, we are interested in the *radial* transport perpendicular to the magnetic flux surfaces, since the large transport coefficients parallel to the magnetic field cause a practically constant density $n_{I,Z}$ on the magnetic flux surface. Even though $n_{I,Z}$ and also the source/sink term $Q_{I,Z}$ are constant on the flux surface, the radial component of $\vec{\Gamma}_{I,Z}$ shows a variation with the poloidal angle θ. One reason is the poloidally varying distance of the flux surfaces being shorter on the outboard than on the inboard. This leads to a poloidal variation of the gradients of density and temperature, which are the driving terms for the radial impurity flux. Another reason is the $1/R$ dependence of the toroidal magnetic field B_T. In Fig.2.1, the poloidal projection of a few flux surfaces are sketched. For one flux surface, the dependence of the gradient and of B_T on θ are shown in a polar plot. Both quantities vary by about a factor of 2.

The correct flux surface average of Eq.(2.1) is derived by the following steps (see Ref.[18]). Inside the last closed flux surface (LCFS), Eq.(2.1) is integrated over the volume V inside a flux surface which leads to.

$$\frac{\partial}{\partial t} \int n_{I,Z} \, dV = - \oint \vec{\Gamma}_{I,Z} \, d\vec{S} + \int Q_{I,Z} \, dV \qquad (2.2)$$

The flux surface shall be labeled with ρ, where ρ rises from centre to edge. Thus, $\nabla\rho/|\nabla\rho|$ is the unit vector $\vec{e}_r$ perpendicular to the flux surface pointing towards the outside of the enclosed volume, and the flux density integral becomes

$$\oint \vec{\Gamma}_{I,Z}\, d\vec{S} = \oint \vec{\Gamma}_{I,Z}\frac{\nabla\rho\, dS}{|\nabla\rho|} = \oint \Gamma_{I,Z}^{\rho}\frac{dS}{|\nabla\rho|} \tag{2.3}$$

where $\Gamma_{I,Z}^{\rho}$ is the *radial* contravariant component of the particle flux density $\Gamma_{I,Z}^{\rho} = \vec{\Gamma}_{I,Z}\nabla\rho$. Using the flux surface average of an arbitrary scalar quantity $\mathcal{F}$

$$\langle\mathcal{F}\rangle = \left(\frac{\partial V}{\partial\rho}\right)^{-1}\oint \mathcal{F}\frac{dS}{|\nabla\rho|} \tag{2.4}$$

and

$$\int \mathcal{F}dV = \int_0^{\rho} d\rho\frac{\partial V}{\partial\rho}\langle\mathcal{F}\rangle \tag{2.5}$$

the continuity equation (2.2) becomes

$$\frac{\partial}{\partial t}\int_0^{\rho} d\rho\frac{\partial V}{\partial\rho}n_{I,Z} = -\frac{\partial V}{\partial\rho}\langle\Gamma_{I,Z}^{\rho}\rangle + \int_0^{\rho} d\rho\frac{\partial V}{\partial\rho}Q_{I,Z} \tag{2.6}$$

which can be differentiated with respect to ρ. For a flux surface geometry, which is independent of time, we arrive at.

$$\frac{\partial n_{I,Z}}{\partial t} = -\left(\frac{\partial V}{\partial\rho}\right)^{-1}\frac{\partial}{\partial\rho}\left(\frac{\partial V}{\partial\rho}\langle\Gamma_{I,Z}^{\rho}\rangle\right) + Q_{I,Z} \tag{2.7}$$

We choose the flux surface label r, which is calculated from the enclosed volume V. The volume V depends on r as the volume of a cylinder with length $2\pi R_{axis}$.

$$r = \sqrt{\frac{V}{2\pi^2 R_{axis}}} \tag{2.8}$$

With this choice, the averaged continuity equation is casted in the familiar cylindrical form.

$$\frac{\partial n_{I,Z}}{\partial t} = -\frac{1}{r}\frac{\partial}{\partial r}r\langle\Gamma_{I,Z}^{r}\rangle + Q_{I,Z} \tag{2.9}$$

For the flux density perpendicular to the magnetic surface, an ansatz with a diffusive and a convective part is used. $D(\theta)$ is the radial diffusion coefficient and $v(\theta)$ is the radial drift velocity, where the dependence on the poloidal angle θ is explicitly denoted. The radial covariant component $\Gamma_{I,Z,r}$ of the flux density is.

$$\Gamma_{I,Z,r} = -D(\theta)\nabla n_{I,Z}\vec{e}_r + v(\theta)n_{I,Z} = -D(\theta)\frac{\partial n_{I,Z}}{\partial r}|\nabla r| + v(\theta)n_{I,Z} \tag{2.10}$$

Here, the density gradient has been seperated into a poloidally dependent and independent part using $\nabla n_{I,Z} = (\partial n_{I,Z}/\partial r)\nabla r$. The radial contravariant flux density is obtained by multiplying with $|\nabla r|$.

$$\Gamma^r_{I,Z} = \Gamma_{I,Z,r}|\nabla r| = -D(\theta)|\nabla r|^2\frac{\partial n_{I,Z}}{\partial r} + v(\theta)|\nabla r|n_{I,Z} \tag{2.11}$$

Thus, we obtain the *radial* impurity transport equation.

$$\frac{\partial n_{I,Z}}{\partial t} = \frac{1}{r}\frac{\partial}{\partial r}r\left(D^*\frac{\partial n_{I,Z}}{\partial r} - v^*n_{I,Z}\right) + Q_{I,Z} \tag{2.12}$$

Here, D^* and v^* are the flux surface averaged transport coefficients.

$$\begin{aligned}
D^* &= \langle D(\theta)|\nabla r|^2\rangle = \frac{1}{4\pi^2 R_{axis}r}\oint D|\nabla r|dS = \frac{1}{4\pi^2 R_{axis}r}\int_0^{2\pi} D(\theta)|\nabla r|\frac{dS}{d\theta}d\theta\\
v^* &= \langle v(\theta)|\nabla r|\rangle = \frac{1}{4\pi^2 R_{axis}r}\oint vdS = \frac{1}{4\pi^2 R_{axis}r}\int_0^{2\pi} v(\theta)\frac{dS}{d\theta}d\theta
\end{aligned} \tag{2.13}$$

For the collisional transport parameters, we know the dependence of D and v on the poloidal angle, and the correct surface averages will be given in Sec.3.1. Fig.2.1 depicts the behaviour for the classical part of the collisional impurity flux. The classical diffusion coefficient D_{CL} has a magnetic field dependence $D_{CL} \propto 1/B^2$, and the polar plot of Fig.2.1 depicts the integrand, which appears in Eq.(2.13). All terms, i. e. the magnetic field dependence, the gradient, and the larger surface on the outboard, favour the radial flux contribution from the outboard side being about a factor of 5 larger than the inboard contribution. The fluxes connected to the classical drift velocity v_{CL} have just the same dependence: v_{CL} is proportional to D_{CL} times a combination of gradients of temperature and density, which leads to $v_{CL} \propto |\nabla r|/B^2$. For the turbulent transport, it is also expected, that the main contribution is on the outboard side, however, the exact poloidal dependence is not known. The superscript $*$ will be omitted from now on.

Outside the LCFS in the regime of open field lines, the one dimensional model is not very well suited. Parallel transport to the divertor/limiter can be considered here in the form of a parallel loss time $\tau_\parallel$. Thus, in the scrape-off layer (SOL), a term $-n_{I,Z}/\tau_\parallel$ is added on the right-hand side of equation (2.12).

The source/sink term $Q_{I,Z}$ couples the transport equation of each ionisation stage with the neighbouring stages.

$$\begin{aligned}
Q_{I,Z} = \quad &- \quad (n_eS_{I,Z} + n_e\alpha_{I,Z} + n_H\alpha^{cx}_{I,Z})n_{I,Z}\\
&+ \quad n_eS_{I,Z-1}n_{I,Z-1}\\
&+ \quad (n_e\alpha_{I,Z+1} + n_H\alpha^{cx}_{I,Z+1})n_{I,Z+1}
\end{aligned} \tag{2.14}$$

$S_{I,Z}$ is the rate coefficient for ionisation of impurity species I in ionisation stage Z, $\alpha_{I,Z}$ is the recombination coefficient for radiative and di-electronic recombination from

ionisation stage Z and $\alpha_{I,Z}^{cx}$ is the respective recombination coefficient due to charge exchange.

The sum of the transport equations for all ions (not the neutral!) of one species is a very useful simplification since all source terms cancel except for the ionisation and recombination between the neutral atom and the single ionised ion.

$$\frac{\partial n_I}{\partial t} = \frac{1}{r}\frac{\partial}{\partial r}r\left(D\frac{\partial n_I}{\partial r} - vn_I\right) + Q_{I,1} \tag{2.15}$$

D and v are average values of the transport coefficients for each ion stage weighted with the fractional abundance of each ion stage at a certain flux surface.

2.2 The Solution for the Total Ion Density

2.2.1 Characteristics of the Solution

Analytic solutions of the radial transport equation exist only for a few cases. The aim of this section is to describe the characteristics of the solution and to define the most important measures, like the equilibration time scale, the particle confinement time, and the penetration probability, where we use the definitions as given by Fußmann [19]. Eq.(2.15), the radial transport equation for the total ion density of one impurity species, shall be rewritten with a slightly different notation.

$$\frac{\partial n}{\partial t} = \frac{1}{r}\frac{\partial}{\partial r}r\left(D(r)\frac{\partial n}{\partial r} - v(r)n\right) + Q(r,t) - \frac{n}{\tau_{\parallel}}\theta(r-a) \tag{2.16}$$

Here we left out the indices for n and Q and added the parallel loss term for radii outside the LCFS with radius $r_{LCFS} = a$. $Q(r,t)$ is the source function, i.e. the number of ionised neutrals minus the number of recombined singly ionised ions per unit volume and unit time. The solutions shall satisfy the following spatial boundary conditions.

$$\left.\frac{\partial n}{\partial r}\right|_{r=0} = 0$$
$$\left.\frac{\partial n}{\partial r}\right|_{r_w} = -\frac{n}{\lambda} \tag{2.17}$$

Typically, λ is of the order of $\approx 1\,\mathrm{cm}$ and is thus small compared to the typical plasma radius of $\approx 1\,\mathrm{m}$.

The solution of the homogeneous time dependent partial differential equation uses the separation ansatz.

$$n(r,t) = \exp\left(-\frac{\mu^2 D_c t}{a^2}\right)u(r) \tag{2.18}$$

D_c is a characteristic value of $D(r)$ and μ is an arbitrary parameter which will be determined from the boundary conditions. This ansatz leads to a differential equation

for the radial function $u(r)$.

$$\frac{1}{r}\frac{\partial}{\partial r}\left(r\frac{D(r)}{D_c}\frac{\partial u}{\partial r}-\frac{v(r)}{D_c}u\right)+\left(\frac{\mu^2}{a^2}-\frac{\theta(r-a)}{\tau_\parallel D_c}\right)u=0 \tag{2.19}$$

The boundary conditions yield an infinite number of discrete eigenvalues $\mu_1<\mu_2<...$ and the eigenfunctions u_n and u_m for different eigenvalues μ_n and μ_m are orthogonal. This can be seen when multiplying the differential equation (2.19) for u_n with u_m and for u_m with u_n and subtracting the two equations. We are then left with the following equation.

$$
\begin{aligned}
\frac{\mu_m^2-\mu_n^2}{a^2}ru_nu_m &= u_m\frac{\partial}{\partial r}\left(r\frac{D(r)}{D_c}\frac{\partial u_n}{\partial r}-\frac{v(r)}{D_c}u_n\right)-u_n\frac{\partial}{\partial r}\left(r\frac{D(r)}{D_c}\frac{\partial u_m}{\partial r}-\frac{v(r)}{D_c}u_m\right)\\
&= \frac{\partial}{\partial r}\left(r\frac{D(r)}{D_c}\left(u_m\frac{\partial u_n}{\partial r}-u_n\frac{\partial u_m}{\partial r}\right)\right)
\end{aligned}
\tag{2.20}
$$

and integration over r yields

$$
\begin{aligned}
\int_0^{r_w}ru_nu_m dr &= \frac{a^2}{\mu_m^2-\mu_n^2}\left[r\frac{D(r)}{D_c}\left(u_m\frac{\partial u_n}{\partial r}-u_n\frac{\partial u_m}{\partial r}\right)\right]_0^{r_w}\\
&= \frac{a^2}{\mu_m^2-\mu_n^2}\frac{r_wD(r_w)}{D_c}\left(u_m(r_w)\frac{\partial u_n}{\partial r}\Big|_{r_w}-u_n(r_w)\frac{\partial u_m}{\partial r}\Big|_{r_w}\right)
\end{aligned}
\tag{2.21}
$$

For $m\neq n$, the integral is zero due to the boundary conditions. For $m=n$, we normalise the eigenfunctions such that the integral equals $1/2\pi$. The eigenfunctions form a complete set.

$$
\begin{aligned}
2\pi\int_0^{r_w}u_nu_m rdr &= \delta_{nm}\\
\sum_n u_n(r)u_n(r') &= \frac{\delta(r-r')}{2\pi r}
\end{aligned}
\tag{2.22}
$$

The solution of the homogeneous equation for $t>t'$ and initial density distribution $n_0(r)$ at $t=t'$ is thus given by:

$$
\begin{aligned}
n_{hom}(r,t) &= \sum_n a_n\exp\left(-(t-t')/\tau_n\right)u_n(r)\\
a_n &= \int_0^{r_w}n_0(r')u_n(r')2\pi r'dr'\\
\tau_n &= \frac{\tau_\perp}{\mu_n^2}\qquad\tau_\perp=\frac{a^2}{D_c}
\end{aligned}
\tag{2.23}
$$

The temporal evolution of the density is thus the sum of the exponentially decaying radial eigenfunctions $u_n(r)$, where the eigenfunction u_n has $n-1$ zeros in the radial

interval. The eigenfunction with u_1 has no zero and the longest decay time τ_1. After all higher eigenmodes have decayed, the density distribution is proportional to u_1 and decays self similar with decay time τ_1.

If the initial density distribution at time $t = t'$ is given by a radial delta function $n_0(r) = N_L\delta(r - r')/2\pi r$, where N_L shall denote the number of particles per unit length of the cylinder, the coefficients a_n are $N_L u_n(r')$. Thus, the probability of finding a particle, which was deposited at r' at time t', within the radial interval $[r, r + dr]$ at time t is.

$$G(r, r', t - t')2\pi r dr = \sum_n \exp\left(-(t - t')/\tau_n\right)u_n(r)u_n(r')2\pi r dr \tag{2.24}$$

where $G(r, r', t - t')$ is the Green's function. With the Green's function, we can construct the solution of the inhomogeneous equation. Since $Q(r', t')2\pi r' dr' dt'$ gives the number of particles N_L, which were deposited per unit length of the cylinder at time t' and radius r', we get by integrating over all times $t' < t$ and all radii r'.

$$n_{inhom}(r, t) = \int\limits_{-\infty}^{t}\int\limits_{0}^{r_w} G(r, r', t - t')Q(r', t')2\pi r' dr' dt' \tag{2.25}$$

We first define the particle confinement time τ_p as the equilibrium impurity ion content N_a inside the LCFS divided by the total ion source rate Φ which shall be constant in time

$$\tau_p = \frac{N_a}{\Phi} = \frac{\int\limits_0^a n_{eq}(r)r dr}{\int\limits_0^{r_w} Q(r)r dr} \tag{2.26}$$

τ_p can be expressed in terms of the eigentimes τ_n by putting a time independent source $Q(r)$ into Eq.(2.25). Integration of the density over all radii $r < a$ leads to

$$\begin{aligned}
\tau_p &= \frac{1}{\Phi_L}\int\limits_0^a\int\limits_{-\infty}^{t}\int\limits_0^{r_w} G(r, r', t - t')Q(r')2\pi r' dr' dt' 2\pi r dr \\
&= \frac{1}{\Phi_L}\sum_n \tau_n \int\limits_0^a u_n(r)2\pi r dr \int\limits_0^{r_w} u_n(r')Q(r')2\pi r' dr' \tag{2.27}
\end{aligned}$$

where $\Phi_L = \int_0^{r_w} Q(r)2\pi r dr$ is the constant source rate per unit length of the cylinder. We can also find another interpretation of τ_p. Let us consider a source which deposits N_L ions per unit length at the initial time t': $Q(r', t') = n_0(r')\delta(t - t')$ with $N_L = \int_0^{r_w} n_0(r')2\pi r' dr'$. The density evolution after this δ-puff is given by Eq.(2.25).

$$n(r, t) = \int\limits_0^{r_w} G(r, r', t - t')n_0(r')2\pi r' dr' \tag{2.28}$$

Now, we calculate the time evolution of the ion content inside the LCFS and normalise with the number of deposited ions at t', which yields the probability $P_a(t - t')$ to find a particle, which was deposited at time t', inside the LCFS at time t.

$$P_a(t - t') = \frac{1}{N_L} \int\limits_0^a n(r, t - t') 2\pi r dr = \frac{1}{N_L} \int\limits_0^a \int\limits_0^{r_w} G(r, r', t - t') n_0(r') 2\pi r' dr' 2\pi r dr \quad (2.29)$$

If the source distribution is within the LCFS, $P_a(t - t')$ equals 1 at time t' and decays to zero for later times. For sources outside the LCFS, which is the usual case for impurities, $P_a(t - t')$ will first rise to a maximum and then decay. The maximum $P_{a,max}$ of P_a shall be defined as the penetration probability into the radial region of closed flux surfaces. Integration of P_a over all times $t > t'$ yields the mean dwell time of a particle inside the LCFS.

$$\tau_d = \int\limits_{t'}^{+\infty} P_a(t - t') dt \quad (2.30)$$

Since the integrand depends only on the time difference $t - t'$, we can substitute the integration variable.

$$\begin{aligned}\tau_d &= \int\limits_{-\infty}^t P_a(t - t') dt' \\ &= \frac{1}{N_L} \int\limits_{-\infty}^t \int\limits_0^a \int\limits_0^{r_w} G(r, r', t - t') n_0(r') 2\pi r' dr' 2\pi r dr dt'\end{aligned} \quad (2.31)$$

Eq.(2.31) has the same form as the first equation of (2.27). Thus, for equal forms of the radial deposition profile the mean dwell time inside the LCFS for a particle originating from a temporal δ-source equals the particle confinement time, the impurity content inside the LCFS divided by the constant source rate for equilibrium conditions.

$$\tau_d = \tau_p \quad (2.32)$$

2.2.2   Analytic Solution for Constant Diffusion

We consider the most simple case with constant diffusion coefficient D, zero drift velocity $v=0$ and treat only the radial range inside the LCFS. The transport equation for the total ion density $n(r, t)$ has the form

$$\frac{\partial n}{\partial t} = D \frac{1}{r} \frac{\partial}{\partial r}\left(r \frac{\partial n}{\partial r}\right) + Q(r, t) \quad (2.33)$$

and for the equilibrium case with constant source.

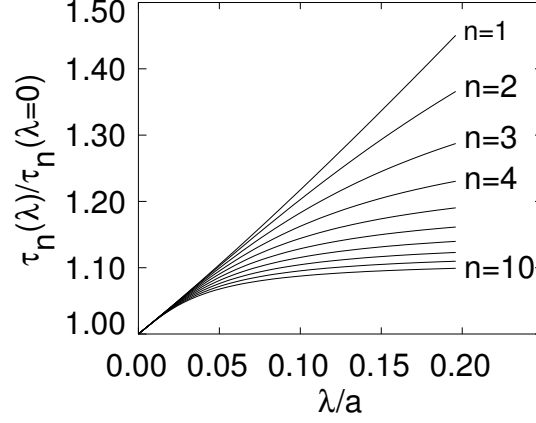$$D \frac{1}{r} \frac{\partial}{\partial r}\left(r \frac{\partial n_{eq}}{\partial r}\right) = -Q(r) \quad (2.34)$$

Figure 2.2: *Dependence of the characteristic decay times τ_n on the decay length λ at the boundary. τ_1 has an offset-linear dependence on λ, while the higher eigentimes saturate at high values of λ.*

The radial boundary is at $r = a$ with

$$\frac{\partial n}{\partial r}\Big|_a = -\frac{n}{\lambda} \tag{2.35}$$

λ is the characteristic decay length in the scrape of layer, which can be estimated to be $\sqrt{D\tau_\parallel}$ being on the order of $1\,\mathrm{cm}$ and thus small compared to a. The equilibrium density distribution, which obeys the boundary conditions is

$$n_{eq}(r) = \frac{1}{D}\left(\frac{\lambda}{a}\Phi_L - \int\limits_r^a \frac{dr'}{r'} \int\limits_0^{r'} Q(\tilde{r})\tilde{r}d\tilde{r}\right) \tag{2.36}$$

where $\Phi_L = 2\pi \int_0^a Q(r)r\,dr$ denotes the number of particles, which are deposited per unit time and unit length of the cylinder. In the following, we just consider a point source at $r = r_s$.

$$Q(r) = \Phi_L \frac{\delta(r - r_s)}{2\pi r_s} \tag{2.37}$$

and the equilibrium density becomes for this case.

$$
\begin{aligned}
n_{eq}(r) &= \frac{\Phi_L}{2\pi D}\left(\frac{\lambda}{a} - \ln(r_s/a)\right) \quad \text{for} \ \ r \le r_s \\
n_{eq}(r) &= \frac{\Phi_L}{2\pi D}\left(\frac{\lambda}{a} - \ln(r/a)\right) \quad \text{for} \ \ r > r_s
\end{aligned}
\tag{2.38}
$$

The density is constant inside the deposition radius r_s and has a logarithmic decay outside of r_s. The particle confinement time τ_p for this point source is obtained by integrating the density profile of Eq.(2.38) over the area within the LCFS.

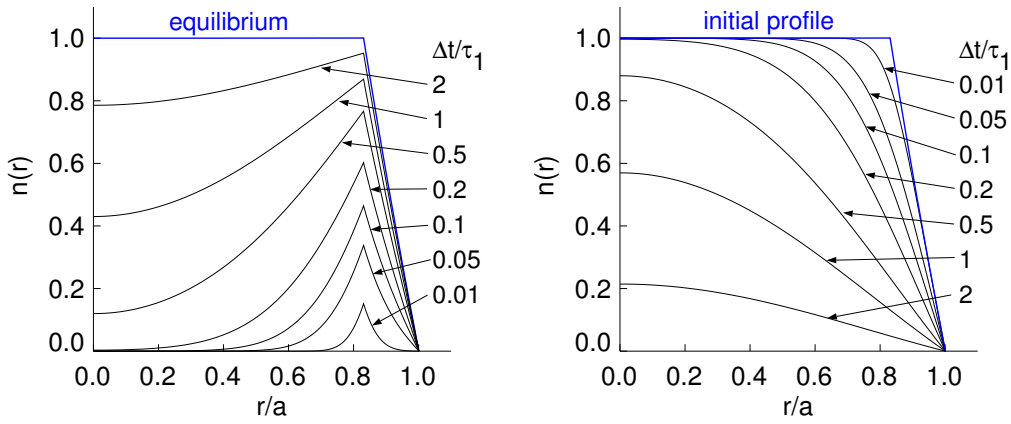$$\tau_p = \frac{1}{2}\frac{a^2}{D}\left(\frac{\lambda}{a} + \frac{1 - (r_s/a)^2}{2}\right) \tag{2.39}$$

Figure 2.3:   *Left graph: The temporal evolution of the density is shown for different time delays after a radial δ-source has been switched on. Right graph: Starting from the equilibrium with source on, the density decay with zero source is shown. The boundary density is zero, and the time delays are normalised to the first eigentime τ_1. The equilibrium density with source on is just the sum of decaying and rising density at equal time delays. For $\Delta t > \tau_1$, the density profile during decay has relaxed to the first eigenfunction, which decays exponentially with time constant τ_1.*

τ_p depends strongly on the deposition radius r_s. For central deposition ($r_s=0$), λ/a can be neglected and the particle confinement time equals $\tau_p = a^2/4D$, which is just the time needed for an average excursion over a radial distance $\Delta r = a$ during a random walk. For impurities, which are ionised very close to the plasma boundary, it is $\Delta r_s = (a - r_s) \ll a$ and the confinement time is strongly decreased. In this case, $\tau_p = a(\lambda + \Delta r_s)/2D$ has only a linear dependence on a.

The separation ansatz for the time dependent homogeneous partial differential equation leads to Bessel's differential equation of zero order for the radial function $u(r)$.

$$\frac{1}{r}\frac{\partial}{\partial r}\left(r\frac{\partial u}{\partial r}\right) + \frac{\mu^2}{a^2}u = 0 \tag{2.40}$$

Normalised eigenfunctions of Eq.(2.40), which are finite at $r = 0$ are

$$u_n(r) = \frac{1}{N_n}J_0(\mu_n\, r/a) \quad N_n = \sqrt{\pi}a\sqrt{1 + (\lambda\mu_n/a)^2}J_1(\mu_n) \tag{2.41}$$

J_0 and J_1 is the zero and first order Bessel function, μ_n is the n-th root of the boundary condition at $r=a$.

$$J_0(\mu) + \lambda\frac{dJ_0}{dr}\Big|_a = J_0(\mu) + \frac{\lambda}{a}\mu J_0'(\mu) = J_0(\mu) - \frac{\lambda}{a}\mu J_1(\mu) = 0 \tag{2.42}$$

For $\lambda=0$, the eigentimes are $\tau_1=0.173\tau_\perp$, $\tau_2=0.0328\tau_\perp$, $\tau_3=0.0134\tau_\perp$, $\tau_4=0.00719\tau_\perp$ with $\tau_\perp=a^2/D$. The dependence of the first 10 eigentimes on λ is shown in fig. 2.2. The expressions for τ_p in terms of of the eigentimes τ_n for the point source at r_s is

$$\tau_p = \sum_n \tau_n \frac{2}{\mu_n(1 + (\lambda\mu_n/a)^2)J_1(\mu_n)}J_0(\mu_n r_s/a) \tag{2.43}$$

and the residence probability $P_a(t)$ for a particle deposited at r_s at $t=0$ is.

$$P_a(t) = \sum_n \exp(-t/\tau_n) \frac{2}{\mu_n(1 + (\lambda\mu_n/a)^2)J_1(\mu_n)} J_0(\mu_n r_s/a) \qquad (2.44)$$

Two examples for the solutions of the time dependent equation with zero boundary density ($\lambda=0$) are shown in Fig.2.3. The left graph shows the density rise after the start of a steady δ-source at $r/a\approx0.8$ and gives the equilibrium profile. For the left graph, this equilibrium was taken as initial profile, and the decay of the density is plotted for zero source. The different time delays are given in units of the first eigentime τ_1. The two evolutions are symmetrical in the sense, that the lost density during the decay just equals the density during the rise phase at the same time delay. For a delay time $\Delta t > \tau_1$, the density profile during decay has relaxed to the first eigenfunction, which decays exponentially with time constant τ_1.

2.2.3 Equilibrium Impurity Density

The second example gives the analytic equilibrium solution for Eq.(2.16) for the case of an impurity source, which is entirely in the scrape off layer (SOL). This situation is encountered for a tokamak with divertor configuration, while a limiter plasma has the source inside the LCFS. Off course, the 1D description is a quite crude approximation to the 3D impurity source distribution in the main chamber and the divertor and the complicated impurity flow patterns in the plasma SOL. The main objective is to discuss the influence of the edge and bulk transport parameters on the equilibrium density on axis $n(0)$ in the simple 1D approximation.

We use a constant diffusion coefficient D_{SOL} in the SOL and set the drift velocity in the SOL to zero $v_{SOL} = 0$. The diffusion coefficient and the drift velocity in the plasma bulk are functions of the radius, which equal the SOL values at the radius of the separatrix $r=a$. Considering the smallness of the scrape-off width w compared to a, we simplify $1/r\, d/dr(rdn/dr) \approx d^2n/dr^2$ in the SOL.

$$\frac{1}{r}\frac{d}{dr}r\left(D(r)\frac{dn}{dr} - v(r)n_1\right) = 0 \quad \text{for } r \le a$$

$$D_{SOL}\frac{d^2n}{dr^2} - \frac{n}{\tau_\parallel} = -Q(r) \quad \text{for } r > a \qquad (2.45)$$

The boundary conditions are.

$$\left.\frac{dn}{dr}\right|_0 = 0 \qquad \left.\frac{dn}{dr}\right|_{r_w} = -\frac{n}{\lambda} \qquad (2.46)$$

The first of the two boundary conditions restricts the drift velocity for $r\to0$: $v(0) = 0$. It exludes solutions which become infinit for $r\to0$. The solutions for the two differential equations shall be continuous at $r=a$.
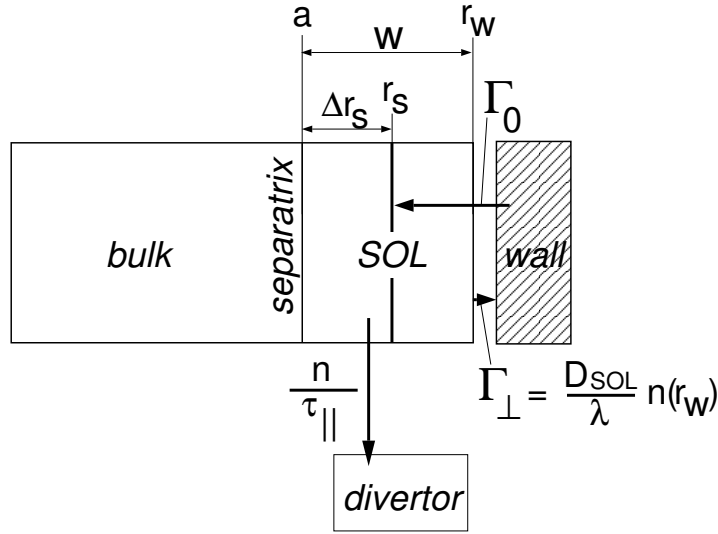
Figure 2.4: *Scheme of the one dimensional impurity transport description.*

At the boundary radius r_w, we have a steady influx of neutral impurities, which originate from the plasma facing wall. The neutral flux density at r_w shall be Γ_0 and the total rate for the influx of neutrals is $\Phi = 4\pi^2 r_w R \Gamma_0$. The neutrals are ionised at a certain radius due to electron collisions, where the radial shape of the source depends on the electron density n_e, the electron temperature T_e, and the velocity distribution of the neutral impurity. Here, we assume the most simple case, where all neutrals are ionised at one fixed radius r_s in the SOL: $Q(r) = \Gamma_0 \delta(r - r_s)$. We will see, that the distance of the radial source location to the LCFS $\Delta r_s = r_s - a$ is a crucial parameter for the equilibrium density at the plasma edge.

They ions leave the plasma by parallel transport to the divertor or by perpendicular transport. The parallel loss is just described by the volumetric loss term with time constant $\tau_{\parallel}$, where $\tau_{\parallel}$ can be estimated from the ion sound speed and the connection length to the divertor. Parallel loss time $\tau_{\parallel}$ and D_{SOL} define the characteristic radial decay length $\lambda_{SOL} = \sqrt{\tau_{\parallel} D_{SOL}}$ for the SOL. In a wide SOL, the radial density profile would have an exponential decay with decay length λ_{SOL} for the case, where the source in the SOL is zero. The perpendicular loss at the edge is given by the boundary condition $\Gamma_{\perp}(r_w) = D_{SOL} n(r_w)/\lambda$. The boundary decay length λ is a mixture of two decay lengths, which are encountered at the plasma edge. For locations with direct plasma wall contact, there will be an impurity outflow on the order of $\Gamma_{\perp}(r_w) = n(r_w) v_{th}$, since all ions, which hit the wall, recombine and can only return as neutrals. This leads to $\lambda = D_{SOL}/v_{th}$ with very small values around $0.1\,\text{mm}$. However, in the area between the limiting wall components, perpendicular diffusion coefficient and parallel loss time to the limiter, will yield a larger characteristic decay length $\lambda = \sqrt{\tau_{\parallel,lim} D_{SOL}}$ on the order of $1\,\text{cm}$. The average λ is close to the second choice for the usual situation with large gaps between the
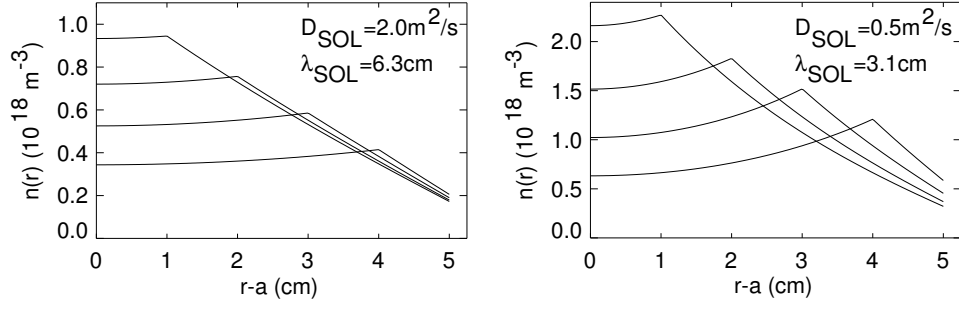
Figure 2.5:   *Radial density profiles in the SOL for different source radii r_s at two different diffusion coefficients D_{SOL}. The common parameters are $\Gamma_0 = 5 \times 10^{19}\,m^{-2}s^{-1}$, $\lambda = 1\,cm$ and $\tau_{\parallel} = 2\,ms$. The density at the separatrix is highest for small Δr_s and small D_{SOL}. The profile inside the source radius is flat for $\Delta r_s \ll \lambda_{SOL}$, i.e. when the time scale for perpendicular diffusion is small against the parallel loss time $\Delta r_s^2 / D_{SOL} \ll \tau_{\parallel}$.*

limiting wall structures. A schematic visualisation of the 1D-model is shown in Fig.2.4. The equilibrium density profile for this model is:

$$
n(r) = \begin{cases}
n(a) \exp\left(- \int_r^a \frac{v(\tilde{r})}{D(\tilde{r})} d\tilde{r}\right) & \text{for } r < a \\[2mm]
n(a) \cosh\left(\frac{r-a}{\lambda_{SOL}}\right) & \text{for } a < r < r_s \\[2mm]
n(a) \cosh\left(\frac{r-a}{\lambda_{SOL}}\right) - \Gamma_0 \frac{\lambda_{SOL}}{D_{SOL}} \sinh\left(\frac{r-r_s}{\lambda_{SOL}}\right) & \text{for } r > r_s
\end{cases}
\tag{2.47}
$$

with the density at the LCFS

$$
n(a) = \Gamma_0 \left(\frac{\lambda_{SOL}}{D_{sol}}\right) \frac{\lambda \cosh[(w - \Delta r_s)/\lambda_{SOL}] + \lambda_{SOL} \sinh[(w - \Delta r_s)/\lambda_{SOL}]}{\lambda \sinh[w/\lambda_{SOL}] + \lambda_{SOL} \cosh[w/\lambda_{SOL}]}
\tag{2.48}
$$

Fig. 2.5 shows a few radial profiles for different source radii and two values of D_{SOL}, which differ by a factor of 4. The radial range just covers the SOL, while the density profile inside the separatrix will be discussed below. The common parameters are $\Gamma_0 = 5 \times 10^{19}\,m^{-2}s^{-1}$, $\lambda = 1\,cm$, $\tau_{\parallel} = 2\,ms$, and $w = 5\,cm$. For the higher diffusion coefficient, the characteristic perpendicular transport time from source location to separatrix $\Delta r_s^2 / D_{SOL}$ is small against the parallel loss time $\tau_{\parallel}$, such that parallel losses are neglegible and the profiles inside of r_s are flat. For the lower diffusion coefficient, parallel losses become important for larger values of Δr_s, where the density decreases considerably towards the separatrix. The density at the separatrix is highest for lowest values of Δr_s and D_{SOL}, while for equal Δr_s, the factor of 4 increase of D_{SOL} leads to about a factor of 2 decrease of the separatrix density.

Several modifications of this results can be found in the literature, which are due to a different choice of λ. For $\lambda = 0$, we get the hard boundary result with $n(r_w) = 0$. For $\lambda = \lambda_{SOL}$, the soft boundary case is obtained, which has $w \gg \lambda_{SOL}$. Finally, the case with $\lambda \to \infty$ would yield a situation without radial losses at r_w. The density at the
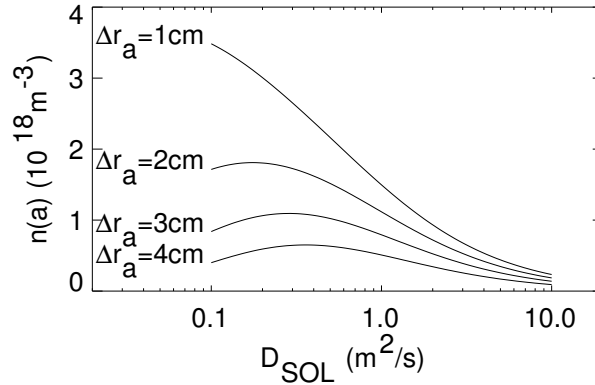
Figure 2.6:   *Separatrix density versus SOL diffusion coefficient: The parameters are* $\Gamma_0=5\times10^{19}\,m^{-2}s^{-1}$, $\lambda=1$ *cm* $w=5\,cm$, *and* $\tau_\parallel=2\,ms$. *The separatrix density* $n(a)$ *is plotted for four different source locations* $\Delta r_s=1\,cm$, $2\,cm$, $3\,cm$, *and* $4\,cm$.

LCFS for first two cases are:

$$n(a) = \Gamma_0 \frac{\lambda_{SOL}}{D_{sol}} \begin{cases} \sinh[(w-\Delta r_s)/\lambda_{SOL}]/\cosh[w/\lambda_{SOL}] & \text{for } \lambda = 0 \\ \exp\left[-\Delta r_s/\lambda_{SOL}\right] & \text{for } \lambda = \lambda_{SOL} \end{cases} \qquad (2.49)$$

For $v(r) = 0$, Engelhardt [20] derived the soft boundary and Post and Lackner [21] the hard boundary result.

Fig.2.6 shows the dependences of $n(a)$ on the diffusion coefficient in the SOL and on the source radius. For low D_{SOL}, $n(a)$ is very sensitive to the radial distance of the source to the separatrix Δr_s, while the dependence on Δr_s is weak at high values of D_{SOL}. For each Δr_s, there exists a maximum of $n(a)$, which is at $D_{SOL} \approx \Delta r_s^2/\tau_\parallel$. For a plasma with higher D_{SOL}, also the electron density usually has a larger decay length in the SOL. The higher electron density shifts the source radius towards the edge, such that Δr_s and D_{SOL} increase simultaneously. Thus, an increasing D_{SOL} should always lead to a decrease of the separatrix impurity density at a given influx.

The goal of this section was to calculate the central density for a given influx and the knowledge of $n(a)$ would be sufficient, if there were no impurity drift velocities in the confined plasma. For zero drift velocity $v(r) = 0$, the absolute value of the diffusion coefficient inside the separatrix is completely irrelevant and the density on axis equals the density at the separatrix: $n(0) = n(a)$. However, the transport inside the separatrix, is characterised by the presence of drift velocities, which leads under special plasma conditions to strong density gradients inside the separatrix. The normalised gradient at radius $r < a$ depends on the ratio of drift velocity to diffusion coefficient: $(1/n)dn/dr = v(r)/D(r)$. Thus, the density on axis depends on a mixture of source location, edge and core transport. Fußmann [19] first included the effect of drift velocities inside the separatrix for the hard boundary case.
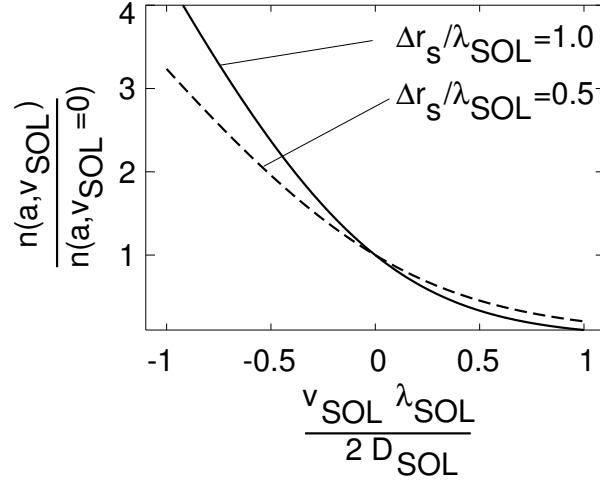
Figure 2.7:   *Separatrix density versus SOL drift parameter $v_{SOL}\lambda_{SOL}/(2D_{SOL})$: For the soft boundary case, the ratio of the separatrix density $n(a)$ with drift to the density without drift is shown for two source locations $\Delta r_s/\lambda_{SOL}=1$ and 0.5. Positive(negative) values of κ denote an outwardly(inwardly) directed drift velocity.*

Finally, we consider the effect of drift velocities in the SOL. For the soft boundary case, the density at the separatrix for $v_{SOL} \neq 0$ is given by.

$$n(a) = \Gamma_0 \frac{\lambda_{SOL}}{D_{SOL}} \frac{1}{\sqrt{1+\kappa^2}+\kappa} \exp\left[-\frac{\Delta r_s(\sqrt{1+\kappa^2}+\kappa)}{\lambda_{SOL}}\right] \tag{2.50}$$

with

$$\kappa = \frac{v_{SOL}\lambda_{SOL}}{2D_{SOL}} = \frac{v_{SOL}}{2}\sqrt{\frac{\tau_\parallel}{D_{SOL}}} \tag{2.51}$$

Positive drift velocities (outward) lead to a decrease of $n(a)$ while negative drift velocities (inward) leader to higher values of $n(a)$. Fig. 2.7 shows, that drifts in the SOL change the equilibrium separatrix density by about a factor of 2, if $v_{SOL} \approx D_{SOL}/\lambda_{SOL}$, e.g. for $\tau_\parallel = 2\,\mathrm{ms}$ and $D_{SOL} = 0.5\,\mathrm{m^2/s}$ a drift velocity of $D_{SOL}/\lambda_{SOL} \approx 16\,\mathrm{m/s}$ causes a change by a factor of 2.

2.2.4   Penetration and Particle Confinement Time

In section 2.2.1, it was found, that particle confinement time τ_p as given in Eq.(2.26) and mean dwell time τ_d as defined in Eq.(2.30) are identical. Using Eq.(2.30), it is tempting to approximate τ_p in the following manner

$$\tau_p = \int_{t'}^{+\infty} P_a(t-t')dt \approx \int_{t'}^{+\infty} P_{a,max} \exp\left(-\frac{t-t'}{\tau_1}\right)dt = P_{a,max}\tau_1 \tag{2.52}$$

This simplification leads to the interpretation, that a particle enters the confined plasma with a penetration factor $P_{a,max}$, where it resides for a time τ_1 before it is lost. τ_1
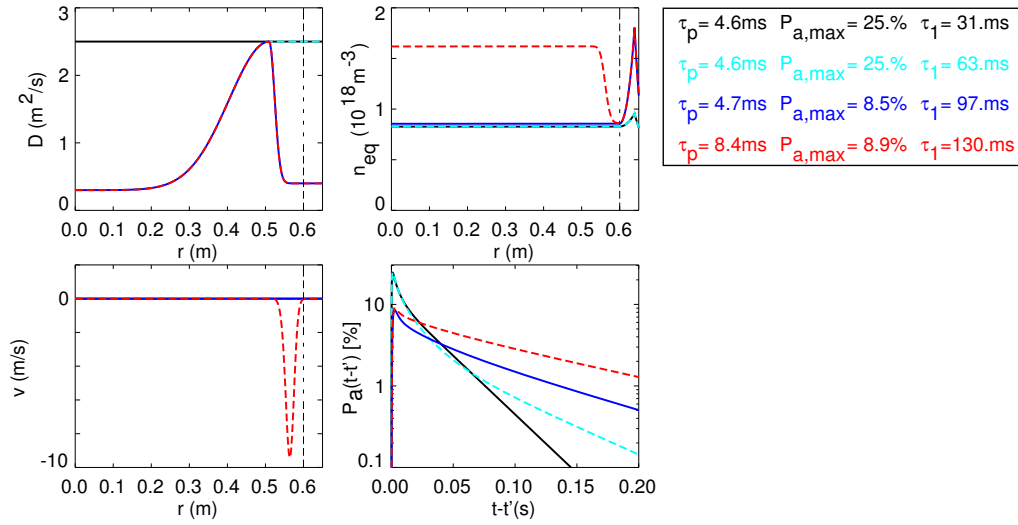
Figure 2.8:   *Equilibrium density profile and time evolution of $P_a(t-t')$ for four different choices of diffusion coefficient and drift velocity (see text for parameters).*

is the 1st characteristic eigentime and can eventually be determined from the decay of spectroscopic signals after a short puff or laser blow-off of the considered impurity. However, such an approach is only valid for order of magnitude approximations as will be shown in the following example.

Fig.2.8 shows the numerical solution of the equilibrium density and the time evolution of $P_a(t - t')$ for four choices of D and v. The same edge parameter as in Fig.2.6 are used, i.e. w=5 cm, $\tau_{\parallel}$=2 ms and soft boundary conditions $\lambda = \lambda_{SOL}$. A radial δ-source is located at Δr_s= 4 cm and the influx is set to Γ_0=5×10^{19} m^{-2}s^{-1} for the equilibrium case. Case 1(black, solid lines) has constant diffusion coefficient $D(r)$=2.5 m^2/s. For the other three cases, the diffusion coefficient decreases to the centre. In the second case (magenta, dashed lines) D_{SOL} is set to 2.5 m^2/s in the SOL, while case 3 (blue, solid lines) and case 4 (red, dashed lines) incorporate an edge transport barrier with D_{SOL}=0.4 m^2/s. Case 4 demonstrates the effect of an additional inward drift inside the LCFS. According to Eq.(2.49), case 1 to 3 have almost equal densities inside the LCFS, while for case 4 the density inside the radial region with inward pinch is increased by a factor of $\approx$2. The plot of $P_a(t - t')$ shows that the assumption of a constant decay time is crude. The legend gives the values of τ_p, $P_{a,max}$ and τ_1 and demonstrates that in this example Eq.(2.52) is only valid within a factor of 1.4(case 4) to 3.4 (case 2).

2.3   Numerical Solution

The impurity transport equations (2.12) for the different ion stages of one impurity species can only be solved numerically. Similarly, the solution of the transport equation

for the sum of all ion stages (2.15) is only known, if the transport coefficients have simple radial dependences, e.g. $D(r) = const.$ and $v(r) = v_a r/a$ or $D(r) = D_0 + D_a(r/a)^2$ and $v(r) = v_a r/a$. Therefore, computer codes, which provide a numerical solution of Eq. (2.12) and (2.15) are indispensable.

A brief description of the preferred numerical schemes shall be given here. We use a matrix notation for the Z transport equations (2.12) of all ion stages of an impurity with atomic number Z.

$$
\begin{aligned}
\frac{\partial \vec{n}}{\partial t} &= \frac{1}{r}\frac{\partial}{\partial r} r\left(\hat{D}(r)\frac{\partial \vec{n}}{\partial r} - \hat{v}(r)\vec{n}\right) - \hat{S}\vec{n} - \hat{R}\vec{n} + \vec{d} \\
&= \hat{D}\frac{\partial^2 \vec{n}}{\partial r^2} + \left(\frac{\hat{D}}{r} + \frac{d\hat{D}}{dr} - \hat{v}\right)\frac{\partial \vec{n}}{\partial r} - \left(\frac{\hat{v}}{r} + \frac{d\hat{v}}{dr}\right)\vec{n} - \hat{S}\vec{n} - \hat{R}\vec{n} + \vec{d} \qquad (2.53)
\end{aligned}
$$

$\vec{n}$ is a vector in the space of of the ionisation stages containing the number densities of the different ionisation stages. $\hat{D}$ and $\hat{v}$ are diagonal matrices with the transport coefficients for each ion stage. $\hat{S}$ and $\hat{R}$ are matrices with the ionisation and recombination rates, i.e. the elements of $\hat{S}$ are the product of n_e and the rate coefficients for electron impact ionisation, while the elements of $\hat{R}$ are the sum of the products of n_e and the rate coefficients for radiative and di-electronic recombination. $\hat{S}$ has a non-zero diagonal and lower diagonal, while $\hat{R}$ has a non-zero diagonal and upper diagonal. $\vec{d}$ has only one non-zero element at $Z = 1$ and describes the source rate by ionisation of neutral impurity atoms.

An unconditionally stable and effective discretisation method for diffusion-convection equations is the Crank-Nicolson scheme. Here, the change of the density during the time step Δt from time point l to $l+1$, is calculated by taking the average values of densities and spatial derivatives at the time points l and $l+1$ for the terms, which appear on the right hand side of Eq.(2.53). With the notation

$$
\vec{n}^{l+1/2} = \frac{\vec{n}^l + \vec{n}^{l+1}}{2} \qquad (2.54)
$$

the Crank-Nicolson scheme has the following form.

$$
\begin{aligned}
\frac{\vec{n}^{l+1} - \vec{n}^l}{\Delta t} &= \hat{D}\frac{\partial^2 \vec{n}^{l+1/2}}{\partial r^2} + \left(\frac{\hat{D}}{r} + \frac{d\hat{D}}{dr} - \hat{v}\right)\frac{\partial \vec{n}^{l+1/2}}{\partial r} - \left(\frac{\hat{v}}{r} + \frac{d\hat{v}}{dr}\right)\vec{n}^{l+1/2} \\
&\quad - \hat{S}\vec{n}^{l+1/2} - \hat{R}\vec{n}^{l+1/2} + \vec{d} \qquad (2.55)
\end{aligned}
$$

An equidistant mesh of N radial grid points with radial step size Δr shall be considered. The spatial derivatives at mesh point k in Eq.(2.55) are replaced by the symmetric three point formulas, which have a truncation error quadratic in Δr.

$$
\begin{aligned}
\left[\frac{\partial f}{\partial r}\right]_k &= \frac{f_{k+1} - f_{k-1}}{2\Delta r} + \frac{\Delta r^2}{6}\left[\frac{\partial^3 f}{\partial r^3}\right]_k + O(\Delta r^4) \\
\left[\frac{\partial^2 f}{\partial r^2}\right]_k &= \frac{f_{k+1} - 2f_k + f_{k-1}}{\Delta r^2} + \frac{\Delta r^2}{12}\left[\frac{\partial^4 f}{\partial r^4}\right]_k + O(\Delta r^4) \qquad (2.56)
\end{aligned}
$$

The truncation error of the finite difference formulation can be calculated by expanding the densities and transport coefficients at the different nodes in a Taylor series and forming the difference with the original transport equation. When expanding around $t + \Delta t/2$ the truncation error reads.

$$
\vec{E}_{CN} = \frac{\Delta r^2}{12}\Big(-\hat{D}\frac{\partial^4 \vec{n}}{\partial r^4} - 2\big(\frac{\hat{D}}{r} + \frac{d\hat{D}}{dr} - \hat{v}\big)\frac{\partial^3 \vec{n}}{\partial r^3} - 2\frac{d^3\hat{D}}{dr^3}\frac{\partial \vec{n}}{\partial r} + 2\frac{d^3\hat{v}}{dr^3}\vec{n}\Big)
$$
$$
+ \frac{\Delta t^2}{24}\Big(\frac{\partial^3 \vec{n}}{\partial t^3} + 3\big(\hat{S} + \hat{R}\frac{\hat{v}}{r} + \frac{d\hat{v}}{dr}\big)\frac{\partial^2 \vec{n}}{\partial t^2} - 3\big(\frac{\hat{D}}{r} + \frac{d\hat{D}}{dr} - \hat{v}\big)\frac{\partial^3 \vec{n}}{\partial r \partial t^2} - 3\hat{D}\frac{\partial^4 \vec{n}}{\partial r^2 \partial t^2}\Big) \quad (2.57)
$$

The truncation error is quadratic in the radial and temporal step sizes.

We arrive at a linear system of $N \times Z$ algebraic equations, which yield the densities at the new time point. The equation for the density of an ion stage at mesh point k contains the densities of the neighbouring radial mesh points as well as the neighbouring ion stages. Thus, the difference formulation is rather similar to that of a two-dimensional transport equation. The coefficient matrix of the linear system can be ordered such, that it has tridiagonal form plus additional terms that are displaced from the main diagonal by the number of ion stages Z which result from ionisation and recombination. An iterative solution of the matrix equation has been used by Behringer [22]. To this end the full matrix equation is split into Z matrix equations on the number of radial mesh points which are solved with the fast Thomas-algorithm. These Z matrix equations are solved in ascending order of the ion charge and the densities of the lower charge state at the time point $l+1$ are known for the calculation of the time-centred ionisation rate into the present charge state. The time-centred recombination rate into the present charge state uses the density of the next higher charge state at $l + 1$ as calculated by the preceeding iteration step. Hulse [23] used an implicit treatment, which leads to a system of equations with a matrix of identical rank and structure, which he directly inverted.

An alternative method has been proposed by Lackner et al [24]. Here, the densities and radial derivatives of the transport part are again treated like in the time-centred Crank-Nicolson scheme, however, for the ionisation and recombination part an alternation between an implicit and explicit method is chosen. Thus, there is a time step which calculates the ionisation rate per volume with the density $\vec{n}^{l+1}$ (implicit) and the recombinations with the densities $\vec{n}^l$ (explicit)

$$
\begin{aligned}
\frac{\vec{n}^{l+1} - \vec{n}^l}{\Delta t} &= \hat{D}\frac{\partial^2 \vec{n}^{l+1/2}}{\partial r^2} + \Big(\frac{\hat{D}}{r} + \frac{d\hat{D}}{dr} - \hat{v}\Big)\frac{\partial \vec{n}^{l+1/2}}{\partial r} - \Big(\frac{\hat{v}}{r} + \frac{d\hat{v}}{dr}\Big)\vec{n}^{l+1/2} \\
&- \hat{S}\vec{n}^{l+1} - \hat{R}\vec{n}^l + \vec{d}
\end{aligned} \quad (2.58)
$$

followed by a time step where $\vec{n}^{l+1}$ is used for the recombinations and $\vec{n}^l$ for the ionisations.

$$
\begin{aligned}
\frac{\vec{n}^{l+1} - \vec{n}^l}{\Delta t} &= \hat{D}\frac{\partial^2 \vec{n}^{l+1/2}}{\partial r^2} + \Big(\frac{\hat{D}}{r} + \frac{d\hat{D}}{dr} - \hat{v}\Big)\frac{\partial \vec{n}^{l+1/2}}{\partial r} - \Big(\frac{\hat{v}}{r} + \frac{d\hat{v}}{dr}\Big)\vec{n}^{l+1/2} \\
&- \hat{S}\vec{n}^l - \hat{R}\vec{n}^{l+1} + \vec{d}
\end{aligned} \quad (2.59)
$$

The method is again unconditionally stable [24] and has the great advantage to lead to Z tridiagonal matrix equations on the number of mesh points, which can very effectively be solved using the Thomas-algorithm. For the first time step Eq.(2.58), the equations are solved in increasing order of the charge state, so that the densities of the lower charge state at the new time point $l+1$ are known when needed for the calculation of the ionisation source into the present charge state. For the second time step Eq.(2.59), the equations for the charge states are solved in decreasing order since the recombination source with the densities at the new time point are now needed.

The truncation error of the two steps

$$
\begin{aligned}
\vec{E}_1 &= \vec{E}_{CN} + \frac{\Delta t}{2}(\hat{S} - \hat{R})\frac{\partial \vec{n}}{\partial t} \\
\vec{E}_2 &= \vec{E}_{CN} - \frac{\Delta t}{2}(\hat{S} - \hat{R})\frac{\partial \vec{n}}{\partial t}
\end{aligned}
\tag{2.60}
$$

are similar to the time-centred scheme, however, additional terms linear in Δt appear, which change sign from step to step. The numerical solution is found to oscillate from time step to time step and has to be taken after an even number of time steps. A detailed treatment of the discretisation scheme (2.58) and (2.59) can be found in App.(A).

At the inner boundary, the plasma axis, a vanishing density gradient and zero drift velocity are requested. For $r \to 0$ the transport equations reads.

$$
\frac{\partial \vec{n}(r=0)}{\partial t} = 2\hat{D}\left[\frac{\partial^2 \vec{n}}{\partial r^2}\right]_{r=0} - \left(2\left[\frac{d\hat{v}}{dr}\right]_{r=0} + \hat{S} + \hat{R}\right)\vec{n}(r=0) + \vec{d}
\tag{2.61}
$$

Here, the second derivative of the densities is replaced by $2(\vec{n}_1 - \vec{n}_0)/\Delta r^2$, while the gradient of the drift velocities at $r = 0$ has to be approximated with the asymmetric two-point formula. Dirichlet boundary conditions at the outermost grid point are easily incorporated by setting the density of the last grid point to the given value. More commonly, a decay length λ is used as boundary condition. In order to maintain a second order truncation error in the radial step size, this boundary condition is implemented with the symmetric three point formula using the fictitious grid point $N + 1$, i.e.

$$
\frac{\partial \vec{n}}{\partial r} = \frac{\vec{n}_{N+1} - \vec{n}_{N-1}}{2\Delta r} = -\frac{\vec{n}_N}{\lambda}
\tag{2.62}
$$

The densities $\vec{n}_{N+1}$ are then replaced by $\vec{n}_{N-1} - (2\Delta r/\lambda)\vec{n}_N$ in equations (2.55), (2.58) and (2.59) respectively.

The numerical implementation usually uses a non-uniform mesh of radial grid points. Close to the last closed flux surface, strong gradients of electron temperature and density appear, which can have decay lengths as low as a few mm. The electron temperature might rise from a few eV to $1\,\text{keV}$ within $2\,\text{cm}$ and strong gradients in the densities of the different ionisation stages can be present. Therefore, the radial step size used in the numerical calculations needs to be around $1\,\text{mm}$ in the boundary region, while in

the central part of the plasma a grid resolution around $1\,\mathrm{cm}$ is usually sufficient. It is advantageous to change the radial grid spacing from centre to edge in order to keep the number of radial mesh points as low as possible. The mesh points shall be equidistant in the coordinate $\rho = \rho(r)$ and a possible choice is for instance.

$$\rho = \frac{r}{\Delta r_{centre}} + \frac{r_{edge}}{k+1}\Big(\frac{1}{\Delta r_{edge}} - \frac{1}{\Delta r_{centre}}\Big)\Big(\frac{r}{r_{edge}}\Big)^{k+1} \qquad (2.63)$$

This choice produces a radial step size Δr which decreases from Δr_{centre} at the axis to Δr_{edge} at the boundary.

$$\Delta r = \Big[\frac{1}{\Delta r_{centre}} + \Big(\frac{1}{\Delta r_{edge}} - \frac{1}{\Delta r_{centre}}\Big)\Big(\frac{r}{r_{edge}}\Big)^{k}\Big]^{-1} \qquad (2.64)$$

Transformation of the transport equation to ρ yields for the radial derivatives $\partial/\partial r = \rho'\partial/\partial\rho$ and $\partial^2/\partial r^2 = \rho'^2\partial^2/\partial\rho^2 + \rho''\partial/\partial\rho$. Using the symmetric three point formulas for the ρ derivatives leads to an increase of the truncation error as compared to uniform grids [25, 26], however, the increase is small as long as the change of Δr for two adjacent grid intervals, i.e. $d^2r/d\rho^2 = -\rho''/\rho'^2$, is low. It is appropriate to keep the change of Δr below $\pm 10\%$.

2.4   Two Chamber Recycling Model

After the impurity source is stopped, the density has initially a faster decrease, which eventually turns into an exponential decay with a longer single time constant τ_d. It was found in section 2.2, that this decay time τ_d equals the longest eigentime τ_1 of the transport equation, which depends on the radial transport parameters. A decay with τ_1 can only be observed for non-recycling impurities, such that the inflow of neutral impurities is really stopped, when switching off the external source. For the light rare gases helium and neon, which completely recycle from the vessel walls as neutrals, the situation is very different, and τ_d usually is much longer than τ_1. The main bottle neck for the density decay is the transport to the pumped volume and to the pump duct. Here, the divertor configuration can achieve the highest values for the retainment of the impurities in the pumped volume. The achievable pumping efficiency depends on a number of parameters: the speed of the pumping system, the neutral main ion density in the pumped volume, the probability, that an impurity, which recycles at the divertor plates, reaches the pumped volume, the plugging of the pumped volume by the divertor plasma, i.e. the probability for an impurity in the pumped volume to reach the main plasma through the divertor fan, and finally the size of possible bypasses. It is especially important to understand these transport paths for helium, since the global confinement time τ_{He}^* of helium is a crucial parameter for the realisation of a burning fusion plasma as discussed in section 1.2.

The key parameters, which describe the puming efficiency, are usually calculated with a simple two chamber model, where the vessel is split into the main plasma volume V_{main} and the pumped volume V_{div} [27, 28]. The impurity particles in the pumped volume are neutral and the pumped particle rate $\Phi_{pump} = S n_{0,div}$ depends on the neutral impurity density $n_{0,div}$ and the pumping speed S. After a characteristic time $\tau_{pump} = S/V_{div}$, neutrals within V_{div} are pumped out. The characteristic pump time shall be long against the characteristic time scales $\tau_{main \to div}$ and $\tau_{div \to main}$ for particle exchange between the two chambers. With an impurity source rate Φ in the main chamber, the rate equations for the particle inventories in both volumes reads.

$$
\begin{aligned}
\frac{dN_{main}}{dt} &= -\frac{N_{main}}{\tau_{main \to div}} + \frac{N_{div}}{\tau_{div \to main}} + \Phi \\
\frac{dN_{div}}{dt} &= \frac{N_{main}}{\tau_{main \to div}} - \frac{N_{div}}{\tau_{div \to main}} - \frac{N_{div}}{\tau_{pump}}
\end{aligned}
\tag{2.65}
$$

This system has a fast eigentime τ_{eq} for equilibration between the two chambers and a slow eigentime τ_d, which equals the characteristic decay time after the source is stopped. With the above assumptions $\tau_{pump} \gg \tau_{main \to div}, \tau_{div \to main}$ these time constants are.

$$
\tau_{eq} = \frac{\tau_{main \to div} \tau_{div \to main}}{\tau_{main \to div} + \tau_{div \to main}} \qquad \tau_d = \tau_{pump}\left(1 + \frac{\tau_{main \to div}}{\tau_{div \to main}}\right)
\tag{2.66}
$$

In equilibrium, the ratio of time constants for particle exchange between the two volumes governs the relative population in the two chambers.

$$
\frac{N_{main}^{eq}}{N_{div}^{eq}} = \frac{\tau_{main \to div}}{\tau_{div \to main}} = \frac{\tau_d}{\tau_{pump}} - 1
\tag{2.67}
$$

The global confinement time τ^* is defined by the total equilibrium inventory for a given source rate Φ, where Φ has to be equal to the removal rate N_{div}^{eq}/τ_{pump}.

$$
\tau^* = \frac{N_{main}^{eq} + N_{div}^{eq}}{\Phi} = \tau_{pump} \frac{N_{main}^{eq} + N_{div}^{eq}}{N_{div}^{eq}} = \tau_{pump}\left(1 + \frac{N_{main}^{eq}}{N_{div}^{eq}}\right) = \tau_d
\tag{2.68}
$$

Thus, the global confinement time τ^* can be determined from the decay time τ_d, if the equilibration between the two chambers is fast against the pump time. It depends on the pump time constant and the ratio of the inventories in the two chambers. A quantity, which is more general, since it does not depend on the used pumping speed, is the compression factor C, which is the ratio of divertor neutral density to the average plasma bulk ion density. This quantity is not easily measured directly since the determination of the mass resolved neutral impurity density in the pumped volume is quite difficult [29, 30, 31]. Equation (2.67) can be used to estimate the compression factor from the decay time.

$$
C = \frac{n_{0,div}}{n_{ion,main}} = \frac{V_{main}}{S\tau_d - V_{div}}
\tag{2.69}
$$

Finally, the compression factor of helium should not be too small compared with the compression of deuterium and tritium in a fusion reactor, since this would necessitate a large throughput of the hydrogen isotopes in the tritium-recycling unit. Thus, the enrichment factor η is another important parameter to characterise the helium transport. For deuterium plasmas it is defined as.

$$\eta = C \frac{n_e^{main}}{2n_{D_2}^{div}} \tag{2.70}$$

For an acceptable D-T throughput, the helium enrichment factor η_{He} should exceed 0.2 in a fusion reactor [32].

2.5   Radial Transport and Charge State Distribution

The charge state distribution in a tokamak plasma is mainly determined by the radial profile of the electron temperature with typical values of 1-20 keV in the centre and a few eV in front of the plasma facing wall components.

For negligible transport, the ion stage distribution reflects a balance of the respective rates for ionisation and recombination. The most important reactions are ionisation by electron impact, radiative and di-electronic recombination. Three body recombination can be neglected due to the low electron densities, while charge exchange reactions from neutral hydrogen to impurity ions can open a further recombination channel in the edge plasma. For balanced reaction rates, the ratio of the densities of two adjacent ionisation stages is.

$$\frac{n_{z+1}}{n_z} = \frac{n_e S_z}{n_e \alpha_z + n_H \alpha_z^{cx}} \tag{2.71}$$

The ionisation rate coefficients S_z has the strongest dependence on the electron temperature T_e and governs the temperature dependence of the above balance. Ionisation by electron impact can only occur, when the colliding electron has a kinetic energy above the ionisation energy $E_{ion,z}$. The ionisation energy of the ions is roughly proportional to $(Z + 1)^2$ and highly charged ions can only be produced in the hot core of the plasma, while lower charge states exist already in the colder edge plasma. Thus, the fractional abundances $f_z = n_z / \sum_z n_z$ of the ion stages form radial shells, and each ion stage occupies a certain radial shell, where the ratio of plasma temperature and ionisation energy is on the order of 1. For low-Z elements, the innermost shell extends up to the axis and contains the fully ionised element.

For the case of argon in a typical ASDEX Upgrade H-mode plasma, the distribution due to the reaction balance is shown in Fig.2.9[b]. The radial coordinate is not linear and has a higher resolution at the edge as used in impurity transport calculations (see previous section). T_e and n_e are depicted in Fig.2.9[d]. In the radial range of the H-mode transport barrier, T_e drops within 2 to 3 cm from around 1 keV to below 100 eV.
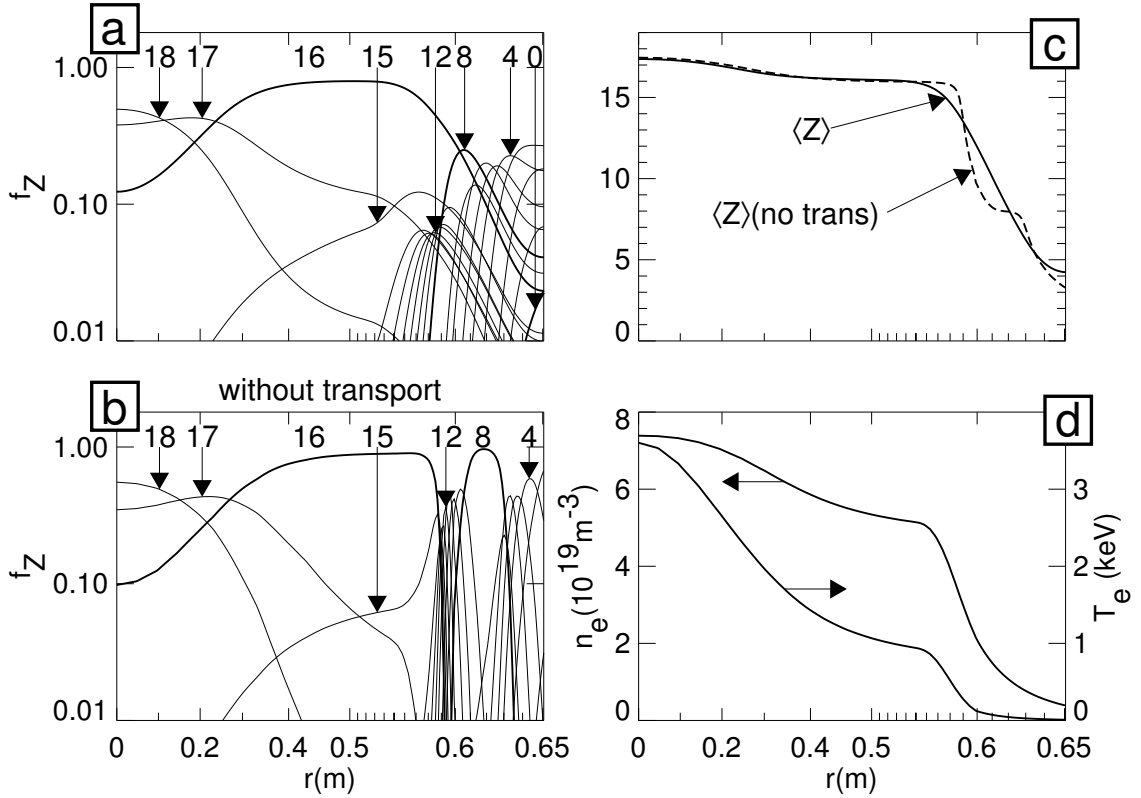
Figure 2.9:   *Equilibrium profiles of the ion stage distribution of argon for T_e- and n_e-profiles of a typical H-mode plasma in ASDEX Upgrade. Figure [a] is the solution of the coupled impurity transport equations with transport coefficients as depicted in Fig.2.8(case 4). The equilibrium distribution assuming local balance of the ionisation and recombination reactions is shown in [a]. Fig.[c] displays the mean ion charge for the two cases.*

The steep temperature gradient causes a steep gradient of the mean charge $\langle Z \rangle$ of argon (Fig.2.9[c]). Ions with a rare gas like electron shell (He-like,Ne-like) are very stable and occupy an especially wide radial shell.

Due to the radial transport the local balance of the ionisation/recombination reactions can not be established in all parts of the plasma, since the characteristic equilibration time can become long compared to the characteristic transport time, with which the ions move up and down the electron temperature gradient. This is especially true for the edge region, where the electron temperature has steep gradients. Ions can travel a considerable distance into a region with higher/lower electron temperature before they are further ionised/recombined. Similarly, ions do not recombine to very low charge states or neutral atoms in a thin cold edge plasma and finally hit the plasma facing walls, where recombination and eventual release as neutral atom can take place. Thus, the shell of a certain ion stage becomes radially more extended compared to the case of local ionisation/recombination balance and is shifted further inward. For the above
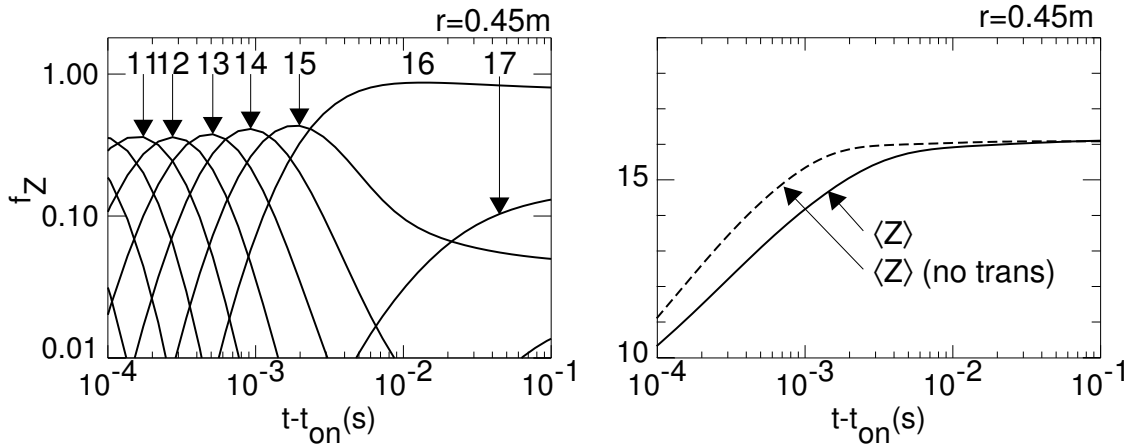
Figure 2.10:   *Temporal evolution of the ion stage distribution of argon at r=0.45 m after switching on the neutral edge source. T_e- and n_e-profiles are the same as in Fig.2.9[d]. The left graph shows the solution of the coupled impurity transport equations with transport coefficients as depicted in Fig.2.8(case 4). The mean ion charge reaches the equilibrium value with a few ms delay compared to the solution of the pure rate equations without transport (right graph).*

example of argon, the impurity transport coefficients of Fig.2.8(case 4) were used in the impurity transport code and the resulting ion stage in temporal equilibrium is shown in Fig.2.9[a]. The fractional abundances with transport can very well be approximated by the previous solution of Fig.2.9[b] for radii inside of $r \approx 0.5$ m, however, in the edge plasma and in the steep gradient region the charge distribution is very different and dominated by transport effects. The different radial shells have a much stronger overlap and the mean charge is also modified (Fig.2.9[c]). It should be mentioned, that the fractional ion abundances shown in Fig.2.9[a] are not only influenced by the transport coefficients, but also by the impurity source and source location as will be shown below. In this example, a temporally constant influx of neutral atoms from the edge radius was used, which yields a fuelling of the singly ionised ions close to the edge.

The time constants for reaching an equilibrium charge distribution are of practical importance, when analysing impurity transport experiments, where the impurity density evolution after the injection of impurities is used to deduce transport coefficients. The temporal evolution after the start of an impurity source depends on the reaction rates, with which a neutral atom is ionised into higher charge states, and on the characteristic transport time, with which the ions reach the hot core of the plasma, so that they can be ionised to higher ionisation stages. Both effects can be separated, when first considering a neutral atom at a certain radius in the hot plasma core, which is thought to be fixed at that radius and just subject to ionisation/recombination collisions. Thus, we solve the coupled reaction equations starting from the neutral atom at this radius. The
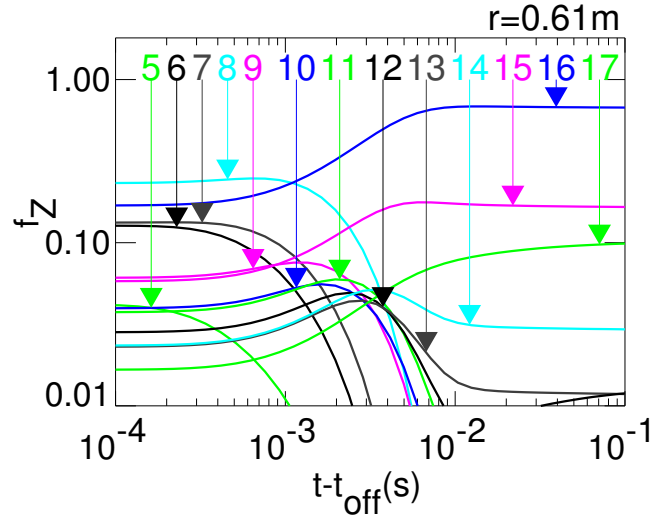
Figure 2.11: *Temporal evolution of the ion stage distribution of argon at r=0.61 m after switching off the neutral edge source. The low charge states disappear within a characteristic transport time and are not fed by recombination from higher charge states.*

resulting time evolution can then be compared to the full solution including transport. Such a comparison is shown in Fig.2.10. For the same plasma paramters as used for Fig.2.9, the evolution of the charge distribution after the start of a constant Ar influx was calculated. On the left hand side, the charge state abundances from the transport calculation is shown for $r = 0.45$ m. The left graph compares the evolution of the mean charge with the solution of the pure rate equations. $\langle Z \rangle$ of the pure reaction equations reaches the equilibrium after ≈ 2 ms. This time is dominated by the ionisation rates of the highest reached charge states, which have the lowest rate coefficients. As expected, $\langle Z \rangle$ of the full solution including transport reaches the equilibrium value with a delay compared to the solution of the pure reaction equations.

Strong deviations from the charge distribution due to pure reaction balance were found in the edge plasma. The cause for these deviations can further be elucidated by considering the case where the constant influx of impurities is suddenly stopped. At $r = 0.61$ m, the calculated charge distribution of argon after the end of the influx is shown in Fig.2.11. All the lower charge states up to a charge of Z=12 disappear from the edge plasma within a characteristic transport time, which is determined by the parallel and perpendicular losses. After this time, only higher ionisation stages, which diffuse out of the plasma core exist in this region. These charge states do not recombine to lower charge states than Z=13 before they are transported out of the edge plasma. Outflowing impurity ions never reach the low charge states before leaving the plasma. Thus, the low charge states at the plasma edge, which we previously found for the equilibrium with constant Ar influx (Fig.2.9[a]), are just fed by the inflowing ions. Their equilibrium distribution is just determined by the neutral influx, the ionisation rate profiles and the transport coef-

ficients. This effect is used in the determination of impurity influxes from spectroscopic measurements of line radiation from low lying charge states. It should be mentioned, that the charge distribution in Fig.2.11 does not include the effect of neutral argon recycling from the wall, which will always produce a population of low charge states in the edge plasma.

3. Transport Processes

A given charged particle is subject to fluctuating forces due to the movement of the other charged particles in the plasma, which cause fluctuations of the electric and magnetic field. We distinguish the fluctuations and the according transport by their length scale. For fluctuation with length scales below or equal to the Debye shielding length λ_D we speak of *Coulomb collisions* and *collisional transport* respectively, while plasma fluctuations with length scales much larger than λ_D cause *turbulence* and *anomalous transport*.

- Coulomb collisions between unlike ions cause radial displacements of the colliding ions and lead to diffusive and convective transport. In the magneto-hydrodynamic treatment, the Coulomb collisions lead to friction forces acting on the centre of mass velocity of the considered ion fluid. Friction forces, which are perpendicular to the magnetic field and the gradients of density and temperature, lead to *classical* transport, while *neoclassical* transport is due to parallel friction forces, where the latter are a consequence of the toroidal geometry. Collisional transport sets a lower limit to the transport coefficients.

- Tokamak plasmas always show the presence of a broad spectrum of fluctuations in plasma density, temperature, and electromagnetic fields. The fluctuations have a scale, which is small compared to the size of the plasma but large compared to λ_D, and a frequency, which is small compared to the plasma frequency ω_{pe}. These fluctuations arise from micro-instabilities which are essentially driven by the radial temperature and density gradients. The associated turbulent transport has little influence on the transport parallel to the field lines. However, turbulence is often the predominant mechanism for transport in the radial direction.

3.1 Collisional Transport

The exact derivation of the collisional transport coefficients is very complex and outside the scope of this work. Especially for many component plasmas, closed formulas can only be achieved when using several approximations. Thus, only a simplified treatment

will be given complemented by numerical results. A detailed mathematical treatment of collisional impurity transport can be found in Ref.[33]. Furthermore, Ref. [34, 35, 36] are recomended.

We consider the equation of motion for the centre of mass velocity $\vec{u}_a$ of species a with charge q_a and mass m_a.

$$m_a n_a \left(\frac{\partial \vec{u}_a}{\partial t} + (\vec{u}_a \cdot \nabla) \vec{u}_a \right) = q_a n_a (\vec{E} + \vec{u}_a \times \vec{B}) - \nabla p_a - \nabla \cdot \boldsymbol{\pi}_a + \sum_{b \neq a} \vec{F}_{ab} \qquad (3.1)$$

where n_a is the particle density, p_a is the pressure, $\boldsymbol{\pi}_a$ the viscosity tensor, and $\vec{F}_{ab}$ is the friction force density exerted on species a by collisions with species b. If the velocity distributions of both species are shifted Maxwellians, where the shift is small against the thermal velocities $v_a = \sqrt{2k_B T_a/m_a}$ and $v_b = \sqrt{2k_B T_b/m_b}$, the friction term is simply proportional to the difference of the centre of mass velocities.

$$\vec{F}_{ab} = m_a n_a \nu_{ab} (\vec{u}_b - \vec{u}_a) = -\vec{F}_{ba} \qquad (3.2)$$

Here, ν_{ab} is the frequency (collision frequency) for momentum transfer from species b onto species a.

$$\nu_{ab} = \frac{16\sqrt{\pi}}{3(4\pi\epsilon_0)^2} \frac{1}{m_a} \left(\frac{1}{m_a} + \frac{1}{m_b} \right) \frac{q_a^2 q_b^2 \ln \Lambda_{ab}}{(v_a^2 + v_b^2)^{3/2}} n_b \qquad (3.3)$$

where $\ln \Lambda_{ab}$ is the Coulomb logarithm. For equal temperatures ν_{ab} simplifies to

$$\nu_{ab} = \frac{4\sqrt{2\pi}}{3(4\pi\epsilon_0)^2} \frac{\sqrt{m_{ab}}}{m_a} \frac{q_a^2 q_b^2 \ln \Lambda_{ab}}{(k_B T)^{3/2}} n_b \qquad (3.4)$$

$m_{ab} = m_a m_b/(m_a + m_b)$ is the reduced mass of particles a and b. For ion-ion collisions the Coulomb logarithm is $\ln \Lambda_{ab} = 30 - \ln(Z_a Z_b \sqrt{n_a Z_a^2 + n_b Z_b^2}/T^{3/2})$ for n_a and n_b in [m^{-3}] and T in [eV]. In the strong magnetic field limit, the collision frequency is much smaller than the gyrofrequency $\omega_{ca} = q_a B/m_a$ and the Larmor radius $\rho_a = v_a/\omega_{ca}$ is much smaller than the gradient lengths of density L_n and temperature L_T.

$$\delta = \frac{\nu_{ab}}{\omega_{ca}} \ll 1 \qquad \delta = \frac{\rho_a}{L_{n,T}} = \frac{v_a}{\omega_{ca} L_{n,T}} \ll 1 \qquad (3.5)$$

Furthermore, we assume to be close to thermal equilibrium with $\vec{u}_a$ being small against the thermal velocity v_a. With these assumptions, the terms in Eq.(3.1) can be ordered in powers of the small parameter δ and the lowest order terms determine the lowest order of $\vec{u}_a$.

$$q_a n_a (\vec{E} + \vec{u}_a^{(0)} \times \vec{B}) - \nabla p_a = 0 \qquad (3.6)$$

while the first order of $\vec{u}_a$ is given by.

$$q_a n_a \vec{u}_a^{(1)} \times \vec{B} = -\sum_{b \neq a} \vec{F}_{ab} \qquad (3.7)$$

The vector product with $\vec{B}$ yields the lowest order velocity perpendicular to the magnetic field $\vec{u}_{\perp a}^{(0)}$.

$$\vec{u}_{\perp a}^{(0)} = \frac{\vec{E} \times \vec{B}}{B^2} - \frac{\nabla p_a \times \vec{B}}{q_a n_a B^2} \tag{3.8}$$

It is the sum of the E×B-drift and the diamagnetic drift. The diamagnetic drift is perpendicular to ∇p_a and $\vec{B}$ and lies in the magnetic surface.

3.1.1 Classical Transport

Classical transport considers the transport due to friction forces perpendicular to ∇p_a and $\vec{B}$. For $\vec{F}_{\perp ab}$, we apply the shifted Maxwellian approximation, and use in Eq.(3.2) the difference of the zero order velocities $(\vec{u}_{\perp b}^{(0)} - \vec{u}_{\perp a}^{(0)})$. Since the E×B-drift is the same for all species, only the difference of the diamagnetic velocities is leading to friction between different fluids. Then $\vec{u}_{\perp a}^{(1)}$ follows from Eq.(3.7).

$$\begin{aligned}
\vec{u}_{\perp a}^{(1)} &= \frac{1}{q_a n_a B^2} \sum_{b \neq a} \vec{F}_{\perp ab} \times \vec{B} \approx \frac{m_a}{q_a B^2} \sum_{b \neq a} \nu_{ab} (\vec{u}_{\perp b}^{(0)} - \vec{u}_{\perp a}^{(0)}) \times \vec{B} \\
&= \frac{m_a}{q_a B^2} \sum_{b \neq a} \nu_{ab} \left(\frac{\nabla p_b}{q_b n_b} - \frac{\nabla p_a}{q_a n_a} \right)
\end{aligned} \tag{3.9}$$

The first order velocity is in the direction of the pressure gradients and multiplication with n_a delivers the flux density $\vec{\Gamma}_{\perp a} = n_a \vec{u}_{\perp a}^{(1)}$. The pressure gradients can be split into the according density and temperature gradients and from ∇p_a we get a term proportional to ∇n_a. The proportionality factor is the classical diffusion coefficient D_{CL}^a for species a.

$$D_{CL}^a = \frac{m_a k_B T}{q_a^2 B^2} \sum_{b \neq a} \nu_{ab} = \frac{1}{2} \rho_a^2 \sum_{b \neq a} \nu_{ab} = \frac{1}{2} \rho_a^2 \nu_a \tag{3.10}$$

The classical diffusion coefficient is identical to the diffusion coefficient of a 'random walk' with Larmor radius ρ_a as characteristic radial step size and a characteristic stepping frequency ν_a. D_{CL}^a is the sum of diffusion coefficients D_{CL}^{ab} due to collisions with each fluid b and for equal temperatures of of all species D_{CL}^a has the following dependencies.

$$D_{CL}^a = \sum_{b \neq a} D_{CL}^{ab} = \frac{4\sqrt{2\pi}}{3(4\pi\epsilon_0)^2} \frac{1}{\sqrt{k_B T} B^2} \sum_{b \neq a} \sqrt{m_{ab}} \; \ln \Lambda_{ab} q_b^2 n_b \tag{3.11}$$

The diffusion coefficient is independent of the charge q_a. The main contributions come from collisions with ions, while friction with electrons can be neglected due to the small electron mass.

The remaining terms in Eq.(3.9) lead to convective terms of the flux density, which depend on the weighted sum of terms proportional to the density gradients ∇n_b and

terms proportional to the temperature gradient. It turns out, that the shifted Maxwellian approximation is only sufficient to calculate these terms for the case of zero temperature gradient. Since the friction force from Coulomb collisions is inversely proportional to the square of the relative velocity, higher order moments of the velocity distribution are important, which are neglected by the shifted Maxwellian approximation. In the presence of a temperature gradient, the first order velocity distribution and the according perpendicular friction force can be calculated from the Fokker-Planck-equation. For equal temperatures the result is [34].

$$\vec{F}_{\perp ab} = -m_a n_a \nu_{ab} \Big(\frac{\nabla p_b}{q_b n_b} - \frac{\nabla p_a}{q_a n_a} - \frac{3}{2} k_B \nabla T \Big[\frac{m_{ab}}{q_b m_b} - \frac{m_{ab}}{q_a m_a} \Big] \Big) \frac{\times \vec{B}}{B^2} = -\vec{F}_{\perp ba} \qquad (3.12)$$

In this expression, the terms due to the diamagnetic drift are retained from the shifted Maxwellian approximation, and an additional term proportional to the temperature gradient appears, which is called the *thermoforce*. This term is due to the diamagnetic heat flux,

$$\vec{q}_{\perp a}^{(0)} = -\frac{5}{2} \frac{p_a}{q_a} \frac{k_B \nabla T_a \times \vec{B}}{B^2} \qquad (3.13)$$

which is obtained from the equation of motion for the second order moment of the velocity distribution. For ion-ion collisions and same directions of ∇p and ∇T, thermoforce and diamagnetic part have opposite direction for $m_a > m_b$ and same direction for $m_a < m_b$. Since the diamagnetic terms are unchanged, there are no alterations for the diffusion coefficient and we get for the classical drift velocity $\vec{v}_{CL}^a$.

$$\vec{v}_{CL}^a = \sum_{b \neq a} D_{CL}^{ab} \frac{q_a}{q_b} \Big[\frac{\nabla n_b}{n_b} - \frac{\nabla T}{T} \Big(\frac{3m_{ab}}{2m_b} - 1 - \frac{q_b}{q_a} \Big(\frac{3m_{ab}}{2m_a} - 1 \Big) \Big) \Big] \qquad (3.14)$$

The drift velocity contributions are proportional to the according diffusion coefficient times the charge ratio q_a/q_b. Thus, transport becomes increasingly convective for elements with higher charge. The density gradient ∇n_b causes a drift in upwards direction of the gradient. When considering only fully ionised ions with $Z \approx m/2$, the multiplier of the $\nabla T/T$ term in Eq.(3.14) equals $1/2(1 - m_b/m_a)$ being positive(negative) for $m_a > m_b$ ($m_a < m_b$). For heavy impurities, the ∇T term drives in the opposite direction of the temperature gradient towards the plasma edge and this outwardly directed drift due to the temperature gradient is called *temperature screening*.

The main effects leading to classical transport are summarised in the cartoon of Fig.3.1. Impurity and hydrogen ions gyrate around the magnetic field which is directed into the paper. Due to the density and temperature gradient, both species have a diamagnetic velocity in the upwards direction, however, for impurities it is of smaller magnitude due to the $1/q$ dependence. The difference in mean velocities causes a friction force on the impurities in the upwards direction, which leads in the depicted case to a drift up the impurity gradient. The temperature gradient might however cancel this effect since
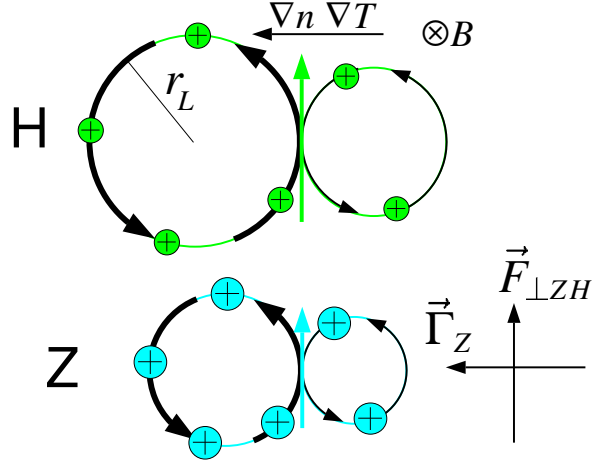
Figure 3.1: *Classical transport from collisions between hydrogen and impurity ions is due to the difference in the diamagnetic velocities, which causes friction forces perpendicular to $\vec{B}$.*

collisions with the upwards rotating fast hydrogen ions are less effective compared to collisions with the slow downwards rotating ions. For zero density gradient of hydrogen and zero temperature gradient, the diamagnetic drift of hydrogen is zero and the friction force on the impurity is always in the opposite direction of its diamagnetic velocity, which gives rise to diffusive transport down the impurity density gradient.

Friction forces perpendicular to the magnetic field in the magnetic surface are not the only cause for collisional transport. For the helical field lines in a tokamak, also parallel friction forces generate due to their toroidal component a radial particle flux. We now take a different approach which leads to an expression for the surface averaged radial particle flux density. The result will serve to calculate the average classical diffusion coefficient needed in the transport equation (2.12) and introduce the new terms, which will be discussed in the next section.

The toroidal angular momentum balance is obtained from Eq.(3.1) by multiplying with major radius R and unit vector in the toroidal direction $\vec{e}_t$. It yields for the Lorentz term

$$Rq_a n_a \vec{e}_t(\vec{u}_a \times \vec{B}) = -q_a n_a u_{a,\Psi} R B_p = -q_a n_a u_{a,\Psi}|\nabla\Psi| = -q_a \Gamma_{a,\Psi}|\nabla\Psi| \qquad (3.15)$$

where $\Gamma_{a,\Psi}$ is the particle flux density perpendicular to the magnetic surface and Ψ is the poloidal flux, which was used to express the poloidal magnetic field: $R B_p = |\nabla\Psi|$. All terms in Eq.(3.1), which contain the gradient of a scalar quantity, i.e. the pressure and the part of the electric field, which is caused from a static potential, cancel due to toroidal symmetry. The inertia terms are of second order in the small parameter δ and can be neglected. The viscosity does not change the average toroidal angular momentum on the flux surface $\langle \vec{e}_t R \nabla \cdot \pi_a \rangle = 0$. Thus, we are left with the toroidal component of

the friction force $F_{a,t}$ and the induced electric field E_t, which determine the average contravariant particle flux density $\langle \Gamma_a^\Psi \rangle = \langle \Gamma_{a,\Psi} | \nabla \Psi | \rangle$. In the radial transport equation (2.12), r was used as flux surface label and the quantity of interest is $\langle \Gamma_a^r \rangle = \langle \Gamma_a^\Psi \rangle (dr/d\Psi)$ with

$$\frac{dr}{d\Psi} = \frac{1}{R_{axis}} \frac{1}{2\pi r} \oint \frac{dl_p}{B_p} \tag{3.16}$$

For circular flux surfaces and large aspect ratio, it is $dr/d\Psi = 1/(R_{axis} B_p)$. Thus, we obtain

$$\langle \Gamma_a^r \rangle = \frac{dr}{d\Psi} \left(n_a \langle R E_t \rangle + \frac{1}{q_a} \langle R F_{a,t} \rangle \right) \tag{3.17}$$

The toroidal components of induced electric field and friction force can be split into the components parallel and perpendicular to the magnetic field.

$$\vec{e}_t = \frac{B_t}{B} \vec{e}_\parallel - \frac{B_p}{B} \vec{e}_\perp \tag{3.18}$$

The perpendicular components yield the classical part of the particle flux.

$$\langle \Gamma_a^r \rangle_\perp = \left(\frac{dr}{d\Psi} \right) \left(\frac{1}{q_a} \left\langle \frac{R B_p F_{a\perp}}{B} \right\rangle + n_a \left\langle \frac{R B_p E_\perp}{B} \right\rangle \right) \tag{3.19}$$

The term, which contains the perpendicular friction force leads to classical transport, and the term with the perpendicular electric field causes the *classical* pinch velocity. The classical pinch velocity $\vec{u}_{CL,pinch} = -E_\perp/B \vec{e}_r = -E_t B_p/B^2 \vec{e}_r$ is small compared with the other drifts, since only the small perpendicular part of the induced electric field produces the radial inward drift. The gradients, which appear in the friction force $F_{a\perp}$ [see Eq.(3.12)] can be replaced by: $\nabla = |\nabla \Psi| \, d/d\Psi = R B_p \, d/d\Psi = R B_p (dr/d\Psi) d/dr$. Finally, the additional $1/B$ dependence of $F_{a\perp}$ has to be taken into account and we obtain for the average diffusion coefficient from Eq.(3.10).

$$\langle D_{CL}^a | \nabla r |^2 \rangle = \left(\frac{dr}{d\Psi} \right)^2 \left\langle \frac{R^2 B_p^2}{B^2} \right\rangle \frac{m_a k_B T}{q_a^2} \sum_{b \neq a} \nu_{ab} \tag{3.20}$$

In the drift velocity of Eq.(3.14), we just have to replace D_{CL}^a by $\langle D_{CL}^a | \nabla r |^2 \rangle$ and the gradients by d/dr.

3.1.2 Pfirsch-Schlüter Transport

Neoclassical transport is due to the parallel component of the friction forces. Eq.(3.17) and Eq.(3.18) give the according averaged radial particle flux.

$$\langle \Gamma_a^r \rangle_\parallel = \left(\frac{dr}{d\Psi} \right) \frac{1}{q_a} \left\langle \frac{R B_t F_{a\parallel}}{B} \right\rangle \tag{3.21}$$

$(R B_t)$ is constant on the magnetic surface and can be taken out of the surface average. The parallel friction forces shall be calculated in a simplified manner by making use of

the shifted Maxwellian approximation (3.2). To this end, the lowest order parallel fluid velocity of all species needs to be known. It is coupled to the lowest order perpendicular fluid velocities $\vec{u}_{\perp a}^{(0)}$, where the coupling is due to the fact, that the $\vec{u}_{\perp a}^{(0)}$ are not divergence free. For reasons of simplicity, we only discuss the diamagnetic velocity. It is smaller on the inside and higher on the outside of the magnetic surface because of the inverse proportionality to the magnetic field strength. Thus, the diamagnetic flows drive the density on the magnetic surface towards an up/down asymmetry where the sign depends on the magnetic field direction and the charge of the species. However, parallel flows build up to counteract this tendency. In lowest order, the particle fluxes must have zero divergence and since in lowest order the density is constant on the magnetic surface, the lowest order flow velocities also must have zero divergence. The diamagnetic velocity can be decomposed into a toroidal and a parallel part using Eq.(3.18).

$$
\begin{aligned}
\vec{u}_{\perp a}^{(0)} &= -\frac{\nabla p_a \times \vec{B}}{q_a n_a B^2} = -\frac{1}{q_a n_a} \frac{\partial p_a}{\partial \Psi} \frac{\nabla \Psi \times \vec{B}}{B^2} = -\frac{1}{q_a n_a} \frac{\partial p_a}{\partial \Psi} \frac{R B_p}{B} \vec{e}_\perp \\
&= \frac{1}{q_a n_a} \frac{\partial p_a}{\partial \Psi} \left(R \vec{e}_t - \frac{R B_t}{B} \vec{e}_\parallel \right)
\end{aligned}
\tag{3.22}
$$

The toroidal part is a rotation with constant angular frequency and has zero divergence. In the parallel part, $R B_t$ is constant and the $1/B$ dependence causes a non-vanishing divergence and the lowest order parallel velocity must cancel this part to guarantee $\nabla \cdot \vec{u}_a^{(0)} = 0$.

$$
\begin{aligned}
\vec{u}_{\parallel a}^{(0)} &= R B_t \frac{1}{q_a n_a} \frac{\partial p_a}{\partial \Psi} \frac{1}{B} \vec{e}_\parallel + C_a \vec{B} \\
&= R B_t \frac{1}{q_a n_a} \frac{\partial p_a}{\partial \Psi} \left[\frac{1}{B} - \frac{B}{\langle B^2 \rangle} \right] \vec{e}_\parallel + \hat{u}_a \frac{B}{\langle B^2 \rangle} \vec{e}_\parallel
\end{aligned}
\tag{3.23}
$$

With the condition $\nabla \cdot \vec{u}_a^{(0)} = 0$, the parallel flow is not completely determined, since an additional flow $\propto \vec{B}$ can be added because the magnetic field has of course zero divergence: $\nabla \cdot \vec{B} = 0$. The constants C_a can be different for different species and lead to parallel friction. It is advantageous to use a differently defined integration constant $\hat{u}_a$ as is introduced in the second line of Eq.(3.23). It has the property, that the surface average $\langle \vec{B} \vec{u}_{\parallel a}^{(0)} \rangle$ equals $\hat{u}_a$. Only the part of the parallel velocity, which is proportional to $\hat{u}_a$, is influenced by viscous forces as will be shown below. With the shifted Maxwellian approximation (3.2), we find two contributions to the transport from parallel friction.

$$
\begin{aligned}
\langle \Gamma_a^r \rangle_\parallel &= \left(\frac{dr}{d\Psi} \right) R B_t \frac{1}{q_a} \left\langle \frac{F_{a\parallel}}{B} \right\rangle \\
&\approx \left(\frac{dr}{d\Psi} \right)^2 (R B_t)^2 \left[\left\langle \frac{1}{B^2} \right\rangle - \frac{1}{\langle B^2 \rangle} \right] \frac{m_a n_a}{q_a} \sum_{b \neq a} \nu_{ab} \left(\frac{1}{q_b n_b} \frac{\partial p_b}{\partial r} - \frac{1}{q_a n_a} \frac{\partial p_a}{\partial r} \right) \\
&+ \left(\frac{dr}{d\Psi} \right) \frac{(R B_t)}{\langle B^2 \rangle} \frac{m_a n_a}{q_a} \sum_{b \neq a} \nu_{ab} (\hat{u}_b - \hat{u}_a)
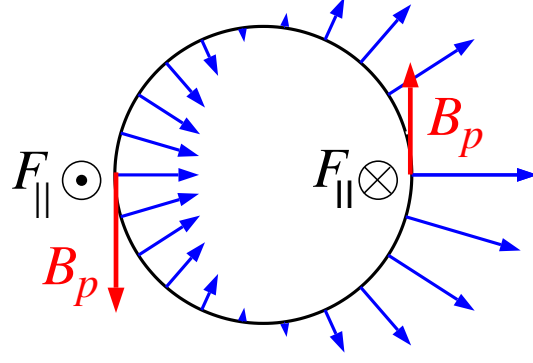\end{aligned}
\tag{3.24}
$$

Figure 3.2:   *The pattern of the Pfirsch-Schlüter fluxes originates from the variation of the parallel flow velocity with the poloidal angle.*

The first term in the sum is called the *Pfirsch-Schlüter* (PS) term, while the second contribution from $\hat{u}$ is called the *Banana-Plateau* (BP) term.

The radial derivative of the pressure p_a in the Pfirsch-Schlüter contribution contains the derivative of the density n_a and the proportionality factor is the diffusion coefficient.

$$\langle D_{PS}^a |\nabla r|^2 \rangle \approx \left(\frac{dr}{d\Psi}\right)^2 (RB_t)^2 \left\langle \frac{1}{B^2} - \frac{1}{\langle B^2 \rangle} \right\rangle \frac{m_a k_B T}{q_a^2} \sum_{b \neq a} \nu_{ab} \qquad (3.25)$$

For the case of circular flux surfaces and in the limit of small inverse aspect ratio $\epsilon = r/R_0$, the magnetic field averages in Eq.(3.25) can be approximated: $RB_t(dr/d\Psi) \approx q/\epsilon$, $1/\langle B^2 \rangle \approx (1 - \epsilon^2/2)/B_0^2$ and $\langle 1/B^2 \rangle \approx (1 + 3\epsilon^2/2)/B_0^2$. In this limit, the Pfirsch-Schlüter diffusion coefficient is a factor of $2q^2$ higher than the classical diffusion coefficient. This factor can be understood by investigating the variation of the PS-fluxes with the poloidal angle θ, which is visualised in Fig.3.2. The diamagnetic velocity depends on θ as $u_\perp \approx u_\perp^0 (1 + \epsilon \cos\theta)$ and the PS-part of the parallel velocity is larger by a factor of $2q$ with a poloidal dependence $u_\parallel \approx 2q \cos\theta \, u_\perp = 2q \cos\theta (1 + \epsilon \cos\theta) \, u_\perp^0$. For the classical fluxes, mainly the toroidal field counts, while for the PS-fluxes, it is the poloidal field, which gives an extra factor of $B_t/B_p \approx q/\epsilon$ between the two fluxes. Thus, the poloidal variation of the PS-flux is $\Gamma_{PS} \approx 2(q^2/\epsilon) \cos\theta (1 + \epsilon \cos\theta)^2 \, \Gamma_{CL}^0$. The dominant term varies with $\cos\theta$, which creates the main feature in Fig.3.2, i.e. the zeros of the radial flux on the upper and lower part of the surface. However, this term does not lead to an average radial flux. Only the term $2\epsilon \cos^2\theta$ has a non-zero average ϵ, which results in the factor $2q^2$ in favour of the PS-flux.

Like in the classical case, the shifted Maxwellian approximation is not sufficient to account for all drift terms depending on the temperature gradient and higher order moments of the parallel velocity distribution have to be considered. The diamagnetic heat flux from Eq.(3.13) has to be accompanied by a zero order parallel heat flux, which assures divergence free total heat flux and introduces the same temperature screening terms as known from the classical case. The parallel particle and heat fluxes do not

completely remove the up/down asymmetry of density and temperature caused by the diamagnetic flows. Since the variation of the temperature on the magnetic surface will be different for species with different charge, energy can be transferred from one species to another through collisions. This collisional coupling becomes important for high collisionalities, i.e. when the collision times are much shorter than the transit time on the flux surface. As a consequence, the larger temperature variations of high-Z impurities are reduced together with the parallel heat flux and the temperature screening in the high collisionality regime is reduced. This effect will be seen below in the numerical solutions of Pfirsch-Schlüter transport.

3.1.3 Banana-Plateau Transport

For the Banana-Plateau term in Eq.(3.24), $\hat{u}_a$ has to be calculated for each species. It can be determined from the surface averaged force balance along the field lines. We obtain from Eq.(3.1) by multiplication with $\vec{B}$

$$\langle B(\nabla \cdot \boldsymbol{\pi}_a)_{\parallel} \rangle = \langle BF_{a\parallel} \rangle \tag{3.26}$$

where we neglected the small contribution due to the induced electric field. The viscosity tensor describes the deviation of the velocity distribution from spherical symmetry, i.e. the anisotropy of the pressure parallel and perpendicular to the magnetic field.

$$\boldsymbol{\pi}_a = (p_{\parallel a} - p_{\perp a})\left(\vec{e}_{\parallel}\vec{e}_{\parallel} - \frac{1}{3}\boldsymbol{I}\right) \tag{3.27}$$

The anisotropy of the pressure varies in the poloidal direction of the flux surface, which leads to a damping of the poloidal flow velocity.

The anisotropy results from the motion of the species in an inhomogeneous magnetic field. Collision free particles, which travel from the outside of the torus to the inside, gain perpendicular kinetic energy $W_{\perp}$ on the cost of parallel energy $W_{\parallel}$ due to the conservation of kinetic energy and the adiabatic invariance of the magnetic moment $\propto W_{\perp}/B$. Particles, which start on the outside of the magnetic surface with $B = B_{min}$, can only pass the high field side with $B = B_{max}$, if the ratio of parallel to perpendicular energy at the low field side is high enough. Otherwise, they are reflected on the high field side and become trapped particles, which move back and forth on the low field side. The velocity space is thus divided into the region of passing particles and trapped particles.

$$\frac{v_{\parallel}^2}{v_{\perp}^2}(B = B_{min}) \begin{cases} > \frac{B_{max}}{B_{min}} - 1 & \text{for passing particles} \\ < \frac{B_{max}}{B_{min}} - 1 & \text{for trapped particles} \end{cases} \tag{3.28}$$

with $(B_{max}/B_{min}) - 1 \approx 2\epsilon$ for the case of high aspect ratios. In the same limit, the fraction of trapped particles is $n_t/n \approx \sqrt{\epsilon}(1.46 - 0.46\epsilon)$. The orbits of trapped particles are
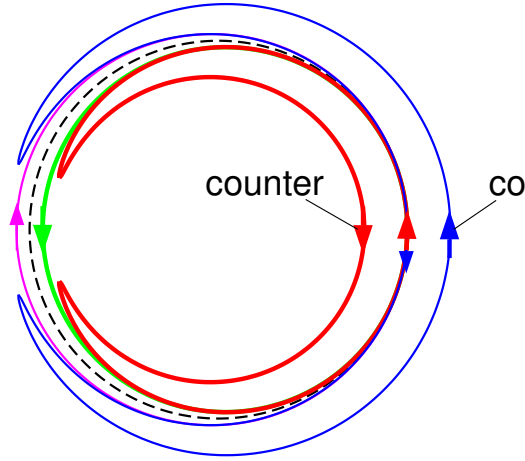
Figure 3.3:   *Poloidal projection of particle orbits for trapped and passing neon ions*
(B_t=2 T, q=1.5, T_i=2 keV, ϵ=0.18) which start in opposite direction on the same radius
at the low-field side of the torus.

stronger influenced by the vertical torus drifts (∇B-drift and centrifugal drift). Fig.3.3
depicts the poloidal projection of the orbit for trapped and passing ions, which start from
the same position on the low field side with opposite parallel velocity. The orbits of the
trapped particles (the so called banana orbits) show wider excursions from the magnetic
surface than the orbits of the passing particles. The width of the banana orbit w_B on the
outside of the orbit is highest for barely trapped particles, i.e. for particles, which have
parallel velocity $v_\parallel \approx v_\perp \sqrt{2\epsilon}$ and are reflected at $\theta = \pi$. It is $w_B \approx \sqrt{\epsilon}\rho_p$, where ρ_p is
the Larmor radius evaluated with the poloidal magnetic field B_p. The passing particles
only have a maximum displacement $\Delta r_{max} \approx \epsilon\rho_p$ from their average radius. Trapped
ions travel along the orbit such, that they move in the direction of the electric current,
when they are on the outside (co) and against the current on the inside (counter) of the
banana (for electrons the direction is reversed). Thus, we find a similar effect on the
parallel flow velocity (and the parallel heat flow) as was obtained for the perpendicular
flow due to the gyro-motion of the ions (Fig.3.1). In the case of constant temperature,
a radial density gradient causes due to the gyro-motion a diamagnetic particle flux of
order $\rho_a v_a \nabla n_a$, and here the analogous parallel particle flux on the outside of the flux
surface is of the order of $w_B v_{\parallel a} \nabla n_{t,a}$.

$$n_{t,a} u_\parallel \approx \epsilon^{3/2} \frac{\nabla p_a}{q_a B_p} \tag{3.29}$$

The passing particle orbits in Fig.3.3 suggest, that for this class of ions, there also exists
a parallel flow velocity due to radial pressure gradients. However, the extra parallel
velocities on the low-field side and the high-field side are in opposite direction and cancel
when averaging over the magnetic surface. There is a more indirect effect on the passing
particles, which are accelerated by scattering of trapped particles into the passing domain
of the velocity distribution.

The evolution of the velocity anisotropies along the flux surface, which we just described for collisionless particles, are of course counteracted by pitch angle scattering, which drives the energy ratio back towards the spherical symmetric value $W_\perp = 2W_\parallel$. The strength of the anisotropy will be low if the collision time is small compared to a typical transit time to travel from the outside to the inside of the torus. The collisionality ν_a^*

$$\nu_a^* = \frac{qR_0}{v_a}\epsilon^{-3/2}\sum_b \nu_{ab} = \frac{\nu_a qR_0}{v_a}\epsilon^{-3/2} \tag{3.30}$$

is used to distinguish the importance of collisions on the particle movement (here the sum includes the term ν_{aa}). For $\nu_a^* > \epsilon^{-3/2}$, the collision time is shorter than the transit time $\tau_T = qR_0/v_a$ of a passing particle with thermal velocity v_a. For $\nu_a^* < 1$, even trapped particles, which because of lower parallel velocity need the longer bounce time $\tau_B = \tau_T/\sqrt{\epsilon}$ to complete their orbit, do not suffer from pitch angle scattering, which would transform them to passing particles. To this end, the direction of the velocity vector of a trapped particle only needs a turn of about $\sqrt{\epsilon}$ and since the effect of the many small angle collisions in the plasma can be understood as a diffusion process in velocity space, the effective collision frequency for this process has an increased value of $\nu_{a,eff} = \nu_a/\epsilon$, where ν_a is the frequency for turning the velocity vector by an angle of order 1. The collisionality regimes are called the banana regime for $\nu_a^* < 1$, the plateau regime for $1 < \nu_a^* < \epsilon^{-3/2}$ and the Pfirsch-Schlüter regime for $\nu_a^* > \epsilon^{-3/2}$.

Coming back to Eq.(3.26), it can be shown from kinetic calculations [33], that the average of the parallel viscous forces depends only on the poloidal component of the moments of the asymmetric velocity distribution for the considered fluid. Only the term proportional to the poloidal flow velocity $u_{p,a}^{(0)}$ shall be taken into account, keeping in mind that terms proportional to higher order moments like the poloidal heat flux are neglected.

$$\langle B(\nabla \cdot \boldsymbol{\pi}_a)_\parallel \rangle = \mu_a \frac{u_{p,a}^{(0)}}{B_p}\langle B^2 \rangle \tag{3.31}$$

$u_{p,a}^{(0)}/B_p$ is constant on the magnetic surface. μ_a is the viscosity coefficient of species a, which depends on the collisionality ν_a^* and thus on the densities and temperatures of all species, however, not on fluid velocities or asymmetries of other species.

In the banana regime with low collisionality $\nu_a^* \ll 1$, the viscous force can be understood from the collisions, which exchange particles between the trapped and passing domain. Particles are lost from the trapped domain with the frequency ν_a/ϵ and accelerate the passing particles. From the passing domain, only a fraction $\approx \sqrt{\epsilon}$ of the collisions will lead back into the trapped domain. With Eq.(3.29), the parallel force density of this effect is.

$$
\begin{aligned}
m_a n_a \frac{du_{\parallel a}}{dt} &= m_a \frac{\nu_a}{\epsilon}\epsilon^{3/2}\frac{\nabla p_a}{q_a B_p} - m_a n_a \nu_a \sqrt{\epsilon} u_{\parallel a} \\
&= -\sqrt{\epsilon}m_a n_a \nu_a \frac{B}{B_p}\left(-\frac{\nabla p_a}{q_a n_a B} + \frac{B_p}{B}u_{\parallel a}\right) \tag{3.32}
\end{aligned}
$$

In the second line of Eq.(3.32), the poloidal components of the parallel velocities were collected in the large brackets. Thus, the simple model leads to the same expression of the viscous force as in Eq.(3.31) and the viscosity coefficient is $\mu_a \approx \sqrt{\epsilon} m_a n_a \nu_a$ for $\nu_a^* \ll 1$.

In the Pfirsch-Schlüter regime with $\nu_a^* > \epsilon^{-3/2}$, particles move during a collision time $1/\nu_a$ only over a small poloidal angle $\Delta\theta_{coll} \approx v_{th}/(qR\nu_a)$ and the parallel velocity will change by an amount.

$$
\begin{aligned}
v_\parallel(\Delta\theta_{coll}) &= v_\parallel(0)\sqrt{1 + \frac{v_\perp^2}{v_\parallel^2}\frac{1}{B}\frac{dB}{d\theta}\,\Delta\theta_{coll}} \\
&\approx v_\parallel(0)\Big[1 + \frac{v_\perp^2}{2v_\parallel^2}\frac{1}{B}\frac{dB}{d\theta}\,\Delta\theta_{coll} - \frac{v_\perp^4}{4v_\parallel^4}\Big(\frac{1}{B}\frac{dB}{d\theta}\Big)^2 (\Delta\theta_{coll})^2\Big] \quad (3.33)
\end{aligned}
$$

When averaging over the whole species, only the term quadratic in $\Delta\theta$ is non zero, because half of the particles move in the positive and half in the negative θ direction. The deviation from spherical symmetry of the velocity distribution will be small due to the high collision frequency and $v_\perp^2/2v_\parallel^2$ can be replaced by 1.

$$
m_a n_a \frac{du_\parallel}{dt} \approx m_a n_a(v_\parallel(\Delta\theta_{coll}) - v_\parallel(0))\nu_a = -m_a n_a v_\parallel(0)\Big(\frac{1}{B}\frac{dB}{d\theta}\Big)^2\Big(\frac{v_{th}}{qR}\Big)^2\frac{1}{\nu_a} \quad (3.34)
$$

The viscosity coefficient is now $\propto \nu_a^{-1}$ and the viscous force decreases with increasing collisionality. Thus, the viscosity coefficient will rise with ν_a in the banana regime, reach a maximum and decrease with $1/\nu_a$ in the Pfirsch-Schlüter regime. The same will be found for the diffusion coefficient of the banana-plateau contribution.

We now continue with the determination of the $\hat{u}_a$ part of the parallel velocity. We replace the poloidal velocity by the parallel and perpendicular components from Eq.(3.22) and Eq.(3.23) using

$$
\vec{e}_p = \frac{B_p}{B}\vec{e}_\parallel + \frac{B_t}{B}\vec{e}_\perp \quad (3.35)
$$

and obtain from the averaged parallel force balance (3.26) a system of equations, which determines the integration constants $\hat{u}_a$.

$$
\mu_a\Big[\hat{u}_a - RB_t\frac{1}{q_a n_a}\frac{\partial p_a}{\partial\Psi}\Big] = \sum_{b\neq a} m_a n_a \nu_{ab}(\hat{u}_b - \hat{u}_a) \quad (3.36)
$$

The $\hat{u}$ are functions of the viscosity coefficients, collision frequencies and the pressure gradients and yield the radial particle fluxes from Eq.(3.24). The solution reads in the most simple case of a pure plasma with hydrogen ions and electrons only.

$$
\langle\Gamma_i^r\rangle_{BP} = \Big(\frac{dr}{d\Psi}\Big)^2\frac{(RB_t)^2}{\langle B^2\rangle}\frac{m_i n_i \nu_{ie}}{e^2}\frac{\mu_{ie}}{\mu_{ie} + m_i n_i \nu_{ie}}\Big(-\frac{1}{n_e}\frac{\partial p_e}{\partial r} - \frac{1}{n_i}\frac{\partial p_i}{\partial r}\Big) \quad (3.37)
$$

The effective viscosity coefficient $\mu_{ie} = \mu_i\mu_e/(\mu_i + \mu_e)$ equals the electronic viscosity coefficient μ_e due to the large mass ratio. In the low collisionality regime $\nu_e^* < 1$, μ_e is

proportional to the collision frequency $\mu_e \propto m_e n_e \nu_{ei} = m_i n_i \nu_{ie}$ and the term with μ_{ie} in Eq.(3.37) becomes constant. For circular plasmas and small inverse aspect ratio, the constant is $\approx \sqrt{\epsilon}$ and another factor $(q/\epsilon)^2$ comes from the quadratic ratio of toroidal and poloidal field. In the low collisionality limit, the BP diffusion coefficient of electrons and ions is a factor of $\approx q^2/\epsilon^{3/2}$ over the classical value and thus the dominant term of the collisional transport.

$$D_{BP}^{e,i} \approx \frac{q^2}{\epsilon^{3/2}} \frac{m_i k_B T \nu_{ie}}{B^2 e^2} = \frac{q^2}{\epsilon^{3/2}} D_{CL}^{e,i} \tag{3.38}$$

Inclusion of higher order moments, adds to Eq.(3.36) the appropriate terms due to the the parallel friction and viscous force. Additionally, there will be a respective equation for the parallel balance of the higher order moments. The higher order moments, i.e. the effect due to the parallel heat flux, are necessary to calculate the temperature screening of the BP transport, however, the calculation becomes very complex for a many component plasma [37] and it is advantageous to calculate the transport coefficients numerically.

During the discussion of the trapped particle orbits, the influence of the induced toroidal electric field has so far been neglected. It leads to a further neoclassical inward drift, the so called Ware pinch [38]. When a collision free trapped particle moves in the co-current direction, it is accelerated by the electric field, and the reflection point shifts towards the high-field side. On the return branch in the counter-current direction, it has to travel against the electric field and the reflection angle is closer to zero than without field. Thus, the poloidal projection of the banana orbits, which were shown to be symmetric to the equatorial plane in Fig.3.3, are actually turned by a certain poloidal angle θ (with $\theta > 0$ for Fig.3.3). Since the particles do not stay equal times above and below the equatorial plane, the radial movement towards and away from the magnetic axis due to the vertical torus drifts is not exactly balanced and the projected orbits do not close on itself, but show rather a small inwardly directed radial shift after the completion of each bounce period. The radial movement of the banana orbits can also be understood from the conservation of the canonical toroidal momentum.

$$p_\phi = m_a R^2 \frac{d\phi}{dt} + q_a R A_\phi = m_a R^2 \frac{d\phi}{dt} + q_a \Psi = const. \tag{3.39}$$

Here, $d\phi/dt$ is the toroidal angular velocity, A_ϕ is the toroidal component of the vector potential, and Ψ is the poloidal magnetic flux. At the turning points of the banana, the toroidal angular velocity is zero and all turning points lay on a surface with $\Psi = const.$ The movement of this surface of constant flux yields the movement of the banana orbit. At a fixed point in space, Ψ is changing due to the induced electric field $\partial\Psi/\partial t = -RE_t$ and the total time derivative is.

$$\frac{d\Psi}{dt} = \frac{\partial\Psi}{\partial t} + \vec{v}_\Psi \; \nabla\Psi = -RE_t + v_\Psi R B_p \tag{3.40}$$

The radial velocity of the flux surface $v_\Psi = (E_t/B_p)$ is inwardly directed. Thus, the single particle picture gives for all species an equal pinch velocity. Averaging over the flux surface and multiplying with the total number of trapped particles gives the radial flux density.

$$\langle \Gamma^r_{ware} \rangle = \kappa_{ware} n f_{trap} \langle \frac{E_t}{B_p} \rangle \tag{3.41}$$

Here, κ_{ware} is a collisionality dependent factor, which becomes zero for high collisionalities, i. e. when only a small part of the banana can be passed between two collisions. For low collisionalities, κ_{ware} is of order unity. The Ware pinch velocity is a factor of $(B/B_p)^2 \approx 100$ higher than the classical pinch velocity. It is important for the main ion species, which has lowest collisionalities, while for the impurities the contribution is usually small compared with the gradient driven pinch terms. It should be noted, that a collisionless passing ion will just gain toroidal angular momentum at the same rate as Ψ is changing locally, and the orbit does not move in space.

3.1.4 Overview of Collisional Transport Coefficients

In Eq.(3.17), it was found, that the average radial flux density $\langle \Gamma^r_a \rangle$ of species a is caused by the toroidal component of the friction forces between a and all other species: $\langle \Gamma^r_a \rangle = \sum_b \langle \Gamma^r_{ab} \rangle \propto (1/q_a) \sum_b \langle RF_{ab,t} \rangle$. $\vec{F}_{ab}$ equals $-\vec{F}_{ba}$ due to momentum conservation and the flux components satisfy $q_a \langle \Gamma^r_{ab} \rangle + q_b \langle \Gamma^r_{ba} \rangle = 0$. This balance of the radial fluxes assures ambipolarity of the total flux: $\sum_a q_a \langle \Gamma^r_a \rangle = 0$. The toroidal friction forces were split into perpendicular and parallel components leading to the classical(CL), Pfirsch-Schlüter(PS) and Banana-Plateau(BP) contribution and also the fluxes of each component alone are balanced and thus ambipolar. Each contribution has a diffusive and a convective term and for equal temperatures of all species one can write formally.

$$\langle \Gamma^r_a \rangle = \sum_{x=CL,PS,BP} \sum_{b \neq a} D^{ab}_x \left[-\frac{dn_a}{dr} + \frac{Z_a}{Z_b} \left(\frac{d \ln n_b}{dr} + H^{ab}_x \frac{d \ln T}{dr} \right) n_a \right] \tag{3.42}$$

The drift velocity of each contribution is proportional to the respective diffusion coefficient multiplied with the ratio of the charge numbers Z_a/Z_b. Balance of the fluxes is reflected in the following symmetries for the diffusion coefficients D^{ab}_x and the temperature gradient factors H^{ab}_x.

$$\begin{aligned} Z_a^2 n_a D^{ab}_x &= Z_b^2 n_b D^{ba}_x \\ \frac{H^{ab}_x}{Z_b} &= -\frac{H^{ba}_x}{Z_a} \end{aligned} \tag{3.43}$$

In Eq.(3.42), the contribution from electrons can be neglected due to the small friction force. The impurity strength parameter $\alpha = Z^2 n^2/(Z_m^2 n_m^2)$ can be used to judge the importance of impurity-impurity collisions. Z and n are charge number and density

of the impurity, while Z_m and n_m are the respective quantities for the main ion. In the trace limit, where $\alpha \ll 1$ for all impurities in the plasma, it is only necessary to consider collisions with the main ion, while for $\alpha \approx 1$ collisions with impurities have to be considered as well. In the second case, not only collisions with other impurities but also between different charge states of one impurity contribute to the radial flux.

The impurity density profile in equilibrium from Eq.(2.47), which assumed no sources inside the separatrix, did only depend on the ratio of drift velocity and diffusion coefficient, i.e. $1/n_a(dn_a/dr) = d\ln n_a/dr = v/D$. In the trace limit, where only collisions with the main ion need to be considered, we find from Eq.(3.42) the relation between impurity density gradient and main ion density gradient in equilibrium.

$$\frac{d\ln n_a}{dr} = \frac{d\ln n_m}{dr}\frac{Z_a}{Z_m}\Big(1 + \frac{\sum_x H_x^{am} D_x^{am}}{\sum_x D_x^{am}}\frac{d\ln T}{d\ln n_m}\Big) = \frac{d\ln n_m}{dr}\frac{Z_a}{Z_m}\Big(1 + H_{tot}\eta_m\Big) \quad (3.44)$$

Here, η_m denotes the ratio of normalised temperature gradient and normalised main ion gradient and $H_{tot} = \sum_x H_x^{am} D_x^{am}/\sum_x D_x^{am}$ is the effective temperature screening factor of all three contributions. For zero temperature gradient, the normalised impurity density gradient is a factor Z_a/Z_m steeper than the normalised main ion density gradient. For non-zero temperature gradient, this factor is usually reduced, since η_m is positive (same direction of both gradients) and H_{tot} is negative. For the case of additional purely diffusive anomalous transport with diffusion coefficient D_{an}, Eq.(3.44) has to be modified with a factor, which gives the fraction of the collisional diffusion coefficient $D_{coll} = \sum_x D_x^{am}$ in the total diffusion coefficient.

$$\frac{d\ln n_a}{dr} = \frac{d\ln n_m}{dr}\frac{Z_a}{Z_m}\frac{D_{coll}}{D_{coll} + D_{an}}\Big(1 + H_{tot}\eta_m\Big) \quad (3.45)$$

Thus, the equilibrium impurity density profile is determined by the gradients of temperature and of the main ion species via D_{coll} and H_{tot} in the case of additional anomalous diffusion and only via H_{tot} in the case of negligible anomalous diffusion.

In the following, results from the numerical code NEOART by A. G. Peeters are shown. NEOART calculates the collisional transport coefficients for an arbitrary number of impurities including collisions between all components. The velocity distribution is expanded in the three first Laguerre polynomials of order 3/2, which are used to define 'velocities'. The first 'velocity' is the mean particle velocity of the component, the second proportional to the heat flow, while the third term in the expansion is not related to well known quantities. For the neoclassical part, the code solves the set of linear coupled equations for the parallel 'velocities' in arbitrary toroidally symmetric geometry for all collision regimes. The classical fluxes are given by Eq.(5.9) and (5.10) in Section [5.] of Hirshman and Sigmar [33]. The equations for the banana plateau contribution are equal to that used by Houlberg [37]. The Pfirsch-Schlüter contribution is calculated from the coupled equations (6.1-2) and (6.14-15) of Hirshman and Sigmar [33], as described in
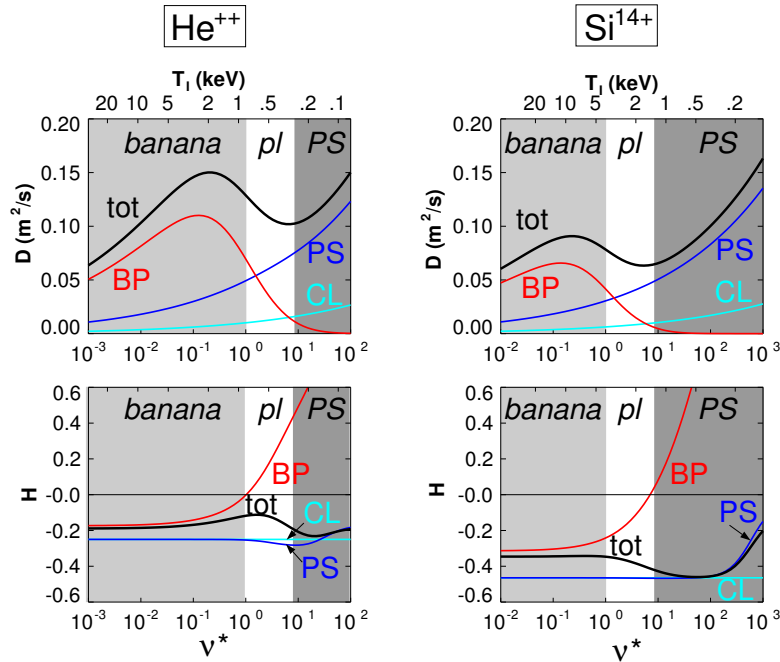
Figure 3.4:   *Classical (label CL), Pfirsch-Schlüter (label PS), banana-plateau term (label BP) and total value (label tot) of diffusion coefficient D and temperature screening factor H for He^{2+} and Si^{+14} as a function of the temperature for a deuterium plasma with fixed electron density n_e=10^{20} m^{-3} and trace impurity density. Magnetic configuration is taken from ASDEX Upgrade for a radial position with q=2.5 and ϵ=0.24. D and H is shown versus the collisionality ν^* of the impurity ion. The different collisionality regimes are indicated.*

Ref. [39]. It applies the reduced charge state formalism [33], which is the correct way to merge the different charge states of one species, such that the matrices, which have to be inverted are only determined by the number of species instead of all charge states of the atoms.

Fig.3.4 shows the transport coefficients of He^{2+} and Si^{14+} in the trace limit in a deuterium plasma. An ASDEX Upgrade equilibrium is taken with B_t=2.5 T and the considered flux surface has q=2.5, ϵ=0.24, trapped particle fraction f_{trap}=0.62. The electron density is n_e=10^{20} m^{-3} and a pure temperature scan with T_e=T_i is performed (see upper x-axis). The data are shown versus the collisionality ν^* of the respective species and the differently shaded regions indicate banana, plateau and Pfirsch-Schlüter regime. In the low collisionality regime, D_{BP} is the most important contribution, while the high collisionality regime is dominated by D_{PS}. We also note, that He^{2+} is for most temperatures in the banana regime. The regime limits of He^{2+} with respect to Si^{14+} occur at temperatures, which are about a factor of 5 lower. In the lower graphs, the weight factors of the normalised temperature gradient H_x of each contribution and the effective factor H_{tot} are depicted. H_{CL} and H_{PS} is always negative and has lower absolute value for He^{2+}
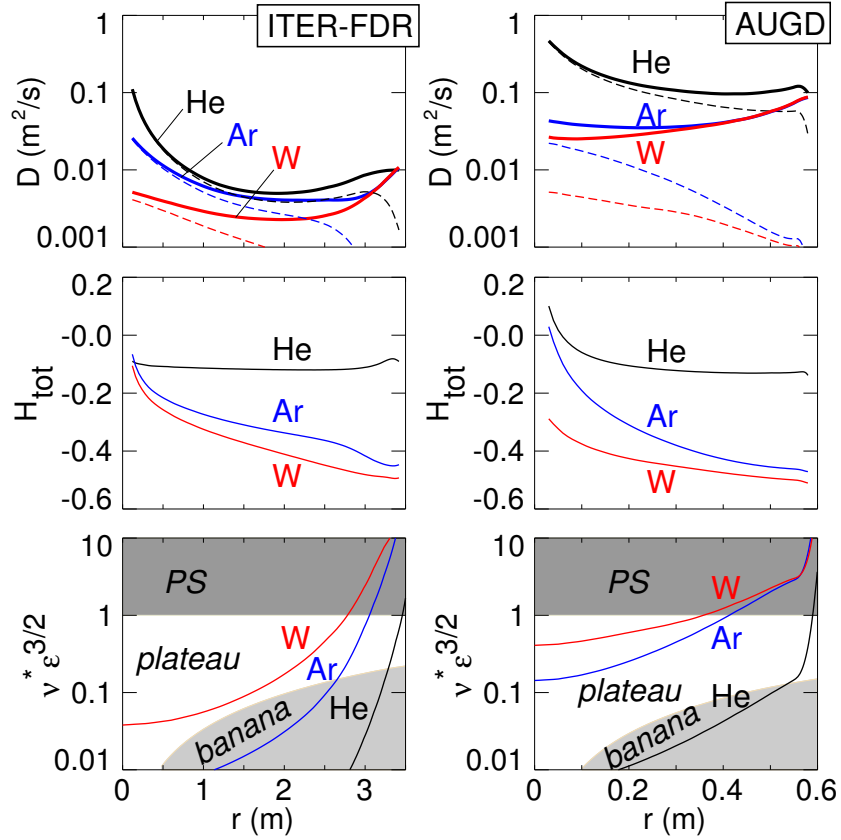
Figure 3.5:   *Radial profiles of collisional diffusion coefficient D, banana-plateau term (dashed lines), total temperature screening factor H_{tot} of He, Ar and W for an ITER-FDR DT-plasma and an ASDEX Upgrade D-plasma with electron density $n_e=10^{20}\,\mathrm{m}^{-3}$ and low impurity densities (trace limit). The lower graphs identify the collisionality of the impurities and show the banana-, plateau-, and PS-regime at low, medium and high collisionalities.*

due to the lower mass. H_{BP} is negative in the regime, where D_{BP} is the dominant diffusion contribution, and becomes positive for increasing ν^*. However, the effective value H_{tot} remains negative in all collisionality regimes. Deep in the PS-regime, we note the reduction of H_{PS} for Si^{14+} at highest collisionalities. This is due to the strong collisional coupling of Si^{14+} and D^+, which leads to energy transfer from Si onto D on the upper and lower part of the flux surface. Thus, the temperature variation of Si^{14+} along the flux surface and the according temperature screening term is reduced.

Fig.3.5 shows radial profiles of the trace limit transport parameter for the three impurities He, Ar and W in a large fusion reactor type tokamak plasma and in ASDEX Upgrade being smaller by a factor of ≈ 5. The fusion reactor type plasma is taken from the ITER-FDR design [40] with major radius $R_0=8.45\,\mathrm{m}$ $B_T=5.7\,\mathrm{T}$, safety factor $q_{95}=3$, $T_i(0)=32\,\mathrm{keV}$ and $n_e=10^{20}\,\mathrm{m}^{-3}$ and the ASDEX Upgrade example has $R_0=1.65\,\mathrm{m}$, $B_T=2.5\,\mathrm{T}$, $q_{95}=3.3$, $T_i(0)=2.5\,\mathrm{keV}$ and $n_e=10^{20}\,\mathrm{m}^{-3}$. The fractional abundance of the

ion stages has been calculated with STRAHL. On axis, the most abundand ion stages of W are W^{+43} in AUGD and W^{+70} in ITER-FDR and Ar^{+17} in AUGD and fully ionised Ar in ITER-FDR. The most pronounced differences in the two plasmas are due to the differences of the collisionalities and the toroidal field. The collisionalities increase with the radius due to the lower edge temperatures and are generally lower in the hotter ITER-FDR plasma (lowest two graphs). Thus, the diffusion coefficient is dominated by the BP-value (dashed lines) in ITER-FDR, while in AUGD this is only the case for the lightest element He. The lower diffusion coefficients in ITER-FDR compared to AUGD reflect the quadratic dependence on B_T. The effective temperature screening factor shows the same variation with impurity mass and varies with radius as expected from the collisionality scan of Fig.3.4. Close to the axis, the standard neoclassical formulation fails and the BP-values diverge, since the basic assumption of banana-width being small against r is not fulfilled.

In the previous examples, the impurity densities were in the trace limit and only collisions with the main ion species determined the collisional transport parameters. In the example of Fig.3.6, the density of one impurity species, i.e. neon, is increased from very low to high values of the impurity strength parameter α_{Ne} and we investigate the equilibrium profiles of Ne and of a second impurity Fe, which has very low concentration. We assume purely collisional transport and the magnetic equilibirum is again taken from an ASDEX Upgrade deuterium plasma. Neon is almost fully ionised for the considered electron temperatures around 1 keV and the impurity strength parameter is thus $\alpha_{Ne} = Z_{Ne}^2 n_{Ne}/Z_D^2 n_D = 100 n_{Ne}/n_D$. The electron density is $n_e = Z_D n_D + Z_{Ne} n_{Ne}$, and α_{Ne}=3 yields a neon concentration $c_{Ne}=n_{Ne}/n_e$ of 2.3%. For α_{Ne}=0.4, the collisions between Fe and Ne are as frequent as bewtween Fe and D: $\nu_{Fe,Ne} = \nu_{Fe,D}$. Fe has an average charge number of $Z\approx20$ at r/a=0.5 and $Z\approx22$ on axis.

The electron density profile is given a Gaussian shape $n_e=n_e(0)\exp(-k_n r^2)$ with $n_e(0)$=$10^{20}\,\mathrm{m^{-3}}$ and $k_n = (1/a)\,\mathrm{m^{-1}}$, such that the gradient length at r/a=0.5 is L=1 m. For very low densities of Ne, the deuterium profile is of course identical to n_e and for high neon densities the n_D profile is calculated from the fixed n_e profile and the impurity densities using quasi-neutrality. The same Gaussian parametrisation is used for the ion temperature T_i with three different choices for the peakedness parameter k_T=0, k_n and $2k_n$. We thus study the effect of the temperature screening and for low impurity densities, the ratio of the normalised T_i gradient and n_D gradient is set to η_D=0, 1 and 2. $T_i(0)$ is changed with k_T such that $T_i(r/a = 0.5)$ is 1 keV for all three choices of the T_i profile. For high values of α_{Ne}, η_D increases from the starting values 1 and 2 due to flattening of the deuterium profile.

The six graphs of Fig.3.6 show radial profiles of the Fe, Ne and D density at low ($\alpha_{Ne} = 0$) and high ($\alpha_{Ne} \approx 3$) Ne density for the cases with constant T_i ($\eta_D = 0$), low ($\eta_D = 1$) and high ($\eta_D = 2$) T_i peaking. All densities are normalised to the density at r/a=0.5.
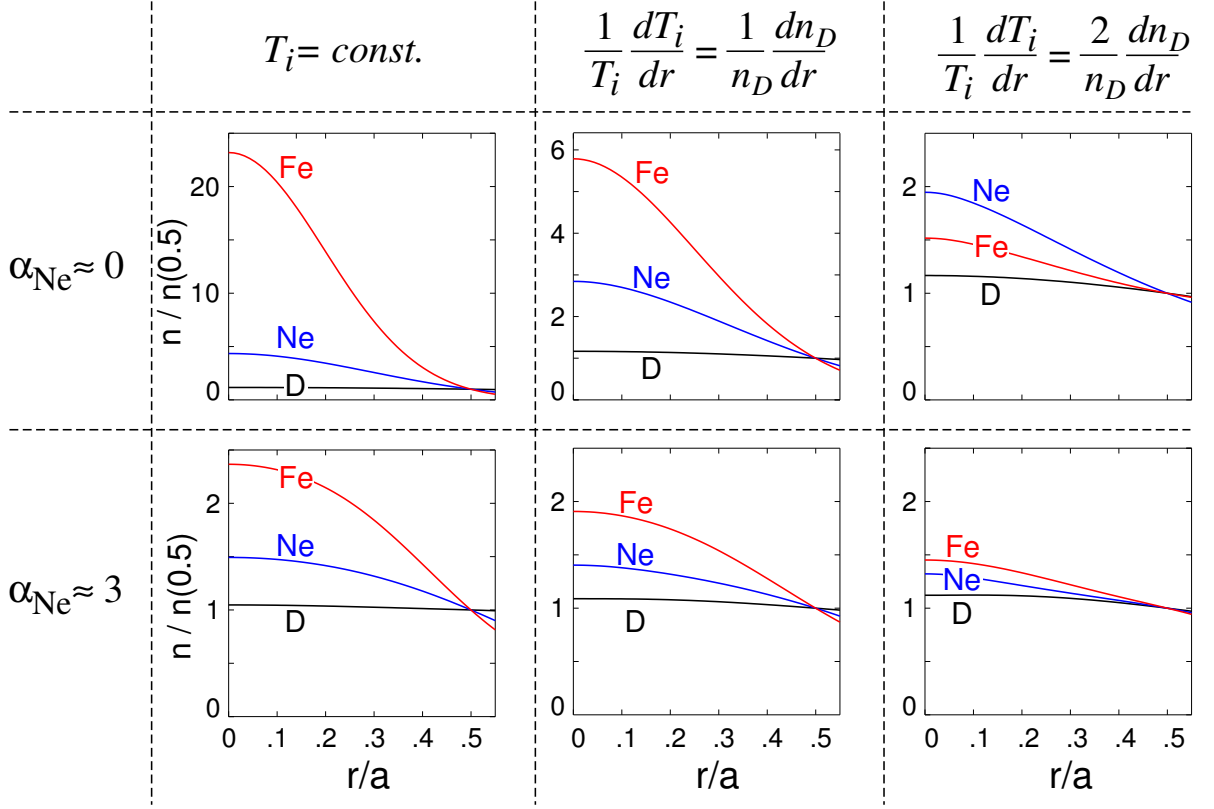
Figure 3.6: *Radial density profiles of Fe, Ne and D at low ($\alpha_{Ne} = 0$) and high ($\alpha_{Ne} \approx 3$) Ne density for the cases with constant T_i ($\eta_D = 0$), low ($\eta_D = 1$) and high ($\eta_D = 2$) T_i peaking. Ne is almost fully ionised with $Z \approx 10$, and Fe has an average charge number of $Z \approx 20$ at $r/a = 0.5$ and $Z \approx 22$ on axis. All densities are normalised to the density at $r/a = 0.5$.*

For $\eta_D = 0$ and low Ne density, Eq.(3.44) yields, that the impurity profiles have a normalised gradient which is Z times as steep as the normalised gradient of deuterium. All profiles have a Gaussian shape and the central values are $n_D(0) = n_e(0) = 1.16 n_e(0.5)$, $n_{Ne}(0) \approx 1.16^{10} n_{Ne}(0.5) = 4.4 n_{Ne}(0.5)$ and $n_{Fe}(0) \approx 1.16^{21} n_{Fe}(0.5) = 23 n_{Fe}(0.5)$. With increasing α_{Ne}, the plasma becomes more and more diluted and the deuterium gradient strongly decreases. For the highest value of α_{Ne}, we find only $n_D(0) = 1.05 n_D(0.5)$ and the peaking of Ne and Fe is strongly reduced. For Ne, the peaking is even 5% below the expected value of $n_{Ne}(0) \approx 1.05^{10} n_{Ne}(0.5) = 1.58 n_{Ne}(0.5)$ due to collisions with electrons. The collision frequency with electrons is only $\approx 3\%$ of the collision frequency with deuterium ions, however, they induce an outward pinch via the normalised n_e density gradient, which is about 4 times the normalised n_D gradient, and the exponent Z_{Ne} has to be reduced by $\approx 10\%$ due to the electron interaction. At $\alpha_{Ne} = 3$, Fe collides mainly with Ne and the normalised gradient of n_{Fe} consequently is $Z_{Fe}/Z_{Ne} \approx 2.1$ times the normalised gradient of n_{Ne}. Disregarding the small electron effect, this is just the gradient we would expect, when considering collisions with deuterium only, since the normalised

n_{Ne} gradient is Z_{Ne}/Z_D times the normalised deuterium gradient. Thus, the main effect of the high neon density is the dilution of the deuterium profile, which still determines the peakedness of Ne and Fe.

When turning on the temperature screening, the peaking of the impurity densities is drastically reduced. The effective temperature screening factors at $r/a = 0.5$ are $H_{tot}^{NeD} = -0.36$ and $H_{tot}^{FeD} = -0.47$. At low values of α_{Ne}, we obtain from Eq.(3.44) a reduction of the normalised gradients by a factor of $(1 - 0.36\eta_D)$ for Ne and $(1 - 0.47\eta_D)$ for Fe and for η_D=2, Fe has even lower normalised gradients at low values of α_{Ne} compared to Ne. The temperature screening factors are lower for smaller radii, and the ratios of the density on axis to the density at half radius are only approximated by $[n_D(0)/n_D(0.5)]^{Z(1-H\eta_D)}$. With increasing α_{Ne}, the dilution does not change the normalised deuterium gradient as drastically as in the case without T_i gradient, however, the remaining decrease of the normalised n_D gradient increases η_D from 1 to 1.7 and 2 to 2.2 respectively. Thus, the effect of the dilution is twofold by lowering of the inward pinch and increase of the temperature screening. In spite of that, the normalised gradient of Fe at $r/a = 0.5$ increases with α_{Ne} in the $\eta_D = 2$ case. For the highest α_{Ne}, the transport of Fe is dominated by the collisions with Ne and here η_{Ne} and H_{tot}^{FeNe} determine the Fe profile. The normalised n_{Ne} gradient is larger than the normalised n_D gradient and the effective temperature screening factor is just $H_{tot}^{FeNe} = -0.21$. Thus the normalised n_{Fe} gradient passes the normalised n_{Ne} gradient. It is obvious, that this behaviour can not be obtained, when considering only the collisions between Fe and the diluted deuterium, as was the case for zero temperature screening.

3.2   Anomalous Transport

The term 'anomalous transport' reflects the surprise, which was aroused by the finding, that experimentally determined heat conductivities exceeded the neoclassical predictions for the ions by one and for the electrons by two orders of magnitude [41]. Also the diffusion coefficient of impurities can be several m^2/s in the experiment, which is about an order of magnitude above the neoclassical value. It is thought, that micro-instabilities associated with *drift waves* are responsible for the observed level of transport [42]. Drift waves are related with the drift motion across the magnetic field in inhomogeneous magnetised plasmas. In the fluid description, the drifts are the diamagnetic drifts due to the gradients of temperature and density, while in the particle picture, the equivalent drifts are the ∇B- and curvature-drift.

From the many possible instabilities, temperature gradient modes seem to be the most promising candidates to explain anomalous transport. The ion temperature gradient (ITG) modes are held responsible for the thermal ion, and the electron temperature

gradient (ETG) and trapped electron modes (TEM) for the thermal electron heat conduction [43]. Interaction between ITG and TEM can account for particle transport and enhance ion heat conduction. A simple physics picture of the toroidal ITG driven instability shall briefly be discussed, while detailed treatments are outside the scope of this work.

Consider a small plasma region on the torus outside as depicted in Fig. 3.7. The magnetic field points into the plane of the paper, while the gradient of temperature and magnetic field show towards the plasma axis. We assume an initial poloidal perturbation of the ion temperature T_i. The ∇B and curvature drift for the ions, which is proportional to $(v_\parallel^2 + v_\perp^2/2)\vec{B} \times \nabla B$, is always directed upwards and varies with the ion temperature. Thus, the ion density n_i above the hot regions will be higher than the equilibrium value, while below the hot region the density will be decreased. The perturbations of the ion density cause the electrons to rearrange along the magnetic field line as to assure quasi-neutrality. We assume here that the electron response is adiabatic, i.e. that electron inertia can be neglected and that the electron distribution along the field line is given by the Boltzmann distribution $n_e = n_0 \exp(e\phi/k_B T_e)$, where ϕ is the electrostatic plasma potential and n_0 is the unperturbed density of ions and electrons. From the quasi-neutrality condition we find in linear order, that the potential perturbations are proportional to the density perturbations $\tilde{n}/n_0 = e\tilde{\phi}/(k_B T_e)$. The associated poloidal electric fields lead to an E×B-drift, which points away from the torus axis in the hot region and towards the torus axis in the cold region. Hence, hot plasma from the inside is transported towards the hot region and cold plasma from the outside towards the colder region and the initial perturbation is increased. This enforcement of the temperature perturbation by the E×B flows only happens on the outboard side of the flux surface, while on the inboard side the direction of the equilibrium temperature gradient is reversed compared to Fig. 3.7 leading to a drift of cold plasma towards the hot regions and vice versa. The radial drift is the same for all plasma particles, since the E×B-drift is independent of particle mass and charge.

For the calculation of the radial particle fluxes, it is essential to include the electron response with greater detail. In the simplified treatment with adiabatic electron dynamics, the time averaged radial electron flux density $\Gamma_e = \langle \tilde{n}_e \tilde{v}_r \rangle \propto \langle \tilde{n}_e \tilde{\phi} \rangle$ is zero, since density and potential perturbation are in phase. The particle fluxes have to be ambipolar and in a pure hydrogenic plasma, also Γ_i has to be zero. Trapped electrons, which are constrained to limited regions at the outboard side of the magnetic field lines, are unable to respond adiabatically to local variations of the electrostatic potential ϕ either leading to an additional destabilisation of the ITG mode or the appearance of a new unstable mode (TEM) in addition to the ITG mode [44].

The temperature gradient modes become unstable, when the temperature gradient parameter $\eta = (d \ln T/dr)/(d \ln n/dr)$ is above a certain critical level. For flat density pro-
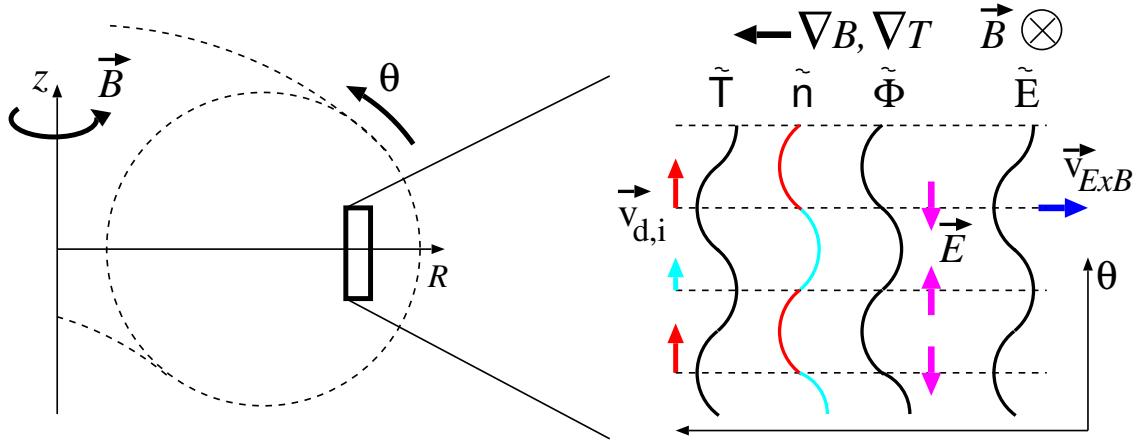
Figure 3.7:   *The toroidal ITG instability: An initial perturbation of the ion temperature causes poloidal density and potential gradients due to the ∇B- and curvature drift. This leads to radial E×B-drifts, which increase of the initial perturbation on the low field side of the torus while the initial perturbation is decreased on the high field side. (courtesy of W. Sutrop)*

files, η is usually replaced by the temperature gradient parameter $\mu = -(R/T)(dT/dr) = R/L_T$ with R being a fixed major radius, e.g. R of the magnetic axis, and L_T being the local temperature decay length. For R/L_T above $R/L_{T,crit}$, the drift wave turbulence and the associated thermal flux becomes strong, such that the temperature gradient is caused to relax back towards the critical gradient. The temperature gradient is thus kept at the critical gradient, more or less vigorously depending on the strength of the turbulence above the threshold. Additional heating power leads rather to an increase of the anomalous thermal diffusivity than to an increase of the temperature gradients as would be expected for a thermal diffusivity, which is independent on the temperature gradients. This behaviour is termed temperature profile resilience or profile stiffness.

The critical temperature gradient and the strength of the turbulence depends on various plasma parameters, such as magnetic shear, normalised pressure β, the ratio of electron to ion temperature, the density gradient and the effective ion charge. Sheared velocity flows associated to sheared radial electric fields play an important role. These can reduce or even suppress the turbulence by de-correlating the turbulent eddies. For the H-mode regime, it is widely accepted, that sheared $\vec{E} \times \vec{B}$ plasma rotation causes a local reduction of the turbulent transport in a narrow zone just inside the separatrix leading to the large temperature pedestals [45, 46]. In the plasma interior, turbulence suppression in internal transport barriers (ITB) is only observed, when the magnetic shear is close to zero or negative [47]. For the ion thermal diffusivity, an interplay of stabilisation by shear flows and low magnetic shear are held responsible for the ITB, while in the electron channel, mainly the magnetic shear counts and the effect of sheared flows are thought to be limited

[48]. For H-mode or L-mode discharges without ITB and positive magnetic shear profiles, the absolute value of the temperature gradient increases from the magnetic axis, where the temperature gradient is zero, with increasing radius until it reaches the critical value at a certain radius. Inside of the radius, at which the critical gradient is encountered, transport is expected to be at the neoclassical level, while outside of that radius it is anomalous and the transport coefficients increase with radius, since more and more deposited heating power is transported to the outside at an almost constant temperature gradient. Thus, the thermal diffusivities have a radial profile which increase with radius. The radius, where transport becomes anomalous, shrinks when the centrally deposited heating power is increased.

There are a number of transport models, which predict anomalous transport parameters based on ITG/TEM physics, e. g. the IFS/PPFL [49], Weiland [50], and the GLF23 [51] models. These models have been tested against experiments and found to predict anomalous heat transport, i. e. the temperature profiles inside of the H-mode pedestal, with an accuracy of about 20% [41, 52]. Particle transport has been explored only recently. Comparisons with experimental density profiles inside of the H-mode pedestal, which were mainly sensitive to the ratio of drift velocity and diffusion coefficient, indicate the important role of the collision frequency of the electrons ν_{ei} with respect to the growth rate of the most unstable modes [53]. Model calculations of impurity transport parameters can be performed with the Weiland model, however, comparisons with experimental values have not yet started.

4. Experimental Methods

Various experimental methods can been applied to gain information about the radial impurity transport, namely the radial diffusion coefficient $D(r)$ and the drift velocity $v(r)$. All methods use a perturbation of the impurity density distribution, which is fast with respect to the characteristic profile equilibration time and a subsequent measurement of the impurity density evolution in the plasma. The total impurity density profile in equilibrium gives only information about the ratio v/D according to Eq.(2.47), since the impurity sources are generally zero in the major part of the plasma. Towards the plasma edge, also the width and position of the radial shells for individual impurity ions contain information about the transport parameters (see section 2.5), however, this method has rarely been applied.

Active changes of the density profile by gas puffing, pellet injection, or laser ablation can be used as well as fast profile perturbations due to plasma instabilities like the sawtooth instability or the edge localised mode (ELM).

4.1 Inducing Perturbations

Perturbative studies are mainly performed by sudden injection of the investigated impurity, however, there are also a few other methods as discussed at the end of this section. The amount of injected impurities has to be adjusted such, that the spectroscopic signals for impurity detection are well measurable with the envisaged time resolution and that the influence on the main plasma parameters like n_e, T_e and P_{rad} is as low as possible.

Gas puffing is the easiest way to inject an impurity into the plasma. The method is of course restricted to the elements, which are available in the gaseous state. Most of these elements are recycling at the vessel walls, and the decay of the impurity density is in most cases dominated by the effective pump time and not by the transport coefficients in the confined plasma. However, the density build-up after the start of the injection can always be used for determination of transport coefficients, as long as the investigated radial range is not to close to the edge, where profile equilibration times will drop below the timescale of the source function, i.e. below $\approx 10\,\mathrm{ms}$. Nevertheless, gas injection using flow rate controlled piezo-electric valves, is the best choice for a number of applications. A

temporally constant concentration of a certain impurity is easily realised with a proper pre-programmed or feedback controlled valve flow and can be used to investigate the equilibrium impurity profile. Sinusoidally modulated puffs of H_2S, SiH_4 and HBr, were used to determine transport coefficients of S, Si and Br from a harmonic analysis of spectral line radiation [54], where the above elements have low recycling probabilities. A similar approach using active charge exchange recombination spectroscopy was used for He and Ne [55, 56].

The laser blow-off (LBO) technique allows to inject non-gaseous elements. Friichtenicht [57] demonstrated, that high-power laser irradiation of a metal film-glass interface can result in efficient vaporisation of the metal and the generation of a highly directional burst of neutral atoms with kinetic energies in the 1-20 eV range. This method was first applied by Marmar et al. [58] on the Princeton Adiabatic Compressor (ATC) tokamak. First transport investigations using LBO of aluminium, were reported by Cohen et al. [59]. The LBO method allows for short impurity injections with a duration around $100\,\mu s$, i.e. a rather well controlled temporal form of the source function, which can not be achieved with most of the gaseous elements due to the high recycling coefficient. The ablated particles are composed of ions, neutral atoms and small atomic clusters depending on the material, the energy density of the irradiating laser and the laser wavelength [60, 58]. The film thickness(0.2-$5\,\mu m$) and the laser spot diameter(1-5 mm) controls the amount of ablated particles, which is typically in the range of 10^{17}-10^{18}.

A Q-switched ruby laser with a pulse energy of 1-5 J at λ=694 nm is most frequently used. Due to the low repetition frequency of this laser, only one LBO per plasma discharge is performed. Higher flexibility was achieved with a Q-switched Nd:YAG laser with pulse energy around 0.6J at λ=1064 nm and a repetition frequency of 20 Hz [61] and with the XeCl excimer laser at λ=308 nm [60]. For multiple pulse operation, the optical system is equipped with a fast steering mechanism for the laser beam, such that each laser pulse hits a fresh surface of the target area.

Another alternative is the injection of small pellets into the plasma. In the most simple case, these are solid pellets of the impurity, e.g. carbon [62] or iron [63], however, a very large perturbation is induced by pure impurity pellets. Cryogenic hydrogen pellets with a small admixture of neon [64] were used in the ASDEX tokamak, and pellets of paraffin mixed with CaF_2 were injected at DIII-D [65]. More complicated pellet designs comprise tracer-encapsulated cryogenic hydrogen pellets, where a small metallic capsule is sorounded by frozen hydrogen [66], or tracer-encapsulated solid pellets, whose shell is formed by polystyrene, $(C_8H_8)_n$ [67, 68]. The tracer-encapsulated pellets aim at a deposition of the capsule material deep inside the confined plasma.

Plasma instabilities might as well lead to a perturbation of the impurity density profile. Especially the sawtooth instability, which appears deep inside the confined plasma at the q=1-surface has been used. Sawtooth oscillations [69, 70] are characterised by a slow

increase of the central temperature and a rapid drop, the so-called sawtooth crash, where thermal energy is expelled from the plasma centre within $\approx 100\,\mu$s. Sawteeth occur, when the safety factor on axis drops below unity and the plasma becomes unstable to the internal kink mode leading to a reconnection of the magnetic field lines and a flattening of the q-profile [71, 72]. Inside a mixing radius r_{mix}, which is somewhat larger than the radius of the q=1-surface, a swtooth crash also flattens the impurity density profile, as has first been described by Seguin and Petrasso [73, 74]. For situations, where the transport inbetween sawtooth crashes is considerably convective with inwardly or outwardly directed drifts, the impurity profile becomes peaked or hollow between the crashes and the fast flattening due to the crash can be utilised to study the transport coefficients between the crashes [75, 76]. The edge localised mode (ELM) appears in the steep gradient region of H-mode plasmas just inside the separatrix. ELM's expell thermal energy and particles from the confined plasma within $\approx 100\,\mu$s and the impurity density perturbation due to ELM's was also used for the determination of edge transport coefficients [77].

Finally, a sudden change of the transport coefficients, e.g. by switching on or off the heating by waves or by neutral beam injection, can be used for transport investigations. The impurity density profile is then evolving from the first equilibrium state before the change to the new equilibrium state. In the source free part of the plasma, this scheme can only be applied, if the two equilibria have different profiles of v/D, i.e. different density gradients. An example for this method is Ref.[78].

4.2 Measurement of Impurity Densities

Measurements of the impurity density are mainly done by passive spectroscopically resolved or wavelength filtered measurements. Passive measurements integrate the radiation along the line-of-sight, while active methods can yield spatially resolved information.

4.2.1 Active Spectroscopy

Active laser spectroscopic methods, like laser induced fluorescence, have only seldomly been used in fusion plasmas. The existing tunable laser systems with sufficient pulse energies can only produce low energy photons, such that measurements were only performed in the cold edge plasma, where atoms or ions with low transition energies exist. The low particle densities create further difficulties to reach detectable signals. Examples of one-photon induced laser fluerscence in the UV and VUV can be found in [79, 80].

Fast neutral beams of hydrogen, helium or lithium with kinetic energies of typically 50-100 keV offer the possibility of a spatially resolved active spectroscopy method: charge exchange recombination spectroscopy (CXRS) [81]. In a collision of a neutral beam atom

with a multiply charged impurity ion A^Z an electron of the neutral can be captured in a highly excited level of the ion and the photons, which are emitted in the consecutive radiative decay, are detected. This method allows for a spectroscopic determination of the density of fully ionised elements, which are otherwise not accessible by passive spectroscopy. This is especially useful for light elements being completely ionised in the major part of the plasma. Using an observation geometry, where line-of-sight and neutral beam are crossed, spatially resolved density measurements are achieved. First measurements of CX-excited radiation on neutral hydrogen beams were performed in the late 1970s on oxygen and carbon [82, 83, 84]. The range of elements was subsequently expanded to Helium and all elements of the 2nd period, and even medium-Z elements like Fe [85, 86] could be diagnosed.

Neutral hydrogen or deuterium beams, which are used for plasma heating, are most frequently employed, and the reaction for the charge exchange recombination reaction, reads.

$$A^{+Z} + H \rightarrow A^{+(Z-1)}(n, l) + H^+ \tag{4.1}$$
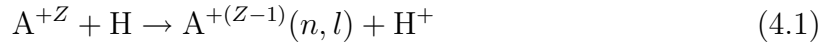
Here, n and l denote the principal and orbital quantum number of the excited level. The charge exchange reaction tends to be a resonant process in that the electron from the neutral beam atom is preferably captured in excited levels, which preserve its orbital energy and radius. The orbital energy is proportional to Z^2/n^2 and for electron capture from ground state hydrogen, orbital energy is preserved for exchange into $n = Z$. The orbital radius scales with n^2/Z , which favours for the same process a capture into $n = Z^{1/2}$. Thus, only for hydrogen both quantities can be conserved, while for highly charged impurity ions, the calculated cross sections reach a maximum at the compromise value $n_{max} = Z^{3/4}$ [87]. The calculated l-distribution of the cross sections shows dominant capture into levels with large l-values for $n < n_{max}$. For $n > n_{max}$, the cross sections maximise at $l \approx n_{max}$, while capture into levels with even larger l-numbers is little [87, 88]. The different quantum mechanical or semi-classical models, which are used to calculate the cross sections are discussed in [89].

The l-distribution of the captured electrons is important for the branching of the radiative transitions of the electron in Δn=1 transitions and transitions with $\Delta n > 1$. Since the selection rule $\Delta l = \pm 1$ has to be obeyed, a radiative transition to a lower level n' is only possible for electrons with orbital quantum number $l \leq n'$. The l-distribution after charge exchange favours $\Delta n = 1$ transitions, such that the electrons mainly cascade down the ladder of n-levels. The emitted intensity on one specific transition starting from level n is thus proportional to a weighted sum of all population rates for charge exchange into levels $\geq n$, where the weighting factors are the probability, that the electron will go through level n during the cascade. The cascade processes can be significantly affected by the surrounding plasma environment, and transfer between the nearly degenerate l-levels of an n-level can be induced, before the electron drops to lower states by spontaneous
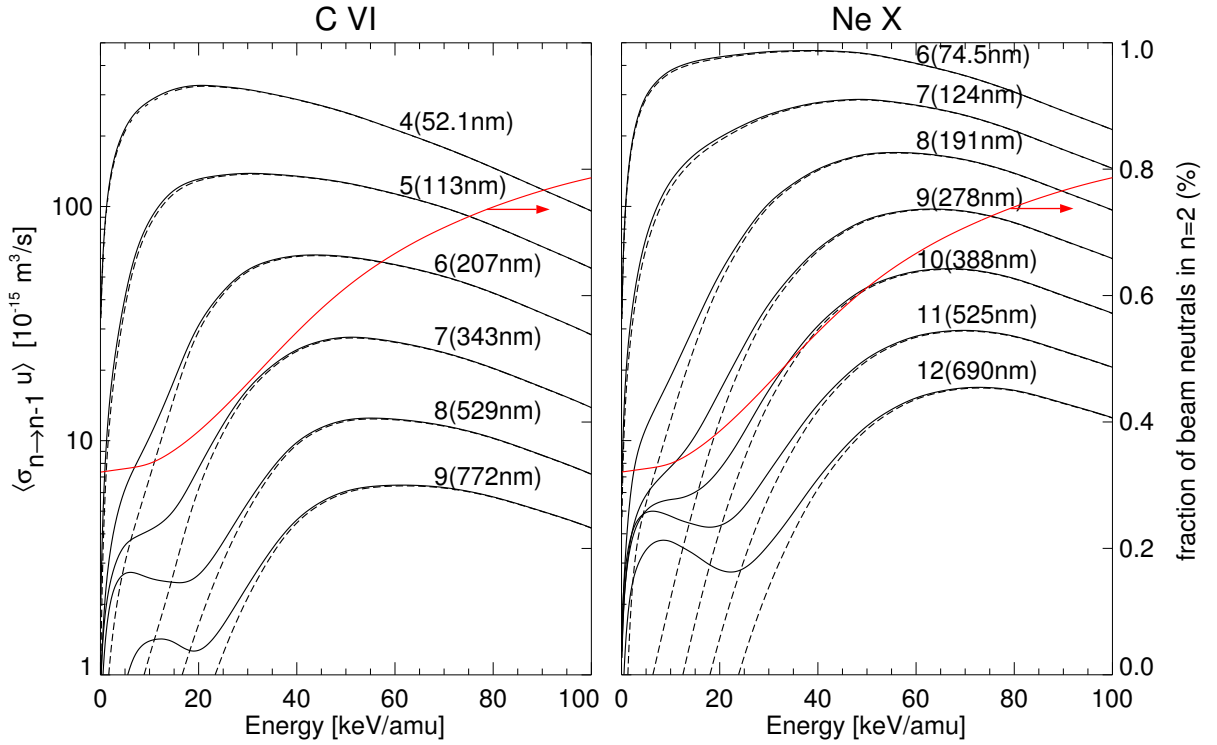
Figure 4.1: *Effective rate coefficients for charge exchange excited $\Delta n=1$ transitions in C VI and Ne X. The full lines give the total coefficients, while the dashed lines are for charge exchange from H(1s) only. The red line shows the fractional abundance of H(n = 2). l-mixing and beam excitation are calculated for $B = 2\,T$, $n_e = 6\times10^{19}\,m^{-3}$, $T_e = T_i = 2\,keV$, $Z_{eff}=1.6$ due to carbon. Atomic data are taken from [3].*

photon emission. Mixing of l-states due to ion-ion collisions and the motional Stark effect are discussed in [88, 90]. The high-n states are more susceptible to these effects, and are driven to a statistical distribution according to the statistical weight $2l + 1$ of each l-level.

A small fraction of the neutral beam atoms are excited to higher n-levels mainly due to electron collisions at low beam energies and ion collisions at high beam energies [91]. Even though this fraction is only on the order of 1%, it can play an important role at low beam energies, where the charge exchange cross section from ground state hydrogen into higher n-levels vanishes [92, 93]. Charge exchange from excited hydrogen neutrals was first observed in argon [94].

All the above effects can be summarised into one effective rate coefficient $\langle\sigma_{n\rightarrow n'}u\rangle$ for charge exchange excited emission on the transition $n \rightarrow n'$ with u being the relative velocity $|\vec{v}_A - \vec{v}_{beam}|$. We can write for the line emission coefficient $\epsilon_{n\rightarrow n'}$.

$$\epsilon_{n\rightarrow n'} = \frac{h\nu}{4\pi}n_{A,z}\sum_{j=1}^{3} n_{H,j}\langle\sigma_{n\rightarrow n'}u_j\rangle \tag{4.2}$$

Here, the sum is over the three velocity species of the hydrogen beam with full, half and third of the maximum kinetic energy. For the determination of the ion density, the hydrogen density for each energy component of the neutral has to be known at the measurement position. The beam attenuation is caused by collisional ionisation by electrons, ions and charge exchange processes, and depends on beam energy, injection geometry, plasma density, temperature profiles, and the Z_{eff} profile. The evaluation of the impurity density is usually done with calculated values for n_H, where the influence of the Z_{eff} profile on the beam attenuation is included in an iterative manner [95, 96]. Alternatively, n_H can be gained from measurements of the Doppler shifted Balmer-α emission from the neutral beam [91].

Since the radiative decay is mainly in $\Delta n = 1$ steps, the strongest emission is found at the lower end of the cascade. However, there are also sufficiently strong transitions with photon energies in the visible wavelength range even for multiply charged ions. Examples for CX-excited hydrogen-like ions are He II(n=4$\rightarrow$3) at λ=469 nm, C VI(n=8$\rightarrow$7) at λ=529 nm, O VIII(n=10$\rightarrow$9) at λ=607 nm, O VIII(n=9$\rightarrow$8) at λ=434 nm, and Ne X(n=11$\rightarrow$10) at λ=525 nm.

CXRS has become a standard diagnostic on magnetic fusion devices equipped with neutral beam injection [95, 97]. The Doppler broadening and the Doppler shift of the CX-excited lines are used for the determination of ion temperature [88] and plasma rotation [98, 99]. The use of visible transitions has the great advantage, that spatially resolved measurements of the impurity density at many positions in the plasma can be performed with a rather flexible experimental setup, that does not require large ports in the plasma vessel. Optical fibres are employed, which transport the light from optical heads inside the plasma vessel to the spectrometer. Each optical fibre observes via a mirror optics, the neutral beam at a different position of the plasma cross-section. At the entrance slit of the spectrometer, the optical fibres are positioned in a vertical line along the slit height, and at the exit of the spectrometer, the spectrum, which belongs to each fibre, can be measured at the respective vertical position. The light detection is done with intensified photodiode array detectors [97], intensified charge-coupled device detectors [100] or back-illuminated charge-coupled device detectors [101]. In impurity transport experiments, density profile evolutions can be measured with a repetition rate of typically 100 Hz and a radial resolution of $\approx$2 cm.

4.2.2   Passive Spectroscopy

Passive spectroscopic measurement of characteristic line radiation is a very sensitive diagnostic for impurity concentrations with a detection limit in the range of 1ppm [102, 103, 104].

The quantitative calculation of line radiation needs the local population density of the

emitting quantum state. For the low electron densities in a tokamak plasma, the calculation is very much simplified, since only two body collisions between electrons and ions (linear in n_e) have to be taken into account, while three body collisions between an ion and two electrons can be neglected, because their collision rates are very small. The equilibration time for the population distribution of the quantum levels of an ion stage is dominated by the time constants of radiative decay, which in most cases are much shorter than the characteristic transport times. Thus, the population of ground level and excited states is in equilibrium and just depends on n_e and T_e. Excited states which can not decay via dipole radiation, the metastable states, have a longer time constant for equilibration, and for the plasma edge, the actual population of levels, which belong to different spin systems might not be equilibrated [105].

For resonance lines, it is often sufficient to consider only collisional excitation from the ground state and radiative decay when calculating the equilibrium distribution. This approximation leads to the so called corona equilibrium. For other levels, however, excitation and de-excitation from other excited levels have to be considered and a collisional-radiative model has to be solved to find the equilibrium distribution [3]. The results of such collisional-radiative models is expressed in terms of effective population rate coefficients due to collisional excitation, recombination or charge exchange with neutral hydrogen. We now consider the usual case, where the rate coefficient due to excitation by electron collisions yields the dominant contribution. The rate of radiative decays per volume from quantum state n of an element A in ion stage Z can then be written as $n_{A,z} n_e X_n^{exc}$, which is formally equal to the corona expression, when the effective rate coefficient X_n^{exc} is replaced by the rate coefficient for collisional excitation from the ground state $\langle \sigma_{1 \to n} v_e \rangle$. From all radiative decays from level n, a fraction $A_{nm} / \sum_{k<n} A_{nk}$ decays on the transition $n \to m$, depending on the branching ratio of the Einstein A-coefficients. When observing the plasma along a certain line-of-sight, the measured radiance L_{nm} on the transition $n \to m$ is obtained by integrating along the coordinate l of the line-of-sight.

$$L_{nm} = \frac{h\nu_{nm}}{4\pi} \frac{A_{nm}}{\sum_{k<n} A_{nk}} \int_{l.o.s.} n_A f_z n_e X_n^{exc} dl \tag{4.3}$$

Here, we used the fractional abundance $f_z = n_{A,Z}/n_A$ for the part of the total density n_A of element A, which is in the ion stage with charge Z. Each charge states of an element is found in a certain radial shell according to the electron temperature profile (see section 2.5), and the line radiation from different ion stages contains information about the density profile of the impurity element.

Naturally, this scheme gives only complete profile information up to the centre of the plasma, if the respective element is not completely ionised. The ionisation energy of the hydrogen like ions is $E_{ion} = Z^2 \, 13.6 \, \text{eV}$, and all light elements up to about Ne(Z=10) are fully ionised for temperatures above $\approx 1 \, \text{keV}$. For the larger tokamak experiments, the main part of the plasma has temperatures above $1 \, \text{keV}$ and line radiation gives only

information about colder plasma regions, which prevents the use of passive spectroscopy
for these elements.

Heavier elements, which yield line radiation in the main part of the plasma, can be
investigated. For transport analysis, the position and width of the respective shells is
crucial. It can be gained from Abel inverted measurements along many line-of-sights
[106] requiring an experimental setup with many VUV or X-ray spectrometers [107].
Alternatively, a spectrometer, which views the plasma on different chords during a series
of identical discharges, can be employed [108]. These expensive techniques were only
rarely used [109]. The common approach uses a single radial chord for each spectrometer,
and the position of the radiating ion is taken from the calculated charge distribution of
the impurity transport model. An example for this approach is a study of argon transport
at TEXTOR [110], where line radiation from ArVII, ArVIII, ArX, ArXII, ArXIV, ArXV,
ArXVI and ArXVII after a short argon puff was measured with a time resolution below
1 ms. The analysis often uses only the time evolution [110, 54] of the different lines due
to the difficulties to obtain an absolute calibration (especially in the VUV) or due to a
lack of reliable atomic data for the effective excitation rates.

Soft X-ray Cameras

The spatial and temporal resolution of the measurements can be strongly enhanced, when
sacrificing the spectral resolution and employing only spectrally filtered measurements
in the soft X-ray wavelength range, i.e. for photon energies in the range from 1-20 keV.
Most commonly, thin beryllium filters with a thickness between 6-500 μm are used to
suppress photons of lower energy. The detecting silicon diodes are operated with reverse
bias voltage, and have a thick depletion layer, where the photons deposit their energy and
form electron-hole pairs due to the internal photo effect, while Compton effect and pair
production can be neglected for the occuring photon energies. The high energy cut-off is
defined by the thickness of the depletion layer of about 100-300 μm. An average energy
of E_{pair} =3.62 eV is needed for the excitation of one electron-hole pair, and the mean
charge per photon is $Q = h\nu/E_{pair}$. For single photon detection, the energy spectrum
of the photons can be gained from the detected current pulses. This technique of *pulse
height analysis* employs Si(Li) diodes. Soft X-ray cameras, however, do not resolve the
single current pulses. Here, the average detector current is measured, which yields the
deposited power of all photons passing the beryllium filter: $I = P/E_{pair} = P\,0.276\,\mathrm{A/W}$.
The transmission of the metal filters as a function of photon energies are well known [111]
and the absolute sensitivity of the whole system can be calculated within an uncertainty
of $\approx$20% [112]. Up to 60 single Si-diodes are used in a single pinhole camera, which
is compact enough to be mounted inside the vacuum vessel and to observe the whole
poloidal cross section of the plasma. The filter should be mounted such that the line-of-
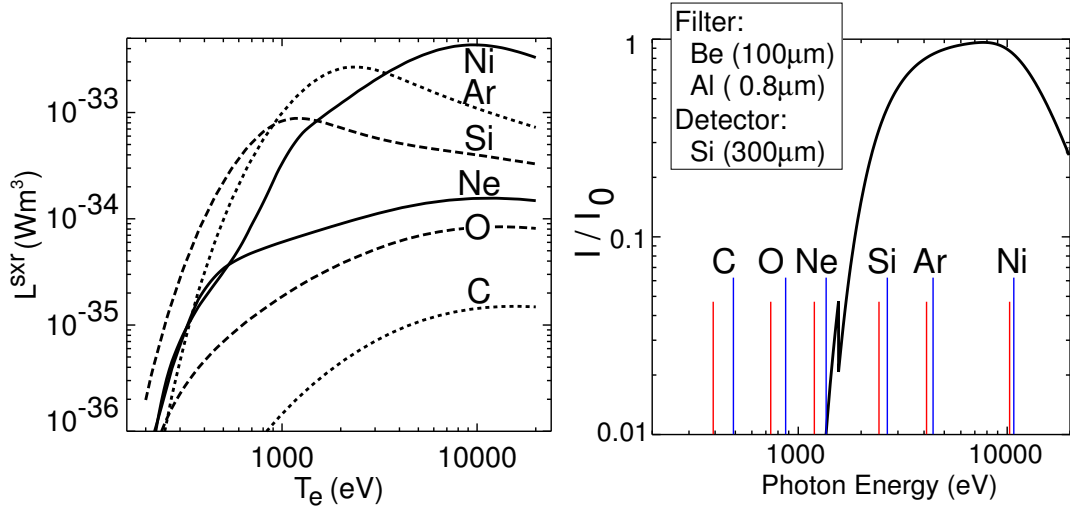
Figure 4.2: *For a detector setup with a $100\,\mu m$ thick Be filter in front of a Si diode of $300\,\mu m$ thickness coated with $0.8\,\mu m$ Al, the spectral filter function is shown on the right side, while the total filtered radiative power coefficients of C, O, Ne, Si, Ar, and Ni are depicted on the right. Ionisation equilibrium is assumed. The ionisation energies of He-like(red) and H-like(blue) stages are added to the graph of the filter function.*

sight from each diode through the pinhole is perpendicular to the filter surface, which guarantees identical absorbing lengths through the filter, i.e. an identical filter function, for each diode. Several camera systems are usually installed and measurements from about 50-100 lines-of-sight are used to obtain the local emission pattern with a time resolution down to $1\,\mu s$.

Band pass filters can be constructed, when identical detectors are placed behind two absorbing filter foils with nearly the same atomic number and with thicknesses adjusted to achieve matched transmission curves except in the energy range between their absorption edges (preferebly K-edges). The difference in the detector output signals for such a system is proportional to the power from photons with energies between the absorption edges. This scheme is named the method of balanced Ross filters [113, 114, 115]. The use of balanced Ross filters for impurity measurements has not been very frequent up to now [116, 117, 118].

The soft X-ray emissivity due to impurity species A can be written as

$$\epsilon_A^{sxr} = n_A n_e L_A^{sxr} = n_A n_e \sum_Z f_{A,z} k_{A,z}^{sxr} \qquad (4.4)$$

where $f_{A,Z}$ is the fractional abundance of the ionisation stage Z and $k_{A,z}^{sxr}$ is the radiative power coefficient of this stage weighted with the photon energy dependence of the detector setup. The $k_{A,z}^{sxr}$ have contributions due to line- and continuum-radiation. The sum term in equation (4.4) is the total radiative power coefficient L_A^{sxr} in the detected spectral range of the detector. In Fig.4.2, the soft x-ray radiative power coefficients of a

few elements are shown versus T_e for the case of a $100\,\mu$m thick Be filter in front of a Si-diode of $300\,\mu$m thickness and a $0.8\,\mu$m Al coating. The fractional abundances are taken from ionisation equilibrium excluding transport. The filter function is shown in the right graph of Fig.4.2. In this graph, also the ionisation energies of the He- and H-like stages are shown for each element. For C and O, the ionisation energies are below the cut-off energy of the filter, and neither line radiation nor the K-edges of the recombination continua can contribute to the detected radiation, which is mainly due to bremsstrahlung only. Ne is marginal, while for Si, Ar and Ni, line radiation and recombination radiation from He- and H-like stages can pass the Be-filter. Thus, the filtered radiative power coefficients of those elements is strongly increased in the T_e range, where the respective ion stages exist.

Soft x-ray cameras measure radiation from all elements in the plasma, and are only useful for perturbative studies. The contribution of the injected impurity is obtained by subtracting the signal before the injection from the signal after injection. For cases, where the intrinsic plasma radiation is dominated by emission from light impurities, like C and O, this background radiation can be well suppressed with a suitable filter as is demonstrated in Fig.4.2. A small amount of an impurity with sufficiently high nuclear charge, e.g. Al or Si, leads to an easily detectable increase of the soft x-ray radiation. Discharges with a sufficiently long and stable flattop are advantageous in order to reduce the amount of the injected impurity as much as possible.

Local Emission from Line-of-Sight Integrated Measurements

From the line-of-sight integrated measurements, local emissivites can be calculated by tomographic inversion. The inversion is considerably simplified, when the emission is constant on magnetic flux surfaces. This assumption is well justified in the confined plasma, since the large transport coefficients parallel to the magnetic field suppress the evolution of gradients on a flux surface. At the end of this section, effects, which lead to poloidal asymmetries on a flux surface, will be discussed.

For the case of constant emission on flux surfaces, the inversion evaluates from the measured line-of-sight integrals the local emissivity $\epsilon(\rho)$, which just depends on a single coordinate, the flux surface label ρ. For circular flux surfaces and observation in one poloidal plane, the special case of an Abel inversion with radius r as flux surface label is obtained. We discuss the indirect inversion procedure, where the local emissivity is described with a certain function $\epsilon(\rho, p_1, p_2, .., p_n)$ which depends linearly or non-linearly on the parameters p_1, p_2, ... p_n. The parameter are found by minimising the squared deviations between the claculated line-of-sight integrals

$$L_k(p_1, p_2, ...p_n) = \int_{\text{kth l.o.s.}} \epsilon(\rho, p_1, p_2, .., p_n) dl \qquad (4.5)$$

and the measured values l_k, which shall have an uncertainty σ_k .

$$\chi^2 = \frac{1}{N} \sum_{k=1}^{N} \frac{[L_k(p_1, p_2, ...p_n) - l_k]^2}{\sigma_k^2} = \min \tag{4.6}$$

This scheme leads to a linear or non-linear system of equations, which is solved with Gauß-Seidel elimination in the linear case or with the Levenberg-Marquardt algorithm in the non-linear case. For the linear case of Abel inversion, examples can be found in Ref.[119], where even polynomials in r were used, and in Ref.[120], where the emissivity is expressed as a sum of cosine functions.

In order to avoid strongly oscillating solutions, regularisation methods have to be employed. The first possibility is to reduce the number of free parameters in the fitting function. Cubic splines with zero derivative at $\rho = 0$ are very useful in this respect, where only in regions with strong gradients a higher density of spline knots is allowed. It is furthermore advantageous to use the exponential of a cubic spline in order to assure, that the fitted emission is always positive. For the second method by Tikhonov [121], a penalty function for the curvature of the solution like $W \int (d^2\epsilon/d\rho^2)^2 d\rho$ is added to the χ^2-term of Eq.(4.6), and the weight factor W of the penalty function is adjusted until χ^2 equals 1, i.e. until the mean deviation equals the experimental uncertainty [122].

Fig.4.3 shows three inverted emission profiles for simulated data sets of a 60 channel soft X-ray camera at ASDEX Upgrade. The simulated data sets were contaminated with normally distributed noise at a level of σ_k/l_k=10% as indicated by the error bars in the upper right figure. A case with strong edge radiation, which is a factor of 10 of the emissivity in the centre, mimics the total radiation profile. It is compared with a typical triangular soft X-ray radiation profile, and a profile with dominant central radiation. Dashed lines show the standard deviation of the inverted emissivity profiles. It can readily be seen, that the relative uncertainty of the inverted profiles is largest in the centre. Only the innermost channels contain information about the profile in the centre and small changes in the line-of-sight integrals transform into large changes of the emissivity due to the short integration path. Additionally, there is a dramatic increase of the relative uncertainty, when the centre is observed through a region with strong edge radiation. Bolometric measurements are thus not very sensitive to small changes of the central emission.

For radiation which originates from outside the last closed flux surface (LCFS), the assumption of constant emission on the flux surface is not fulfilled and the radiation increases strongly when approaching the divertor or the limiter. This effect is very pronounced for the total radiation, but can be neglected for the soft X-ray radiation, which is predominantly produced inside the LCFS.

Inside the LCFS, the emission might be modulated due to macroscopic MHD modes, where this asymmetry with respect to the unperturbed flux surfaces can be removed by
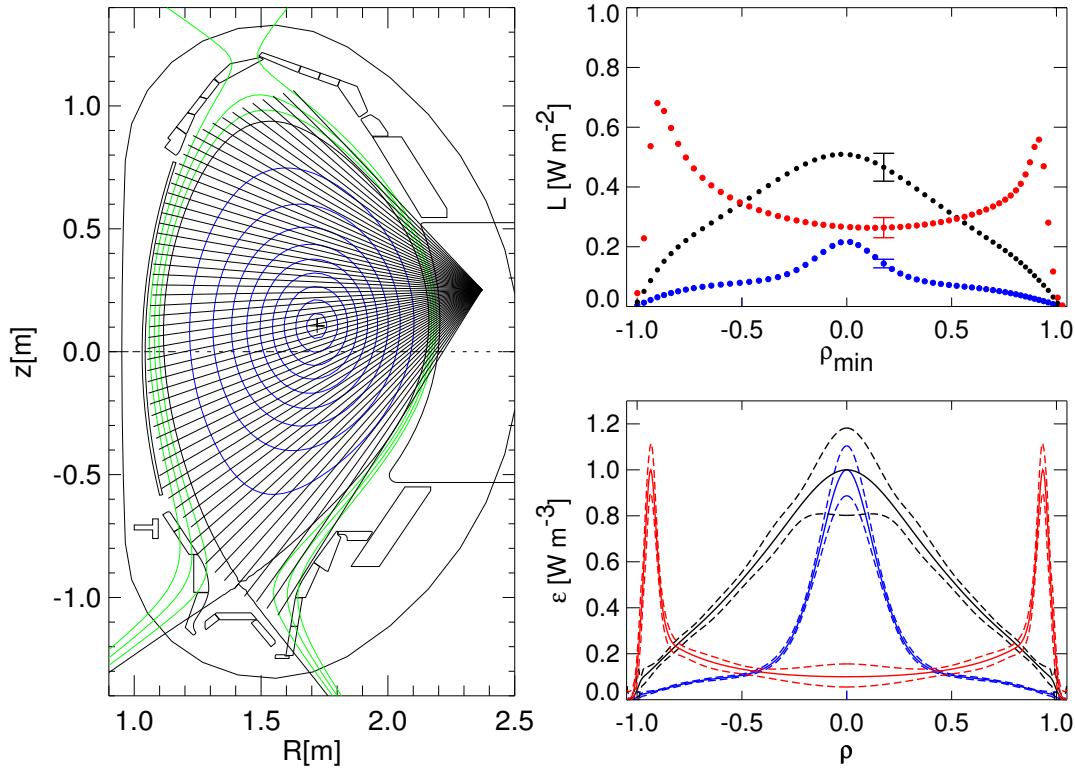
Figure 4.3:   *Examples for the inversion of line-of-sight integrated emission profiles of a 60 channel soft X-ray camera at ASDEX Upgrade. The data sets (upper right) were simulated with a 10% relative measurement uncertainty. The uncertainty of the unfolded emission profiles (lower right) is shown with dashed lines. The profile with strong edge radiation mimics a total radiation profile as it would be seen by a bolometer camera.*

using measurements, which are temporally averaged over many oscillation cycles. An example of such an emissivity modulation, which has been observed after the injection of tungsten in ASDEX Upgrade, is shown in Fig.4.4. Here, tungsten accumulated on the $q=1$ surface in a magnetic (m=1,n=1)-island, which rotates with about $10\,\mathrm{kHz}$ in the toroidal direction. The geometric dimensions of the island can be estimated from the spatial and temporal structure of the oscillating soft x-ray signals [123, 124] and are depicted in Fig.4.4.

The vertical torus drifts (or, equivalently, the divergence of the diamagnetic drifts) drive the densities towards an up-down asymmetry and lead to parallel return flows. The resulting up-down asymmetry for main ions and electrons can be neglected, however, parallel friction between main ion and impurity ions sweeps impurities with the return flows, and the resulting impurity asymmetry has opposite direction from the vertical drift direction. The asymmetry shall be described with $n = n_0(1 \pm \gamma \sin \theta)$, where θ is the poloidal angle and γ is the relative amplitude. For the ordering assumptions in section 3.1, i.e. collision frequency much smaller than the gyro frequency and gyro radius much
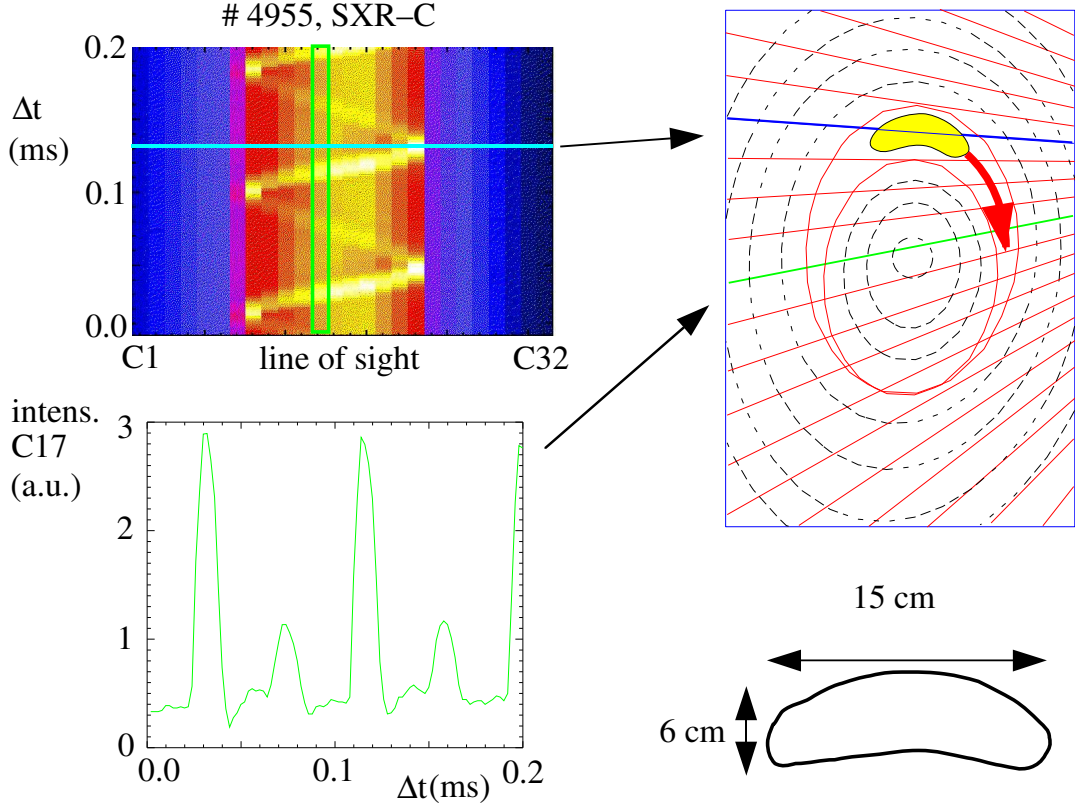
Figure 4.4: *Modulation of the line-of-sight integrated soft x-ray signals due to accumulation of tungsten in a toroidally rotating (m=1,n=1)-island. The camera had a 6μm thick Be-filter. The geometrical dimensions of the island are estimated from the temporal and spatial structure of the intensity oscillations [123].*

smaller than gradient lengths, the amplitude γ is much smaller than the inverse aspect ratio ϵ. Non-linear extension of the neoclassical theory towards high collision frequencies predict that γ can reach a maximum value of ϵ [125, 126]. Experimental measurements of these small asymmetries need precise knowledge of the flux surface and line-of-sight geometry, and at the edge, an assessment of the asymmetry due to the impurity source distribution. Quantitative agreement of experiment and theory [127] is not always found [128].

In plasmas, which exhibit a fast toroidal rotation, the impurity density on the outboard side of the flux surface can be increased with respect to the inboard side due to the centrifugal force on the impurity ions. In the force balance equation (3.1), the centrifugal force enters in the term $m_a n_a (\vec{u}_a \cdot \nabla)\vec{u}_a = -m_a n_a \omega^2 R \vec{e}_R$, where ω is the toroidal angular frequency and R is the major radius. In lowest order, the centrifugal force term, the electric field term and the pressure gradient term along the magnetic field are retained in Eq.(3.1). For constant temperature T_a on the flux surface, the density ratio of the outermost to the innermost poloidal position on the flux surface with major radii R_{out}
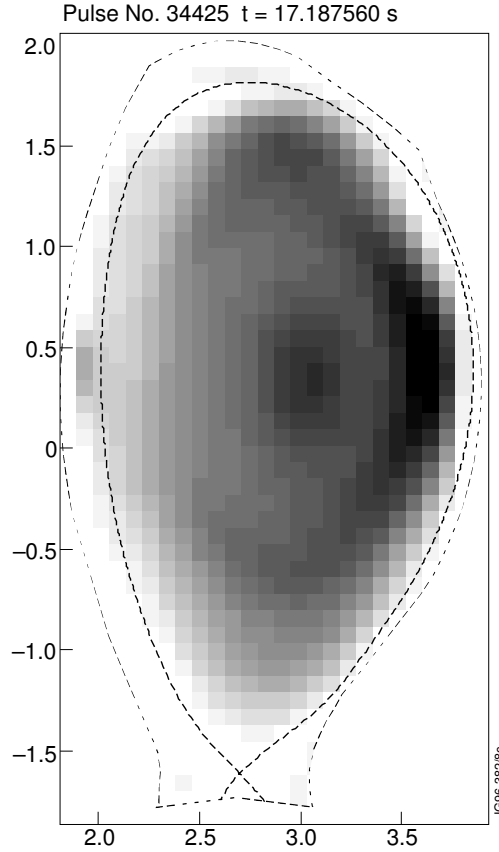
Figure 4.5: *Tomographic reconstruction of the soft x-ray emissivity distribution during the high performance phase of a hot ion H-mode in JET. The inversion used data from 210 lines-of-sight from many soft x-ray cameras with a 250μm thick Be-filter. The strong in/out asymmetry of the peripheral emission and the central peak is attributed to nickel radiation. (from [129])*

and R_{in} is then given by [130]

$$\frac{n_a(R_{out})}{n_a(R_{in})} = \exp\left[\frac{m_a\omega^2(R_{out}^2 - R_{in}^2)}{2k_BT_a} - \frac{eZ_a\Delta\phi}{k_BT_a}\right].$$ (4.7)

For the electrons, the centrifugal force term can be neglected due to the small mass. The unknown difference of the electrostatic potential $\Delta\phi$ follows from the quasi-neutrality condition $\sum n_a Z_a = 0$. In a plasma of main ion D with low impurity concentrations (trace limit), the quasi-neutrality is only maintained by the electrons and the deuterium ions.

$$\frac{n_e(R_{out})}{n_e(R_{in})} = \exp\left[\frac{e\Delta\phi}{k_BT_e}\right] = \exp\left[\frac{m_D\omega^2(R_{out}^2 - R_{in}^2)}{2k_BT_i} - \frac{eZ_D\Delta\phi}{k_BT_i}\right] = \frac{n_D(R_{out})}{n_D(R_{in})}$$ (4.8)

The temperature T_i shall be equal for all ion species, and the second term in the exponent of Eq.(4.7) reads for an impurity ion with mass m_I and charge Z_I.

$$\frac{eZ_I\Delta\phi}{k_BT_i} = \frac{m_I\omega^2(R_{out}^2 - R_{in}^2)}{2k_BT_i}\frac{Z_Im_D}{m_I}\frac{T_e/T_i}{1 + Z_DT_e/T_i}.$$ (4.9)

Thus, the $\Delta\phi$-term reduces the exponent by a factor of 2 when equal electron and ion temperature and fully ionised impurities with $Z_I m_D/m_I \approx 1$ are assumed. For this case, the asymmetry is finally

$$\frac{n_I(R_{out})}{n_I(R_{in})} \approx \exp\left[\frac{m_I \omega^2 (R_{out}^2 - R_{in}^2)}{4 k_B T_i}\right] = \exp\left[\epsilon \frac{v_\Phi^2}{v_{th}^2}\right] \tag{4.10}$$

where $\epsilon = (R_{out} - R_{in})/(R_{out} + R_{in})$ is the inverse aspect ratio, $v_\Phi = \omega(R_{out} + R_{in})/2$ is the average toroidal velocity and $v_{th} = \sqrt{k_B T_i/m_I}$ is the thermal velocity. The asymmetry of electrons and deuterium ions is very weak, since it is reduced by a factor $\exp\left(\sqrt{m_D/m_I}\right)$. For a flux surface at half radius in a tokamak with aspect ratio 3, we have $\epsilon \approx 0.15$ and the out/in density ratio is a factor of 2 for $v_\phi = \sqrt{\ln 2}\, v_{th}/\sqrt{\epsilon} \approx 2.15 v_{th}$. For impurity concentrations above the trace limit, $\Delta\phi$ increases and leads to a reduction of the asymmetry, while for a plasma with $T_e < T_i$, $\Delta\phi$ decreases. Fig.4.5, which is taken from Ref.[129], shows an example for a strong in/out asymmetry. In a hot-ion H-mode at JET, soft x-ray emission from Ni revealed this in/out density asymmetry for a situation with $v_\phi \approx 3 v_{th}$.

4.3 Evaluation of Transport Coefficients

Radial profiles of the fully ionised impurity ions from CXRS or the soft X-ray radiation can be used to calculate the total density of the injected impurity, if the fractional abundances of the ion stages are known. In section 2.5, it was shown, that the fractional abundances of the most populated ion stages are only weakly influenced by the transport parameters in a large part of the main plasma, and can be calculated directly from the ionisation and recombination rates, i. e. for radii below $r \approx 0.5\,\mathrm{m}$ for the examples shown in Fig.2.9 and Fig.2.10. Thus, the total impurity density evolution after a single impurity injection or during a sinusoidally modulated impurity puff can be gained up to some radius and can be used to determine the transport coefficients without making use of impurity transport codes. The direct evaluation methods, which either work in the time domain or use a harmonic analysis shall be described in the section 4.3.1 and 4.3.2. Section 4.3.3 describes a few enhancements which can be incorporated when using full impurity transport calculations.

4.3.1 Single Impurity Injections

For the total impurity density, the source term in the transport equation can be neglected in the major part of the confined plasma. In this case, the radial flux density $\Gamma(r, t)$ of the total impurity density at radius r can be evaluated from the temporal change of the

respective density $n(r,t)$ inside of r.

$$\Gamma(r,t) = -\frac{1}{r}\int_0^r \frac{\partial n(\tilde{r},t)}{\partial t}\tilde{r}d\tilde{r} \tag{4.11}$$

The transport coefficients can then be gained from the dependence of the normalised flux density Γ/n on the normalised density gradient $[1/n][\partial n/\partial r]$.

$$\frac{\Gamma(r,t)}{n(r,t)} = -D(r)\frac{1}{n(r,t)}\frac{\partial n(r,t)}{\partial r} + v(r) \tag{4.12}$$

We assume, that the perturbation by the impurity puff is small, such that the transport coefficients are not changing during the evolution of the density profiles in the plasma. Thus, $D(r)$ and $v(r)$ are only functions of the radius. In this case, a plot of the normalised flux density versus the normalised density gradients yields a straight line with a slope of $-D(r)$ and an offset of $v(r)$. Shortly after the puff, there is an influx phase with negative values for $\Gamma(r,t)$ followed by an outflux phase with positive $\Gamma(r,t)$. For times, which are long compared to the second eigentime of the transport equation, the density at all radii decays exponentially with the first eigentime τ_1. Then, Γ/n becomes constant, and the transport coefficients can only be determined if measurements are taken before that phase. For diffusive transport, the arrival time of the density perturbation scales quadratically with the radial distance between source and measurement location, i.e. $\Delta t \approx \Delta r^2/D$, while the width of the density distribution is about equal to Δr. At the edge, a higher temporal and radial resolution is thus needed to resolve the density evolution after a puff, e.g. $\Delta t = 2.5\,\mathrm{ms}$ for Δr=5 cm and $D = 1\,\mathrm{m}^2/\mathrm{s}$.

Fig.4.6 and Fig.4.7 demonstrate the method for a radially constant diffusion coefficient $D(r) = 1\,\mathrm{m}^2/\mathrm{s}$ and zero drift velocity. The right graph of Fig.4.6 shows the calculated evolution of the density for several times after a short puff at $t = 0\,\mathrm{s}$, which deposits particles at $r = 0.64\,\mathrm{m}$. For the measurement of the density evolution, two cases with different spatial and temporal resolutions were assumed. For the first case, the equidistant radial measurement points have a radial spacing of 5 cm and a temporal distance of 5 ms, while for the second case, the radial and temporal resolution are increased by a factor of 2, i.e. Δr=2.5 cm and Δt=2.5 ms. The measurement uncertainty shall have a statistical component with 5% of the measurement value and a constant instrumental uncertainty of 0.025 in the units of Fig.4.6. The resulting error bars are depicted for three density profiles in Fig.4.6.

The derivatives are approximated with the symmetric three point formula and the radial integral with the trapezoidal rule, which yields at the radial measurement point k and
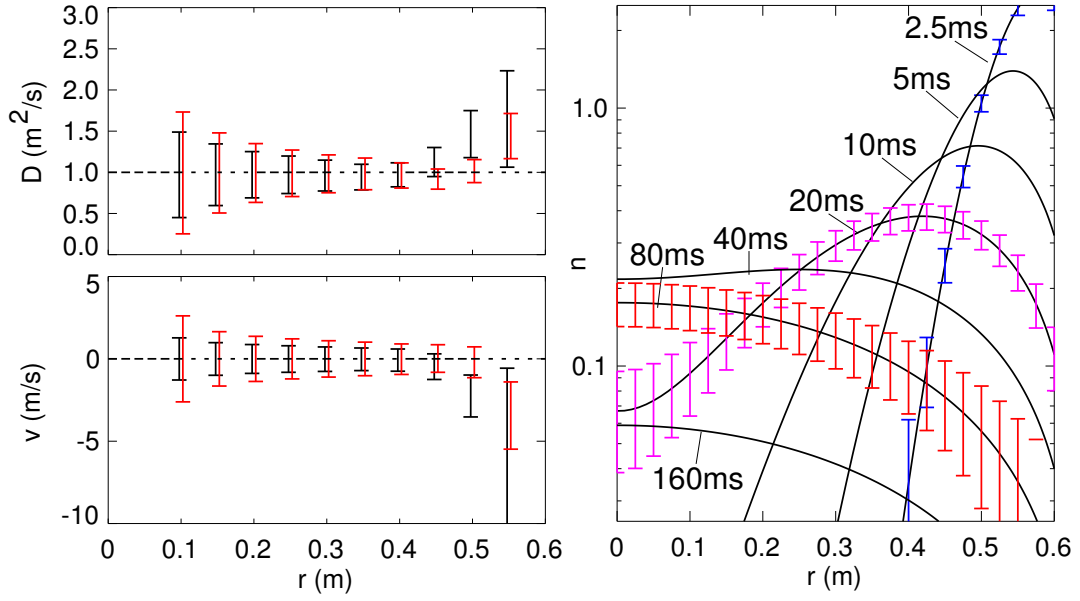
Figure 4.6: *Right graph: Calculated density evolution after a short puff at $t = 0\,\mathrm{s}$ for radially constant diffusion coefficient $D = 1\,\mathrm{m^2/s}$ and $v = 0\,\mathrm{m/s}$. Left graphs: Evaluated transport coefficients from the straight line fit of the normalised fluxes versus the normalised gradients for two spatial and temporal resolutions of the measurement (black: $\Delta r = 5\,\mathrm{cm}$, $\Delta t = 5\,\mathrm{ms}$; red: $\Delta r = 2.5\,\mathrm{cm}$, $\Delta t = 2.5\,\mathrm{ms}$). The error bars are evaluated from the density measurement uncertainties shown in the right graph.*

at temporal measurement point j.

$$\frac{\partial n(r_k, t_j)}{\partial r} = \frac{n(r_{k+1}, t_j) - n(r_{k-1}, t_j)}{2\Delta r}$$

$$\frac{1}{r_k}\int_0^{r_k} n(\tilde{r}, t_j)\tilde{r}d\tilde{r} = N(r_k, t_j) = \frac{1}{r_k}\left[\Delta r \sum_{i=1}^{k-1} n(r_i, t_j)r_i + \frac{\Delta r}{2}n(r_k, t_j)r_k\right]$$

$$\Gamma(r_k, t_j) = -\frac{N(r_k, t_{j+1}) - N(r_k, t_{j-1})}{2\Delta t} \tag{4.13}$$

The uncertainties for these quantities are readily computed from the uncertainties of the densities. In Fig.4.7, the resulting normalised fluxes are shown as a function of the normalised gradients for two radii from the measurement with the higher resolution. Both quantities have an uncertainty and the straight line fit has to weight the individual measurement point according to the two error bars. The χ^2-method for fitting a straight line $y(x) = a + bx$ through measurement point (x_i, y_i) with uncertainties in both coordinates can be performed with the following merit function.

$$\chi^2(a, b) = \sum_{i=1}^N \frac{(y_i - a - bx_i)^2}{\sigma_{yi}^2 + b^2\sigma_{xi}^2} \tag{4.14}$$

A routine for minimising this merit function, which also yields error estimates for a and b, can be found in [131]. In Fig.4.7, the data points from the analysis at $r = 0.3\,\mathrm{m}$ are
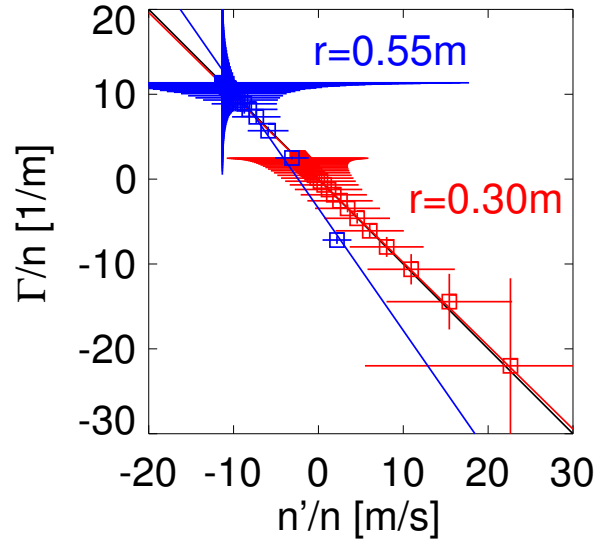
Figure 4.7:   *Evaluated normalised fluxes versus the normalised gradients at two radii for the density evolution of Fig.4.6. The measurement resolution is Δr=2.5 cm and Δt=2.5 ms. The diagonal has the slope equivalent to D =1 m²/s. At the larger radius r =0.55 m, the temporal resolution is insufficient to detect the gradients in the influx phase.*

on the diagonal, i.e. on the line with a slope equivalent to $D = 1\,\mathrm{m^2/s}$, while the data points for $r = 0.55\,\mathrm{m}$ show deviations from this line, which are much larger than the error bars. For the larger radius, the spatial and temporal gradients are too large and can not be measured with the resolutions of Δr=2.5 cm and Δt=2.5 ms. At $t = 5\,\mathrm{ms}$, the density wave has already passed the radius $r = 0.55\,\mathrm{m}$ and only one data point represents the inflow phase. Fig.4.6 gives the evaluated transport coefficients and their uncertainties from the fit routine. For the radial range 0.1-0.55 m, D and v are compared with the set values (dashed lines) for both resolutions using black error bars for the lower resolution (Δr=5 cm , Δt=5 ms) and red error bars for the higher resolution (Δr=2.5 cm , Δt=2.5 ms). Inside of $r = 0.4\,\mathrm{m}$, the lower resolution is sufficient and yields smaller error bars. The gradients can be determined with less uncertainty due to an increase of the density differences for the lower resolution. Outside of $r = 0.4\,\mathrm{m}$, the higher resolution yields better results and can be used up to $r = 0.5\,\mathrm{m}$. For $r = 0.55\,\mathrm{m}$, the resolution is insufficient and the flux can only be explained with the smeared measured gradient when using higher transport coefficients. Especially, the data points in the influx phase have smallest relative uncertainty due to the high density and are strongly weighted in the fit, which yields an inward pinch to explain the strong influx with the measured near zero gradient.

4.3.2 Modulated Gas Puffs

Sinusoidally modulated gas puffs offer another possibility to deduce the transport coefficients [54, 55, 56]. The method needs long stationary discharge phases for the recording of several oscillation periods, but has the advantage that rather low puff levels lead to sufficiently accurate measurements of the modulation amplitude A and phase ϕ. Thus, the impurity perturbation can be kept quite low.

We compare the harmonic analysis method, with the analysis of fluxes and gradients after a short gas puff or a laser injection and discuss the evolution of the total impurity density with zero sources like in the previous section. The impurity influx shall be sinusoidally modulated with angular frequency ω and shall be sufficiently small, such that the transport parameters are independent of time. In this case, the impurity densities will also be modulated with the same frequency ω, and the amplitude $A(r)$ and phase $\phi(r)$ are gained from the sine and cosine transform of the density modulation.

$$
\begin{aligned}
a_1(r) &= \frac{2}{T} \int_t^{t+T} n(r, \tilde{t}) \cos\left(\omega \tilde{t}\right) d\tilde{t} \\
b_1(r) &= \frac{2}{T} \int_t^{t+T} n(r, \tilde{t}) \sin\left(\omega \tilde{t}\right) d\tilde{t} \\
A(r) &= \sqrt{a_1(r)^2 + b_1(r)^2} \qquad \tan\left(\phi(r)\right) = \frac{a_1(r)}{b_1(r)}
\end{aligned}
\tag{4.15}
$$

Here, T is the time of one or more modulation periods. The transport parameters at a certain radius r can then be determined from the radial profile of amplitude and phase up to r.

$$
\begin{aligned}
D(r) &= -\frac{\omega}{r} \left(\frac{d\phi}{dr}\right)^{-1} \frac{1}{A(r)} \int_0^r A(\tilde{r}) \cos\left(\phi(\tilde{r}) - \phi(r)\right) \tilde{r} d\tilde{r} \\
v(r) &= -\frac{\omega}{r} \frac{1}{A(r)} \int_0^r A(\tilde{r}) \sin\left(\phi(\tilde{r}) - \phi(r)\right) \tilde{r} d\tilde{r} + D(r) \frac{1}{A(r)} \frac{dA(r)}{dr}
\end{aligned}
\tag{4.16}
$$

For comparison with the single puff method, we use again a radially constant diffusion coefficient $D(r) = 1\,\mathrm{m^2/s}$ and zero drift velocity. In this case, the ratio of the complex amplitudes $\tilde{n}$ of the density modulation at two radii is given by a ratio of zero order complex Bessel functions J_0.

$$
\frac{\tilde{n}(r)}{\tilde{n}(r_0)} = \frac{J_0(\exp(-i\pi/4)kr)}{J_0(\exp(-i\pi/4)kr_0)} \quad \text{with } k = \sqrt{\frac{\omega}{D}}.
\tag{4.17}
$$

The lower measurement resolution from the above example with $\Delta r{=}5\,\mathrm{cm}$ and $\Delta t{=}5\,\mathrm{ms}$ is taken. The modulation frequency is $f{=}5\,\mathrm{Hz}$. Fig.4.8 shows the density modulation for six radii. The measurement uncertainty is assumed to be worse compared to the example in section 4.3.1 with a statistical component of 10% of the measurement value. The resulting error bars are depicted for the outermost measurement point in Fig.4.8. A
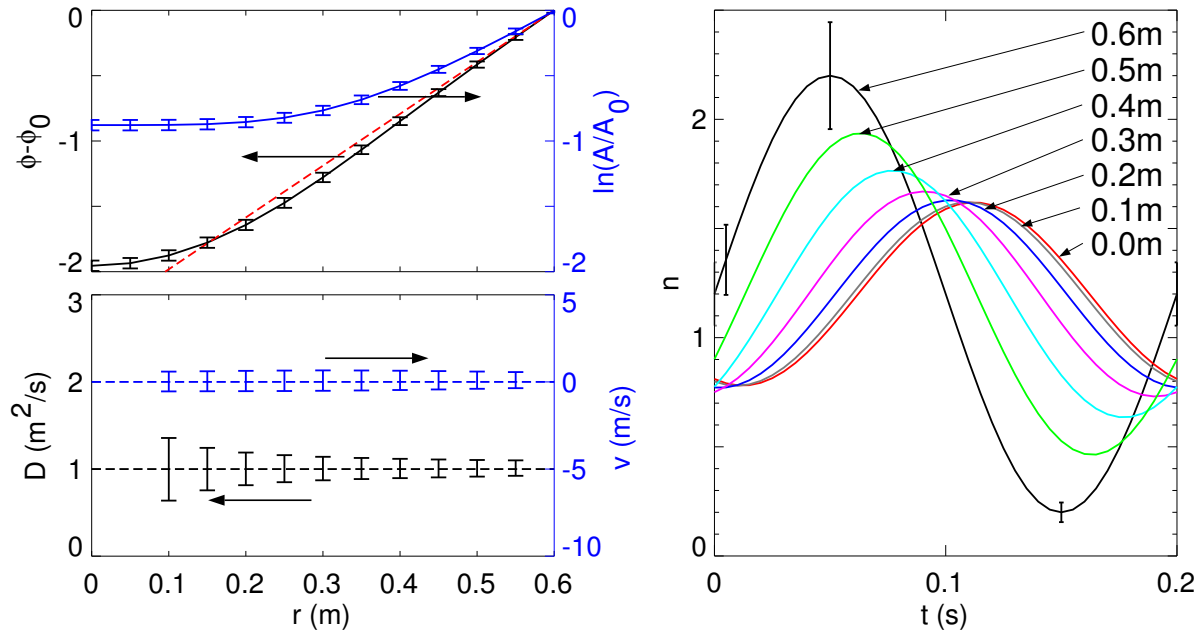
Figure 4.8:   *Right graph: Calculated density evolution for sinusoidally modulated influx with frequency 5 Hz, a radially constant diffusion coefficient D=1 m^2/s and v=0 m/s. Left graphs: Profiles of amplitude and phase and transport coefficients assuming a spatial and temporal resolution of Δr=5 cm and Δt=5 ms. The error bars are evaluated from the density measurement uncertainties shown in the right graph.*

time interval of 4 modulation periods(800 ms) shall be available for the determination of amplitude and phase. The required integrals of Eq.(4.15) and (4.16) are approximated by the trapezoidal rule and the symmetric three point formula is used for the derivatives in Eq.(4.16). The radial profile of phase and amplitude and the respective uncertainties are shown in the upper left graph of Fig.4.8. The dashed line gives the evolution of phase and amplitude in the slab approximation, which yields $d\phi/dr = d(\ln A)/dr = \sqrt{\omega/(2D)}$ and is valid for $r\sqrt{\omega/D} \gg 1$. The lower left graph of Fig.4.8 depicts the resulting transport coefficients. The uncertainties of D and v are rather low due to the long 'integration' time compared to the single injection experiment, even though the uncertainty assumption for the single density measurement was increased. The uncertainty increases with decreasing radius, since the radial gradients of amplitude and phase become small. Towards the edge, there is no large systematic error observable due to the finite radial and temporal measurement resolution. Here, the temporal and radial gradients are much weaker compared to the single injection and even a lower measurement resolution is sufficient. The density evolution can off course also be analysed in the time domain and the fit of normalised fluxes versus normalised gradients delivers the same results as the harmonic analysis.

Thus, the modulated gas puff experiment seems to be advantageous compared to the sin-

gle injection. However, pre-requisites for such experiments are long stationary discharge phases and impurity species, which do not show too much recycling at the vessel walls or are pumped sufficiently well, such that the modulated gas puff is not superimposed by a much stronger flux of recycling impurities.

4.3.3 Transport Code Calculations

Numerical solutions of the coupled radial impurity transport equations as described in section 2.3 have to be used when the influence of transport on the ion stage balance becomes large. For a given set of transport parameters, the code calculates the profile evolution of the densities of all ion stages, which are compared with CXRS measurements or are used to evaluate the line-of-sight integrated data from passive spectroscopy.

The evaluation of transport parameters from code calculations are usually performed by adjusting manually the profiles of $D(r)$ and $v(r)$ until a match of measured and calculated time traces is achieved. Examples for the analysis of line-of-sight integrated spectroscopic measurements are given in Ref.[110, 61, 54, 64, 132]. Examples for the application to soft X-ray measurements after laser blow-off can be found in Ref.[133, 134, 135], and usage of several diagnostics is presented in Ref. [136, 137].

The one dimensional treatment of the plasma edge outside the last close flux surface is off course a rather crude description of the two or even three dimensional impurity flux patterns. Here, the different code parameters like the decay time $\tau_{||}$ due to parallel losses, the perpendicular loss at the outermost grid point, the fraction of recycling impurities, the transport parameters in the SOL, and the time evolution of the neutral influx is just adopted to satisfy the time evolution of the emission from lower ionisation stages. Reliable information about the flux surface averaged transport parameters can only be expected from comparison of code results and measurements within the last closed flux surface.

If the total impurity density evolution is known up to a certain radius, numerical solutions of the radial transport equation for the total impurity density can be employed, which use the density evolution at the outermost measurement radius as boundary condition. The computation time is sufficiently short to incorporate the respective subroutine into a χ^2-fit routine using the Levenberg-Marquardt algorithm. This offers the possibility for a few enhancements compared to the methods used in the previous two sections.

The evaluation procedures in sections 4.3.1 and 4.3.2 did not impose any relations on the transport coefficients at neighbouring measurements points, which can lead to strong radial oscillations of $D(r)$ and $v(r)$, if the data quality of the density measurements is not very good. A further regularisation, which suppresses such oscillations for the radial profiles of the transport coefficients, can be incorporated, when the evolution of the impurity density at all measurement points is fitted. The strategy is to use radial
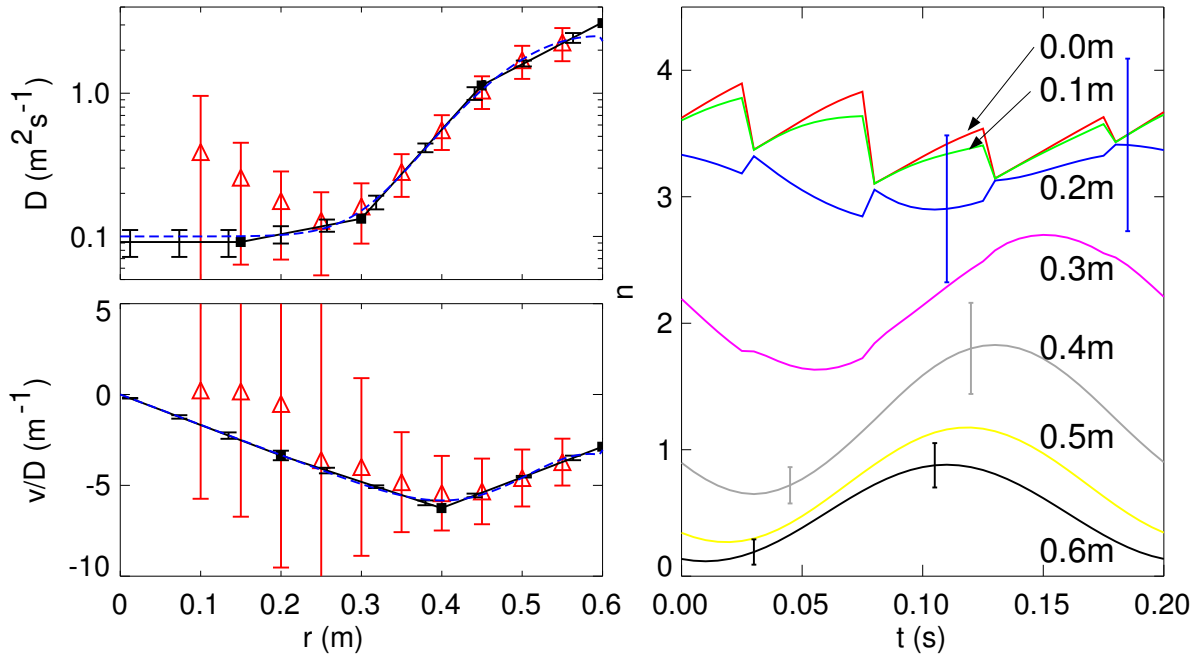
Figure 4.9:   *Right graph: Density evolution for sinusoidally modulated influx with frequency of 5 Hz, and transport parameters as shown with dashed lines in the left graphs, i. e. a diffusion coefficient, which increases with radius, and an inwardly directed drift velocity. The effect of sawteeth oscillations with frequency of 20 Hz was included by periodically flattening the density profile within r_{mix}=0.25 m. Left graphs: Profiles and uncertainties of the evaluated transport coefficients assuming a spatial and temporal resolution of Δr=5 cm and Δt=5 ms using the fit method (black) and the fourier method (red) from section 4.3.2. The error bars are evaluated from the uncertainties of the density measurement as shown in the right graph.*

functions for the transport parameters with the lowest number of free parameters, which yield $\chi^2 \approx 1$. For example, $D(r)$ can be parametrised by specifying the logarithms of D on an equally spaced radial grid, which are linearly interpolated. This parametrisation avoids the appearance of negative diffusion coefficients in the fit procedure. Furthermore, $D(r)$ should be kept constant inside the innermost grid point in order to avoid large scatter of $D(0)$, which is sensitive to the second derivative of the density on axis and thus very uncertain. It is advantageous to use the drift parameter v/D instead of v in the fitting routine, and the most simple parametrisation is again an equally spaced radial grid of drift parameters, which is linearly interpolated. On the axis the drift parameter has to be zero.

Another enhancement is the separation of the transport induced by sawtooth crashes from the transport in the quiet phase between the crashes. Sawtooth crashes are known to cause a nearly complete flattening of the impurity density inside a certain mixing radius [73, 76]. The magnetic reconnection during the collapse happens on a time scale

of a few $100\,\mu$s. The associated density flattening leads to an outward/inward flux, if the density profile before the collapse is peaked/hollow. This effect is easily incorporated into the transport code, where at the collapse time a complete flattening of the density inside the mixing radius r_{mix} is invoked obeying the particle conservation. The mixing radius r_{mix} can experimentally be determined from the soft X-ray profiles. Thus, the transport due to sawtooth crashes can be excluded from the fitted transport coefficients, which shall describe the plasma properties without macroscopic MHD instabilities.

An example for the fitting procedure is shown in Fig.4.9. A sinusoidally modulated influx with frequency of $5\,$Hz is assumed. The diffusion coefficient has now a more realistic shape, which is low in the plasma centre and increases towards the plasma edge and there shall also be an inward pinch. The set values are shown as blue dashed lines in the left graphs of Fig.4.9. Furthermore, a sawtooth oscillation with frequency of $20\,$Hz shall be present, which flattens the impurity density inside of $r_{mix}{=}0.25\,$m at the times of each sawtooth collapse. The spatial and temporal measurement resolution is $\Delta r{=}5\,$cm and $\Delta t{=}5\,$ms. The right graph of Fig.4.9 shows the density evolution for every second channel during one period of the modulated influx. It can be observed, that the density increases towards the centre in contrast to the case with purely diffusive transport as shown in Fig.4.8. The central channels are strongly disturbed by the sawtooth crashes. The statistical uncertainty of the density measurement is set to 20% as illustrated by the error bars. The fit functions for the transport coefficients are parametrised as described above with four equally spaced grid points for D and three grid points for v/D. Four influx modulation periods are used for the fit, and the pre-set transport parameters are found with rather small satistical uncertainties. The density evolution was also processed with the harmonic analysis of section 4.3.2, which determines the pre-set transport parameters with higher uncertainty outside the sawtooth mixing region, while inside the mixing region, the averaging over the sawteeth oscillations produces a systematic error yielding too high diffusion coefficients and too low inward pinch parameters.

5. Experimental Results

Measurements of the radial impurity transport behaviour will be summarised in this chapter. Most information about the transport properties of the plasma was gained from perturbative experiments, which investigated the temporal evolution of the impurity density profile after a disturbance.

Impurity injection experiments are the most common form of perturbative studies. Here, the determination of a single decay time constant is the easiest measurement, which has widely been used. For non-recycling impurities, the decay time is dominated by the region with slowest transport, which the impurity has to pass in order to leave the plasma, while for elements, which recycle from the vessel walls, the main bottle neck is the transport to the pump duct. Thus, the interpretation of the decay times is rather limited without further knowledge on the spatial profiles of the transport coefficients.

A deeper insight can only be gained by the determination of radially resolved transport coefficients, which can be compared with the transport coefficients of the energy transport or with theoretical predictions, i. e. with code calculations of neoclassical transport (codes for turbulent impurity transport are just emerging). The measurement tools of these studies have been described in the preceeding chapter.

The form of the equilibrated density profiles gives only the ratio of radial drift velocity and diffusion coefficient, if the source location is in the scrape-off layer. Even though the single transport coefficients can not be resolved, there is great interest in the equilibrium density profiles with respect to a burning fusion plasma, where low central impurity concentration have to be achieved, and low values for the ratio of central to edge impurity concentration are required. Thus, it is of high interest to assess the plasma conditions, which lead to the detrimental effect of central impurity accumulation, and to devise counter measures.

5.1 Decay Times

When injecting an impurity into a tokamak plasma, the increase of the spectral line radiation is followed by a decrease, which eventually becomes an exponential decay with a single time constant τ_d. This decay time τ_d is determined by the longest eigentime

of the transport equation, and after all higher eigenmodes have vanished, the impurity density in the whole plasma has a constant spatial profile, which decays with τ_d. For the measurement, the required time resolution is rather low and the determination of τ_d was one of the first methods to study impurity transport. For a recycling impurity, like most gaseous impurities, the decay is usually dominated by the time constant, with which the impurity is pumped out of the vessel, and only for a non-recycling impurity τ_d gives information about the radial transport coefficients in the plasma. For a non-recycling impurity, τ_d equals to the first eigentime τ_1 of the radial transport equation. In contrast to the energy transport, information about τ_1 is not very valuable to estimate the particle confinement time τ_p, which is much smaller than τ_1 due to the impurity source location at the plasma edge (see section 2.2.3). The particle confinement time would be equal to τ_1, if the source function had the radial shape of the first eigenfunction of the transport equation, which depending on the heating method might look rather similar to the power deposition profile of the plasma heating. Thus, it is sensible to compare τ_1 with the energy confinement time τ_E to gain insight in the relation of radial impurity and energy transport.

Decay time studies of non-recycling impurities were performed with laser blow-off (LBO) injection [58]. First investigations on ATC were performed using only VUV lines from lower ionisation states of aluminium (AlV - AlXI) [59], while silicon LBO experiments on Alcator-A [138] included VUV lines from SiXI and SiXII as well as X-ray lines of SiXIII and SiXIV, where it turned out, that the He-like line from the plasma centre has a systematically longer decay time than the Li-like line being emitted more towards the edge. Injection of V, Cr, and Ni into TFR plasmas showed the same difference for the decay of central and more peripheral line emission [139]. This discrepancy was simply due to the fact, that the VUV lines became to weak in order to measure the late decay rate [140]. This problem is often encountered for the emission from charge stages which are predominantly fed by ionisation. When the source has disappeared, these charge states are only weakly populated by recombination, the charge state distribution shifts towards higher ion stages (see Fig.2.11), and line radiation from the lower charge states becomes very low. The fractional abundance of the higher charge states in the plasma bulk, which are more evenly fed by recombination and ionisation, does not decay and their emission can be measured for a longer time. Furthermore, if the diffusion coefficient has a strong radial dependence or if there is a high inward pinch in the central part of the plasma, it takes very long until the decay of central and peripheral impurity density is governed by the same time constant τ_1, which is practically not measurable (see for example Fig.5.13). Most prominent are the cases with large central inward pinch, where the central line emission does not decay during the discharge period, e. g. [139, 141].

Scaling laws for the impurity decay times have been proposed for ohmic and L-mode plasmas. Extensive experiments on ohmic plasmas in the Alcator-C tokamak were carried

out by Marmar et al. [142], and the found scaling of the decay time was

$$\tau_{Alcator-C}[ms] = 7.5 \times 10^{-2}\frac{a\ m_M}{q}\left(\frac{R^{0.75}Z_{eff}}{Z_M}\right) \qquad (5.1)$$

where a[cm] and R[cm] are the minor and major plasma radius, m_M[amu] and Z_M are mass and charge of the main ion species respectively. The dependences inside the brackets were not verified as firmly as the proportionality to am_Mq^{-1}. A dependence of the decay time on impurity mass or charge was tested for aluminium, silicon, and titanium finding equal decays for these elements. This scaling was found not to be in agreement with a data set gained for ohmic and L-mode plasmas in JET and Tore Supra, and Mattioli et al. [143] proposed

$$\tau_{JET,TS}[ms] = 7.4V^{0.70\pm0.08}I_p^{0.31\pm0.09}\left(\frac{P}{n_e}\right)^{-0.57\pm0.03} \qquad (5.2)$$

with plasma volume V[m^3], plasma current I_p[MA], heating power P[MW] and line averaged density n_e[10^{19}m^{-3}]. The measured decay times varied between 0.25-1 times the measured energy confinement times τ_E. The influence of the plasma elongation κ and triangularity δ on the decay times was investigated in ohmic plasmas in TCV [144]. The increase of the elongation from 1.6 to 2.3 produced a threefold decrease of τ_d from three times the energy confinement time of the electrons τ_{Ee} to $\tau_d \approx \tau_{Ee}$. For the triangularity scan with -0.16< δ <0.6, the ratio τ_d/τ_{Ee} was almost unchanged.

For the H-mode, no attempts were made to obtain such scaling laws for the decay times. In type-I Elmy H-mode plasmas in ASDEX Upgrade, it was shown that the decay time is only determined by the edge transport through the H-mode barrier [77]. Thus, the decay time does not contain information about the transport coefficients in the plasma interior. The edge transport becomes even more dominant in the ELM free H-mode, where there is almost no loss of impurities through the edge barrier. For Ni injection into JET, a comparison of the decay times is shown in [145]: the typical decay times in L-mode were 150-200 ms, while the H-mode decay took several seconds. Also for L-mode discharges at JET and Tore Supra, indications for a weak edge transport barrier were found from the modelling of the evolution of the soft X-ray emission after LBO [146, 134] as well as from the simulation of the spectral emission characteristics of intrinsic C and Ni [147], and also the decay times in L-mode might have a strong influence by the edge transport.

Decay time studies for the light rare gases helium and neon, which completely recycle from the vessel walls, mainly give information about the transport to the pumped volume and to the pump duct. The decay times for recycling impurities can be interpreted with a simple two chamber model [27, 28]. It was discussed in section 2.4, how the global confinement time τ^*, the compression factor C and the enrichmant factor η are estimated from the decay time τ_d.

Studies of the global confinement of helium were performed most often, which reflects the importance of τ_{He}^* for the realisation of a burning fusion plasma (see section 1.2). An overview of helium exhaust experiments in tokamaks is given in [9]. In ASDEX Upgrade, helium in the divertor was pumped by turbomolecular pumps, while JET, DIII-D and JT-60U employed an argon frosting technique to adsorb helium on the divertor cryopumps. Effective helium exhaust has been demonstrated in H-mode plasmas with type-I ELMs in DIII-D [30] with $\eta_{He} \approx 1$, ASDEX Upgrade [148, 149] with η_{He} between 0.2 and 1, JT-60U [150, 151, 152] with $\eta_{He} \approx 1$, and JET [153, 154] with η_{He} in the range 0.2-0.5. These values are above the required value of 0.2, which sould be exceeded to obtain an acceptable D-T throughput in in a fusion reactor [32]. In internal transport barrier (ITB) discharges with helium beam injection, the global helium confinement time depended on the strength of the ITB. In JT-60U discharges with reversed shear and strong ITB, the injected helium fuelled inside the barrier, and helium accumulated inside the ITB, leading to ratios of $\tau_{He}^*/\tau_E \approx 15$ [151]. Weakening of the ITB reduced the scaled energy confinement time $\tau_E/\tau_{ITER-89P}$ from 2.4 to 1.2 and the scaled global residence time of He reduced to $\tau_{He}^*/\tau_E \approx 8$. At JET, helium beam injection into a reversed shear discharge with a weak ITB showed very good helium removal with helium enrichment factor in the range 0.4-0.6 [155]. Typically, the enrichment factors for argon and neon are well above unity [156, 30, 153].

5.2   Perturbative Transport Studies

Here, the main experimental findings from perturbative impurity transport studies in the plasma bulk of discharges in conventional modes, i. e. mainly H-mode and L-mode regimes, and for discharges with internal transport barriers are summarised. In many experiments, the evolution of the brightness from a few emission lines after impurity injection did not allow for the determination of the radial profiles of the transport coefficients. In these cases, transport simulations were performed with a radially constant diffusion coefficient eventually including drift velocities with a constant drift parameter $\alpha = v(r)a^2/(2D(r)r)$. Such investigations will not be considered. In this section, we rather concentrate on the determination of radially resolved transport coefficients, which were obtained from impurity profile measurement predominantly using charge exchange recombination spectroscopy (CXRS) or the soft X-ray diagnostic.

For the low-Z elements, CXRS is the most important experimental tool. Perturbative studies were performed with helium, nitrogen and neon. Short gas puffs were injected during the steady phase of the discharge and impurity fluxes were inferred from the measured density evolution for normalised radii below 0.8. The transport coefficients at a certain radial position are determined from the offset-linear dependence of the normalised impurity fluxes on the normalised density gradients assuming time independent transport

parameters (see 4.3.1).

Wade et al. [157] determined the transport coefficients of He in DIII-D H-mode plasmas with type-I ELMs at three different NBI heating powers P_{NBI}=4.5, 9.3, and 12 MW, and observed a rise of the diffusion coefficient with the heating power. For different confinement regimes, L-mode, ELM free H-mode, type-I ELMy H-mode and VH-mode, the diffusion coefficient of He was found to rise from centre to edge, and the ratio of the helium diffusion coefficient D_{He} and the effective heat diffusivity χ_{eff} was approximately equal to 1 for all cases. These observations were also consistent with measurements in TFTR [158], that indicated $D_{He}/\chi_{eff} \approx 1$ in both L-mode and supershot regimes. In dimensionally similar ELMing H-mode discharges at DIII-D with identical safety factor q, normalised pressure β, and ion collisionality ν_i^*, the normalised ion gyro-radius ρ_i^* was varied by a factor of $\approx$1.6. The diffusion coefficient of He was determined for $r/a < 0.5$. The variation of D_{He} and χ_{eff} indicated a gyro-Bohm-like scaling $D_{He} \propto B^{-1}$ [159].

Comparison of He and Ne in DIII-D L-mode plasmas showed equal transport coefficients for both impurities, however, in VH-mode only the much lower diffusion coefficients were similar, while the drift velocities were remarkably different [160]. In a more elaborate work, these differences in VH-mode were studied in greater detail for helium, nitrogen and neon [161]. It was found, that for the central part of VH-mode plasmas with normalised radii $\leq$ 0.4, the experimental drift velocities are in agreement with neoclassical values, which were calculated with the NCLASS code [37]. The neoclassical drift velocities increase with the impurity charge and for the special case of the VH-mode plasmas, which have a flat main ion profile and strong central ion temperature gradient, the temperature screening term becomes dominant, such that the drift velocities were outwardly directed for all three species. The collisionality of the three elements were in the "banana" regime. The experimentally determined diffusion coefficient of He, N, and Ne were very similar within the data scatter and about a factor of 3 above the neoclassical values, which were also very similar for the investigated elements.

In ASDEX Upgrade, transport coefficients of Ne and He were determined in NBI-heated H-, CDH- and L-mode discharges [162, 163]. Fig.5.1 shows the range of transport coefficients found with this method for all investigated discharges. It includes H-, CDH- and L-mode plasmas with toroidal field 1.9< B_T[T] <2.7, total heating powers 2.0< P_{tot}[MW] <9.1, line averaged densities 4.5< $\bar{n}_e$[10^{19}m^{-3}] <12, effective mass of the main ion 1.2< m_{eff}[amu] <1.9 and fixed plasma current I_p=1 MA. The diffusion coefficient rises towards the plasma edge where it is more than an order of magnitude above the neoclassical diffusion coefficient, i. e. mainly determined by anomalous transport. D has a similar profile shape and magnitude as the effective heat diffusivity χ_{eff} and displays the same degradation with heating power as χ_{eff}: $D \propto \sqrt{P}$. Also the dependence on the isotope mass of the background plasma $D \propto m_{eff}^{-0.666\pm0.047}$ is as expected from the isotope dependence of τ_E-scalings. There is thus a strong link between the anomalous impurity
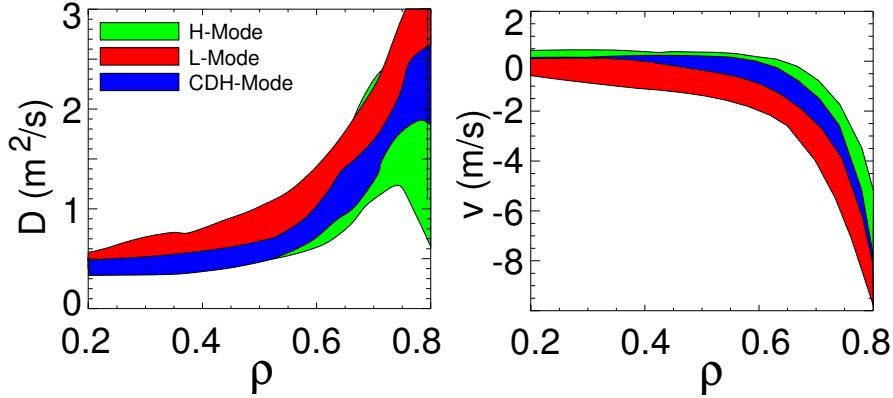
Figure 5.1: Transport coefficients for Ne and He found in ASDEX Upgrade H-, CDH-, and L-mode discharges versus the poloidal flux label ρ. The differently coloured areas show the range of coefficients which were measured in the different confinement regimes.

transport coefficients and the heat diffusion coefficient, which has also been observed for the transport of the main ion species [164, 165, 166]. The diffusion coefficient of He and Ne is independent of the injected species within the uncertainties of the measurement. At ρ=0.8, inward drift velocities approximately proportional to D with $v/D \approx$-3.5 m^{-1} are observed. The magnitude of v/D decreases with decreasing radius. In the centre at ρ=0.2 the diffusion coefficient is quite low, i. e. in the range of 0.3-0.6 m^2/s, where these values are effective diffusion coefficients including the transport due to sawtooth crashes. In CDH-discharges [167, 168] without sawteeth, even lower central values $D \approx 0.1 \text{m}^2/\text{s}$ were measured and accumulation of Ne was observed inside of $\rho \approx 0.5$ (see below).

Since the investigations of Seguin et al. at Alcator-C [73], it is known that sawtooth collapses effectively flatten the impurity density inside a certain mixing radius r_{mix} being approximately $\sqrt{2} r_{q=1}$, where $r_{q=1}$ is the radius of the flux surface with safety factor $q = 1$. The analysis of the CXRS measurements in sawtoothing L-mode and H-mode plasmas averaged over the sawteeth, and the evaluated central diffusion coefficient is thus above the diffusion coefficient between the collapses. In order to separate the sawteeth effect from the transport in the time intervals between sawtooth crashes, measurements with soft X-ray cameras were used due to their excellent time resolution. The detection of injected impurities from the change of soft X-ray radiation was mostly used for medium-Z impurities from Al up to Ni, however, there were also experiments with Ne, Kr, and Xe. Lighter elements than Ne do not emit sufficiently energetic line radiation to pass the conventionally used Be-filters.

In JET L-mode discharges, the transport in the quiet phase between the sawtooth crashes was investigated by analysing soft X-ray data after LBO of metallic impurities (Fe, Ni, and Ag) [135]. The investigated discharges explored a wide range of parameters I_p=2-7 MA, B_T=1.45-3.4 T, $\langle n_e \rangle$=1-5 $\times 10^{19}$ m^{-3} and heating powers up to 20 MW. Most
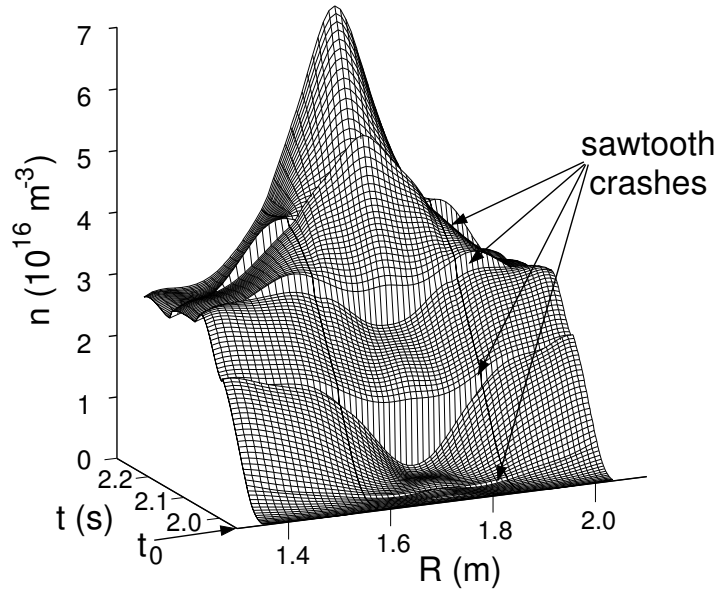
Figure 5.2: At time t_0 argon was injected into a steady state phase of an H-mode discharge in ASDEX Upgrade. The density evolution of argon is shown versus the major radius R in the mid plane. The magnetic axis is at $R_0 = 1.72$m.

discharges were run in ^{4}He and some in D_2 with Z_{eff}=3-4 for both working gases. No dependences of the transport parameters on impurity species and working gas was found being not in contradiction to the Alcator-C scaling ($\tau_{Alcator-C} \propto Z_{eff}m_M/Z_M$) since Z_{eff} did not significantly vary between the two working gases. The data were modelled by a radial impurity transport code using a smoothed step function for the diffusion coefficient with $D(r) = D_{out}$ in the edge region, $D(r) = D_{in}$ in the centre, with D_{out} being much larger than D_{in} and an approximately constant drift parameter $\alpha = v(r)a^2/(2D(r)r) \approx 1$. D_{out} could be determined with a typical uncertainty of $\pm 30\%$ and D_{in} with $\pm 70\%$. The transition radius from high to low diffusion coefficient varied between 0.6 and 1.45 m depending upon the values of I_p and B_T and was identified to be associated with shear s =0.5$\pm$0.15. D_{in} was never substantially lower than 0.1 m^2/s or higher than 0.3 m^2/s, and a *moderate* anomalous contribution to D_{in} was concluded from comparisons with estimates of the neoclassical diffusion coefficient D_{neo}. D_{out} showed a marked increase with increasing values of $P_{heat}/\langle n_e \rangle$, and T_e, but no clear dependence on n_e could be detected, when the T_e profile was kept constant.

At ASDEX Upgrade, a set of experiments [76] was performed, where the transport of low to high Z-impurities (neon, argon, krypton and xenon) was investigated in the centre($\rho \leq 0.4$) of H-mode discharges with 5 MW heating power from the 60 kV NI beams and line averaged density $\bar{n}_e$= 7.5 $\times$ 10^{19} m^{-3}. In Fig.5.2 an example of Ar injection is shown. Ar is puffed for 1s and the density evolution after the start of the puff at t_0 =1.95s is shown versus the major radius at the mid plane for $\rho \leq$0.7. The magnetic
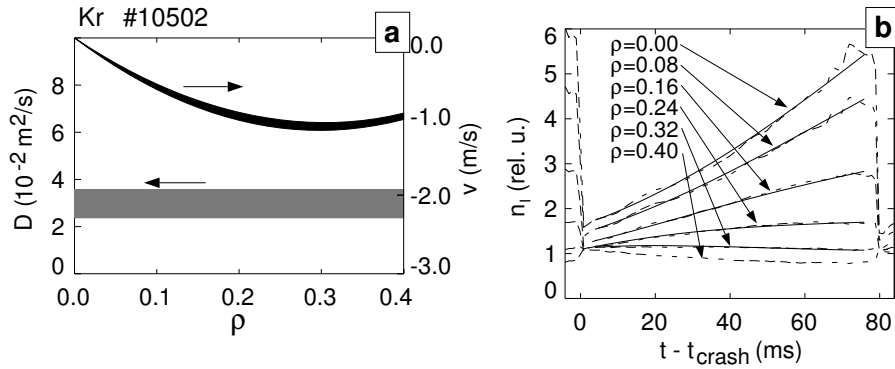
Figure 5.3: Kr density evolution for several poloidal flux labels ρ (Fig.5.3b, dashed lines) and the solution of the transport equation (Fig.5.3b , solid lines) with D and v from Fig.5.3a.

axis is at $R_0 = 1.72\,\text{m}$. At $t = 2.05\,\text{s}$, the argon density in the major part of the plasma is already considerably increased but very little argon has reached the centre. Steep radial gradients build up indicating, that the diffusion coefficient must be very small. This situation persists until the first sawtooth crash occurs. The crash leads to a flattening of the impurity density, i. e. a strong increase of the central transport. After about four crashes a quasi stationary situation is reached. The impurity density develops a pronounced peaking in the quiescent phase of the sawtooth, which is flattened by every crash. Due to the slow evolution in the centre, this feature can not be seen in the first cycles and the central transport parameters were evaluated by analysing the temporal evolution of the impurity density profile between sawtooth crashes in the stationary phase of the gas puff.

Diffusion coefficients and drift velocities were evaluated by analysing the temporal evolution of the density profile between sawtooth crashes, where each crash caused a fast perturbation, i. e. a complete flattening of the impurity profile. The radial transport equation was solved for a time interval from $3\,\text{ms}$ after the last sawtooth crash to $3\,\text{ms}$ before the next crash in the radial range $\rho < 0.4$, where the initial distribution at $t_{crash} + 3\text{ms}$ and the density development at $\rho = 0.4$ were chosen as the boundary conditions for the solution. A constant value was used for D and a linear function for the drift parameter $\alpha = va^2/(2Dr) = \alpha_0 + \alpha_1 r$. The three coefficients D, α_0 and α_1 of these test functions were computed by applying a non-linear χ^2–fit to the measured density development for $\rho < 0.4$. An example of the fitting procedure is shown in Fig.5.3. One sawtooth period for Kr is depicted. Note, that the sawtooth period is too short to reach an equilibrium distribution of the impurity density and that the sawtooth crash leads to a flattening of the Kr density profile. Even in the short phase in between sawteeth, the central Kr density rises by a factor of 3, demonstrating the necessity of sawteeth for a tolerable central impurity content. Assuming a standard deviation of 20% for the impurity den-
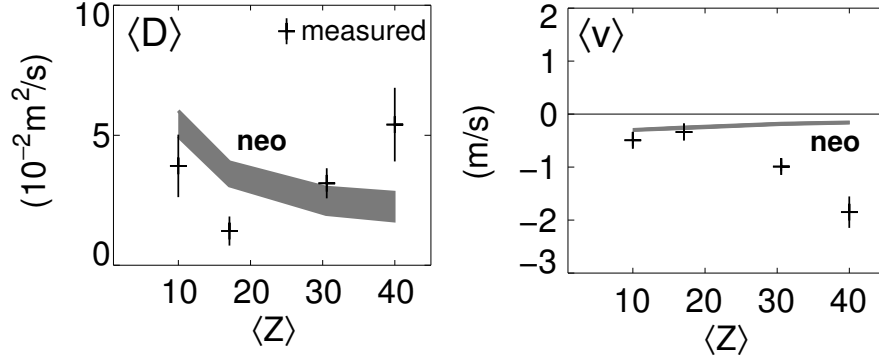
Figure 5.4: Line averaged values over the radial range $0.1 < \rho < 0.3$ of measured and neo-classical diffusion coefficient D and drift velocity v as a function of the mean atomic charge of the impurity $\langle Z \rangle$ in that radial range. The neoclassical values are shown as bands representing the cases without and with collisions with C/O.

sity the standard deviation of D and v was calculated from the curvature of χ^2 in the fit parameter space and is shown as bands in Fig. 5.3.

Fig.5.4 depicts the line averaged diffusion coefficient $\langle D \rangle$ and drift velocity $\langle v \rangle$ for the radial range $0.1 < \rho < 0.3$ obtained from typically 10 sawtooth cycles versus the line averaged impurity charge $\langle Z \rangle$ in the same radial range. With rising impurity charge Z, the convective transport increasingly dominates over the diffusive transport, which is very small with $\langle D \rangle \leq 6 \times 10^{-2} \mathrm{m}^2/\mathrm{s}$. The drift velocity is always inwardly directed. For Kr and Xe the ratio $\langle v/D \rangle$ reaches enormous values of $\langle v/D \rangle \approx -35 \mathrm{m}^{-1}$.

Neoclassical transport parameters were calculated with a combination of STRAHL and NEOART [76, 8, 39]. The neoclassical values are shown in Fig. 5.4 as bands representing the three cases with and without inclusion of collisions with C/O for a flat and a peaked concentration profile with $c_C \approx 1\%$ and $c_O \approx 0.1\%$. The total neoclassical diffusion coefficient is dominated by the banana-plateau values for low Z and by the sum of the classical and the Pfirsch-Schlüter contributions for high Z. The diffusion coefficient D_{neo} decreases with rising Z and is in the same range as the measurements. Anomalous diffusion is obviously ineffective in the plasma centre. The drift velocity v_{neo} is dominated by the banana-plateau value for all Z and is more or less constant. For low to medium Z the measurement is well reflected by v_{neo}, for high Z the deviation is strong. The neoclassical calculations assume constant impurity density on a flux surface. Due to the centrifugal force toroidal rotation causes a poloidal gradient of the impurity density on the flux surface with the maximum density appearing on the outboard side of the tokamak [130]. The observed poloidal variation of the impurity density is small for the lighter elements Ne and Ar. However, for the heavier elements Kr and Xe with higher toroidal Mach numbers around 2, poloidal asymmetries are important. For Kr, the asymmetry is clearly observable and the density on the outboard side exceeds the inboard value by up
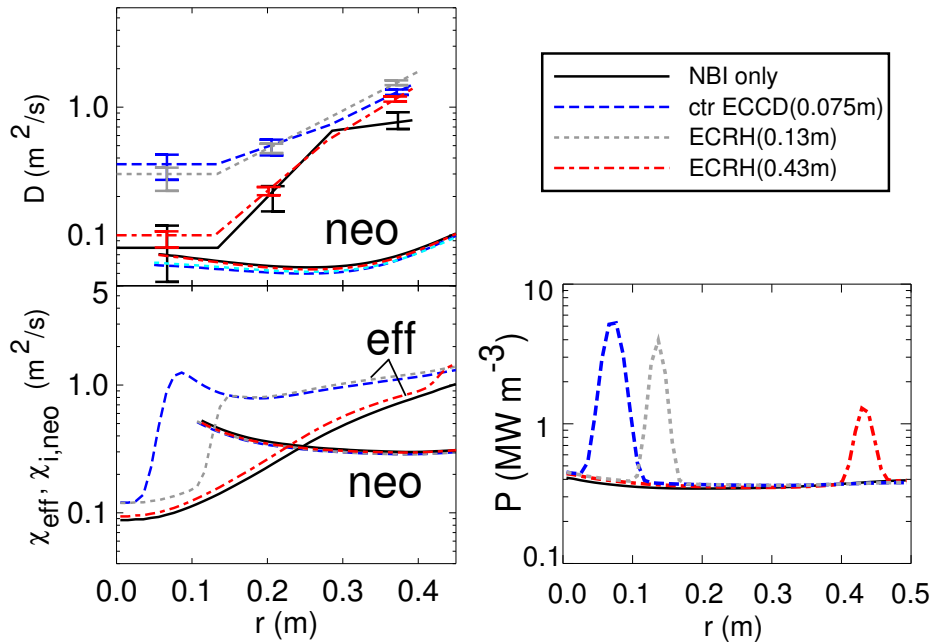
Figure 5.5:   *Measured and neoclassical diffusion coefficent of Si, measured effective and neoclassical ion heat diffusivity, for a series of H-mode discharges at ASDEX Upgrade with NBI heating (P_{NBI}=5 MW) and additional ECR heating at different radial positions r=0.075 m, 0.13 m, and 0.43 m (P_{ECRH}=0.8 MW). The various power deposition profiles are shown in the right graph.*

to 50%. This effect is not taken into account by the neoclassical calculations and might account for the discrepancy of the pinch velocity.

Ida et al. [75] was the first to determine the transport coefficients from the time-varying impurity distributions after sawtooth crashes. In PBX H-mode discharges, he also found a strong Z-dependence of the central impurity drift velocity. In this case, the temporal evolution of Z_{eff} during the buildup phase of sawteeth (dominated by low Z elements C and O) and of the total radiated emissivity (dominated by medium Z elements Fe and Ni) could best be described when using $D = 0.1\,\mathrm{m^2/s}$ for both types of species and a Z-dependent drift parameter α with $\alpha(Z \approx 20)/\alpha(Z \approx 8) = 5$.

In another study at ASDEX Upgrade, the influence of the heating profile on the transport coefficients of silicon in type-I ELMy H-mode discharges was investigated [169]. The total heating power was in the range from 4.2-5.8 MW, and variations of the heating profile were achieved by using NBI heated discharges at high and low density, by additional heating with ECRH in the centre or at the edge, and by using pure ICRH with central or periferal power deposition. It was found that the central transport of Si was neoclassical for low central power deposition and became anomalous, when the heating power in the centre was high. Further out, Si diffusion is always strongly anomalous.

An example is shown in Fig.5.5. The experimentally determined diffusion coefficent

of Si is compared with the neoclassical values calculated with NEOART for four heat deposition profiles shown in the right graph. All discharges had 5 MW of NBI heating and in three discharges 0.8 MW ECRH were added using different deposition radii $r=0.075$ m, 0.13 m, and 0.43 m. For the pure NBI case and for off-axis ECRH, D can be explained by neoclassical transport inside of $r\approx0.15$ m. There is a drastic change of the transport parameters for the cases with central ECR heating. χ_{eff} rises by up to a factor of 10 for radii greater or equal to the deposition zone, while the local change of χ_{eff} is small at the edge due to the small change of total heating power by ECRH. In the core, also the measured diffusion coefficient of Si increases with additional central ECRH by a factor of 3 to 4.5 to values around $D=0.3\,\mathrm{m^2/s}$, while in the radial range around $r=0.4$ m, there is only a minor change between the different heating scenarios. Thus, it is obvious, that the addition of central ECRH leads to an increase of the turbulent diffusion coefficient of Si in the plasma core, which is a factor ≥3 above the neoclassical level. The differences of ECR heating at $r=0.13$ m and at $r=0.075$ m can not be resolved with the restriction on the number of nodes for the fitting function of D. Similar results were obtained with ICRH. For a discharge with central ICRH deposition, D was above the neoclassical level by a factor of 2, and the turbulent contribution vanished for off-axis ICRH heating.

Perturbative transport studies in plasmas with strong internal transport barriers (ITB) are more complicated than in conventional scenarios. Up to now, plasmas with a strong ITB do not have long steady phases with constant plasma parameters. The evolving electron density, electron temperature, and impurity concentration make it especially difficult to detect the injected impurity by the change of the soft X-ray emission. CXRS measurements are less affected even though a constant plasma background, where signal changes are only due to the density evolution of the puffed impurity, is advantageous. The assumption, that the transport parameters do not change during the analysed time interval, is probably not severely violated as long as the barrier is not too short living.

Efthimion et al. [170] studied helium and tritium transport in TFTR plasmas with extended reversed shear and internal transport barrier (ERS regime). He was detected with CXRS and T from the collimated neutron detector array via the 14 MeV neutrons from the DT fusion reaction. The q-profile had a minimum at $r/a \approx 0.4$ with $q_{min} \approx 2.2$ and q_0 on axis was in the range 4-5. The electron density inside of $r/a \approx 0.4$ was strongly peaking and analysis of the electron balance indicated, that nearly all of the neutral beam electron fuelling rate within the reversed shear region accounted in the density rise, $\partial n_e/\partial t$, i. e. little particle flux was leaving the reversed shear region. The analysis of the helium and tritium puff experiments also showed, that the respective diffusion coefficients within the reversed shear region is by a factor of ≈ 10 lower than outside of $r/a \approx 0.4$ and that this low diffusion coefficient can be explained by neoclassical transport according to calculations with the NCLASS code. Both diffusion coefficients were approximately equal and equal to the effective thermal diffusion coefficient $D_{He} \approx D_T \approx \chi_{eff}$.

Helium transport in reversed shear plasmas with ITB were investigated in JT-60U by Takenaga et al. [55]. Here, the ITB has a rather different appearance, since the suppression of the anomalous transport is localised in a narrow radial region just inside the radius with minimum q. Modulated He puffs were used and the transport parameters were determined from the radial profiles of the amplitudes and phases using Eq.(4.16). The reversed shear region is wider in the JT-60U plasma with q_{min} slightly above 2 at $r/a \approx 0.55$ and q_0 is between 5 and 6. There is a strong gradient in T_i in the range r/a =0.45-0.55 and in n_e in the range r/a=0.4-0.5. Inside of the electron barrier n_e is very flat, and the the ion temperature gradient is low again. The measured diffusion coefficient of helium was $0.2\,\mathrm{m}^2/\mathrm{s}$ in the barrier and $\approx 1\,\mathrm{m}^2/\mathrm{s}$ inside and outside of the ITB.

For JET ITB discharges with flat monotonic shear profile, transport of LBO injected Ni was determined by the change of the soft X-ray emission and by measurement of Ni line emission by Chen et al. [141]. A low diffusion coefficient of D =0.05 m^2/s was found inside the ITB, i. e. for r/a <0.4, in accordance with neoclassical values of 0.03-0.06 m^2/s. The diffusion coefficient outside the ITB was about an order of magnitude larger at a value of D =0.6 m^2/s. Line radiation from Be-like Ni, which is emitted outside the ITB, had a fast rise and decay after the LBO, while lines from inside the ITB, emitted by the Li-like and He-like stage, did not decay after the initial rise during the remaining discharge time of $\approx 0.8\,\mathrm{s}$.

The perturbative studies, which have been discussed, indicate the following conclusion on the contribution of anomalous and neoclassical transport. In the outer part of the plasma bulk, impurity transport is always anomalous with similar values for the diffusion coefficients D and the effective heat diffusion coefficient χ_{eff}. The anomalous D has no strong dependence on impurity charge or mass. For conventional confinement modes, the turbulent transport in the plasma core is low for cases, where the central heating is low, while central wave heating increases again the anomalous diffusion coefficient. For advanced confinement modes with reversed or flat shear inside a certain radius, the anomalous diffusion coefficient can be strongly reduced even for high central heating powers. The suppression of turbulent diffusion is either inside a narrow region inside the radius with minimum q or in the whole radial range inside that radius.

5.3   Central Accumulation

The term impurity accumulation describes the situation, where the impurity density gradient is much stronger peaked than the main ion density gradient, i. e. $(1/n_{imp})dn_{imp}/dr \gg (1/n_m)dn_m/dr$. Central impurity accumulation has been observed since the first tokamak plasmas [171, 172, 173].

In the previous section, it was found that impurity transport in the plasma centre can be predominantly neoclassical and it is the low anomalous transport, which causes concern about the danger of impurity accumulation, because the peaking due to neoclassical drifts is not suppressed by large anomalous diffusion coefficients (see Eq.(3.45)). Since v_{neo}/D_{neo} is approximately proportional with the impurity charge Z, high-Z elements have a stronger tendency to accumulate [174]. The direction of the neoclassical drifts are determined by the ratio of the normalised main ion density gradient to the normalised main ion temperature gradient, where the former causes an inward pinch and the latter an outward pinch (temperature screening). A peaking of the main ion density is thus a necessary pre-requiste for neoclassical impurity accumulation, and all experimental observations of impurity accumulation coincide with the appearance of peaked main ion density profiles. The peakedness of the main ion density can either be caused by an inward pinch or by the fuelling from NBI heating beam or pellets in combination with a low main ion diffusion coefficient. Due to the stiffness of the ion temperature profile in conventional confinement modes, $d(\ln T_i)/dr$ and the according temperature screening usually does not become large enough to balance the inward pinch due to the main ion gradient. An outwardly directed neoclassical impurity pinch in the plasma core was only found in one case: in VH-mode plasmas at DIII-D [161].

The importance of the main ion density profile for the accumulation of impurities can be seen from observations at various tokamaks, where a strong main ion density peaking was invoked by injection of hydrogenic pellets. For ohmic Alcator-C plasmas, peaked profiles of carbon and molybdenum evolved after the pellet injection [175]. Strong peaking of carbon and oxygen was also measured in ohmic plasmas at TEXT with pellet injection [176]. In H-mode plasmas at JET with pellet enhanced perfomance (PEP-mode), accumulation of carbon was found with CXR spectroscopy [177].

For H-mode discharges at ASDEX Upgrade, the characteristics of the total radiation profile in the main plasma was collected for a number of discharges [178]. During the experimental campaign, where these discharges were performed, almost all tiles of the central column were covered with tungsten [178], which due to its high Z is very critical with respect to neoclassical transport. Fig.5.6[a,b] shows the rather wide range of central densities and temperatures included in the data base. In Fig.5.6[c], the radiation fluxes of bolometer channel 24 are drawn versus the according signals of bolometer channel 27, whose lines-of-sight are tangent to the flux surfaces with poloidal flux label ρ= 0.4 and 0.7. Fig.5.6[d] depicts the behaviour of channel 21 versus 24, where the former has a line-of-sight through the plasma axis. Open symbols are used for discharges without central wave heating by ECR or ICR, and circles represent plasmas without sawteeth. The two more peripheral channels show a simple proportionality between each other for all cases. The data points for the central channel 21 versus channel 24 have a branch, where both brightnesses are propotional to each other, and a branch where the central
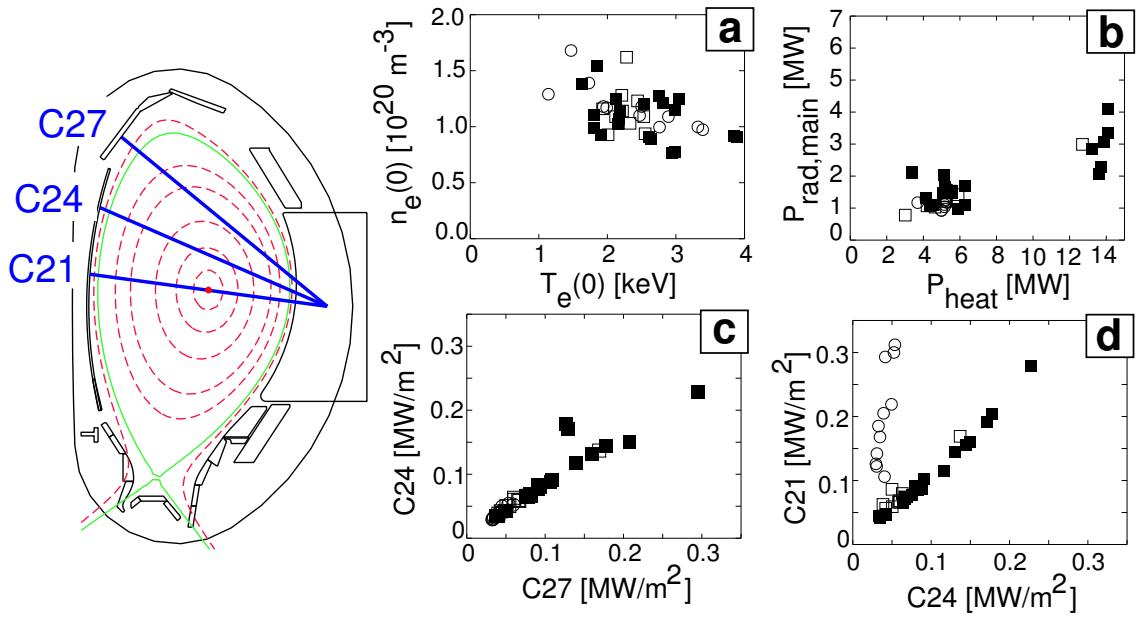
Figure 5.6:   Characteristics of the total radiation profiles in the main plasma for different H-mode discharges at ASDEX Upgrade: (a) shows the range of central electron densities versus central electron temperatures, (b) gives the total main plasma radiation versus the total heating power, (c) and (d) depict the relation of the brightnesses of two bolometer lines-of-sight as indicated in the left drawing. Open symbols represent discharges without central wave heating and circles are used for plasmas without sawteeth. Note the occurence of strong central radiation for plasmas without sawteeth and without central wave heating.

channel can have much larger brightness than the channel tangent to $\rho \approx 0.4$. These large differences can only be explained by strong central radiation of medium-Z to high-Z elements, like Fe, Cu or W, which must have a large density gradient inside of $\rho \approx 0.4$. This central accumulation appears only for discharges without central wave heating and without sawteeth. Outside of $\rho \approx 0.4$, strong gradients of the total radiation are not observed, indicating that anomalously dominated impurity transport does not lead to strong impurity gradients or large inward pinches for these impurities.

In all ASDEX Upgrade discharge scenarios, where impurity accumulation was observed, low central heating was used, peaked electron densities were present and sawteeth were eventually lost as will be demonstrated in the following examples. A discharge scenario with peaked electron density at high line averaged density $\bar{n}_e \approx 1.2 \times 10^{20}\,\mathrm{m}^{-3}$ is the CDH-mode [167, 168]. Here, accumulation of the injected radiating impurity neon could only be avoided if the sawtooth activity was maintained. The accumulation of neon in CDH-mode discharges could be simulated with $D = D_{neo}$ and $v = 1.5 \times v_{neo}$ in the central region of the plasma [179]. In high density H-modes with pure NBI-heating at $\bar{n}_e \approx 1.4 \times 10^{20}\,\mathrm{m}^{-3}$ and triangularity $\delta = 0.3$ [164], a similar signature was observed.

Constant gas puffing caused a constant edge density and a steadily increasing central electron density. Eventually, the sawtooth activity stopped and impurities accumulated in the centre as inferred from the evolution of soft X-ray and bolometric profiles. Additional central heating with ICRH or partial replacement of NBI-heating by central ICRH prevented from electron density peaking and no impurity accumulation was observed. Due to the stiff T-profiles central heating increases the central heat conductivity χ and most likely the anomalous D. The effect of central heating on the impurities is thus twofold by reducing the neoclassical inward drifts proportional to the density gradient and by increasing the anomalous diffusion. This behaviour could also be observed in off axis NBI-heated H-mode discharges at lower line averaged densities $\bar{n}_e \approx 8 \times 10^{19} \, \mathrm{m}^{-3}$. When the NBI energy was reduced from 60 keV to 35-40 keV, a peaked electron density profile was observed accompanied by an eventual loss of sawteeth leading to high central tungsten concentrations of $\approx 4 \times 10^{-5}$ [180, 181, 178]. The evolving electron density peaking and tungsten accumulation can be stopped by addition or partial replacement of NBI with central ECRH heating. After switching off ECRH n_e peaking and tungsten concentration rise again [181].

A reduction of central tungsten confinement by application of central ECRH could also be demonstrated in improved H-mode discharges at average triangularity of δ=0.35 [178, 78]. Improved H-mode plasmas are characterised by a loss of the sawtooth activity and generally improved confinement over ordinary H-modes. They can be performed in quasi steady state [182] and the operational space has recently been enlarged towards higher densities by increasing the triangularity of the plasma shape to δ=0.35 [183]. As in ordinary H-mode discharges at $\delta \approx 0.35$ without central heating, the density was observed to peak slowly throughout the discharge and a very strong peaking of the radiation power inside a poloidal flux label of $\rho \approx 0.3$ occurred, which can only be explained by accumulation of tungsten and other metallic impurities.

The effect of central ECRH on the impurity behaviour is demonstrated in Fig.5.7. Various time traces of the improved H-mode discharge #15524 with I_p=1 MA, B_T=2.5 T, δ=0.35 and constant NBI heating power P_{NI}=5 MW are shown. Central ECRH is applied from t=2.5-4.5 s with P_{ECRH}=1.2 MW from 2.5 to 3 s and P_{ECRH}=0.8 MW from 3 to 4.5 s. During the ECRH phase, the thermal confinement time τ_E is reduced by $\approx 17\%$ with respect to the pure NBI phase, while the scaled thermal confinement is only slightly reduced with $\tau_E / \tau_{ITERH-98p(y,th,2)} \approx 1.2$. The frequency of the type-I ELM's changes from f_{ELM}=50 HZ to f_{ELM}=70 Hz. n_e, T_e and T_i is depicted for ρ=0 and ρ=0.5. Only the central values are influenced with an increase of central T_e and a decrease of central n_e. A much stronger effect is found on the tungsten concentrations c_w, which are derived from spectroscopic measurements. c_w at ρ=0.75 is deduced from the W-quasi-continuum, which is emitted from ions around W^{28+} [102] and c_w at ρ=0.1 from a Ni-like (W^{46+}) line at λ=0.793 nm [103]. Accumulation of tungsten is suppressed by ECRH, i.e. the central
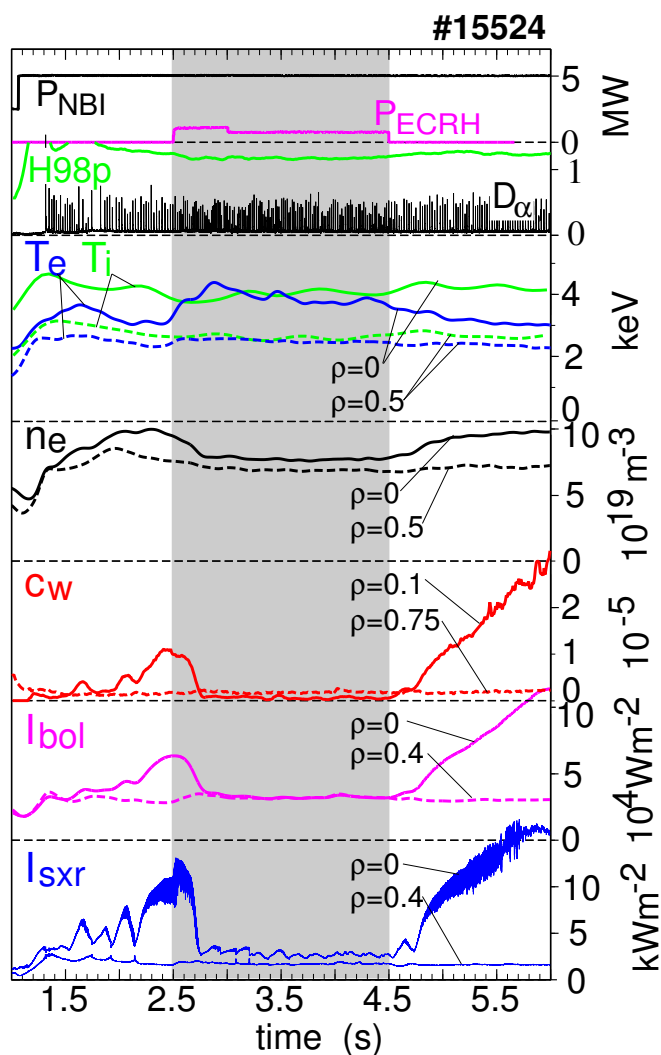
Figure 5.7: Time traces for the improved H-mode discharge #15524 at ASDEX Upgrade.

W-concentration is reduced to the constant edge value of $c_W \approx 10^{-6}$. After the ECRH phase, c_W at $\rho=0.1$ is steadily increasing and reaches $\approx 3 \times 10^{-5}$ at t=6 s, which is 30 times the edge value. Total and soft X-ray radiation also evolve a strong peaking in the phases without ECRH. The total central emission is approximately a factor of 4 above the value calculated for pure tungsten accumulation and a strong rise of central Fe lines were also found. The soft X-ray data show m=1-mode activity without sawteeth, when ECRH is off. In the ECRH phase there are three minor sawtooth crashes at t=2.95, 3.1 and 3.2 s, after the accumulation has disappeared.

Fig. 5.8 shows the result of impurity transport simulations for the above discharge #15524. Dashed lines give radial profiles for a time slice during the ECRH phase (t=3.5–4.5 s) and solid lines are used for t=5.8–6.0 s, which is at the end of the second pure NBI-heating phase. Neoclassical impurity transport coefficients were calculated numerically
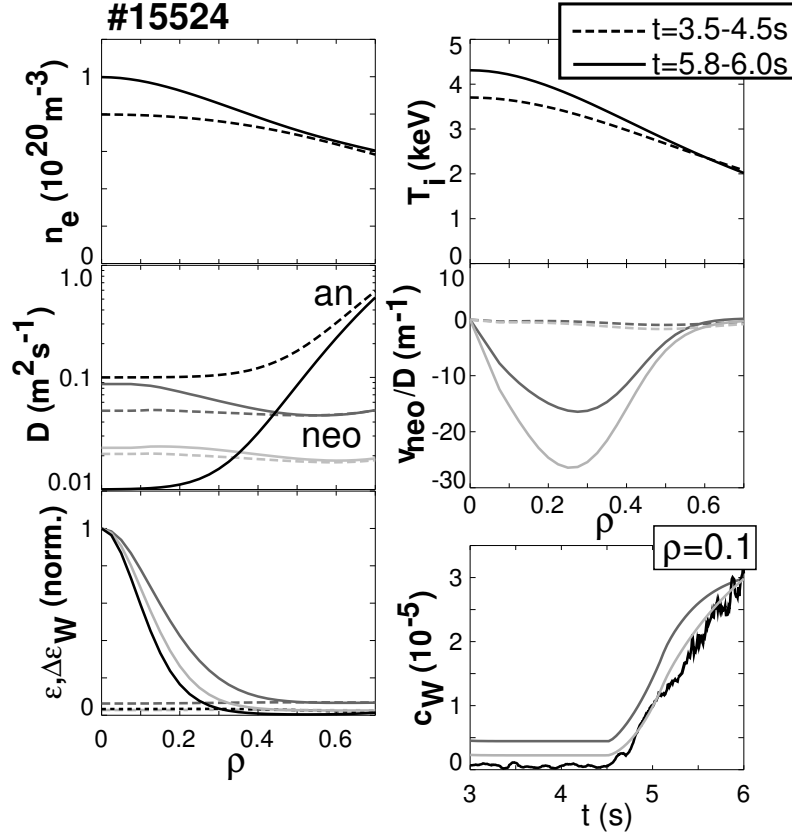
Figure 5.8: Measured profiles of n_e, T_i, neoclassical transport coefficients of tungsten with (dark grey) and without (light grey) inclusion of additional impurities, used D_{an}, calculated tungsten radiation and measured total radiation for two time slices of the ASDEX Upgrade discharge #15524. In the lower right corner, a time traces of measured and simulated central tungsten concentration are shown.

with NEOART [39, 8, 33], which can include the effect of impurity-impurity collisions for an arbitrary number of species. The transport simulation starts at t=1.5 s with flat impurity concentrations and the impurity densities at the edge are kept constant during the simulation. In one case (light grey) only W was taken into account, while in the second case (dark grey) additional impurities were considered with 'typical' concentrations of 5% He, 1% C, 0.5% O, 0.02% Fe at the edge. n_e, T_e and T_i profiles were taken from measurements and n_i followed from the impurity ion distributions and quasi-neutrality. C, O, Fe and W are in the plateau regime with W at the Pfirsch-Schlüter limit, while D and He are in the banana regime. The anomalous diffusion coefficient was assumed to be equal for all impurity species and to decay from edge to centre, where the central value was chosen to be $D_{an}(0)$=0.1 m^2/s during ECRH and below neoclassical values during pure NBI heating. These choices are based on the results from perturbative impurity transport studies with and without central ECRH as discussed in the previous section

5.2. The increased central diffusion coefficient with the additional central power flux from ECRH is interpreted to be a consequence of profile stiffness [164]. Analysis of the local heat diffusivities with ASTRA [184] yields an increase of central χ_i and χ_e. For ρ=0.3 both values change from $\approx$0.2m^2/s with ECRH off to $\approx$0.7m^2/s with ECRH on. The calculated values of v/D are small in the ECRH phase, mainly due to the rather flat density profile and partly due to the increased D_{an}. In the pure NBI-phase, the density peaking increases, while D_{an} becomes small and v/D reaches large negative (inward pinch) values inside ρ=0.5. In the case with inclusion of all impurities, the inward pinch is smaller and the v/D-profile is broader. The simulated W profile evolves the strongest peaking of all impurities as expected from Eq.(3.45). The calculated peaking of W is smaller than experimentally observed. This can be seen by comparing the calculated tungsten radiation profiles with the unfolded total radiation, which shows an even stronger peaking, even though there have to be large contributions from less peaked medium-Z metals to the total radiation. Similarly, the high central tungsten concentrations at the end of the discharge can only be simulated when setting the edge concentrations to 2-5 times the measured values depending on the inclusion of other impurities in the simulation. Perfect agreement can be achieved with a v/D profile that reaches a minimum value of -50 m^{-1}. Thus, the main features of the impurity flattening with ECRH and the strong peaking without ECRH are well described by the simulation and calculated v/D values agree with the measurement within a factor of 2. It should be mentioned, that also the evolution of the main ion density can be understood by a higher anomalous diffusion being connected to higher χ in the ECRH phase. The increase of D_{an} counteracts the neoclassical inward drift due to the Ware pinch [164, 165]. Tungsten has a much higher collisionality and the Ware pinch, which is included in the simulations was found to yield a negligible contribution to the drift of W. For t=5.8–6 s, the T_i gradient is increased and the related outwardly directed drift velocity is $\approx$50% above the value during the ECRH phase. Thus, the central radiation is still not large enough to change the temperature screening and to trigger the instability described in [185].

Experiments with a tungsten test limiter in TEXTOR 94 by van Oost et el. [186] showed a central accumulation of tungsten for ohmically heated discharges, which had a density above a critical value of n_{cr} =2.5×10^{19}m^{-3}. In such discharges, additional central heating by ICRF reduced the central tungsten concentration by more than an order of magnitude. In Alcator C-Mod discharges, a strong density peaking and impurity accumulation inside of r/a $\approx$0.5 was found for discharges with off-axis ICR heating [187]. The impurity accumulation was deduced from the strongly peaked total radiation profiles and the Ar^{16+} line emission profiles. When a minor amount of central ICR heating was added to the predominant off-axis ICR heating, a further rise of central density and impurity peaking could be arrested. Following the results at ASDEX Upgrade, avoidance of impurity accumulation by central ECR heating has also been successfully demonstrated
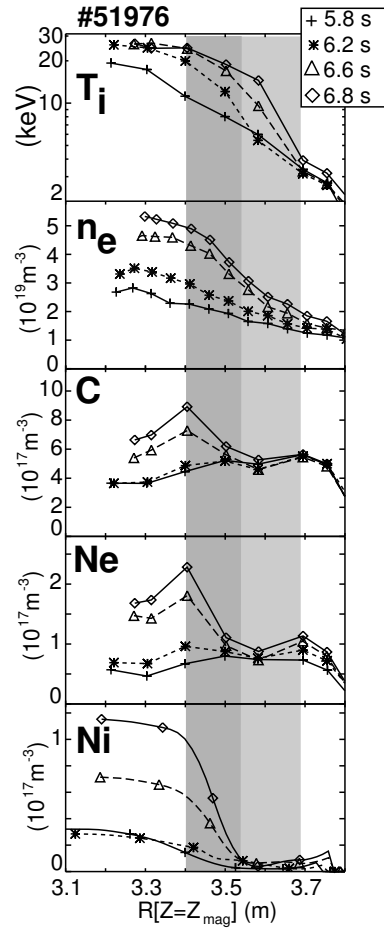
Figure 5.9: *Evolution of the radial profiles of T_i, n_e, n_C, n_{Ne} and n_{Ni} for the JET discharge #51976 with strongly reversed shear ('current hole' discharge) and internal transport barrier. The radial co-ordinate is the major radius R at the height of the magnetic axis $Z=Z_{mag}$.*

in quiescent double barrier discharges at DIII-D for the case of nickel [188] and in high β_p discharges at JT-60U [189].

Low anomalous impurity transport was also measured in discharges with strong internal transport barrier and peaking of impurities is observed in ITB plasmas, where the degree of the peaking depends strongly on the impurity charge. Takenaga et al. [189] compared the profile evolution of helium, carbon, and argon in JT-60U discharges, which had strongly reversed magnetic shear with a central current hole and an ITB at $r/a \approx 0.6$. The temperatures and densities of all species have a box like profile in such plasmas with a strong negative gradient in the barrier region and a flat part part in the radial range of the current hole for $r/a < 0.4$. Helium peaked less than the electron density, carbon had a profile shape similar to n_e and argon peaking was a factor of 2.6 stronger than that of n_e. Helium was introduced by gas valves and by helium beams and the peaking

of helium was increased but still below the n_e value when using beam injection. For quiescent double barrier (QDB) discharges at DIII-D, West et al. [65] observed a strong accumulation of nickel and copper and a weak accumulation of carbon. The profile of the safety factor in such discharges was only mildly reversed with q always above 1. The profiles were not as box like as in JT-60U, and the ion temperature rises strongly between normalised radii of 0.6 and 0.2, while the electron density peaks from $r/a \approx 0.5$ inwards. The Z_{eff} profile peaked inside of $r/a \approx 0.5$ mainly due to Ni and Cu.

Impurity behaviour in JET internal transport barrier discharges with reversed shear has been investigated for low-Z and medium-Z elements [190]. The analysed high performance discharges had a current profile with strongly reversed shear and a central 'current hole' at the start time of the main heating power phase [191]. The shear reversal was induced by applying Lower Hybrid Current Drive (LHCD) during the current ramp up before the application of the main heating power. Fig.5.9 gives the evolution of C, Ne and Ni densities in discharge #51976 [192] with a high performance ITB of $\approx 1\,\text{s}$ duration. The plasma is constantly heated with $17\,\text{MW}$ of NBI and $4\,\text{MW}$ of ICRH. The total neutron rate reaches a maximum value of $4.1 \times 10^{16}\,\text{s}^{-1}$. The toroidal field is $B_T = 3.4\,\text{T}$ and the rising plasma current has a maximum value of $I_p = 2.4\,\text{MA}$. Before the formation of the strong barrier, at t=5.8 s, T_i has an almost constant gradient length for the depicted radial range, and the impurity density profile is hollow or mildly peaked. A strong barrier in T_i, T_e and n_e forms at t$\approx$5.9 s. At t=6.2 s, the normalised T_i gradient is increased at a mid plane radius of $R \approx 3.5\,\text{m}$. The radius with increased normalised T_i gradient shifts towards larger radii for the following time slices due to an expansion of the barrier width and due to the increasing Shavranov shift. For the later times, the radial region of the T_i barrier location is depicted by a vertical light grey bar. Inside that region T_i becomes progressively flat. Here, n_e and the impurity densities develop the strongest gradient and the radial region with increased density gradients is given by a darker grey bar. The impurity peaking increases with the impurity charge Z and is weakest for C and very strong for Ni. At t=6.9 s, the dominant Z_{eff} contribution is due to Ni and reaches a value of ΔZ_{eff}=1.5 for Z_{eff}=3.5 causing a dilution of $\Delta n_e/n_e$=6%. Thus, the profile of the main ion density n_D has not much reduced peaking compared with n_e.

The observed impurity accumulation is a pure transport effect due to convective particle flows. The radial transport of C, Ne and Ni has been simulated for #51976 with the impurity transport code STRAHL. In Fig.5.10, various profiles for three time points during the ITB phase t=6.2, 6.6, and 6.8 s are shown and compared with measurements. n_e(Fig.5.10a), T_i (Fig.5.10b), and T_e profiles were taken from the experiment. n_D follows from the impurity ion distributions and quasi neutrality. The classical, Pfirsch-Schlüter and banana-plateau contribution of the transport parameters were numerically evaluated by solving the coupled equations for the parallel velocities of a four component plasma
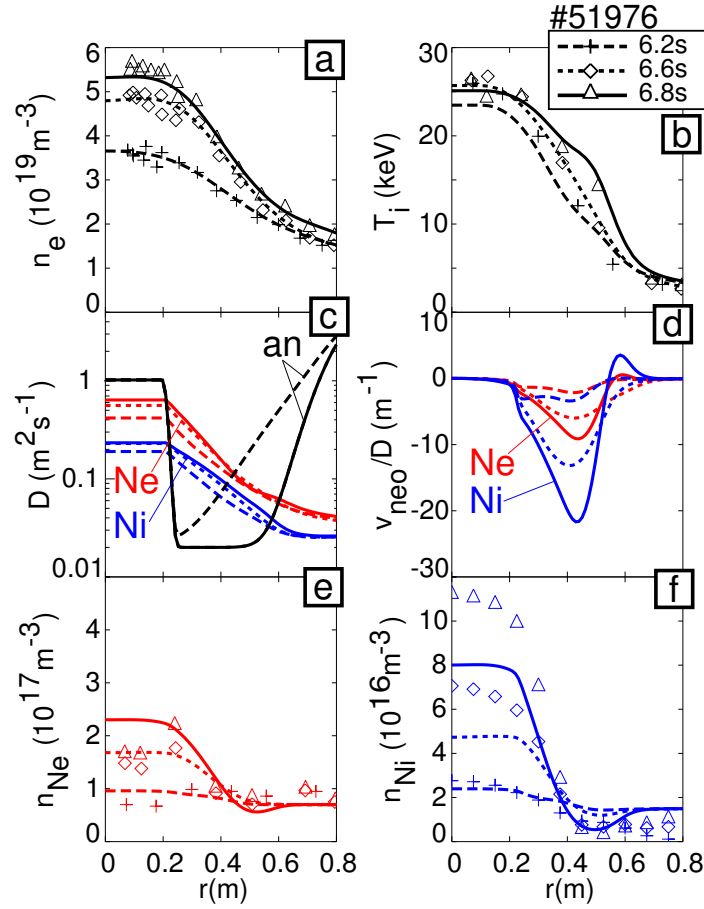
Figure 5.10: *Three radial profiles of n_e, T_i, D_{an}, D_{neo}, v_{neo}/D, n_{Ne} and n_{Ni} from the impurity transport simulation of the JET discharge #51976. The overlaid symbols give experimentally measured profiles.*

(D,C,Ne,Ni) with NEOART [39, 33, 8] using the fractional abundances of the different ion stages from the impurity transport code. Collisions between the different impurity species are included in the calculation of the neoclassical transport parameters. The value of D_{an}, which is assumed to be equal for all species, is set ad hoc. Close to the axis ($r{\leq}0.2\,$m) the poloidal field becomes very low, the orbits of trapped particles are very large and standard neoclassical theory may not be applied. Here, the measured profiles are flat and a high value of $D_{an}{=}1\,$m^2/s is used to describe this situation. For $r{>}0.2\,$m, the anomalous diffusion coefficient is chosen to be below D_{neo} with $D_{an}{=}0.02\,$m^2/s for radii inside the radius of the ITB and to increase from the ITB radius towards the edge. The radial evolution of the ITB radius is thus reflected in a broadening of the region with low D_{an} (see Fig.5.10c). Transport analysis of this discharge was performed by Budny [193]. The ratio of the ion thermal diffusivity to the neoclasscical diffusivity χ_i/χ_{neo} was found to decrease strongly in the ITB to values around 1, and adds support to the assumption of low impurity diffusion coefficient in the ITB.

The simulation starts at t=5.8 s using radially constant impurity density with n_C=5×10^{17}m^{-3}, n_{Ne}=7×10^{16}m^{-3}, and n_{Ni}=1.5×10^{16}m^{-3}. Fixed impurity densities at r=0.8 m are used as boundary condition. During the ITB phase, the neoclassical transport becomes increasingly convective with inwardly directed (negative) drift velocities in the radial region with weaker temperature gradient and pronounced electron peaking while in the region with strong temperature gradient v$_{neo}$ is close to zero or outwardly directed in the case of Ni. For Ne and Ni, the according diffusion coefficients D_{neo} are shown in Fig.5.10c while the ratio v$_{neo}$/(D_{neo}+D_{an}) is depicted in Fig.5.10d. The plot of v$_{neo}$/D demonstrates, that transport is more convective for Ni, the element with higher Z compared to Ne and stronger peaking is expected for Ni. This can be seen in Fig.5.10e and Fig.5.10f, where the simulated density profile of Ni evolves a much stronger peaking than Ne. While the measured Ne densities are well described by the model, there is still not enough peaking of Ni in the simulation. The central density at t=6.8 s is n_{Ni}=8×10^{16}m^{-3}, i.e. 27% below the measured value. An artificial increase of the neoclassical drift of Ni by a constant factor of 1.4 yields a perfect match of measured and simulated profile evolution. When choosing the value of D_{an} inside the ITB a factor of 5 higher, i.e. D_{an}=0.1 m^2/s, the central Ni density rises only to n_{Ni}=6.4×10^{16}m^{-3} at t =6.8 s and an increase of the neoclassical drift by a factor of 1.8 is needed to fit the observed Ni peaking.

The screening effect due to the ion temperature gradient, which induces an outwardly directed contribution to the neoclassical drift velocity, was tested by two additional simulations. When retaining the ion temperature gradient in the pressure driven thermodynamic force while setting the thermodynamic force due to the ion temperature gradient to zero, the inward convection becomes much too large and the central Ni density at t=6.8 s is 350% above the measured value. When neglecting the ion temperature gradient in both thermodynamic forces the central Ni density evolves to values 80% above the measurement. Thus, the screening due to the ion temperature gradient yields an important contribution to v_{neo} even though it is not sufficient to suppress the accumulation of Ni. Due to the uncertainties in the choice of D_{an} and in the measured gradients, it is difficult to quantify the goodness of the neoclassical transport description, however, there is certainly qualitative agreement between measured impurity evolution and the simulation, which assumes a dominating neoclassical transport.

Finally, the peaking of the main ion species D has been investigated. When assuming purely diffusive transport for D, the formation of the strong n_D gradient in the radial range r=0.3-0.5 m can be explained from the centrally peaked particle fuelling density due to the NBI heating together with a diffusion coefficient of D≈0.1 m^2/s in this radial range. However, it cannot be excluded, that the transport of D also contains additional inward/outward pinch velocities combined with a higher/lower diffusion coefficient.

5.4 Impurity Transport in the H-Mode Barrier

The radial impurity transport in the edge region of H-mode plasmas is temporally modulated when Edge Localised Modes (ELMs) are present. ELMs expel impurities from the confined plasma and are essential to achieve stationary H-mode discharges with low impurity concentrations. Assessments of the transport parameters in the edge region of ELM free H-mode plasmas on ASDEX [194], JET [195, 196, 132, 145], DIII-D [197] and Alcator C-Mod [109, 198] showed, that the assumption of an inward drift is indispensable to explain the rapid rise of impurity radiation [194, 195], the observed shape of the total [196] and soft X-ray(SXR) radiation [198] and the SXR and VUV radiation from injected impurities using Laser Blow-Off [132, 145, 109]. Transport simulations of the experimental findings were most sensitive to the ratio of drift velocity v and diffusion coefficient D and the used values in the barrier region were in the range $v/D \approx -(50\text{-}100)\,\mathrm{m}^{-1}$.

The above mentioned investigations are in some respect indirect, since they are not based on a measure of the impurity density evolution in the H-mode barrier, which has to be detected with very high spatial resolution of a few mm on a dense grid of measurement points to resolve the large gradients. Furthermore, a high temporal resolution of $\approx 100\,\mu$s is required to follow the impurity evolution during an ELM cycle and to determine transport parameters from the density evolution. T_e and n_e, whose profiles exhibit very steep gradients, need to be known with the same precision for the transformation of the radiation measurements to impurity densities. The required mapping of the different measurements on the flux surface geometry creates a further challenge for the precision of magnetic equilibrium reconstruction.

At ASDEX Upgrade, 1D simulations of impurity transport in the H-mode barrier were performed for a discharge with several $\approx 50\,$ms long ELM free H-mode phases and Ne puffing [199]. An inward pinch with $v/D \approx -30\,\mathrm{m}^{-1}$ had to be used inbetween ELMs, where the modeling of the measured radiation patterns yielded only the ratio v/D as a robust quantity.

Independent determination of v and D can be achieved, when combining the analysis of supplementing transport experiments, using constant impurity puffing and laser blow-off injection respectively. In the first experiment[200], neon was puffed during the plateau phase of an H-mode discharge with type-I ELMs, ELM frequency $f_{ELM} \approx 100$Hz and discharge parameters: P_{NI}=5 MW (D→D$^+$), B_T=2.5 T, I_p=1.2 MA, q_{95}=3.3, average triangularity δ=0.15, and $\bar{n}_e$=6.3×10^{19}m^{-3} = 0.4 $\bar{n}_{GW}$. At the edge, T_e and n_e were measured with the vertical Thomson scattering system, while the measurements with the DCN interferometer and the ECE radiometer complemented the profiles in the core. The soft X-ray camera system was equipped with 12μm thick Be-filters (detection efficiency >0.1 for photons with energies > 0.84 keV) and had a radial resolution of $\Delta R \approx 10$ mm. A slow radial shift of the plasma column by ΔR=2 cm was performed to get a dense
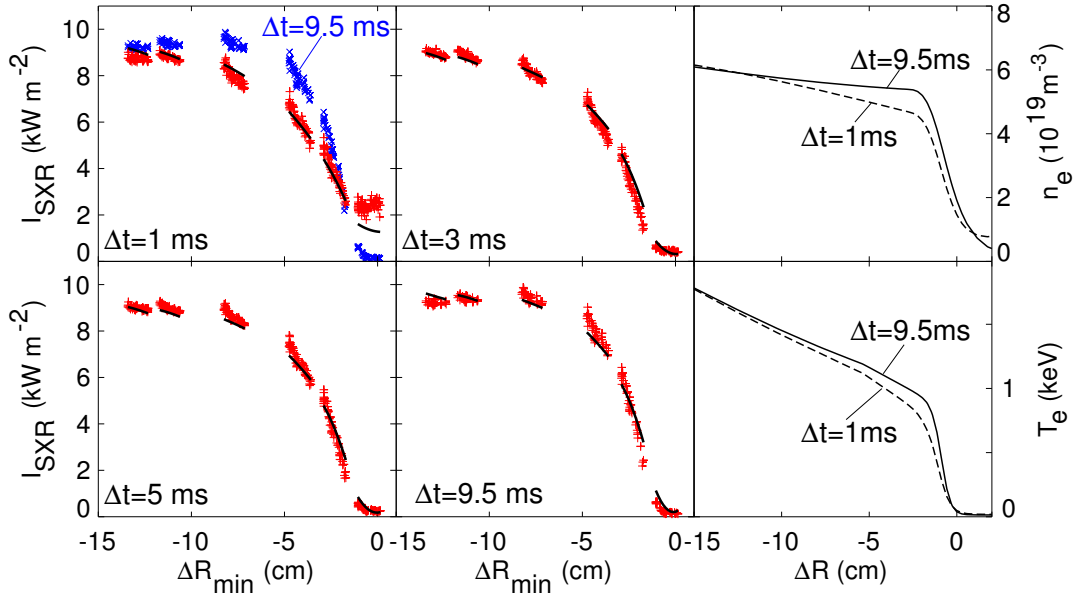
Figure 5.11: For the H-mode discharge #13158 with Ne puffing, the SXR radiation flux I_{sxr}, n_e, and T_e are shown versus the radial distance ΔR of the flux surface to the separatrix for different times during an ELM cycle. The measured SXR radiation (red and blue symbols) is dominated by Ne line radiation of the H- and He-like ion. The black dashed lines are calculated SXR radiation fluxes applying the impurity transport model from Fig.5.12.

spatial grid of measurement points for T_e, n_e and SXR radiation. Measurements during many ELM cycles were overlayed by mapping onto the time difference to the start of the preceding ELM Δt_{ELM} in order to determine the time evolution of T_e, n_e and soft X-ray radiation during an average ELM cycle.

In Fig.5.11 radial profiles of the SXR radiation flux I_{sxr}, T_e, and n_e are shown versus the radial distance ΔR of the flux surface to the separatrix at the low field side in the equatorial plane of the plasma. T_e and n_e are shown for a time point shortly after the ELM at Δt_{ELM}=1 ms and shortly before the next ELM at Δt_{ELM}=9.5 ms. I_{sxr} is depicted for four time points during an ELM cycle and the radial coordinate is the minimum ΔR of the line-of-sight. The SXR profiles are dominated by the line radiation of He- and H-like Ne with photon energies around 1 keV. A strong modulation of I_{sxr} during an ELM cycle is observed for $\Delta R_{min} \geq -10$ cm, which can not be explained by the change of T_e or n_e. This is particularly obvious for the channels which are nearly tangent to the separatrix. Here, each ELM produces a large positive spike in a plasma region with $T_e \approx 100$eV.

The temporal evolution of I_{sxr} was simulated by a 1D edge impurity transport model, whose features are shown in Fig. 5.12. The ELM is assumed to cause a strong rise of the diffusion coefficient in the edge region, while the drift velocity is assumed to be
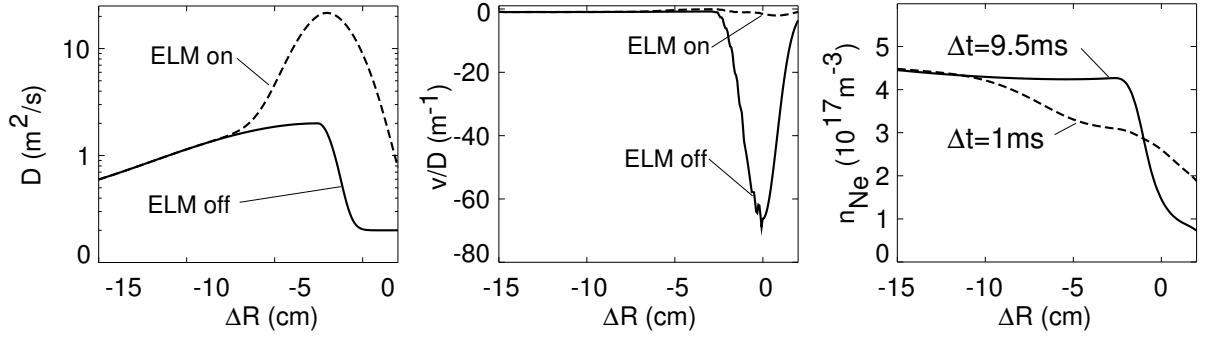
Figure 5.12: Edge profiles of D and v used in the model for the impurity transport during an ELM and in between ELMs versus ΔR and the resulting Neon density distribution.

negligible for the impurity transport during an ELM. At the start of the ELM a large diffusion coefficient with D_{max}=20 m^2/s is switched on followed by a linear decrease to the Pre-ELM values during 1.5 ms. This large diffusion coefficient can only cause a loss of the impurity content if the impurity density in the edge of the confined region develops a negative slope in the quiescent phase of an ELM cycle. Since the impurity source is located outside the separatrix, an inwardly directed pinch must be present in the phase between ELMs. For the pinch velocity in between ELMs a parametrisation is used which connects the drift parameter v/D to the electron density gradient length with $v/D=d(\ln n_e)/dr$, where v/D is assumed to decay in the SOL. The resulting v/D-profile (see Fig. 5.12) reaches a minimum value of $-70\,\mathrm{m}^{-1}$. The equilibrium density ratio between pedestal top and separatrix $F_{peak} = \exp\left[-\int_r^a (v/D)dr\right]$ of the chosen v/D-profile is F_{peak}=5 being very similar to the peaking factor F_{peak}=4.5 used in [199], where the width of the inward pinch region was given a larger radial extent. D is set to decrease from the edge to the centre for $\Delta R<-2.5\,\mathrm{cm}$ as shown in previous experiments on impurity transport in ASDEX Upgrade H-mode plasmas [162, 163, 76] with a maximum value of D_{max}=2m^2/s. For $\Delta R>-2.5\,\mathrm{cm}$, a strongly decreasing diffusion coefficient is chosen which reaches the edge value D_{edge}=0.2m^2/s at $\Delta R\approx-1\,\mathrm{cm}$. The resulting loss of impurity content in the confined plasma during an ELM is $\approx$7%. The Ne profile before and after the ELM is shown in Fig.5.12. It evolves a strong negative gradient between ELMs, which is flattened during the ELM.

For the calculation of the SXR radiation during an ELM cycle, neon, carbon and silicon are considered. The C concentration is taken from charge exchange recombination spectroscopy (CXRS) with values of $c_C \approx$1% and a Si concentration of 0.04% is assumed in accordance with the SXR emission before the start of the Ne-puff. The SXR radiation of Ne exceeds the contributions of the other species by about a factor of 4. The anomalous part of the transport is expected to be independent of Z [35] and equal transport coefficients for all impurities are used disregarding the Z-dependence of the neoclassical part of the transport. The Ne densities are adjusted to give a good fit of the innermost
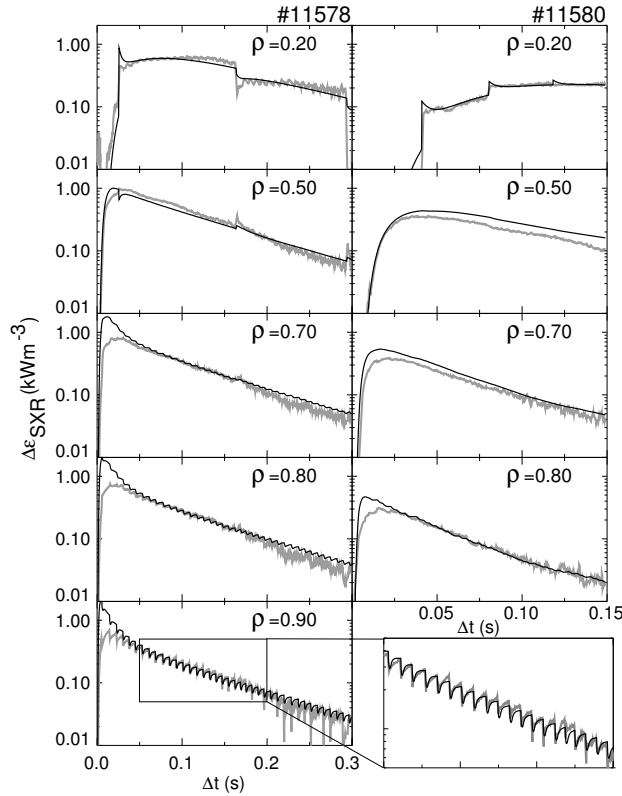
Figure 5.13: Measured (grey) and modelled (black) time traces of the offset reduced SXR emission after Laser Blow-Off of Si in H-mode discharges with type-I ELMs and different ELM frequency of $130\,\mathrm{Hz}$ (#11578) and $270\,\mathrm{Hz}$ (#11580). The edge transport parameters during an ELM cycle are as in Fig.5.12. Note the excellent agreement of simulated and measured time evolution during ELMs at ρ=0.9 in #11578! For #11580, $\Delta\epsilon_{sxr}$ at ρ=0.9 is below noise level. The jumps of $\Delta\epsilon_{sxr}$ at ρ=0.2 are caused by sawteeth which in the model are simply described by complete flattening of the impurity density inside a mixing radius.

line-of-sight of the SXR camera for the time point before the ELM. The calculated SXR emission is integrated along the lines-of-sight and the evolution of the calculated radiation fluxes is in agreement with the measurements as shown in Fig. 5.11. A variation of D_{edge} around the model value of $0.2\,\mathrm{m^2/s}$ was tested. When changing D_{edge} the inward pinch velocity has to be adjusted until the particle loss during an ELM is again $\approx$7%. For D_{edge}=$0.05\,\mathrm{m^2/s}$ the minimum value of v/D is $-150\,\mathrm{m^{-1}}$ and for D_{edge}=$1\,\mathrm{m^2/s}$ the minimum value of v/D is $-18\,\mathrm{m^{-1}}$. The resulting emission profiles before the ELM are somewhat too steep(flat) with the high(low) edge diffusion coefficient, however, for the lines-of-sights of the SXR camera simulated and measured radiation fluxes agree always within $\pm$20% independent of the used combination of D_{edge} and v/D.

Additional information about the value of D_{edge} is gained from the analysis of the density evolution of LBO-injected Si, where the same edge transport model is applied. In Fig.5.13

the time traces of the offset reduced SXR emission $\Delta\epsilon_{sxr}$ at several radial positions are compared with the modeling result for two type-I ELMy H-mode discharges with different ELM frequencies of 130 Hz(#11578) and 270 Hz (#11580). The decay time constants for the two discharges differ by about a factor of 2 (85 ms for #11578 and 48 ms for #11580). When the edge barrier is described with a reduced diffusion coefficient without ELM model the different decay times can be simulated with effective edge diffusion coefficients of $0.25\,\mathrm{m^2/s}$ for #11578 and $0.8\,\mathrm{m^2/s}$ for #11580.

For the ELM model, the same edge transport parameters as described above (see Fig.5.12) are used in both discharges and the different decay times are found to be due to the change in ELM frequency. Again, other values of D_{edge} were tested. For each D_{edge}, the observed decays can only be obtained when the v/D profile is chosen as in Fig.5.12, i. e. with a minimum value of $-70\ \mathrm{m^{-1}}$. However, only the transport coefficients depicted in Fig.5.12 with $D_{edge}=0.2\,\mathrm{m^2/s}$ explain both transport situations. Thus, combined analysis of the quasi stationary situation, where the variation during an ELM cycle is investigated, and of the decay time after LBO of non-recycling impurities improves the transport description of the H-mode edge and gives separate values for D and v in the barrier region.

5.5 Summary of Experimental Findings

Experimental information about impurity transport has been obtained from the impurity density profile during steady phases, from profile evolutions after density perturbations or plasma parameter changes, and from simple decay time studies without radial resolution. For recycling impurities, decay time studies allow for an estimate of the characteristic measures for the impurity flows into the pump duct. Most attention was drawn to the global confinement of heilum, and on many tokamks, very effective helium exhaust could be demonstrated for H-mode plasmas with type-I ELMs.

In the confined plasma, measurements of radially resolved transport coefficients could be obtained, which can be summarised as follows. In the major part of the plasma interior, the measured impurity transport coefficients are dominated by turbulent transport, i.e. they are roughly an order of magnitude above the expected values considering only Coulomb collisions. Turbulent transport is suppressed in the central part of the plasma, when the central heat deposition is weak. A strong reduction of anomalous impurity transport is also measured in transport barriers, which might be either an internal transport barrier or the H-mode edge barrier.

The impurity diffusion coefficient, connected with the plasma turbulence, is approximately equal to the effective heat diffusion coefficient, and no strong dependence on impurity mass or charge was found. A strong turbulent impurity pinch, which would

lead to impurity accumulation, has never been observed.

For the case of suppressed turbulent transport in the central plasma or in an ITB, the measured transport coefficients are consistent with the neoclassical values. The pinch velocity rises with the impurity charge and is almost always directed towards the plasma axis. The peakedness of the main ion density is the main drive for the inward drift of the impurities. Heavier impurities are strongly accumulating in the plasma centre, while impurities of lower charge are much less peaked. The accumulation can be controlled by addition of central heating for conventional confinement modes, however, in the case of strong internal transport barriers this scheme has not been successful. Within the H-mode barrier, a strong inward convection is present, whose dependence on impurity charge has not yet been resolved by direct measurements.

MHD events like sawteeth and ELMs lead to a flattening of the density profiles in the respective radial range.

6. Conclusions for Next Step Devices

For the realisation of a burning fusion plasma, it is necessary to keep the impurity concentrations below a certain critical level in order to avoid large energy losses by radiation and reduction of the α-heating power by dilution of the fuel species deuterium and tritium. The limits of the allowed concentrations decrease with the nuclear charge of the impurity species and vary between $\approx 2\%$ for Be and $\approx 10^{-4}$ for W, when assuming for He, a global confinement time of $5\tau_E$. The actual concentrations depend on the production rate and on the impurity transport. This work focused on the radial impurity transport, it's mathematical description, the underlying physical phenomena, the experimental methods and experimental results in comparison with theoretical models. The main question remains, whether the present knowledge is sufficient, to predict impurity transport and the expected impurity concentrations in a burning fusion plasma. It has to be said, that predictive calculations of the impurity densities are not yet possible. To this end, the impurity production at all plasma facing components and the impurity flows in the scrape-off layer would be needed, which requires a calculation of the plasma parameters and the transport coefficients in the edge plasma. Measurements of the two-to three-dimensional distributions of sources and flows are very difficult, and there is no validated model, which would allow for the calculation of the impurity densities at the edge of the confined plasma, e. g. at the top of the H-mode pedestal. Thus, the situation is similar to the predictions of energy transport, where the theory-based models only calculate the profiles inside of the H-mode pedestal with given pedestal values for temperatures and density. For the energy transport, there is however a huge database of energy confinement times, which does not exist for the particle confinement time of impurities, since the total impurity source rates are generally not known.

Therefore, the first step towards impurity density predictions is a calculation of the profiles for a given impurity density at the edge of the confined plasma. There are codes for the collisional impurity transport parameters, for the turbulent part, however, the codes deliver only transport coefficients or fluxes for electrons and heat. Here, the experimental observations can be used, that the impurity diffusion coefficient, connected with the plasma turbulence, is approximately equal to the effective heat diffusion coefficient without significant dependence on impurity mass or charge. Thus, a possible approach
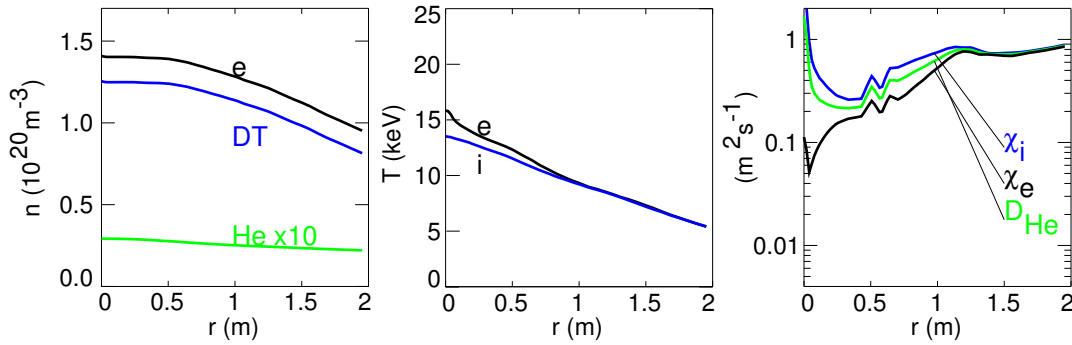
Figure 6.1: Predictions for density and temperature profiles in ITER-FEAT for the $Q = 10$ reference scenario with inductive operation using GLF23 [184].

is to use the anomalous transport parameters from the electrons for all elements, or to set $D_{an} = (\chi_i + \chi_e)/2$. It is important to realize, that an anomalous impurity transport, which does not depend on impurity mass or charge, can never lead to impurity accumulation [174]. Actually, only v_{an}/D_{an} has to be the same for main ions and impurity ions, in order to avoid accumulation due to plasma turbulence. This is not the case for the collisional transport, where we found the increase of v_{neo}/D_{neo} with impurity charge, such that the relative strength of anomalous and neoclassical fluxes becomes crucial. In the major part of the confined plasma, impurity transport is expected to be predominantly anomalous, but for the central part, anomalous and neoclassical transport will become similar or neoclassical fluxes might even dominate. Due to the unknown size of the turbulent transport in the plasma centre, the predictions of impurity density profiles in the confined plasma are therfore still case studies, where the turbulent component in the inner part is varied.

For ITER-FEAT, the spectrum of predictions, which can be achieved for various assumptions about the anomalous impurity transport, shall be illustrated. The starting point is a calculation of heat and particle transport for the reference scenario with inductive operation using the ASTRA code [184, 201]. The main parameters are: $R = 6.2$ m, $a = 2.4$ m, $B_T = 5.3$ T, $I_p = 15$ MA, $U_{loop} = 0.075$ V, $P_{NBI} = 40$ MW, $P_{fus} = 400$ MW. The anomalous fluxes of electrons and heat are calculated with the GLF23 code [51], which is based on ITG/TEM physics. GLF23 does not treat impurity transport and only diffusive transport of Helium is considered, with $D_{an} = (\chi_i + \chi_e)/2$. Dilution and radiative losses by Be(2%) and Ar(0.12%) are included using fixed concentrations. In Fig.6.1, the resulting profiles of n_e, $n_{DT} = n_D + n_T$, n_{He}, T_e, and T_i are shown with the anomalous heat diffusion coefficients χ_i and χ_e. The transport coefficients are not delivered by GLF23, which just returns radial fluxes. There is an inwardly directed particle drift, which leads to the peaking of n_e and n_{DT}.

In the next step, impurity transport is considered for He, Be, Ar and W inside of $r/a = 0.8$. All elements are given a fixed edge concentration: $c_{He} = 2.3\%$, $c_{Be} = 2\%$, $c_{Ar} = 0.1\%$,
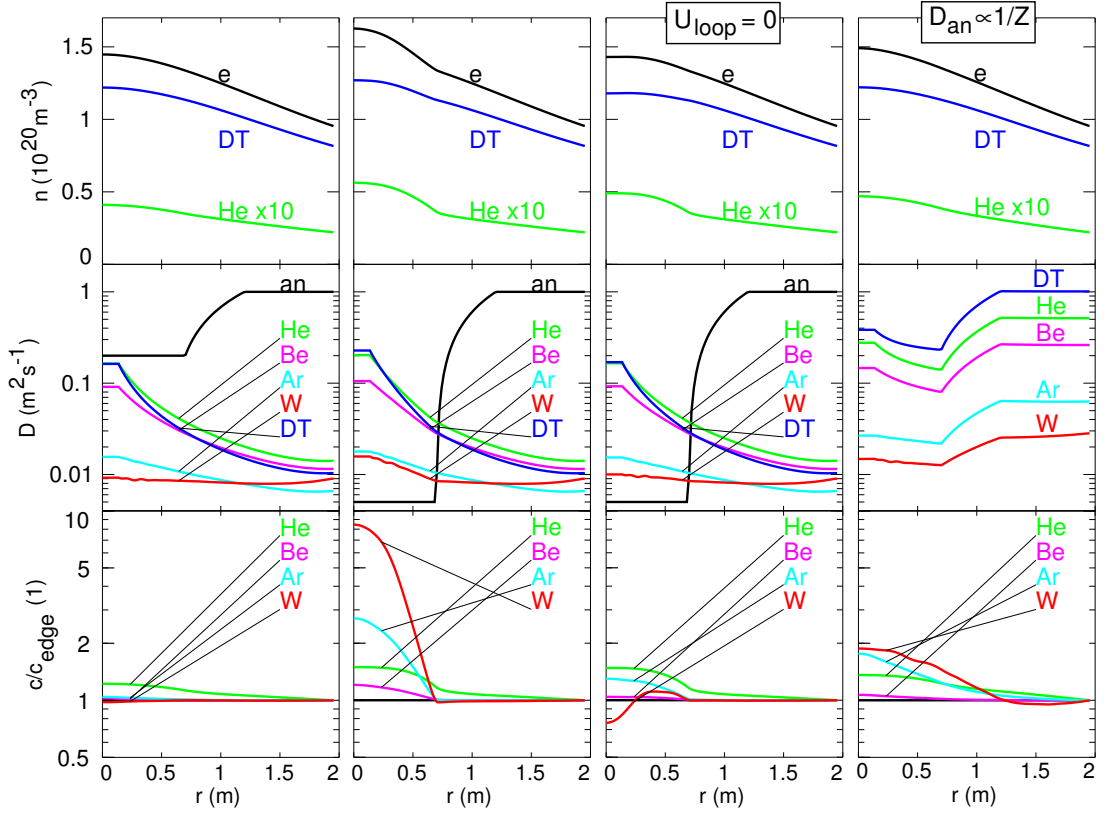
Figure 6.2: Simulated density profiles of D+T, He, Be, Ar and W in ITER-FEAT for the $Q = 10$ reference scenario with inductive operation using different assumptions about anomalous impurity transport. 1st column: dominant anomalous transport in centre as in Fig.6.1 with D_{an} and v_{an} equal for all ions. 2nd column: dominant neoclassical transport in centre. 3rd column: dominant neoclassical transport in centre and Ware pinch switched off. 4th column: D_{an} and v_{an} scale with $1/Z$. The second row gives anomalous and neoclassical diffusion coefficients for column 1-3, and total diffusion coefficients for colum 4.

and $c_W = 0.001\%$. The anomalous diffusion coefficient is given a very simple shape with constant levels for $r < 0.7\,\mathrm{m}$ as well as for $r > 1.2\,\mathrm{m}$, which are linearly interpolated for $0.7\,\mathrm{m} < r < 1.2\,\mathrm{m}$, and at the beginning, the inner and outer levels are chosen to be at $D_{an,in} = 0.2\,\mathrm{m}^2/\mathrm{s}$ and $D_{an,out} = 1\,\mathrm{m}^2/\mathrm{s}$, which approximately reflects the GLF23 profile of $(\chi_i + \chi_e)/2$ from Fig.6.1. The anomalous drift velocity v_{an} is adopted to fit the n_{DT} profile, which was calculated by GLF23. D_{an} and v_{an} are assumed to be equal for all ions. D_{neo} and v_{neo} for the 6 components D, T, He, Be, Ar, and W is calculated with NEOART (see Sec. 3.1.4). The transport of all ions is calculated, n_e follows from the condition of quasi-neutrality, and the profiles of T_e, T_i, and consequently also of the fusion reaction coefficient are kept fixed.

Fig.6.2 shows the equilibrium density profiles, the diffusion coefficients, and the radial shape of the impurity concentrations normalised to their edge value for four different

cases. In the first column, the D_{an} levels were taken at about $(\chi_i + \chi_e)/2$ as given by GLF23. He is slightly more peaked compared to Fig.6.1, since the anomalous drift has been taken into account. D_{neo} is below D_{an} for all species and all radii, and neoclassical transport has almost no influence. Since D_{an} and v_{an} are equal for all species, the concentrations of Be, Ar and W are radially constant. The profiles of the second column are calculated for the case of a low anomalous diffusion coefficient in the inner region, i. e. lower than the neoclassical value of all species. It represents the worst case estimate with respect to He removal and neoclassical impurity accumulation. For He, the additional peaking is predominantly caused by the central fusion source at the lower diffusion coefficient, which requires a larger gradient to maintain the radial flux. For the other impurities, the central peak in the concentration is caused by the neoclassical inward pinch, and rises with the impurity charge. D and T are still peaked in the inner region, even though the anomalous inward pinch plays no role. This is due to the neoclassical Ware pinch as is demonstrated in the third column. Here, the Ware pinch was switched off by artifically setting U_{loop} to zero. The main ion peaking in the neoclassically dominated radial range disappears, the drive for the neoclassical peaking of Be, Ar and W is lost, and their concentration profiles are almost flat. Only for He, the profile is nearly unchanged, since here the peaking was mainly caused by the central fusion source. A strong dependence of turbulent diffusion on impurity mass or charge has not been found experimentally. Nevertheless, the influence of an anomalous diffusion coefficient, which decreases with impurity charge is demonstrated in the 4th column. Here, only the ratio v_{an}/D_{an} is taken not to depend on impurity charge. For D and T, the same levels as in the first column are chosen, and for the other impurities D_{an} shall be proportional to Z^{-1}. Here, D, T, and Be are similarly peaked due to v_{an}, while the high-Z elements feel the neoclassical pinch, which is driven by the peaked low-Z elements. The He profile is not strongly influenced.

As long as turbulent transport is dominant, no impurity accumulation is expected from present experimental experience, which tells, that v_{an}/D_{an} does not increase significantly with ion charge. Only for very low anomalous transport, central accumulation of high-Z elements is found, which is driven by the peaking of the main ion species due to the Ware pinch. The GLF23 results for inductive operation without a central transport barrier suggest sufficient anomalous transport, even in the inner plasma region. Thus, a prediction for the impurity profile shapes in a next step device is mainly a question of validated models of turbulent impurity transport in the confined plasma. However, there is still much work needed, to arrive at a complete picture of the impurity source distribution and the impurity flows in the scrape-off layer in order to understand impurity confinement in fusion plasmas.

A. Detailed Numerical Solution Scheme for the Impurity Transport Equation

The discretisation of the coupled impurity transport equations (2.12) and the numerical solution scheme as given in equations(2.58,2.59) is described in detail. We rewrite Eq.(2.12) for the ion stage z.

$$\frac{\partial n_z}{\partial t} = \frac{1}{r}\frac{d}{dr}r(D_z(r)\frac{dn_z}{dr} - v_z(r)n_z) - \frac{n_z}{\tau_{||}} + R_z + Q_z \qquad (A.1)$$

The parallel loss in the SOL is approximated by a volume loss term with characteristic decay time $\tau_{||}$. The volume sources due to recombination and ionisation between ions with $z' = z \pm 1$ are contained in the reaction term R_z.

$$R_z = n_e(S_{z-1}n_{z-1} + \alpha_z n_{z+1}) - n_z n_e(S_z + \alpha_{z-1}) \qquad (A.2)$$

Q_z describes an external source, e.g. fuelling of singly ionised ions by ionisation of neutrals or generation of He^{++} ions by fusion of D and T.

The mesh points shall be equidistant in the coordinate $\rho = \rho(r)$. Transformation of the transport equation to ρ yields with $d\rho/dr = \rho'$.

$$\frac{\partial n_z}{\partial t} = D_z\rho'^2\frac{d^2n_z}{d\rho^2} + \left((\rho''+\frac{\rho'}{r})D_z + \rho'^2\frac{dD_z}{d\rho} - \rho'v_z\right)\frac{dn_z}{d\rho} - \left(\frac{v_z}{r} + \rho'\frac{dv_z}{d\rho} + \frac{1}{\tau_{||}}\right)n_z + R_z + Q_z \quad (A.3)$$

The change of the density at the radial mesh point i during a time step Δt, i.e. from t to $t + \Delta t$, is calculated by taking the spatial derivatives of the density at time $t + \Delta t/2$. This approach leads to the Crank-Nicolson difference scheme. Denoting the densities at the old time with superscript 0 and the densities at the new time step with 1 the derivatives at the ith mesh point are given by.

$$\begin{aligned}
\frac{dn_z}{dt} &= \frac{n_{z,i}^1 - n_{z,i}^0}{\Delta t} \\
\frac{dn_z}{d\rho} &= \frac{n_{z,i+1}^0 + n_{z,i+1}^1 - n_{z,i-1}^0 - n_{z,i-1}^1}{4\Delta\rho} \\
\frac{d^2n_z}{d\rho^2} &= \frac{n_{z,i+1}^0 + n_{z,i+1}^1 - 2n_{z,i}^0 - 2n_{z,i}^1 + n_{z,i-1}^0 + n_{z,i-1}^1}{2\Delta\rho^2}
\end{aligned} \qquad (A.4)$$

The following notation for the derivatives of diffusion coefficient and drift velocity is used

$$
\begin{aligned}
\frac{dD_z}{d\rho} &= \frac{D_{z,i+1} - D_{z,i-1}}{2\Delta\rho} = \frac{\Delta D_z}{2\Delta\rho} \\
\frac{dv_z}{d\rho} &= \frac{v_{z,i+1} - v_{z,i-1}}{2\Delta\rho} = \frac{\Delta v_z}{2\Delta\rho}
\end{aligned}
\tag{A.5}
$$

This yields the discretisation of the transport equation.

$$
\begin{aligned}
n_{z,i}^1 - n_{z,i}^0 &= \frac{\Delta t}{2}\frac{D_z\rho'^2}{\Delta\rho^2}(n_{z,i+1}^0 + n_{z,i+1}^1 - 2n_{z,i}^0 - 2n_{z,i}^1 + n_{z,i-1}^0 + n_{z,i-1}^1) \\
&+ \frac{\Delta t}{2}\left(\left(\frac{\rho''}{2\Delta\rho} + \frac{\rho'}{2r\Delta\rho}\right)D_z + \frac{\rho'^2}{4\Delta\rho^2}\Delta D_z - \frac{\rho'}{2\Delta\rho}v_z\right)(n_{z,i+1}^0 + n_{z,i+1}^1 - n_{z,i-1}^0 - n_{z,i-1}^1) \\
&- \frac{\Delta t}{2}\left(\frac{v_z}{r} + \frac{\rho'}{2\Delta\rho}\Delta v_z + \frac{1}{\tau_{\|}}\right)(n_{z,i}^0 + n_{z,i}^1) + \Delta t R_z + \Delta t Q_z
\end{aligned}
\tag{A.6}
$$

With $p = \rho'/(2\Delta\rho)$ and $q = \rho''/(2\Delta\rho)$ the equation reads.

$$
\begin{aligned}
n_{z,i}^1 - n_{z,i}^0 &= \frac{\Delta t}{2}4p^2 D_z(n_{z,i+1}^0 + n_{z,i+1}^1 - 2n_{z,i}^0 - 2n_{z,i}^1 + n_{z,i-1}^0 + n_{z,i-1}^1) \\
&+ \frac{\Delta t}{2}\left(\left(q + \frac{p}{r}\right)D_z + p^2\Delta D_z - pv_z\right)(n_{z,i+1}^0 + n_{z,i+1}^1 - n_{z,i-1}^0 - n_{z,i-1}^1) \\
&- \frac{\Delta t}{2}\left(\frac{v_z}{r} + p\Delta v_z + \frac{1}{\tau_{\|}}\right)(n_{z,i}^0 + n_{z,i}^1) + \Delta t R_z + \Delta t Q_z
\end{aligned}
\tag{A.7}
$$

The reaction term changes it form each time step according to equations(2.58,2.59). A time step (I) with implicit treatment of ionisation and explicit treatment of recombination is followed by a time step (II) with explicit treatment of ionisation and implicit treatment of recombination.

$$
R_z = \begin{cases}
n_e(S_{z-1}n_{z-1,i}^1 + \alpha_z n_{z+1,i}^0 - n_{z,i}^1 S_z - n_{z,i}^0\alpha_{z-1}) & \text{(I)} \\
n_e(S_{z-1}n_{z-1,i}^0 + \alpha_z n_{z+1,i}^1 - n_{z,i}^0 S_z - n_{z,i}^1\alpha_{z-1}) & \text{(II)}
\end{cases}
\tag{A.8}
$$

This difference method leads to the solution of a tridiagonal matrix equation for each ion stage on the number of mesh points.

$$
an_{z,i-1}^1 + (b + b^R)n_{z,i}^1 + cn_{z,i+1}^1 = d + d^R
\tag{A.9}
$$

The coefficients $(b + b^R)$ are on the main diagonal, a stands in the lower, c in the upper diagonal and $(d + d^R)$ on the right hand side. The coefficients with superscript R are due to ionisation/recombination reactions.

$$
\begin{aligned}
a &= -2p^2 D_z\Delta t + \frac{\Delta t}{2}\left(\left(q + \frac{p}{r}\right)D_z + p^2\Delta D_z - pv_z\right) \\
b &= 1 + 4p^2 D_z\Delta t + \frac{\Delta t}{2}\left(\frac{v_z}{r} + p\Delta v_z + \frac{1}{\tau_{\|}}\right) \\
c &= -4p^2 D_z\Delta t - a \\
d &= -an_{z,i-1}^0 + (2 - b)n_{z,i}^0 - cn_{z,i+1}^0 + \Delta t Q_z
\end{aligned}
\tag{A.10}
$$

$$b^R = \Delta t \begin{cases} n_e S_z & \text{(I)} \\ n_e \alpha_{z-1} & \text{(II)} \end{cases}$$

$$d^R = \Delta t \begin{cases} n_e(S_{z-1}n^1_{z-1,i} + \alpha_z n^0_{z+1,i} - n^0_{z,i}\alpha_{z-1}) & \text{(I)} \\ n_e(S_{z-1}n^0_{z-1,i} + \alpha_z n^1_{z+1,i} - n^0_{z,i}S_z) & \text{(II)} \end{cases} \tag{A.11}$$

For case (I), the m_z matrix equations are solved in ascending order of z and the density $n^1_{z-1,i}$ of the next lower stage at the new time point is known when needed in the d^R term of the equation for $n^1_{z,i}$. For case (II), $n^1_{z+1,i}$ is needed and the matrix equations are solved in descending order of z.

At the axis $r = 0$, the density gradient and the drift velocity is zero. Expanding density and drift velocity in the vicinity of $r = 0$ yields the transport equation for $r \to 0$.

$$\frac{\partial n_z}{\partial t} = 2D_z(0)\Big[\frac{d^2n}{dr^2}\Big]_{r=0} - 2\Big[\frac{dv_z}{dr}\Big]_{r=0}n_z(0) + R_z + Q_z \tag{A.12}$$

The derivative of v_z at $r = 0$ is replaced by $(v_{z,1} - v_{z,0})/\Delta r$ and the discretisation is.

$$\begin{aligned} n^1_{z,0} - n^0_{z,0} = & \ 2\Delta t \frac{D_z}{\Delta r^2}(n^0_{z,1} + n^1_{z,1} - n^0_{z,0} - n^1_{z,0}) \\ & - \frac{\Delta t}{2}\frac{v_{z,1} - v_{z,0}}{\Delta r}(n^0_{z,0} + n^1_{z,0}) + \Delta t R_z + \Delta t Q_z \end{aligned} \tag{A.13}$$

The coefficients are.

$$\begin{aligned} a &= 0 \\ b &= 1 + 2\Delta t\frac{D_z}{\Delta r^2} + \frac{\Delta t}{2}\frac{v_{z,1} - v_{z,0}}{\Delta r} \\ c &= -2\Delta t\frac{D_z}{\Delta r^2} \\ d &= (2 - b)n^0_{z,0} - cn^0_{z,1} + \Delta t Q_z \end{aligned} \tag{A.14}$$

At the outermost radial mesh point k, the density shall decay with decay length λ.

$$\frac{dn_z}{dr} = -\frac{n_{z,k}}{\lambda} \tag{A.15}$$

The boundary condition defines the density at the virtual mesh point k+1 in terms of the densities at k and k-1

$$\frac{dn_z}{dr} = p(n_{z,k+1} - n_{z,k-1}) = -\frac{n_{z,k}}{\lambda} \qquad n_{z,k+1} = n_{z,k-1} - \frac{n_{z,k}}{p\lambda} \tag{A.16}$$

Eq.(A.7) is modified for the outermost grid point k by replacing the densities at k+1 with Eq.(A.16). Furthermore, derivatives of D_z and v_z are neglected.

$$\begin{aligned} n^1_{z,k} - n^0_{z,k} = & \ \frac{\Delta t}{2}8p^2 D_z\Big(-(1 + \frac{1}{2p\lambda})(n^0_{z,k} + n^1_{z,k}) + n^0_{z,k-1} + n^1_{z,k-1}\Big) \\ & - \frac{\Delta t}{2}\frac{1}{p\lambda}\Big((q + \frac{p}{r})D_z - pv_z\Big)(n^0_{z,k} + n^1_{z,k}) \\ & - \frac{\Delta t}{2}\Big(\frac{v_z}{r} + \frac{1}{\tau_{||}}\Big)(n^0_{z,k} + n^1_{z,k}) + \Delta t R_z + \Delta t Q_z \end{aligned} \tag{A.17}$$

The coefficients are.

$$
\begin{aligned}
a &= -4p^2 D_z \Delta t \\
b &= 1 + 4p^2 D_z \Delta t \left(1 + \frac{1}{2p\lambda}\right) + \frac{\Delta t}{2} \frac{1}{p\lambda}\left(\left(q + \frac{p}{r}\right)D_z - pv_z\right) + \frac{\Delta t}{2}\left(\frac{v_z}{r} + \frac{1}{\tau_\parallel}\right) \\
c &= 0 \\
d &= -an^0_{z,k-1} + (2 - b)n^0_{z,k} + \Delta t Q_z
\end{aligned}
\tag{A.18}
$$

For the hard boundary case $n_{z,edge} = 0$, the coefficients are.

$$
\begin{aligned}
a &= 0 \\
b + b^R &= 1 \\
c &= 0 \\
d + d^R &= 1
\end{aligned}
\tag{A.19}
$$

Bibliography

[1] H.-S. Bosch and G. M. Hale, Improved Formulas for Fusion Cross-Sections and Thermal Reactivities, Nucl. Fusion **32**(4), 611–631 (1992), Erratum in **33**(12), 1919 (1993).

[2] H.-S. Bosch and G. M. Hale, New Evaluation of the Fusion Cross-Sections, in *Proc. of the 17th European Conference on Controlled Fusion and Plasma Heating, Amsterdam, 1990*, volume 14B of *Europhysics Conference Abstracts*, pages 873–876, Petit-Lancy, 1990, EPS, Part II.

[3] H. P. Summers, Atomic Data and Analysis Structure Users Manual, Atomic data and analysis structure users manual, JET-IR 06 (Abingdon: JET Joint Undertaking) (1994).

[4] D. Post, R. V. Jensen, C. B. Tarter, W. H. Grasberger, and W. A. Lokke, Steady-state radiative cooling rates for low-density high-temperatures plasmas, At. Data Nucl. Data Tables **20**, 397–439 (1977).

[5] D. Post, J. Abdallah, R. E. H. Clark, and N. Putvinskaya, Calculations of energy loss due to atomic processes in tokamaks with applications to the ITER divertor, Phys. Plasmas **2**, 2328–2336 (1995).

[6] G. Becker, Transport simulations of ITER with empirical heat diffusivity scaling, Nucl. Fusion **38**(2), 293–312 (1998).

[7] G. Becker, Study of radiation limits in fusion reactor scenarios, Nucl. Fusion **39**(7), 937–948 (1999).

[8] R. Dux and A. G. Peeters, Neoclassical Impurity Transport in the Core of an Ignited Tokamak Plasma, Nucl. Fusion **40**(10), 1721–1729 (2000).

[9] H.-S. Bosch, Die Physik der Alpha-Teilchen in einem Fusionsreaktor mit Deuterium-Tritium-Plasmen, Technical Report IPP-1-325 – Habilitationsschrift Humboldt-Univ. Berlin, Max-Planck-Institut für Plasmaphysik (IPP), Garching(DE), 2000.

[10] Y. I. Kolesnichenko, The Role of Alpha Particles in Tokamak Reactors, Nucl. Fusion **20**(6), 727–780 (1980).

[11] W. Eckstein, C. García-Rosales, and J. Roth, Threshold energy for sputtering and its dependence on angle of incidence, Nucl. Instrum. Methods Phys. Research B **83**, 95–109 (1993).

[12] C. García-Rosales, W. Eckstein, and J. Roth, Revised formula for sputtering data, J. Nucl. Mater. **218**, 8–17 (1994).

[13] W. Eckstein, C. García-Rosales, J. Roth, and W. Ottenberger, Sputter Data, Technical Report IPP 9/82, Max-Planck Institut für Plasmaphysik, Garching, Germany, 1993.

[14] J. Roth, Chemical erosion of carbon based materials in fusion devices, J. Nucl. Mater. **266-269**, 51–57 (1999).

[15] J. Neuhauser, The physics of power exhaust from toroidal magnetoplasmas, Plasma Phys. Controlled Fusion **34**(13), 2015–2022 (1992).

[16] A. Kallenbach, H.-S. Bosch, S. de Peña Hempel, R. Dux, M. Kaufmann, et al., Possible Divertor Solutions for a Fusion Reactor. Part I: Physical Aspects Based on Present Day Divertor Operation, Fusion Eng. Design **36**, 101–108 (1997).

[17] J. Mandrekas, W. M. Stacey, and F. A. Kelly, Robustness of radiative mantle plasma power exhaust solutions for ITER, Nucl. Fusion **37**(7), 1015–1031 (1997).

[18] F. L. Hinton and R. D. Hazeltine, Theory of plasma transport, Rev. Mod. Phys. **48**(2), 239–308 (1976).

[19] G. Fußmann, Analytical Modelling of Impurity Transport in Toroidal Devices, Nucl. Fusion **26**(8), 983–1002 (1986).

[20] W. Engelhardt, G. Becker, K. Behringer, D. Campbell, A. Eberhagen, et al., Divertor Efficiency in ASDEX, J. Nucl. Mater. **111-112**, 337–342 (1982).

[21] D. E. Post and K. Lackner, Plasma Models for Impurity Control Experiements, in *Physics of Plasma-Wall Interactions in Controlled Fusion Devices*, edited by R. Behrisch and D. Post, pages 627–692, New York, 1986, Plenum Press.

[22] K. Behringer, Description of the impurity transport code STRAHL, 'Description of the impurity transport code STRAHL', JET-R(87)08, JET Joint Undertaking, Culham (1987).

[23] R. A. Hulse, Numerical Studies of Impurities in Fusion Plasmas, Nucl. Tech./Fusion **3**, 259–272 (1983).

[24] K. Lackner, K. Behringer, W. Engelhardt, and R. Wunderlich, An Algorithm for the Solution of Impurity Diffusion under Finite Reaction Rates, Zeitschrift für Naturforschung **37a**(5), 931–938 (1982).

[25] J. F. Thompson, Z. U. A. Warsi, and C. W. Mastin, *Numerical Grid Generation, Foundations and Applications*, North-Holland, New-York, 1st edition, 1985.

[26] C. A. J. Fletcher, *Computational Techniques for Fluid Dynamics*, Springer, Berlin Heidelberg New-York, 2nd edition, 1997.

[27] A. Kallenbach, R. Dux, V. Mertens, O. Gruber, G. Haas, et al., H-Mode Discharges with Feedback-Controlled Radiative Boundary in the ASDEX Upgrade Tokamak, Nucl. Fusion **35**(10), 1231–1246 (1995).

[28] J. Roth, K. Krieger, and G. Fussmann, Divertor retention for recycling impurities, Nucl. Fusion **32**, 1835–1844 (1992).

[29] K.-H. Finken, K. H. Dippel, W. Y. Baek, and A. Hardtke, Measurement of helium gas in a deuterium environment, Rev. Sci. Instrum. **63**, 1–7 (1992).

[30] M. Wade, J. Hogan, S. Allen, N. Brooks, D. Hill, et al., Impurity enrichment studies with induced scrape-off layer flow on DIII-D, Nucl. Fusion **38**, 1839–1860 (1998).

[31] W. Ullrich, Helium Transport in ASDEX Upgrade, Laborbericht 1/321, IPP Garching – Doktorarbeit Universität Augsburg, Juli 1999.

[32] A. S. Kukushkin, H. Pacher, G. Janeschitz, A. Loarte, D. Coster, et al., Basic divertor operation in ITER-FEAT, Nucl. Fusion **42**, 187–191 (2002).

[33] S. P. Hirshman and D. J. Sigmar, Tokamak Impurity Transport, Nucl. Fusion **21**(9), 1079–1201 (1981).

[34] F. L. Hinton, Collisional Transport in Plasmas, in *Basic Plasma Physics I*, edited by A. A. Galeev and R. N. Sudan, volume 1 of *Handbook of Plasma Physics*, section 1.5, pages 147–198, North-Holland, Amsterdam, 1st edition, 1983.

[35] G. Fußmann, Teilchentransport in magnetisch eingeschlossenen Plasmen, Technical Report 1/273, IPP, Garching, Germany, Dec. 1992, Habilitationsschrift.

[36] P. Helander and J. Sigmar, *Collisional Transport in Magnetized Plasmas*, Cambridge Univ. Press, Cambridge, 1st edition, 2002.

[37] W. A. Houlberg, K. C. Shaing, S. P. Hirshman, and M. C. Zarnstorff, Bootstrap current and neoclassical transport in tokamaks of arbitrary collisionality and aspect ratio, Phys. Plasmas **4**(9), 3230–3241 (1997).

[38] A. A. Ware, Pinch-Effect oscillations in an unstable tokamak plasma, Phys. Rev. Lett. **25**, 916–919 (1970).

[39] A. G. Peeters, Reduced Charge State Equations that Describe Pfirsch Schlüter Impurity Transport in Tokamak Plasma, Phys. Plasmas **7**(1), 268–275 (2000).

[40] International Atomic Energy Agency (IAEA), Technical Basis for the ITER Final Design Report, Cost Review and Safety Analysis (FDR), ITER EDA Documentation Series 16, IAEA, Vienna, 1998.

[41] ITER Physics Expert Groups, Plasma Confinement and Transport, Nucl. Fusion **39**(12), 2175–2235 (1999).

[42] W. Horton, Drift Waves and Transport, Rev. Mod. Phys. **71**(3), 735–778 (1999).

[43] F. Ryter, J. Stober, A. Stäbler, G. Tardini, H.-U. Fahrbach, et al., Confinement and Transport Studies of Conventional Scenarios in ASDEX Upgrade, Nucl. Fusion **41**(5), 537–550 (2001).

[44] A. J. Reed, A. H. Kritz, G. Bateman, G. Rewoldt, W. M. Tang, et al., Drift mode growth rates and associated transport, Phys. Plasmas **6**, 1162–1167 (1999).

[45] K. H. Burrell, T. N. Carlstrom, E. J. Doyle, D. Finkenthal, P. Gohil, et al., Physics of the L-mode to H-mode transition in tokamaks, Plasma Phys. Controlled Fusion **34**, 1859–1869 (1992).

[46] K. H. Burrell et al., Physics of the L-mode to H-mode transition in tokamaks, Phys. Plasmas **4**, 1499–1519 (1997).

[47] R. C. Wolf, Internal Transport Barriers in Tokamak Plasmas, Plasma Phys. Controlled Fusion **45**, R1–R91 (2003).

[48] K. Lackner, S. Günter, F. Jenko, A. G. Peeters, and R. C. Wolf, Transport barriers in electron and ion transport dominated regimes, Plasma Phys. Controlled Fusion **42**, B37–B50 (2000).

[49] M. Kotschenreuther, W. Dorland, M. A. Beer, and G. W. Hammett, Quantitative prediction of tokamak energy confinement from first-principles simulations with kinetic effects, Phys. Plasmas **2**, 2381–2389 (1995).

[50] H. Nordman, J. Weiland, and A. Jarmen, Simulation of toroidal drift mode turbulence driven by temperature gradients and electron trapping, Nucl. Fusion **30**, 983–996 (1990).

[51] R. E. Waltz, G. M. Staebler, W. Dorland, G. W. Hammett, M. Kotschenreuther, et al., A gyro-Landau-fluid transport model, Phys. Plasmas **4**, 2482–2496 (1997).

[52] G. Tardini, A. G. Peeters, G. V. Pereverzev, F. Ryter, J. Stober, et al., Comparison of Theory Based Transport Models with ASDEX Upgrade Data, Nucl. Fusion **42**(3), 258–264 (2002).

[53] C. Angioni, A. G. Peeters, G. V. Pereverzev, F. Ryter, G. Tardini, et al., Density Peaking, Anomalous Pinch, and Collisionality in Tokamak Plasmas, Phys. Rev. Lett. **90**, 205003 (2003).

[54] K. Krieger, G. Fußmann, and ASDEX team, Determination of Impurity Transport Coefficients by Harmonic Analysis, Nucl. Fusion **30**, 2392–2396 (1990).

[55] H. Takenaga, A. Sakasai, Y. Koide, Y. Sakamoto, H. Kubo, et al., Impurity Transport in Reversed Shear and ELMy H-Mode Plasmas of JT-60U, J. of Plasma and Fus. Res. **75**(8), 952–966 (1999).

[56] H. Takenaga, K. Nagashima, A. Sakasai, N. Asakura, K. Shimizu, et al., Particle Confinement and Transport in JT-60U, Nucl. Fusion **39**(11Y), 1917–1928 (1999).

[57] J. F. Friichtenicht, Laser-generated pulsed atomic beams, Rev. Sci. Instrum. **45**, 51–56 (1974).

[58] E. S. Marmar, J. L. Cecchi, and S. A. Cohen, System for Rapid Injection of Metal Atoms into Plasmas, Rev. Sci. Instrum. **46**, 1149–1154 (1975).

[59] S. A. Cohen, J. L. Cecchi, and E. S. Marmar, Impurity Transport in Quiescent Tokamak Plasma, Phys. Rev. Lett. **35**, 1507–1510 (1975).

[60] S. K. Mattoo, L. Wirtz, A. Pospieszcyck, and B. Schweer, Laboratory Studies of Metal Atomic Beams Produced by Means of UV-Laser Radiation, Nucl. Instrum. Methods Phys. Research B **124**, 579–590 (1997).

[61] R. Neu, K. Asmussen, R. Dux, P. N. Ignacz, M. Bessenrodt-Weberpals, et al., Behaviour of Laser Ablated Impurities in ASDEX Upgrade Discharges, in *Europhysics Conference Abstracts (Proc. of the 22th EPS Conference on Controlled Fusion and Plasma Physics, Bournemouth, 1995)*, edited by B. Keen, P. Stott, and J. Winter, volume 19C, part I, pages 65–68, Geneva, 1995, EPS.

[62] E. S. Marmar and J. L. Terry, Measurement of the internal magnetic field in tokamaks utilizing impurity pellets: A new detection technique, Rev. Sci. Instrum. **61**, 3081–3083 (1990).

[63] S. Morita, E. Kawatoh, K. Ohkobo, et al., Impurity Pellet Injection into Current Driven Plasmas of the JIPP T-IIU Tokamak, Nucl. Fusion **30**, 938–944 (1990).

[64] K. H. Behringer and K. Büchel, Impurity Transport Studies in ASDEX by Means of Neon-Seeded Pellets, Nucl. Fusion **29**, 415–422 (1989).

[65] W. P. West, M. R. Wade, C. M. Greenfield, E. J. Doyle, K. H. Burrell, et al., Energy, particle and impurity transport in quiescent double barrier discharges in DIII-D, Phys. Plasmas **9**(5), 1970–1980 (2002).

[66] S. Sudo, H. Itoh, and K. Khlopenkov, Tracer-encapsulated cryogenic pellet production for particle transport diagnostics, Rev. Sci. Instrum. **68**, 2717–2724 (1997).

[67] K. V. Khlopenkov and S. Sudo, Production and acceleration of tracer encapsulated solid pellets for particle transport diagnostics, Rev. Sci. Instrum. **69**, 3194–3198 (1998).

[68] N. Tamura, S. Sudo, K. V. Khlopenkov, et al., Impurity transport studies by means of tracer-encapsulated solid pellet injection in neutral beam heated plasmas on LHD, Plasma Phys. Controlled Fusion **45**, 27–41 (2003).

[69] S. von Goeler, W. Stodiek, and N. Sauthoff, Studies of Internal Disruptions and m=1 Oscillations in Tokamak Discharges with Soft-X-Ray Techniques, Phys. Rev. Lett. **33**, 1201–1203 (1974).

[70] F. Porcelli, D. Boucher, and M. N. Rosenbluth, Model for sawtooth period and amplitude, Plasma Phys. Controlled Fusion **38**, 2163–2186 (1996).

[71] I. Furno, C. Angioni, F. Porcelli, H. Weisen, R. Behn, et al., Understanding sawtooth activity during intense electron cyclotron heating experiments on TCV, Nucl. Fusion **41**, 403–420 (2001).

[72] A. Letsch, H. Zohm, F. Ryter, W. Suttrop, A. Gude, et al., Incomplete reconnection in sawtooth crashes in ASDEX Upgrade, Nucl. Fusion **42**, 1055–1059 (2002).

[73] F. H. Seguin and R. Petrasso, Effects of Internal Disruptions on Impurity Transport in Tokamaks, Phys. Rev. Lett. **51**, 455–458 (1983).

[74] R. Petrasso, F. H. Seguin, N. G. Loter, et al., Fully Ionized and Total Silicon Abundances in the Alcator-C Tokamak, Phys. Rev. Lett. **49**, 1826–1829 (1982).

[75] K. Ida, R. J. Fonck, S. Sesnic, R. A. Hulse, and B. LeBlanc, Observation Z-Dependent Impurity Accumulation in the PBX Tokamak, Phys. Rev. Lett. **58**(2), 116–119 (1987).

[76] R. Dux, A. G. Peeters, A. Gude, A. Kallenbach, R. Neu, et al., Z-Dependence of the Core Impurity Transport in ASDEX Upgrade H-Mode Discharges, Nucl. Fusion **39**(11), 1509–1522 (1999).

[77] R. Dux, Impurity Transport in ASDEX Upgrade, Fusion Tech. **44**, 708–715 (2003).

[78] R. Dux, C. Giroud, R. Neu, A. G. Peeters, J. Stober, et al., Accumulation of impurities in advanced scenarios, J. Nucl. Mater. **313-316**, 1155–1160 (2003).

[79] P. Bogen and E. Hintz, Plasma Models for Impurity Control Experiments, in *Physics of Plasma-Wall Interactions in Controlled Fusion*, edited by D. E. Post and R. Behrisch, pages 211–280, New York, 1984, Plenum Press.

[80] B. Schweer, P. Bogen, E. Hintz, D. Rusbüldt, S. Goto, et al., Application of laser-induced fluorescence to the measurement of the release, the transport and the ionization of Ti-atoms at the ASDEX divertor plates, J. Nucl. Mater. **111–112**, 71–74 (1982).

[81] R. C. Isler, An overview of charge-exchange spectroscopy as a plasma diagnostic, Plasma Phys. Controlled Fusion **36**, 171–208 (1994).

[82] R. C. Isler, Observation of the Reaction $H^0 + O^{8+} \rightarrow H(O^{7+})^*$ during Neutral-Beam Injection into ORMAK, Phys. Rev. Lett. **38**, 1359–1362 (1977).

[83] V. V. Afrosimov, Y. S. Gordeev, Z. A. N., et al., Light-Impurity Diagnostics in the T-4 Tokamak, Sov. J. Plasma Phys. **5**, 551–556 (1979).

[84] A. N. Zinov'ev, A. A. Korotko, E. R. Krzhizkanovskil, V. Afrosimov, and Y. S. Gordeev, Radial distribution of the concentration of oxygen nuclei in the plasma of the T-10 Tokamak, JETP Lett. **32**, 539–542 (1980).

[85] R. J. Knize, R. J. Fonck, R. B. Howell, et al., Utilization of Charge Exchange Recombination Spectroscopy for the Study of Metallic Ion Transport in TFTR, Rev. Sci. Instrum. **59**, 1518–1520 (1988).

[86] B. C. Stratton, E. J. Synakowski, P. C. Efthimion, et al., Measurement of Iron Transport in the TFTR Tokamak by Charge Exchange Recombination Spectroscopy, Nucl. Fusion **31**, 171–175 (1991).

[87] R. E. Olson, n, l distributions in A^{q+} + H electron-capture collisions, Phys. Rev. A **24**, 1726–1733 (1981).

[88] R. J. Fonck, D. S. Darrow, and K. P. Jaehnig, Determination of plasma-ion velocity distribution via charge-exchange recombination spectroscopy, Phys. Rev. A **29**(6), 3288–3309 (1984).

[89] B. Bransden and M. McDowell, *Charge Exchange and the Theory of Ion-Atom Collisions*, volume 82 of *The International Series of Monographs on Physics*, Clarendon Press, Oxford, 1992.

[90] J. Spence and H. P. Summers, The recombination and level populations of ions. III. The role of charge exchange from neutral hydrogen, J. Phys. B: At. Mol. Phys. **19**, 3749–3776 (1986).

[91] H. Anderson, M. G. von Hellermann, R. Hoekstra, L. D. Horton, A. C. Howman, et al., Neutral beam stopping and emission in fusion plasmas I: deuterium beams, Plasma Phys. Controlled Fusion **42**, 781–806 (2000).

[92] M. G. von Hellermann, R. Jaspers, H. P. Summers, and K. D. Zastrow, Recent progress in beam emission an CX spectroscopy, in *Advanced Diagnostics for Magnetic and Inertial Fusion*, edited by P. E. Stott, A. Wootton, G. Gorini, et al., pages 205–208, New York,NY, 2002, Kluwer.

[93] C. F. Maggi, L. D. Horton, B. Zaniol, P. Franzen, H. Meister, et al., Neutral beam energy scan experiments in ASDEX Upgrade for impurity density evaluation with CXRS, in *Europhysics Conference Abstracts (CD-ROM, Proc. of the 30th EPS Conference on Controlled Fusion and Plasma Physics, St. Petersburg, 2003)*, volume 27A, pages P–1.63, Geneva, 2003, EPS.

[94] J. E. Rice, E. S. Marmar, J. L. Terry, E. Källne, and J. Källne, Observation of charge-transfer population of high-n levels in Ar^{+16} from neutral hydrogen in the ground and excited states in a tokamak plasma, Phys. Rev. Lett. **86**, 50–53 (1986).

[95] M. G. von Hellermann, W. Mandl, H. P. Summers, H. Weisen, A. Boileau, et al., Visible charge exchange spectroscopy at JET, Rev. Sci. Instrum. **61**, 3479–3486 (1990).

[96] A. Boileau, M. von Hellermann, L. D. Horton, J. Spence, and H. P. Summers, The deduction of low-Z ion temperature and densities in the JET tokamak using charge exchange recombination spectroscopy, Plasma Phys. Controlled Fusion **31**, 779–804 (1989).

[97] P. Gohil, K. H. Burrell, R. J. Groebner, J. Kim, W. C. Martin, et al., The Charge Exchange Recombination Diagnostic System on the DIII-D Tokamak, in *Proceedings of the 14th IEEE/NPSS Symposium on Fusion Engineering*, pages 1199–1204, New York, 1992, IEEE.

[98] R. E. Bell, L. E. Dudek, B. Grek, D. W. Johnson, and R. W. Palladino, Tokamak fusion test reactor poloidal rotation diagnostic, Rev. Sci. Instrum. **70**, 821–826 (1999).

[99] H. Meister, A. Kallenbach, A. G. Peeters, A. Kendl, J. Hobirk, et al., Measurement of Poloidal Flow, Radial Electric Field and $E \times B$ Shearing Rates at ASDEX Upgrade, Nucl. Fusion **41**(11), 1633–1644 (2001).

[100] A. Kallenbach and H.-M. Mayer, Characteristics of a Freely Programmable ICCD Detector for Multichord Particle Influx Measurements on the ASDEX Upgrade Tokamak, Rev. Sci. Instrum. **64**(5), 1257–1262 (1993).

[101] K. H. Burrell, D. H. Kaplan, P. Gohil, et al., Improved charge coupled device detectors for the edge charge exchange spectroscopy system on the DIII-D tokamak, Rev. Sci. Instrum. **72**, 1028–1033 (2001).

[102] K. Asmussen, K. B. Fournier, J. M. Laming, R. Neu, J. F. Seely, et al., Spectroscopic Investigation of Tungsten in the EUV Region and the Determination of its Concentration in Tokamaks, Nucl. Fusion **38**(7), 967–986 (1998).

[103] R. Neu, K. Fournier, D. Bolshukhin, and R. Dux, Spectral lines from highly charged tungsten ions in the soft-X-ray region for quantitative diagnostics of fusion plasma, Physica Scripta **T92**, 307 (2001).

[104] D. Bolshukhin, R. Neu, D. Schlögl, R. Dux, and ASDEX Upgrade Team, Measurement of Spurious Impurity Concentrations in ASDEX Upgrade by X Ray Spectroscopy, Rev. Sci. Instrum. **72**(11), 4115–4124 (2001).

[105] T. Pütterich, R. Dux, J. Gafert, A. Kallenbach, R. Neu, et al., Carbon Influx Studies in the Main Chamber of ASDEX Upgrade, Plasma Phys. Controlled Fusion **45**(10), 1873–1892 (2003).

[106] K. Behringer, W. Engelhardt, G. Fußmann, and the ASDEX Team, Particle Transport Phenomena in ASDEX, in *Proc. IAEA Tech. Comm. Meeting, Garching, 1981*, page 42, Garching, 1981, Max-Planck-Institut für Plasmaphysik.

[107] J. E. Rice and E. S. Marmar, Five-Chord High-Resolution X-Ray Spectrometer for Alcator C-Mod, Rev. Sci. Instrum. **61**, 2753–2755 (1990).

[108] M. A. Graf, J. E. Rice, J. L. Terry, et al., Spectroscopic Measurements of Impurity Transport Coefficients and Penetration Efficiencies in Alcator C-Mod Plasmas, Rev. Sci. Instrum. **66**, 636–638 (1995).

[109] J. E. Rice, J. L. Terry, J. A. Goetz, Y. Wang, E. S. Marmar, et al., Impurity transport in Alcator C-Mod plasmas, Phys. Plasmas **4**(5), 1605–1609 (1997).

[110] W. Biel, I. Ahmad, C. J. Barth, G. Bertschinger, R. Dux, et al., Progress in impurity transport studies on TEXTOR using new VUV spectrometers with high time resolution, in *Europhysics Conference Abstracts (CD-ROM), Proc. of the 28th EPS Conference on Controlled Fusion and Plasma Physics, Funchal, 2001*, volume 25B, page P4.015, Geneva, 2001, EPS.

[111] B. L. Henke, E. M. Gullikson, and J. C. Davis, X-ray interactions - photoabsorption, scattering, transmission, and reflection at E=50-30,000 eV, Z=1-92, At. Data and Nucl. Data **54**, 181–342 (1993).

[112] C. Fuchs, Calibration of Detectors for Plasma Diagnostics in the Soft X-Ray Region, Diplomarbeit 1/292, IPP, Garching, Germany, 1995.

[113] P. A. Ross, Polarization of x-rays, Phys. Rev. **28**, 425 (1926).

[114] P. Kirkpatrick, On the Theory and Use of Ross Filters, Rev. Sci. Instrum. **10**, 186–191 (1939).

[115] P. Kirkpatrick, Theory and Use of Ross Filters. II, Rev. Sci. Instrum. **15**, 223–229 (1944).

[116] N. E. Lanier, S. P. Gerhardt, and D. J. den Hartog, Low-cost, robust filtered spectrometer for absolute intensity measurements in the soft x-ray region, Rev. Sci. Instrum. **72**, 1188–1191 (2001).

[117] I. N. Bogatu, J. S. Kim, D. H. Egdell, T. Snider, N. H. Brooks, et al., X-ray Ross filter method for impurity transport studies on DIII-D, Rev. Sci. Instrum. **72**, 1192 (2001).

[118] S. Hokin, R. Fonck, and P. Martin, A simple multifoil spectrometer for routine carbon and oxygen measurements, Rev. Sci. Instrum. **63**, 5038–5040 (1992).

[119] T. Shimizu and T. Horigome, Indirect Abel Inversions by Power Series and SALS, Contrib. Plasma Phys. **29**, 307–314 (1989).

[120] G. Pretzler, H. Jäger, T. Neger, H. Philipp, and J. Woisetschläger, Comparison of Different Methods of Abel Inversion using Computer Simulated and Experimental Side-On Data, Z. Naturforsch. **47a**, 955–970 (1992).

[121] A. N. Tikhonov, Solution of incorrectly formulated problems and regularization method, Dokl. Akad. Nauk. **151**, 501 (1963).

[122] R. Wunderlich, W. Scheider, and K. Lackner, Entfaltung von Bolometersignalen am Tokamak ASDEX Upgrade (Fall 1: auf Flußflächen konstanter Emissivität), Technical Report IPP 5/37, Max-Planck-Institut für Plasmaphysik (IPP), Garching(DE), 1992.

[123] K. Asmussen, Untersuchungen zum Verhalten von Wolfram in Tokamakplasmen, Technical Report 10/2, IPP, Garching, Germany, Mar. 1996, Ph.D. thesis TU Munich, June 95.

[124] D. Naujoks, K. Asmussen, M. Bessenrodt-Weberpals, S. Deschka, R. Dux, et al., Tungsten as Target Material in Fusion Devices, Nucl. Fusion **36**(6), 671–687 (1996).

[125] D. J. Sigmar, G. S. Lee, C. T. Hsu, and K. W. Wenzel, Nonlinear collisional impurity transport including bifurcations, and coupling to rippling mode, in *Theory of Fusion Plasmas, Proc. Joint Varenna-Lousanne Int. Workshop, Varenna, 1990*, edited by E. Sindoni, F. Troyon, and J. Vaclavik, pages 65–97, Bologna, 1990, EPS.

[126] C. T. Hsu and D. J. Sigmar, Transport induced by ion-impurity friction in strongly rotating, collisional tokamak plasma, Plasma Phys. Controlled Fusion **32**, 499–539 (1990).

[127] R. D. Durst, Vertical asymmetries in soft X-ray emissivity in COMPASS-C, Nucl. Fusion **32**, 2238–2242 (1992).

[128] J. E. Rice, J. L. Terry, E. S. Marmar, and F. Bombarda, X-ray observations of up-down impurity asymmetries in Alcator C-Mod plasmas, Nucl. Fusion **37**, 241–249 (1997).

[129] B. Alper, A. W. Edwards, R. Gianella, R. D. Gill, C. Ingesson, et al., Strong Asymmetries in Impurity Distribution of JET Plasmas, in *Europhysics Conference Abstracts (Proc. of the 23rd EPS Conference on Controlled Fusion and Plasma Physics, Kiev, 1996)*, edited by D. Gresillon, A. Sitenko, and A. Zagorodny, volume 20C, part I, pages 163–166, Petit-Lancy, 1996, EPS.

[130] J. A. Wesson, Poloidal distribution of impurities in a rotating tokamak plasma, Nucl. Fusion **37**(5), 577–581 (1997).

[131] W. H. Press, B. P. Flannery, S. A. Teukolsky, and W. T. Vetterling, *Numerical Recipies in C*, Cambridge Univ. Press, Cambridge, 2nd edition, 1992.

[132] N. Hawkes, Z. Wang, R. Barnsley, K. Behringer, S. Cohen, et al., Transport Studies during Sawteeth and H-Modes on JET using Laser Ablation, in *Europhysics Conference Abstracts (Proc. of the 16th EPS Conference on Controlled Fusion and Plasma Physics, Venice, 1989)*, edited by S. Segre, H. Knoeptel, and E. Sindoni, volume 13B, part I, pages 79–82, Petit-Lancy, 1989, EPS.

[133] M. Mattioli, M. Erba, T. Dudok de Wit, et al., Enhanced Transport of Impurity Ions and Electron Heat Tore Supra Ohmic Discharges Following Nickel Laser Blow-Off Injection, Nucl. Fusion **38**(2), 189–206 (1998).

[134] M. Mattioli, C. De Michelis, and A. L. Pecquet, Laser blow-off injected impurity transport in L-mode Tore Supra plasmas, Nucl. Fusion **38**(11), 1629–1635 (1998).

[135] R. Giannella, L. Lauro-Taroni, M. Mattioli, B. Alper, B. Denne-Hinnov, et al., Role of current profile in impurity transport in JET L mode discharges, Nucl. Fusion **34**(9), 1185–1202 (1994).

[136] M. E. Puiatti, M. Valisa, M. Mattioli, T. Bolzanella, A. Bartolon, et al., Simulation of the time behaviour of impurities in JET Ar-seeded discharges and its relation with sawtoothing and RF heating, Plasma Phys. Controlled Fusion **45**, 2011–2024 (2003).

[137] R. Dux, A. Kallenbach, M. Bessenrodt-Weberpals, K. Behringer, H.-S. Bosch, et al., Measurement and Modelling of Neon Radiation Profiles in Radiating Boundary Discharges in ASDEX Upgrade, Plasma Phys. Controlled Fusion **38**(7), 989–999 (1996).

[138] E. S. Marmar and J. E. Rice, Confinement of Injected Silicon in the Alcator-A Tokamak, Phys. Rev. Lett. **45**, 2025–2028 (1980).

[139] TFR Group, A spectroscopic study of laser injected metallic impurities into TFR tokamak plasmas, Phys. Lett. **87A**, 169–174 (1982).

[140] S. L. Allen, H. W. Moos, E. S. Marmar, and J. E. Rice, Radial Dependence of Decay Times of Emissions from Injected Impurities in Alcator-A Tokamak, Nucl. Fusion **23**, 303–309 (1983).

[141] H. Chen, N. C. Hawkes, L. C. Ingesson, N. J. Peacock, and M. G. Haines, Impurity Transport with Strong and Weak Internal Thermal Barriers in JET Optimized Shear Discharges, Nucl. Fusion **41**(1), 31–46 (2001).

[142] E. S. Marmar, J. E. Rice, J. L. Terry, and F. H. Seguin, Impurity Injection Experiments on the Alcator C Tokamak, Nucl. Fusion **22**(12), 1567–1575 (1982).

[143] M. Mattioli, R. Giannella, R. Myrnäs, C. de Michelis, B. Denne-Hinnov, et al., Laser Blow-Off Injected Impurity Particle Confinement Times in JET and Tore Supra, Nucl. Fusion **35**, 1115–1124 (1995).

[144] E. Scavino, J. S. Bakos, R. Dux, H. Weisen, and TCV team, Effects of plasma shape on laser blow-off injected impurity transport in TCV, Plasma Phys. Controlled Fusion **45**, 1961–1974 (2003).

[145] D. Pasini, R. Giannella, L. Lauro-Taroni, M. Mattioli, B. Denne-Hinnov, et al., Measurements of Impurity Transport in JET, Plasma Phys. Controlled Fusion **34**(5), 677–684 (1992).

[146] B. Denne-Hinnov, R. Giannella, L. Lauro-Taroni, G. Magyar, M. Mattioli, et al., Evidence of an edge impurity transport barrier in JET L-mode plasmas, in *Europhysics Conference Abstracts (Proc. of the 20th EPS Conference on Controlled Fusion and Plasma Physics, Lisboa, 1993)*, edited by J. A. Costa Cabral, M. E. Manso, F. M. Serra, and F. C. Schüller, volume 17C, part I, pages 55–58, Geneva, 1993, EPS.

[147] K. D. Lawson, L. Lauro-Taroni, R. Giannella, N. A. C. Gottardi, N. C. Hawkes, et al., Impurity Transport in JET L-mode discharges, Technical Report JET-P(99)03, JET Joint Undertaking, Abingdon, UK, 1999.

[148] H.-S. Bosch, W. Ullrich, D. Coster, O. Gruber, G. Haas, et al., Helium Transport and Exhaust with an ITER-like Divertor in ASDEX Upgrade, J. Nucl. Mater. **290–293**, 836–839 (2001).

[149] R. Neu, J. C. Fuchs, A. Kallenbach, C. Maggi, V. Rohde, et al., The ASDEX Upgrade Divertor IIb - A Closed Divertor for Strongly Shaped Plasmas, Nucl. Fusion **43**(10), 1191–1196 (2003).

[150] A. Sakasai, H. Takenaga, N. Hosogane, S. Sakurai, N. Akino, et al., Helium exhaust in ELMy H-mode plasmas with W-shaped pumped divertor of JT-60U, J. Nucl. Mater. **266-269**, 312–317 (1999).

[151] A. Sakasai, H. Takenaga, S. Higashijima, T. Nakano, H. Tamai, et al., Helium Exhaust and Forced Flow Effects with Both-leg Pumping in W-shaped Divertor of JT-60U, in *Plasma Physics and Controlled Nuclear Fusion Research 2000*, pages IAEA–CN–77/EX5/5, Vienna, 2000, IAEA.

[152] A. Sakasai, H. Takenaga, H. Kubo, N. Akino, S. Higashijima, et al., Helium exhaust in divertor-closure configuration with W-shaped divertor of JT-60U, J. Nucl. Mater. **290-293**, 957–961 (2001).

[153] M. Groth, P. Andrew, W. Fundamenski, H. Guo, D. Hillis, et al., Helium and neon enrichment studies in the JET Mark IIAP and Mark IIGB divertors, Nucl. Fusion **42**, 591–600 (2002).

[154] K. H. Finken, M. von Hellermann, D. Hillis, P. Morgan, S. Cox, et al., Experiments on Helium Enrichment and Removal at JET, in *Europhysics Conference Abstracts (CD-ROM), Proc. of the 28th EPS Conference on Controlled Fusion and Plasma Physics, Funchal, 2001*, volume 25B, page P5.006, Geneva, 2001, EPS.

[155] K.-D. Zastrow, M. Brix, R. Dux, K.-H. Finken, C. Giroud, et al., Helium ash simulation studies with divertor Helium pumping in JET internal transport barrier

discharges, in *29th Conf. on Controlled Fusion and Plasma Physics, Montreux (2002), O5.02*, EPS, 2002.

[156] H.-S. Bosch, D. Coster, R. Dux, G. Haas, A. Kallenbach, et al., Particle Exhaust Studies in ASDEX Upgrade, Plasma Phys. Controlled Fusion **39**(11), 1771–1792 (1997).

[157] M. R. Wade, D. L. Hillis, J. T. Hogan, R. Maingi, M. M. Menon, et al., Helium Transport and exhaust studies in enhanced confinement regimes in DIII-D, Phys. Plasmas **2**(6), 2357–2365 (1995).

[158] E. J. Synakowski, P. C. Efthemion, G. Rewoldt, B. C. Stretton, W. M. Tang, et al., Helium, iron, and electron particle transport and energy transport studies on the Tokamak Fusion Test Reactor, Phys. Fluids B **5**, 2215–2228 (1993).

[159] M. R. Wade, T. C. Luce, and C. C. Petty, Gyroradius Scaling of Helium Transport, Phys. Rev. Lett. **79**, 419–422 (1997).

[160] M. R. Wade, D. G. Whyte, R. D. Wood, and W. P. West, Characterization of Core Impurity Transport and Accumulation in Various Operating Regimes in DIII-D, in *Europhysics Conference Abstracts (Proc. of the 23rd EPS Conference on Controlled Fusion and Plasma Physics, Kiev, 1996)*, edited by D. Gresillon, A. Sitenko, and A. Zagorodny, volume 20C, part I, pages 287–290, Petit-Lancy, 1996, EPS.

[161] M. R. Wade, W. A. Houlberg, and L. R. Baylor, Experimental Confirmation of Impurity Convection Driven by the Ion-Temperature Gradient in Toroidal Plasmas, Phys. Rev. Lett. **84**(2), 282–285 (2000).

[162] S. de Peña Hempel, R. Dux, A. Kallenbach, H. Meister, and ASDEX Upgrade Team, Low-Z-Impurity Transport Coefficients at ASDEX Upgrade, in *Europhysics Conference Abstracts (Proc. of the 24th EPS Conference on Controlled Fusion and Plasma Physics, Berchtesgaden, 1997)*, edited by M. Schittenhelm, R. Bartiromo, and F. Wagner, volume 21A, part IV, pages 1401–1404, Petit-Lancy, 1997, EPS.

[163] S. de Peña Hempel, Untersuchungen zum Transport leichter Verunreinigungen an ASDEX Upgrade, Technical Report 10/8, IPP, Garching, Germany, July 1997, Doctoral thesis TU Munich, June 97.

[164] J. Stober, C. Fuchs, M. Kaufmann, B. Kurzan, F. Meo, et al., Dependence of the Density Shape on the Heat Flux Profile in ASDEX Upgrade High Density H-Modes, Nucl. Fusion **41**, 1535–1538 (2001).

[165] J. Stober, O. Gruber, M. Kaufmann, R. Neu, F. Ryter, et al., Behaviour of Density Profiles of H-Mode Discharges in ASDEX Upgrade, Plasma Phys. Controlled Fusion **44**(5A), A159–A164 (2002).

[166] J. Stober, R. Dux, O. Gruber, L. Horton, P. Lang, et al., Dependence of Particle Transport on Heating Profiles in ASDEX Upgrade, in *Proc. of the 19th IAEA Conference, Fusion Energy, Lyon, France, October 2002, (CD-ROM)*, pages IAEA–CN–94/EX/C3–7Rb, Vienna, 2002, IAEA.

[167] O. Gruber, A. Kallenbach, M. Kaufmann, K. Lackner, V. Mertens, et al., Observation of Continuous Divertor Detachment in H-Mode Discharges in ASDEX Upgrade, Phys. Rev. Lett. **74**(21), 4217–4220 (1995).

[168] J. Neuhauser, M. Alexander, G. Becker, H.-S. Bosch, K. Büchl, et al., The Compatibility of High Confinement Times and Complete Divertor Detachment in ASDEX Upgrade, Plasma Phys. Controlled Fusion **37**(11A), A37–A51 (1995).

[169] R. Dux, R. Neu, A. G. Peeters, G. Perverzev, A. Mück, et al., Influence of the heating profile on impurity transport in ASDEX Upgrade, Plasma Phys. Controlled Fusion **45**, 1815–1825 (2003).

[170] P. C. Efthimion, S. von Goeler, W. A. Houlberg, E. J. Synakowski, M. C. Zarnstorff, et al., Observation of particle transport barriers in reverse shear plasmas on the Tokamak Fusion Test Reactor, Phys. Plasmas **5**(5), 1832–1838 (1998).

[171] V. I. Gervids and V. A. Krupkin, Investigation of Impurity Diffusion in a Tokamak by Special Methods, JETP Lett. **18**, 60–62 (1973).

[172] W. Engelhardt, O. Klüber, D. Meisel, H. Murmann, S. Sesnic, et al., Accumulation of impurities and stability behaviour in the high-density regime of PULSATOR, in *Plasma Physics and Controlled Nuclear Fusion Research 1978*, volume 1, pages 123–133, Vienna, 1978, IAEA.

[173] R. C. Isler, S. Kasai, L. E. Murray, et al., Impurity Sources and Accumulation in Ohmically Heated ISX-B Discharges, Phys. Rev. Lett. **47**(5), 333–337 (1981).

[174] G. Fußmann, A. R. Field, A. Kallenbach, K. Krieger, K.-H. Steuer, et al., Impurity Transport and Neoclassical Predictions, Plasma Phys. Controlled Fusion **33**(13), 1677–1695 (1991).

[175] R. Petrasso, D. J. Sigmar, K. W. Wenzel, et al., Observation of Centrally Peaked Impurity Profiles Following Pellet Injection in the Alcator-C Tokamak, Phys. Rev. Lett. **57**, 707–710 (1986).

[176] E. J. Synakowski, A. Bengston, A. Ouroua, et al., Spectroscopic Measurements of Light Impurity Peaking after Pellet Injection on TEXT, Nucl. Fusion **29**(2), 311–315 (1989).

[177] L. Lauro Taroni, B. Alper, R. Giannella, K. Lawson, F. Marcus, et al., Impurity Transport of high performance discharges in JET, in *Europhysics Conference Abstracts (Proc. of the 21th EPS Conference on Controlled Fusion and Plasma Physics, Montpellier, 1994)*, edited by E. Joffrin, P. Platz, and P. Stott, volume 18B, part I, pages 1312–1315, Geneva, 1994, EPS.

[178] R. Neu, V. Rohde, A. Geier, A. Kallenbach, K. Krieger, et al., New Results of the Tungsten Programme in ASDEX Upgrade, J. Nucl. Mater. **313–316**, 118–128 (2003).

[179] R. Dux, A. Kallenbach, K. Behringer, R. Neu, S. de Peña-Hempel, et al., Measurement and Modelling of Impurity Transport in Radiating Boundary Discharges in ASDEX Upgrade, in *Europhysics Conference Abstracts (Proc. of the 23rd EPS Conference on Controlled Fusion and Plasma Physics, Kiev, 1996)*, edited by D. Gresillon, A. Sitenko, and A. Zagorodny, volume 20C, part I, pages 95–98, Petit-Lancy, 1996, EPS.

[180] R. Neu, K. Asmussen, K. Krieger, A. Thoma, H.-S. Bosch, et al., The Tungsten Divertor Experiment at ASDEX Upgrade, Plasma Phys. Controlled Fusion **38**, A165–A179 (1996).

[181] R. Neu, R. Dux, A. Geier, A. Kallenbach, R. Pugno, et al., Impurity Behaviour in the ASDEX Upgrade Divertor Tokamak with Large Area Tungsten Walls, Plasma Phys. Controlled Fusion **44**(6), 811–826 (2002).

[182] O. Gruber, R. C. Wolf, R. Dux, C. Fuchs, S. Günter, et al., Stationary H-Mode Discharges with Internal Transport Barrier on ASDEX Upgrade, Phys. Rev. Lett. **83** (1999).

[183] A. C. C. Sips, G. D. Conway, R. Dux, A. Herrmann, J. Hobirk, et al., Progress Towards Steady-state Advanced Scenarios in ASDEX Upgrade, Plasma Phys. Controlled Fusion **44**(5A), A151–A157 (2002).

[184] G. Pereverzev and P. N. Yushmanov, ASTRA Automated System for TRansport Analysis in a Tokamak, 'ASTRA Automated System for Transport Analysis in a Tokamak', IPP-5/98, Max-Planck-Institut für Plasmaphysik, Garching, Germany (Feb. 2002).

[185] M. Z. Tokar, J. Rapp, G. Bertschinger, L. Könen, A. Krämer-Flecken, et al., Nature of High-Z Impurity Accumulation in Tokamaks, Nucl. Fusion **37**(12), 1691–1708 (1997).

[186] G. Van Oost, A. M. Messiaen, V. Philipps, et al., Auxiliary heating experiments with a tungsten test limiter in TEXTOR 94, in *Europhysics Conference Abstracts (Proc. of the 22th EPS Conference on Controlled Fusion and Plasma Physics, Bournemouth, 1995)*, edited by B. Keen, P. Stott, and J. Winter, volume 19C, part I, pages 345–348, Geneva, 1995, EPS.

[187] J. E. Rice, P. T. Bonoli, E. S. Marmar, S. J. Wukitch, R. L. Boivin, et al., Double transport barrier plasmas in Alcator C-Mod, Nucl. Fusion **40**, 510–519 (2002).

[188] P. Gohil, L. R. Baylor, K. H. Burrell, E. J. Casper, T. A. Doyle, C. M. Greenfeld, et al., Recent experimental studies of edge and internal transport barriers in the DIII-D tokamak, Plasma Phys. Controlled Fusion **45**, 601–620 (2003).

[189] H. Takenaga, S. Higashijima, N. Oyama, L. Bruskin, Y. Koide, et al., Relationship between particle and heat transport in JT-60U plasmas with internal transport barrier, in *Proc. 19th IAEA Fusion Energy conference, Lyon*, volume IAEA-CN-94, pages EX/C3–5Rb, Vienna, 2002, IAEA.

[190] R. Dux, C. Giroud, K.-D. Zastrow, and JET EFDA contributors, Impurity transport in internal transport barrier discharges on JET, Nucl. Fusion **44**, 260–264 (2004).

[191] N. C. Hawkes, B. C. Stratton, T. Tala, et al., Observation of Zero Current Density in the Core of JET Discharges with Lower Hybrid Heating and Current Drive, Phys. Rev. Lett. **87**(11), 115001 (2001).

[192] C. D. Challis, X. Litaudon, G. Tresset, Y. F. Baranov, A. Bècoulet, et al., Influence of the q-profile shape on plasma performance in JET, Plasma Phys. Controlled Fusion **44**(7), 1031–1055 (2002).

[193] R. V. Budny, R. Andre, A. Bécoulet, C. D. Challis, G. D. Conway, et al., Microturbulence and flow shear in high-performance JET ITB plasma, Plasma Phys. Controlled Fusion **44**, 1215–1228 (2002).

[194] M. Keilhacker, G. Fussmann, G. von Gierke, J. Janeschitz, M. Kornherr, et al., Confinement and Beta-Limit Studies in ASDEX H-Mode Discharges, in *Plasma Physics and Controlled Nuclear Fusion Research 1984*, volume 1, pages 71–85, Vienna, 1984, IAEA.

[195] K. Behringer, B. Denne, A. Edwards, N. Gottardi, M. von Hellermann, et al., Impurity Transport in JET during H-Mode, Monster Sawteeth and after Pellet Injection, in *Europhysics Conference Abstracts (Proc. of the 15th EPS Conference on Controlled Fusion and Plasma Physics, Dubrovnik, 1988)*, edited by S. Pesic and J. Jacquinot, volume 12B, part I, pages 338–341, Petit-Lancy, 1988, EPS.

[196] R. Giannella, K. Behringer, B. Denne, N. C. Hawkes, M. von Hellermann, et al., Behaviour of Impurities during the H Mode at JET, in *Europhysics Conference Abstracts (Proc. of the 16th EPS Conference on Controlled Fusion and Plasma Physics, Venice, 1989)*, edited by S. Segre, H. Knoeptel, and E. Sindoni, volume 13B, part I, pages 209–212, Petit-Lancy, 1989, EPS.

[197] M. E. Perry, N. H. Brooks, D. A. Content, R. A. Hulse, M. A. Mahdavi, et al., Impurity Transport during the H Mode in DIII-D, Nucl. Fusion **31**(10), 1859–1875 (1991).

[198] T. Sunn Pedersen, R. S. Granetz, A. E. Hubbard, I. H. Hutchinson, E. S. Marmar, et al., Radial Impurity Transport in the H mode transport barrier region in Alactor C-Mod, Nucl. Fusion **40**(10), 1795–1804 (2000).

[199] A. Kallenbach, R. Dux, A. Bard, S. de Peña Hempel, J. C. Fuchs, et al., Radiative Cooling and Improved Confinement in ASDEX Upgrade, in *Europhysics Conference Abstracts (Proc. of the 24th EPS Conference on Controlled Fusion and Plasma Physics, Berchtesgaden, 1997)*, edited by M. Schittenhelm, R. Bartiromo, and F. Wagner, volume 21A, part IV, pages 1473–1476, Petit-Lancy, 1997, EPS.

[200] R. Dux, A. Peeters, A. Gude, A. Kallenbach, R. Neu, et al., Measurement of Impurity Transport Coefficients in the Confined Plasma of ASDEX Upgrade, in *Plasma Physics and Controlled Nuclear Fusion Research 2000*, pages IAEA–CN–77/EXP5/32, Vienna, 2000, IAEA.

[201] G. V. Pereverzev and O. V. Zolotukhin, Predictive Simulation of ITER Performance with Theory-Based Transport Models, in *Europhysics Conference Abstracts (CD-ROM, Proc. of the 30th EPS Conference on Controlled Fusion and Plasma Physics, St. Petersburg, 2003)*, edited by R. Koch and S. Lebedev, volume 27A, pages P–3.138, Geneva, 2003, EPS.